Molecular dissection of ionotropic glutamate receptor delta-family interactions with trans-synaptic proteins

Jordan Clay

A thesis submitted in partial fulfilment of the requirements for the degree of *Doctor of Philosophy* at the University of Oxford

Jesus College

Nuffield Department of Clinical Medicine

Division of Structural Biology

University of Oxford

Trinity Term 2012

Molecular dissection of ionotropic glutamate receptor delta-family interactions with trans-synaptic proteins

Jordan Clay

A thesis submitted in partial fulfilment of the requirements for the degree of Doctor of Philosophy

Jesus College, Nuffield Department of Clinical Medicine, Division of Structural Biology,

University of Oxford, Trinity Term 2012

Abstract

Correct functioning of the brain relies upon the precise connectivity between the billions of neurons that make up this crucial organ. Aberrations in the formation of these elaborate neural networks lead to neurodegenerative and neuropsychiatric disorders. A synapse-spanning molecular triad, involving members of the Neurexin, Cbln and ionotropic glutamate receptor delta families of proteins, is crucial for the accurate formation and proper function of synapses in the cerebellum. This trans-synaptic complex has been implicated in the molecular mechanisms behind motor control and motor learning, and furthermore individual members have been linked to diseases such as Alzheimer's, autism spectrum disorders and schizophrenia.

The major findings presented in this thesis include: crystal structures of the amino-terminal domains (ATD) of the two members of the ionotropic glutamate receptor delta (iGluR-Delta) family, functional characterisation of the effects of disrupting the ATD interface in one member of the iGluR-Delta family, a crystal structure of the C1q domain of Cbln1, biophysical analysis of the molecular interactions within the Neurexin-Cbln1-GluD2 trans-synaptic complex, as well as evidence for the domain arrangement of the ecto-domain of the iGluR-Delta proteins. Together, these data enhance our knowledge of the molecular details of this macro-molecular complex and provide evidence to support models for the mechanisms of their involvement in synapse formation and function, thereby making a contribution to the vast and medically relevant field of molecular neurobiology.

Acknowledgements

Firstly I would like to thank my supervisor, Dr. Radu Aricescu for giving me the opportunity to undertake my DPhil in his laboratory as well as for all his enthusiastic, energetic and encouraging supervision and support. I would also like to thank Dr. Christian Siebold and Prof. Yvonne Jones, from the Division of Structural Biology, for their additional support and advice. I must also thank my collaborators in the laboratories of Prof. Michisuke Yuzaki (Keio University, Japan) and Dr. Terunaga Nakagawa (University of California, San Diego) for their assistance in different aspects of this challenging project. Thanks must go to Prof. Chris O'Callaghan (Nuffield Department of Clinical Medicine), Dr David Staunton (Department of Biochemistry) and Prof. Anton van der Merwe (Department of Pathology) for access to surface plasmon resonance equipment. I would like to thank all members of the Division of Structural Biology for providing an excellent environment to work in, with special thanks going to: Amber Clayton, Dr. Charlotte Coles, Margaret Jones, Dr. Paul Miller, Aletheia Lee, Nikos Mitakidis, Benjamin Bishop, Dr. Ross Robinson, Dr. Yuguang Zhao, Dr. Geoff Sutton, Dr. Elena Seiradake, Dr. Tomas Malinauskas and Dr. Luke Yates for their practical assistance, advice and discussion as well as everyday badinage. I must thank the staff at Diamond Light Source, Oxfordshire, and the European Synchrotron Facility, Grenoble, for giving me the opportunity to collect X-ray diffraction data. I thank the Medical Research Council for funding my studentship, as well as Jesus College and the University of Oxford for their backing. Finally, I would like to thank my Mum and Dad, my brother Jarvis, my Grandma and Hannah for their continued love, support and encouragement throughout my DPhil.

Table of Contents

Chapter 1:

Introduction

1.1 The Synpase and Synaptic Plasticity

1.1.1 The Synapse

It has been estimated that there are approximately 100 billion interconnected neurons in the human brain (Azevedo et al, 2009; Herculano-Houzel, 2012). The remarkable complexity of this organ is revealed when considering this astounding number of electrical cells along with the fact that each neuron has the potential to receive and make connections with an average of roughly 10 000 others (Drachman, 2005). Our brains are involved in controlling countless convoluted processes, including cognitive and behavioural functions such as emotions, intelligence, consciousness, speech, perception, learning and memory, as well as mechanical and physiological processes such as movement and the maintenance of homeostatic conditions throughout the body. Involvement in all of these crucial and abstruse operations is possible due to the elaborate connectivity between individual neurons in the brain, and the dynamic nature of neural communication (Shepherd & Huganir, 2007).

The site of connection and communication between individual neurons is termed the synapse (See Fig 1.1). Synapses are classified into two broad general categories: either excitatory or inhibitory (Cline, 2005). Santiago Ramon y Cajal's 'neuron doctrine' states that: the neuronal synapse is the basic cellular unit of all aspects of brain function (Agnati et al, 2007). Thus, to allow involvement in the complicated processes listed above, the cellular and molecular mechanisms that regulate synapse formation and function must be incredibly intricate and exquisitely synchronized.

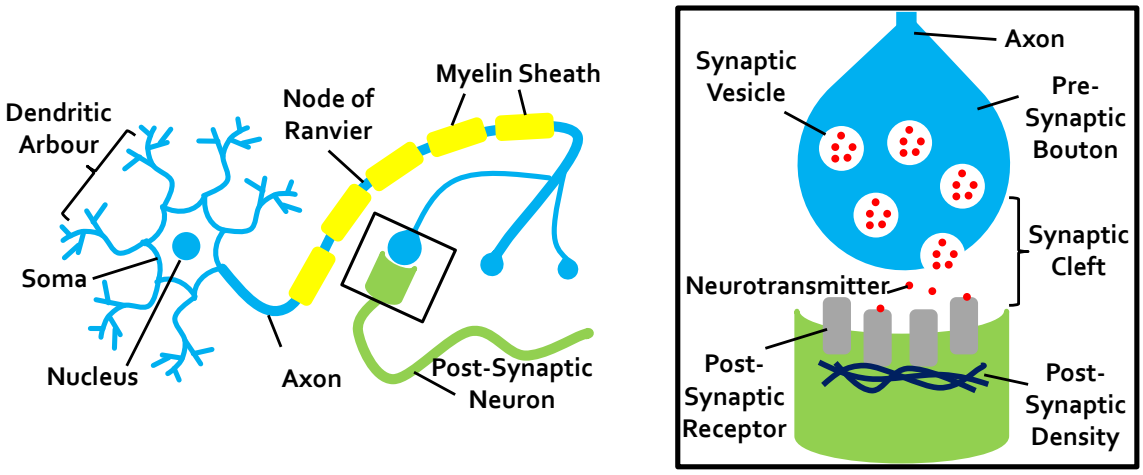

Figure 1.1. The Synapse: *A schematic representing a generic neuron and synaptic connection; key features are labelled.*

Thousands of individual proteins have been shown to be present at synapses, this complement of proteins has been named the 'synaptome' (Bayes et al, 2011), underscoring the molecular complexity of these fascinating features. Identification of how the individual components of this synaptome interact in a dynamic and regulated manner is imperative to the understanding of normal formation and maintenance of synapses, as well as recognising the molecular mishaps underlying a multitude of medical conditions (Grant, 2012). For example, age-dependent cognitive decline and many neurological and psychiatric disorders including autism spectrum disorders (ASDs), schizophrenia, Alzheimer's disease and other forms of dementia, are linked to synaptic perturbations (Clare et al, 2010; Penzes et al, 2011; Selkoe, 2002; Sudhof, 2008). Furthermore it is becoming increasingly apparent that synaptic proteins can become targeted in autoimmune conditions – for example certain forms of encephalitis and ataxia – raising the prospect of treating certain neurological conditions using immunotherapies (Lancaster et al, 2011; Rogers et al, 1994; Vincent et al, 2011).

The synaptic cleft component of this 'synaptome' consists of copious neurotransmitter and other cell surface receptors, adhesion molecules, proteoglycans and secreted proteins, which together establish an intricate network of interactions connecting the pre-synaptic neuron to the post-synaptic cell (Dalva et al, 2007; Shen & Scheiffele, 2010). However, little is known about the higher order organisation of the cleft molecules once they are incorporated in a trans-synaptic network of interactions (Lucic et al, 2005; Zuber et al, 2005). Furthermore, virtually nothing is known about the functional consequences, in both normal and pathological instances, of such supra-molecular arrangements. Therefore, this molecular fabric, impacting on all aspects of synaptic development and function, offers a largely uncharted and intriguing target of study.

This thesis aims to contribute towards defining the principles of synaptic organisation and to open avenues towards a future understanding of native synapses in molecular detail. To achieve this, focus was placed upon a prototypical molecular triad, Neurexin1-Cbln1-GluD2, that spans the cleft of excitatory cerebellar synapses, physically linking the axons of cerebellar granule cells and the dendrites of Purkinje cells, the sole output neuron of the cerebellar cortex (Uemura et al, 2010). Specifically, the objective was to provide structural information, in as much detail as possible, about these molecules and to characterise their interactions using X-ray crystallography in combination with complementary biochemical and biophysical techniques.

1.1.2 Synaptic Plasticity

Synaptic plasticity is the activity-dependent change in the strength of signalling at a synapse. Long-Term synaptic Potentiation (LTP) and Long-Term synaptic Depression (LTD) are the two prevailing cellular models of synaptic plasticity (Malenka & Bear, 2004). These changes in the potency of synaptic signalling are thought to underlie information storage in the brain (Shepherd &

Huganir, 2007). Moreover, LTP and LTD provide an example of how communication between individual neurons can be modified in response to various stimuli.

1.1.3 LTP

LTP is the activity-dependent enhancement in the transmission of synaptic signalling and leads to a persistent increase in the size of the evoked post-synaptic response (Bliss & Gardner-Medwin, 1973; Bliss & Lomo, 1973). This phenomenon has been demonstrated at a number of different types of synapse; however the mechanism underlying this process could be dissimilar at distinct sites and at different times during development (Malenka & Bear, 2004). As an example, *N*-methyl-d-aspartate (NMDA) receptor (See Section 1.3) dependent LTP in the CA1 region of the hippocampus is one of the most well characterised paradigms (Figure 1.2) (Bliss & Collingridge, 1993). In this model, NMDA receptors act as molecular coincidence detectors, whereby they perceive temporally simultaneous yet originally separate input signals; in the case of NMDA receptors, activation requires both ligand binding *and* depolarization of the post-synaptic neuron (Bliss & Collingridge, 1993). The requirement for the latter is a result of a voltage dependent block of the NMDA channel by magnesium ions (Mayer et al, 1984; Nowak et al, 1984). Depolarization is mediated by other ion channels such as α-amino-3-hydroxy-5-methyl-4-isoxazole-propionic acid (AMPA) receptors (See Section 1.3.1) (Collingridge et al, 1983). Once activated and the channels of NMDA receptors are open, an influx of calcium ions leads to the activation of multiple intracellular signalling cascades (Malenka & Bear, 2004). There is strong evidence from multiple studies that calcium/calmodulin-dependent protein kinase II (CaMKII) has a crucial role as a mediator of NMDA receptor-dependent LTP, with one of the known CaMKII targets of phosphorylation being the AMPA receptor subunit GluA1 (Malenka & Nicoll, 1999). Other kinases that have been implicated in LTP include cAMP-dependent protein kinase (PKA), protein kinase C (PKC), the mitogen-activated protein kinase (MAPK) cascade, phosphatidylinositol-3-kinase (PI3 kinase) and Src (Malenka & Bear, 2004). There

are several consequences of protein kinase activation in the context of LTP; substrate phosphorylation leads to increased conductance of AMPA receptors, due to modification of their biophysical properties (Benke et al, 1998; Lee et al, 2003), and increased number of AMPA receptors at the post-synaptic membrane, due to modification in AMPA receptor exo- and endocytotic trafficking pathways (Shepherd & Huganir, 2007). In addition to this, longer term structural changes at the LTP synapse are mediated by alterations in gene transcription – through transcription factors such as cAMP response element-binding (CREB) – and protein synthesis (Malenka & Bear, 2004). Hence, LTP leads to changes in the molecular make-up of the synapse with the result being more potent signal transmission at that particular connection.

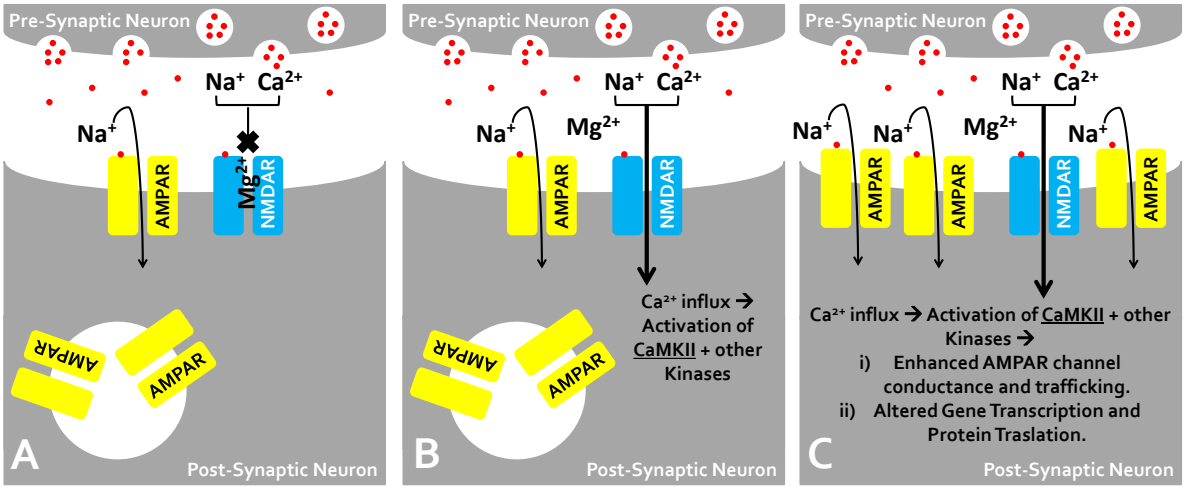

Figure 1.2. Long-Term Synaptic Potentiation: *A schematic representing NMDA receptor-mediated LTP.* ***A:*** *Under resting conditions NMDA receptors (NMDAR) are impermeable due to an Mg^{2+} mediated block.* ***B:*** *Following both ligand binding and depolarization of the post-synaptic neuron, NMDA receptors (NMDAR) allow a Ca^{2+} influx into the post-synaptic cell resulting in the activation of a variety of protein kinases.* ***C:*** *The consequences of this protein kinase activation are changes in AMPA receptor (AMPAR) channel conductance and membrane trafficking, as well modifications in transcription and translation in the post-synaptic cell.*

1.1.4 LTD

LTD is the persistent activity-dependent attenuation in the strength of synaptic signalling and one example, cerebellar LTD is thought to underlie certain forms of motor learning (Ito, 1989). As is the case for LTP, LTD has been observed at multiple sites throughout the brain and a rich diversity of mechanisms exist, depending upon the particular type of LTD (Malenka & Bear, 2004). One of the most well understood mechanisms underlying cerebellar LTD is at the parallel fibre (PF)-Purkinje cell (PC) synapse (See Section 1.2) (Ito, 2002). Similarly to LTP (Section 1.1.3), LTD is a consequence of a modification in the membrane trafficking of AMPA receptors (See Section 1.3.1); LTD is a result of an increase in the amount of clathrin-mediated AMPA receptor endocytosis (Wang & Linden, 2000). At the PF-PC synapse, release of the neurotransmitter glutamate by PF leads to the activation of metabotropic glutamate receptor 1 (mGluR1) and following this, the stimulation of phospholipase C (PLC) which cleaves phosphatidylinositol 4,5-bisphosphate (PIP_2) thus releasing inositol 1,4,5-trisphosphate (IP_3), IP3 then binds to and opens IP_3 receptor channels (IP_3R) leading to the release of intracellular calcium ions from the endoplasmic reticulum (ER) (Ito, 2002). Glutamate release by PF also leads to activation of AMPA receptors which mediate the depolarization of the post synaptic membrane and in turn trigger the opening of voltage-gated calcium channels (VGCC), the action of which further augments the rise in cytoplasmic calcium concentrations (Fitzjohn & Collingridge, 2002). A consequence of this calcium signal is the activation of PKC which phosphorylates GluA2 AMPA subunit C-terminal tails at Serine 880 (Chung et al, 2003). This specific phosphorylation event causes the switching of post-synaptic density (PSD) anchoring protein from GRIP1 to PICK1 (Steinberg et al, 2006). The Ca^{2+} signal also activates calcineurin, a protein phosphatase, which dephosphorylates stargazin, an AMPA receptor auxiliary subunit providing another connection to the PSD (Nomura et al, 2012). The combined outcome of all these molecular processes is an increase in AMPA receptor endocytosis producing long-lasting structural changes to the synapse and a decrease in the strength of synaptic signalling (Ito, 2002). It is also noteworthy

that the post-synaptic transmembrane receptor GluD2 has a vital role in mediating LTD at the PF-PC (Kashiwabuchi et al, 1995), the mechanism of which is discussed in detail in Section 1.4.3.

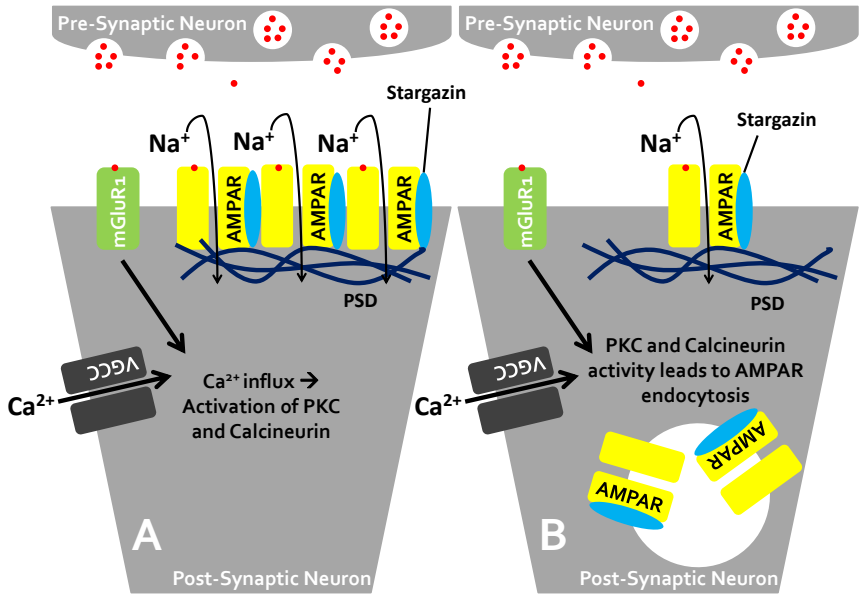

Figure 1.3. Long-Term Synpatic Depression: *A schematic displaying mGluR1-mediated LTD.* ***A:*** *mGluR1 and VGCC activation causes an increase in cytoplasmic Ca^{2+}, activating PKC and calcineurin.* ***B:*** *AMPAR endocytosis results from the actions of PKC and calcineurin.*

1.2 The cerebellum

1.2.1 The Function of the cerebellum

The cerebellum is a neuroanatomical structure that is located in the posterior cranial fossa, beneath the cerebral hemispheres (Figure 1.4 A). It is often termed the "little brain" as it only accounts for roughly 10 % of the volume of the brain. Despite this small size however, it contains more than 50 % of the total number of neurons in the brain, underscoring the importance of the cerebellum as a processing centre (Vogel, 2005) (Manto and Pandolfo, 2002).

Traditionally, the cerebellum has been considered the centre of the brain that is primarily responsible for the coordination of movement and motor learning (Vogel, 2005). In light of the

observations that after ablation of the cerebellum motor ability was not completely lost but was lacking refinement and fine control, it was suggested that the cerebellum was an area of the brain that does not initiate the signals that result in movement but is involved in the coordination and fine tuning of these signals. Some of the most common symptoms following cerebellar pathology include ataxia, limb clumsiness, gait disturbance, speech difficulties and affected balance, reinforcing the idea that the cerebellum is mainly involved in motor control (Glickstein et al, 2009).

In addition to the roles in motor coordination and learning ascribed to the cerebellum, more recent anatomical and functional evaluations of the cerebellum reveal a wider functional role in processes such as language, mood, visuospatial abilities and other executive functions including attention, planning and working memory, problem solving, verbal reasoning and multi-tasking (O'Halloran et al, 2012). Analysis of the global neural connections of the cerebellar neurons, functional magnetic resonance imaging (MRI) and positron emission tomography of brains in healthy and diseased individuals have afforded this further insight into cerebellar function (O'Halloran et al, 2012).

Furthermore the importance of the cerebellum is highlighted by its association with highly complex neuropsychiatric and neurodegenerative disorders. For example, a wide-range of studies consistently link the cerebellum with the etiopathogenesis of autism spectrum disorders (ASDs) (Fatemi et al, 2012). In addition to this, cerebellar dysfunction has been identified in other syndromes such as attention deficit hyperactivity disorder (ADHD), schizophrenia, depression and bipolar disorder (Fatemi et al, 2012; O'Halloran et al, 2012).

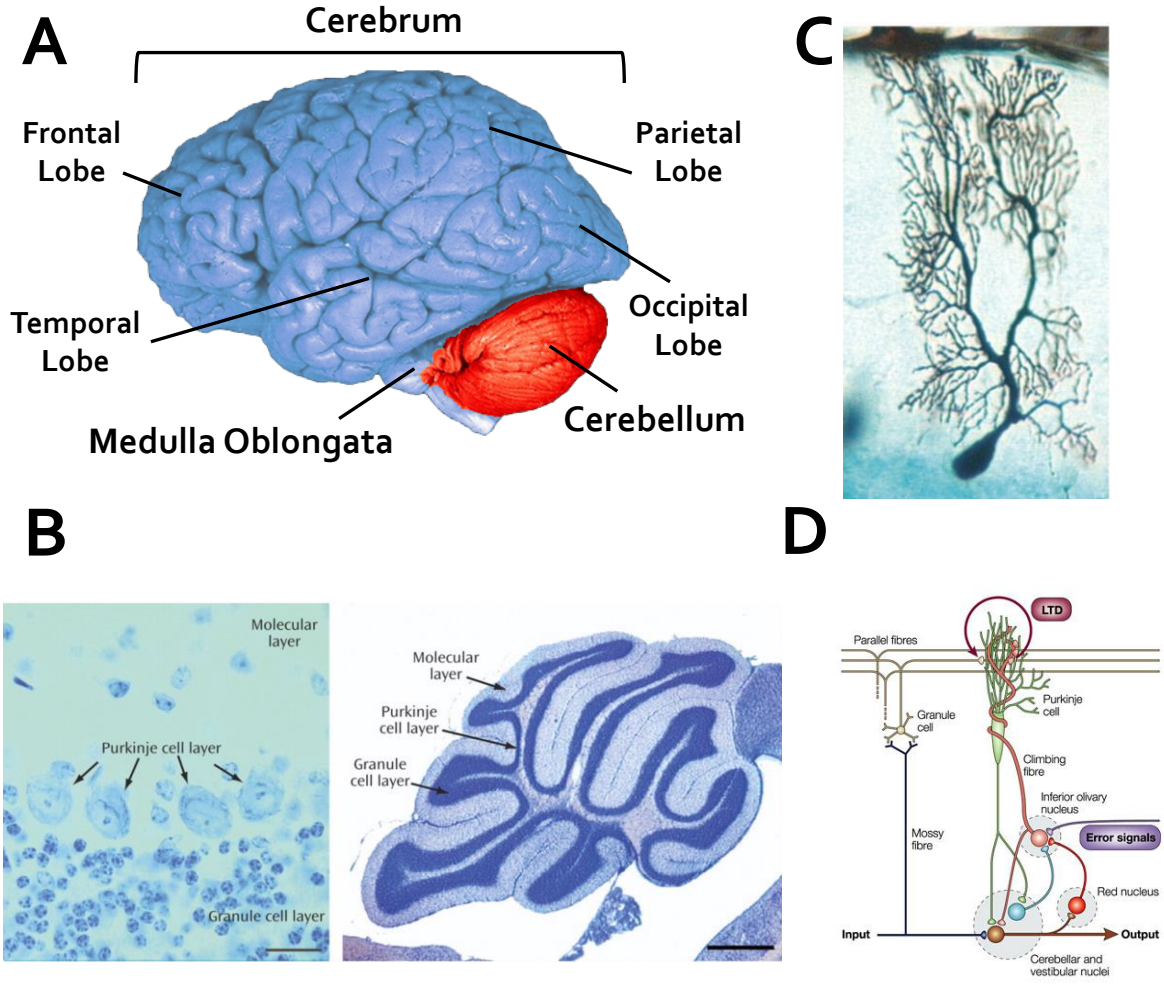

Figure 1.4: The cerebellum. ***A:*** *A schematic representing the various regions of the human brain. The cerebellum is highlighted in red.* ***B:*** *Histological stained samples of mouse cerebellum with the cellular layers of the cerebellar cortex labelled.* ***C:*** *A Purkinje cell visualised with Golgi's stain displaying an extensive and elaborate dendritic arbour.* ***B*** *and* ***C*** *are adapted from (Vogel, 2005).* ***D:*** *A schematic representing the major cellular connections in the cerebellum, adapted from (Ito, 2002).*

1.2.2 Cells of the cerebellum: Cerebellar Granule Cells and Purkinje Cells

The cerebellum consists of two anatomical components, the cerebellar cortex and cerebellar nuclei. The outer surface of the cerebellum is highly convoluted, containing many folds and fissures. Split into distinct layers, the cellular organisation of the cerebellar cortex is fairly simple, being composed of the molecular layer, the Purkinje cell layer and the granule cell layer (Figure 1.4 B). The molecular

layer is mainly made-up of the dendrites of Purkinje cells and granule cell axons. Granule cells are extremely abundant, small neurons, i.e. the diameter of the soma is ~6-8 µm, and are densely packed within the granule cell layer. Granule cells receive an input from mossy fibres originating in nuclei of the pons, and output onto Purkinje cells (Figure 1.4D). The Purkinje cell layer forms the junction between the molecular layer and the granule cell layer and is comprised of Purkinje cell soma. Purkinje cells are relatively large neurons, with a soma ~80 µm in diameter, and some of the most elaborate and distinctive neurons in the brain owing to the extensive, finely branched dendritic arbour (Figure 1.4 C) which is virtually two-dimensional, allowing these neurons to be arranged in parallel. Purkinje cells receive two inputs: one from the cerebellar granule cell Parallel Fibres (PF), and one from Climbing Fibres (CF) (Figure 1.4D). CF originate in the inferior olive and are thus called because their axons wrap around and climb around the Purkinje cell dendrites (Figure 1.4D). Purkinje cells are the major direct output neuron of the cerebellar cortex sending inhibitory connections to the deep cerebellar nuclei and some other extracerebellar regions such as the vestibular nuclei (Figure 1.4D) (Vogel, 2005) (Manto and Pandolfo, 2002).

1.3 Ionotropic Glutamate Receptors

1.3.1 The iGluR superfamily: Members, Functions and Disease

Ionotropic glutamate receptors (iGluRs) are a superfamily of ligand-gated cation channels (Traynelis et al, 2010). As the name suggests, with a few exceptions, these receptors bind the neurotransmitter glutamate as their endogenous ligand. Glutamate is *the* major excitatory neurotransmitter in the Central Nervous System (CNS) and thus iGluRs are a major class of receptors for excitatory synaptic neurotransmission (Dingledine et al, 1999; Traynelis et al, 2010). In addition to this crucial role in excitatory neurotransmission, iGluR superfamily members are also pivotal players in the molecular mechanisms behind important neurophysiological phenomena such

as LTP and LTD (See Section 1.1.2-4), hence iGluRs have a vital role in the changing communication between neurons (Malenka & Bear, 2004; Shepherd & Huganir, 2007).

The iGluR superfamily consists of 18 gene products that are classified into four sub-families named after the synthetic agonists they were originally found to bind (Dingledine et al, 1999). Subunits GluA1-4 constitute the α-amino-3-hydroxy-5-methyl-4-isoxazole-propionic acid (AMPA) receptor subfamily (Boulter et al, 1990; Honore et al, 1982). GluK1-5 compose the Kainate receptor subfamily (Hollmann et al, 1989; Simon et al, 1976). GluN1, GluN2A-D and GluN3A-B comprise the *N*-methyl-d-aspartate (NMDA) subfamily (Kumar et al, 1991). Lastly, GluD1-2 form the Delta-iGluR subfamily (Lomeli et al, 1993). The functional oligomeric state of iGluRs is a tetramer and there is strict subfamily specificity of oligomerization. Several sites of alternative splicing, and mRNA editing, within the various members of the iGluR superfamily produces a rich diversity of receptor subunits beyond the 18 gene products (Dingledine et al, 1999; Traynelis et al, 2010).

Many neurological disorders have been linked to iGluR dysfunction; for example: stroke, Alzheimer's disease, Parkinson's disease, dementia, neuropathic pain, major depression, schizophrenia, behavioural disorders, and class A drug addictions (Conrad et al, 2008; Dingledine et al, 1999; Kemp & McKernan, 2002; Traynelis et al, 2010; Van den Oever et al, 2008). Therefore, there is exciting therapeutic potential from studying the role of iGluRs in a variety of major diseases.

1.3.2 Modular Domain Architecture

The subunits that form the iGluR superfamily range in length between 883-1484 amino acids, and each iGluR subunit is composed of the same modular semi-autonomous domain architecture

comprising, the extracellular amino-terminal domain (ATD), the extracellular ligand-binding core (LBC), the multi-pass transmembrane domain (TMD) and the intracellular C-terminal domain (CTD) (Figure 1.5) (Traynelis et al, 2010).

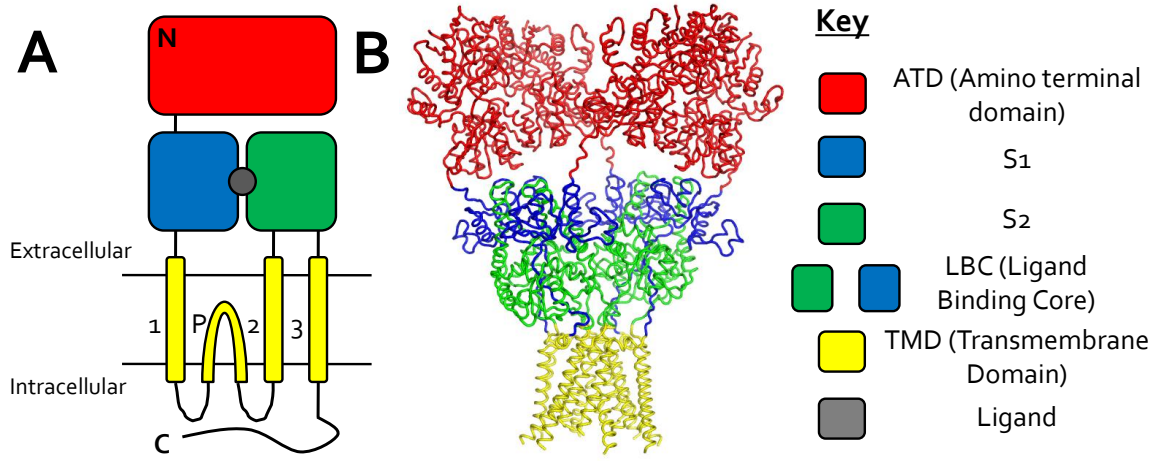

Figure 1.5: iGluR Subunit Structure. ***A:*** *Schematic representation of the common modular architecture of a single iGluR subunit.* ***B:*** *Cartoon representation of the GluA2 tetramer highlighting the modular domain architecture of iGluRs (PDB code 3KG2, (Sobolevsky et al, 2009)).*

The ATD is roughly 400-450 amino acids in length and is the most divergent extracellular domain, in terms of sequence similarity (Traynelis et al, 2010). The iGuR ATD has structural homology to the metabotropic glutamate receptor mGluR1 LBC as well as to the bacterial periplasmic leucine/isoleucine/valine-binding proteins (LIVBP) (Clayton et al, 2009; Paoletti et al, 2000). Unlike these two proteins however, the iGluR ATD has not been found to bind amino acids as ligands (Traynelis et al, 2010). Nevertheless, the ATD has been implicated in a diverse range of roles (Hansen et al, 2010) such as regulating iGluR subunit-selective assembly (Ayalon et al, 2005; Leuschner & Hoch, 1999; Meddows et al, 2001), controlling ion channel open probability (Gielen et al, 2009), influencing deactivation and desensitization, directing agonist potency (Yuan et al, 2009), as well as harbouring binding sites for Zn^{2+} and allosteric modulators such as ifenprodil, in the example of GluN2 subunits (Karakas et al, 2009; Karakas et al, 2011). Furthermore, and most relevant to this thesis, the ATD has been suggested as a site for mediating protein-protein

interactions. For example *N*-cadherin (Saglietti et al, 2007) and the neuronal pentraxins NP1 and NARP (O'Brien et al, 1999; Sia et al, 2007) have been suggested to bind AMPA ATDs and the ephrin receptor EphB (Dalva et al, 2000; Takasu et al, 2002) has been suggested to bind the ATD of NMDA-subtype NR1 subunits. Several crystal structures of a number of iGluR ATDs have been reported; these will be discussed in more detail in Section 1.3.4.

The LBC is composed of a bilobal Venus flytrap domain formed from two non-contiguous extracellular stretches of amino acids termed S1 and S2 (Figure 1.5). The LBC is smaller, ~250 amino acids, and has greater sequence similarity between different iGluR subunits, relative to the ATD (Traynelis et al, 2010). Like the ATD, the LBC has homology to bacterial proteins, the bilobal lysine/arginine/ornithine-binding proteins (LAOBP) (Yuzaki, 2003). As suggested by the name of this domain, the LBC is the site of endogenous ligand binding in iGluRs. Glutamate is the endogenous ligand for most subunits; however GluN1, GluN3A-B and GluD1-2 all bind glycine and D-Serine. The site of agonist binding is the interlobal cleft and the residues important for this function are highly conserved across the iGluRs (Traynelis et al, 2010). Of the 18 gene products that form the iGluR superfamily, crystal structures of the LBC of 11 different iGluR subunits have been reported (Ahmed et al, 2009; Armstrong & Gouaux, 2000; Furukawa & Gouaux, 2003; Furukawa et al, 2005; Gill et al, 2008; Mayer, 2005; Naur et al, 2007; Venskutonyte et al, 2011; Yao et al, 2008). All the crystal structures have confirmed the agonist binding site and clamshell-like conformation, where s1 forms the bulk of the N-terminal lobe and s2 forms the majority of the C-terminal lobe. In addition, extensive structural investigations on isolated LBCs in *apo*, ligand- and antagonist-bound states have provided insights into agonist-induced channel opening and desensitization (Sun et al, 2002). For example, when in the *apo* state LBCs are in an open conformation and agonist binding induces closure of the cleft, this probably sparks a rearrangement in the short LBC-TMD linker which drives channel opening. This movement would result in instability in the TMD and LBC dimer

interface which is rectified by further rearrangements allowing the receptor to enter a desensitized state (Mayer, 2011b; Traynelis et al, 2010). However this mechanism is yet to be verified from crystal structures of intact transmembrane constructs of iGluRs in different conformations.

The TMD domain forms the ion channel and is composed of three α-helices, TM1, 3 and 4, and a re-entrant P-loop, TM2, from each subunit, arranged with 4-fold symmetry. The TM3 helix from each subunit lines the inside of the cation channel and the amino acids forming TM3 are highly conserved across the iGluR superfamily indicating a conserved mechanism of ion permeation (Sobolevsky et al, 2009). The TM4 helix is found at the exterior of the TMD and mediates extensive inter-subunit contacts (Sobolevsky et al, 2009), highlighting the crucial role of the TM4 helix in iGluR assembly (Wollmuth & Sobolevsky, 2004). iGluR TMDs have low sequence homology with the inverted ion channel domain of K^+ channels (Traynelis et al, 2010).

The intracellular CTD varies in length depending upon the particular iGluR subunit and is the most divergent domain across the family overall. Thought to be largely unstructured, the CTD is known to have many protein docking motifs, such as PDZ binding motifs (Traynelis et al, 2010). Numerous intracellular proteins have been found to bind to iGluR C-terminal tails including cytoskeletal, scaffolding, adaptor, anchoring, and signalling proteins; suggesting that protein docking at the CTD has countless roles in mediating intracellular signalling as well as receptor endocytosis and exocytosis (Traynelis et al, 2010). The proteins that bind iGluR CTDs will interact with numerous other proteins suggesting that the CTD may act as a seed for the formation of post-synaptic mega-complexes that form the PSD, potentially containing over 1400 proteins (Bayes et al, 2011). Thus, when embedded in such a PSD complex, iGluRs could be involved in regulating spatial and temporal specificity of signalling, and equally the PSD regulate iGluR function (Traynelis et al, 2010).

1.3.3 Tetrameric Structure of iGluRs

Low resolution single-particle electron microscopy (EM) studies on native and recombinant AMPA receptors demonstrated that this iGluR had an internal two-fold rotational symmetry axis; furthermore these extensive studies of AMPA receptor complexes by single-particle EM have revealed a great deal about the mechanism of trafficking and maturation, i.e. that assembly of these receptors takes place by a dimer of dimers mechanism (Nakagawa, 2010; Nakagawa et al, 2005; Shanks et al, 2010; Tichelaar et al, 2004).

The only crystallographic structure of an intact transmembrane (TM) construct of an iGluR is that of the homomeric rat GluA2 to 3.6 Å (Sobolevsky et al, 2009). This breakthrough achievement provides a greater insight into the arrangement of the various domains in iGluRs (Figure 1.6). In agreement with the EM data, this crystal structure confirmed an overall 2-fold symmetry; however this overall symmetry masks higher symmetry at different domain levels. For example, the TMD has four-fold symmetry consistent with the architecture found in some tetrameric voltage-gated ion channels. The extracellular domains are loosely packed assemblies with distinct ATD and LBC layers. Both layers have a dimer of dimers assembly but the inter-subunit connections are different at each level due to a subunit crossover resulting from two alternative conformations adopted by GluA2 subunits in the tetramer. To clarify, following Figure 1.6, it is clear that two subunit conformations termed A/C and B/D can be observed (Figure 1.6 B); in the ATD layer, A interacts with B and this is equivalent to the C-D interaction (Figure 1.6 C), whereas in the LBC layer, A interacts with D and this corresponds the B-C interaction (Figure 1.6 D), consequently producing the aforementioned subunit crossover (Mayer, 2011a; Sobolevsky et al, 2009). In the ATD layer, in addition to the common A-B and C-D interfaces, there is a unique B-D interface at the closest point

to the global 2-fold symmetry axis, mediating the dimer of dimers arrangement; this unique interface was first observed in a crystal structure of a tetrameric assembly of GluA2 ATDs (Clayton et al, 2009) and was corroborated by the crystal structure of the GluA2 transmembrane homotetramer (Sobolevsky et al, 2009). This remarkable subunit crossover has many potential consequences on the assembly, function and allosteric regulation of iGluRs (Mayer, 2011a; Sobolevsky et al, 2009).

Whilst this 3.6 Å homomeric GluA2 TM tetramer is a notable accomplishment, it is still unclear exactly how this structure changes in conformation upon agonist binding and channel opening, which would require both *apo* and agonist bound TM structures. Additionally there is an indication, based on the GluN1-GluN2B NMDA ATD heteromeric structure, that the packing of the ATD layer in NMDA receptors is different to that shown in Figure 1.6, and thus this may affect overall domain packing of the whole molecule (See Section 1.3.4 (Karakas et al, 2011)). Therefore it is essential that additional TM structures of heteromeric forms and of other iGluR family members are obtained to verify if the global domain assembly seen in the GluA2 homotetramer is common for all the members of the iGluR superfamily and to yield a detailed understanding of the structural mechanisms behind iGluR function.

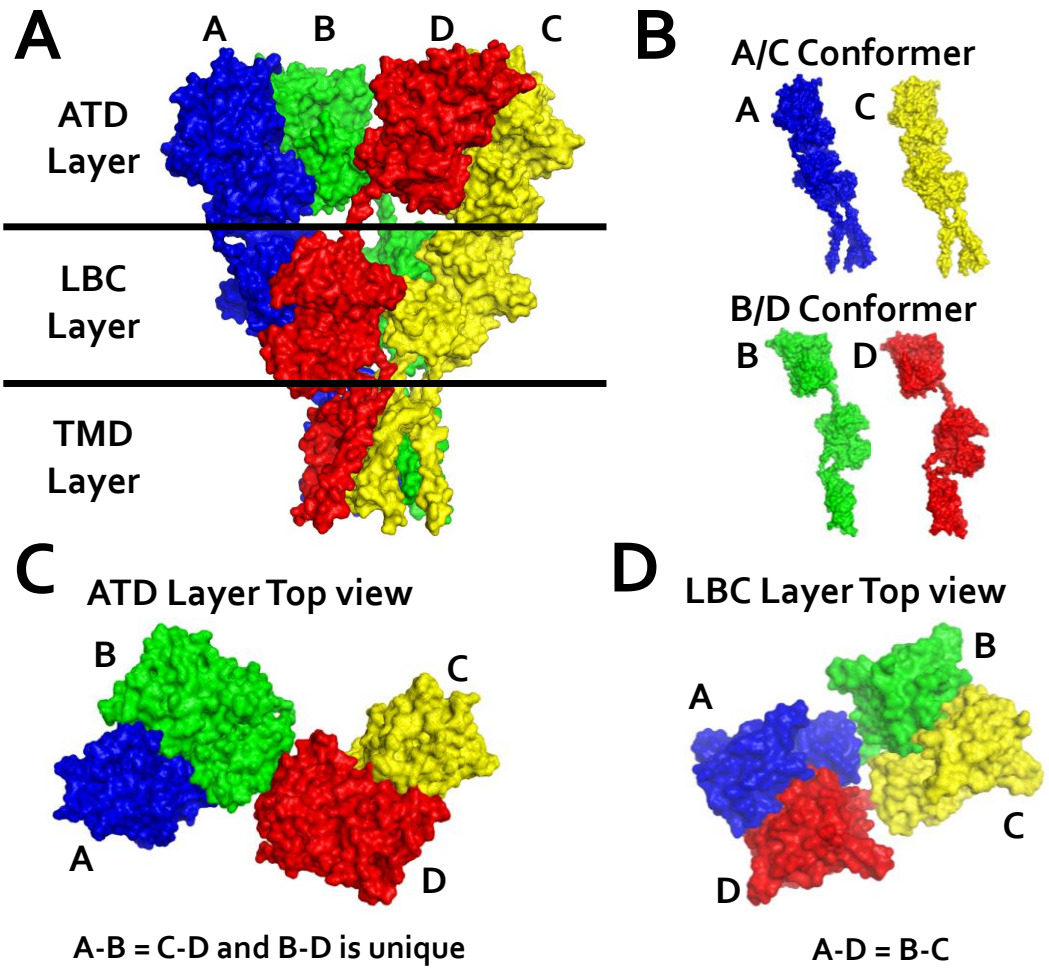

Figure 1.6: Tetrameric Arrangement of GluA2. *Surface representations of the 3.6 Å crystal structure of the GluA2 homotetramer (3KG2, (Sobolevsky et al, 2009)).* ***A:*** *Global, side view of the layered arrangement of the GluA2 heterotetramer.* ***B:*** *Two different conformations of the same polypeptide chain exist in the GluA2 homotetramer, A/C and B/D.* ***C:*** *Top view of the ATD layer displaying the equivalent A-B and C-D interfaces and the unique B-D interface.* ***D:*** *Top view of the LBC layer highlighting the specific subunit interfaces.*

1.3.4 Comparison of iGluR ATDs

Between 2009 and 2011, high resolution crystal structures of the following iGuR ATDs were published: GluA1, GluA2 and GluA3 AMPA ATDs (Clayton et al, 2009; Jin et al, 2009; Sukumaran et al, 2011; Yao et al, 2011); the GluK2, GluK3, GluK5 and GluK2-GluK5 heterodimer Kainate ATDs

(Kumar & Mayer, 2010; Kumar et al, 2009; Kumar et al, 2011); and the GluN1, GluN2B and GluN1-GluN2B heterodimer NMDA ATDs (Farina et al, 2011; Karakas et al, 2009; Karakas et al, 2011).

This wealth of high resolution structural data for iGluR ATDs confirms the overall fold conservation but also reveals striking differences between NMDA and non-NMDA iGluR ATDs (Figure 1.7). Non-NMDA ATDs exist as dimers in solution and packed in crystals suggesting that a dimer is the basic unit of non-NMDA ATDs (Furukawa, 2012; Mayer, 2011a). Also, if we define the most N-terminal ATD lobe as R1 and the most C-terminal ATD lobe as R2, in non-NMDA ATDs there are substantial R1-R1 and R2-R2 interactions (Figure 1.7 A-B). In contrast, the GluN2B ATD exists as a monomer in crystals and solution (Karakas et al, 2009), but will form a heterodimer with GluN1 (Karakas et al, 2011). Another conspicuous feature of NMDA ATDs, when compared to non-NMDA, is that there is a difference in the relative R1-R2 lobe orientation due to a roughly 50^{o} twist (Figure 1.7 D). Furthermore, rather than the symmetrical and extensive R1-R1 and R2-R2 interactions in non-NMDA ATDs (Figure 1.7 A-B), in the heteromeric NMDA ATD dimer the interaction is asymmetric and mediated mainly by the R1 lobe of each subunit (Figure 1.7 C). This alternative subunit packing and the additional freedom the R2 lobe enjoys in the NMDA arrangement could be the reason that ATD-binding allosteric modulators, such as ifenprodil, are known for NMDA receptors but not for non-NMDA iGluRs (Furukawa, 2012; Mayer, 2011a).

This structural information of iGluR ATDs is clearly of great value; however additional work still needs to be done to understand the functional consequences of these molecular details. Additionally, the structures of the many other members of the iGluR superfamily remain to be solved and much work still needs to be done to understand the heteromeric arrangement of the

various iGluR members; perhaps most noticeable, is the absence of any structural data of the ATDs of the Delta iGluR subfamily.

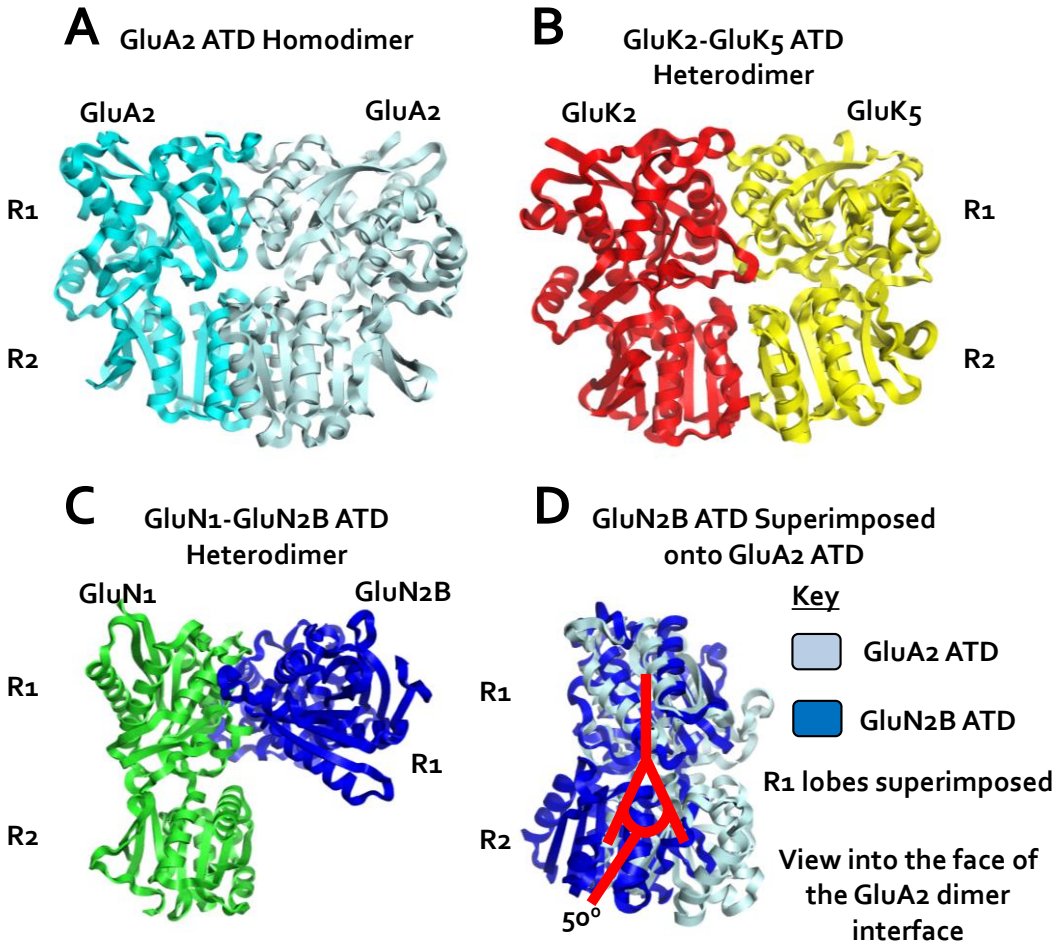

Figure 1.7: iGluR ATDs. *Cartoon representations of various iGluR ATDs.* ***A:*** *GluA2 homodimer (2WJW, (Clayton et al, 2009)) defining N-terminal lobe R1 and the C-terminal lobe R2.* ***B:*** *GluK2-GluK5 ATD heterodimer (3QLU, (Kumar et al, 2011)) presented to highlight the similar R1-R1 and R2-R2 interface when compared to GluA2 ATD homodimer in* ***A****.* ***C:*** *GluN1-GluN2B ATD heterodimer (3QEL, (Karakas et al, 2011)). GluN1 ATD is orientated in an equivalent position to the subunits in the GluA2 ATD homodimer and GluK2-GluK5 ATD heterodimer to emphasise the alternative arrangement of the GluN2B subunit in the NMDA ATD heterodimer assembly.* ***D:*** *GluN2B ATD (3JPW, (Karakas et al, 2009)) superimposed onto GluA2 ATD (2WJW, (Clayton et al, 2009)). An equivalent helix in the R1 lobe was used as the position of superimposition. The proteins are presented with a view into the face of the GluA2 dimer interface. Red lines highlight the central axis of individual lobes of the two ATDs, demonstrating the R1-R2 inter-lobal 50° twist in the GluN2B ATD, relative to the GluA2 ATD.*

1.4 A Trans-Synaptic Ternary Protein Complex

Synapse formation is vital to the development of neural networks and the elucidation of the molecular mechanisms behind this process is a requirement for the complete understanding of brain development, neural wiring, higher brain functions as well as neurological and neuropsychiatric disorders (See Section 1.1.1). Several trans-synaptic protein complexes have been demonstrated to have a role in synapse formation; for example Neurexin-Neuroligin (Graf et al, 2004), SynCAM (Biederer et al, 2002), SALMs (Ko et al, 2006), N-cadherins (Togashi et al, 2002), EphB-ephrin (Kayser et al, 2006), LAR-NGL3 (Woo et al, 2009), and PTPδ-Slitrk3 (Takahashi et al, 2012).

Another example of a trans-synaptic protein complex is that involving pre-synaptic Neurexin (Section 1.7) and post-synaptic GluD receptors (section 1.5), members of the iGluR superfamily (See Section 1.3), mediated by members of the Cbln family (Section 1.6). This Neurexin-Cbln-GluD (Uemura et al, 2010; Yasumura et al, 2012) molecular triad is the focus of this thesis.

The most thoroughly characterised variant of this trans-synaptic triad involves βNeurexin1, Cbln1 and GluD2, which is localised at the PF-PC synapse in the cerebellum, due to the restricted expression pattern of GluD2 in the brain (Figure 1.8). This ternary complex is essential for correct synapse formation in the cerebellum as well as being crucial for the correct alignment of pre-synaptic and post-synaptic zones at the PF-PC synapse (Schmid & Hollmann, 2010). In addition to providing a structural link to the pre-synaptic cell and the post synaptic neuron, there is evidence that this ternary complex signals in both the anterograde and retrograde directions and that members of this complex are essential for synaptic plasticity at the PF-PC synapse, highlighting the

role for the βNeurexin1-Cbln1-GluD2 triad in multiple signalling pathways (Schmid & Hollmann, 2010; Uemura et al, 2010).

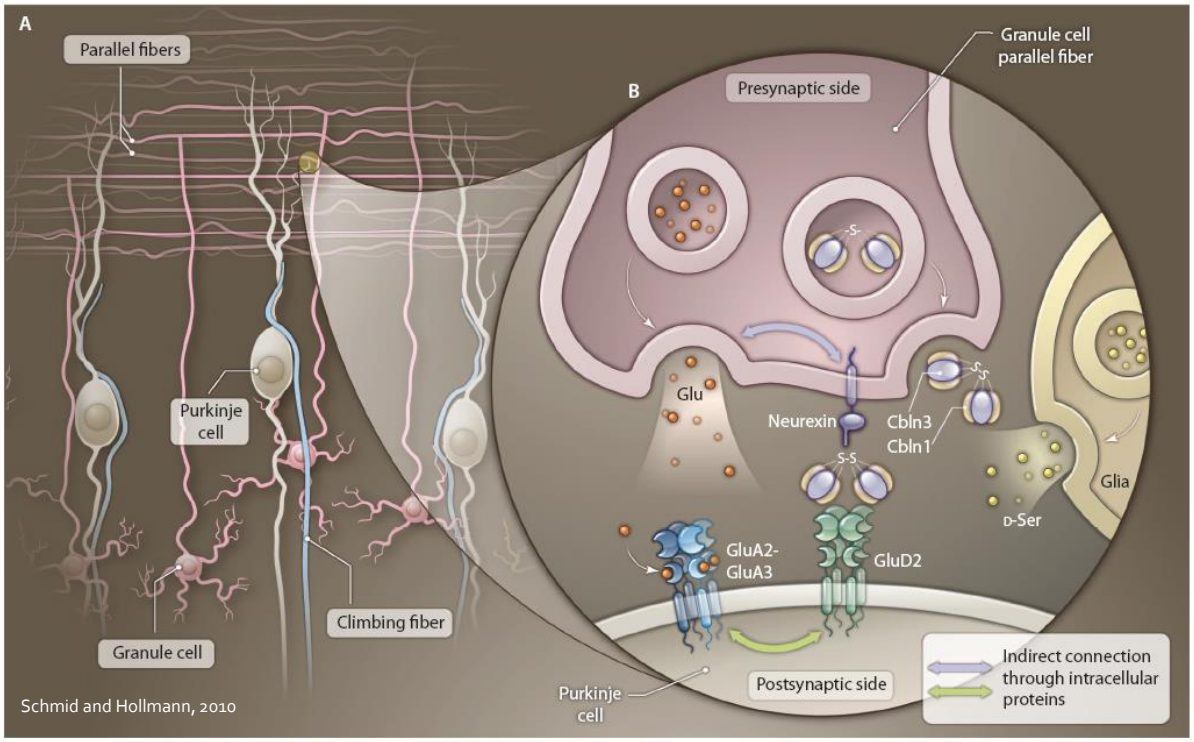

Figure 1.8: The Neurexin-Cbln1-GluD2 Trans-Synaptic Bridge. A: Cartoon representation of Purkinje cells, the main output neuron of the cerebellar cortex. Purkinje cells receive inputs from two types of neurons, Climbing Fibres and Parallel Fibres. **B:** At the Parallel Fibre-Purkinje cell synapse, a trans-synaptic complex is formed between β-Neurexin + SS4 and GluD2, mediated by the secreted Cbln1. This complex signals bidirectionally, inducing both pre- and post-synaptic differentiations, and is essential for correct synapse formation and function in the cerebellum. Figure adapted from (Schmid & Hollmann, 2010).

The homologue of GluD2, GluD1 has a broader expression pattern; yet it has been noted that GluD1 can also form a trans-synaptic triad, interacting with Neurexin isoforms containing splice site 4 through various members of the Cbln family. This was demonstrated using a cellular binding assay where Human Embryonic Kidney (HEK) cells transfected with splice site 4 containing Neurexins were able to cluster soluble GluD1 ATD protein on their cell surface in a Cbln-dependent manner (Yasumura et al, 2012). Furthermore, in an analogous manner to the GluD2-containing ternary

complex, this GluD1 version was able to induce synaptic specializations in co-cultures between HEK cells and cortical neurons, in a Cbln-dependent manner, highlighting the ability of GluD1-containing trans-synaptic bridges to act as a bidirectional signalling complex (Yasumura et al, 2012). Further details regarding the individual members of this trans-synaptic triad are provided in Section 1.5-1.7.

1.5 The Delta iGluRs

1.5.1 An Orphan Receptor?

The Delta-iGluRs have a very restricted expression pattern. GluD1 is highly expressed in the cochlea inner hair cells and at low levels throughout the adult central nervous system (CNS). During development, however, GluD1 is expressed extensively in the forebrain, particularly in the caudate nucleus (Lomeli et al, 1993). GluD2 is expressed very specifically in the Purkinje cells in the immature and mature cerebellum and is restricted to synapses with Parallel fibres (PF-PC synapses) in the adult cerebellum (See Section 1.2) (Landsend et al, 1997; Zhao et al, 1998).

Whilst AMPA, Kainate and NMDA iGluRs were discovered and named due to the synthetic agonists they bind, the Delta iGluRs were originally thought to be orphan receptors – that is without a ligand – as they did not form functional channels when expressed alone or in combination with other iGluR subunits, and they did not bind glutamate or related compounds in radioligand binding assays (Traynelis et al, 2010).

Subsequent structural and isothermal calorimetry (ITC) studies using the isolated LBC of GluD2 revealed its ability to bind D-serine and glycine, and that ligand binding induced LBC cleft closure.

However, application of D-Serine or glycine did not stimulate any detectable ion channel function in GluD2 expressed alone or in combination with other iGluR subunits. Nevertheless, upon application of D-Serine and glycine to a mutant GluD2 – known as Lurcher (See Section 1.5.2) – the spontaneous channel activity, characteristic of this mutant, was reduced in a concentration-dependent manner. Taken together, this demonstrates that GluD2 has the ability to bind a ligand, and that LBC cleft-closure induces a global conformational change that alters the properties and perhaps relative orientation of the TMD helices (Naur et al, 2007).

Contrariwise to this however, when the LBC of GluD2 was genetically excised and replaced with that of GluK2, the resulting chimeric protein produced glutamate-gated ion channels with measurable currents, unlike wild-type GluD2. Furthermore, production of the inverse chimera - GluK2 with the GluD2 LBC transplanted into it – effectively silenced the GluK2 ion channel, that is no passive ion channel flux was measured (Schmid et al, 2009). These observations indicate that the TMD of GluD2 has the properties to allow the passage of ions but suggests that the LBC of GluD2 operates in a fundamentally different manner to that of other iGluRs.

1.5.2 Knock-Out Mice Studies

Due to the lack of pharmacological tools that stimulate detectable ion channel properties in the Delta iGluRs, delineation of their function has been hampered somewhat in comparison to the other iGluR family members. Consequently, knock-out (KO) mice have been used as the primary tool for investigating the biological roles of the enigmatic Delta iGluRs.

In agreement with the expression of GluD1 in the inner ear hair cells, GluD1 KO mice exhibit a deficiency in high frequency hearing (Gao et al, 2007). In addition, GluD1 KO mice also show a number of abnormal social and emotional behaviours. For example, GluD1 KO mice were found to be hyperactive and aggressive as well as displaying depressive behaviour, lower anxiety-like behaviour, and lower social interaction (Yadav et al, 2012). Furthermore, application of lithium – a drug that is used in the treatment of bipolar disorder, characteristic symptoms of which include cycles of mania and depression – rescued the depression-like phenotype displayed by the GluD1 KO mice. Moreover, analysis of the molecular composition of synapses from the prefrontal cortex and the amygdala areas, that have been linked to controlling social and emotional behaviours, from GluD1 KO mice revealed altered expression of various other iGluRs and other pre- and post-synaptic markers. Altogether this suggests a role for GluD1 in the development of normal neuronal circuitry and correct molecular composition of synapses in areas of the brain that control emotional and social behaviours (Yadav et al, 2012).

Intriguingly, GluD1 was found to induce synapse formation in co-cultures between HEK cells, expressing GluD1, and cerebellar neurons as well as neurons of the entorhinal cortex. Additionally, GluD1 was able to induce synapse formation between HEK cells and hippocampal neurons only when an exogenous molecule Cbln1 (See Section 1.5) was added. Notably, cerebellar neurons and those of the entorhinal cortex naturally express Cbln1. Another point of note is that synaptogenic activity was dependent upon the ATD of GluD1 (Ryu et al, 2012). Thus it is tempting to link the social and emotional impairments of GluD1 KO mice to aberrant synapse formation and organisation in the absence of GluD1.

GluD2 KO mice demonstrate a whole host of prominent phenotypes such as: ataxia, impaired motor learning, impaired Purkinje cell LTD, aberrant synapse formation between Parallel Fibers and Purkinje Cells (PF-PC), as well as atypical synapse formation between Climbing Fibers and Purkinje cells (CF-PC) (Kashiwabuchi et al, 1995). Another observation from GluD2 KO mice was a mismatch between the length of pre- and post-synaptic zones and aberrant organisation of the PSD (Takeuchi et al, 2005). Taken together this suggests a crucial role for GluD2 in the control of motor coordination, synaptic plasticity (See Section 1.1.2-4) and in the formation of correct synaptic connections in the cerebellum.

Interestingly, there are several spontaneous mouse mutants in the locus of the gene that encodes GluD2 which have similar phenotypes to GluD2 KO mice. Several of these mutants – known as *hotfoot* mice due to the tottering, ataxic phenotype they display when moving – have deletions in the ATD of GluD2, for example hotfoot-4J mice have a 170 amino acid deletion from the ATD, pointing to an important role for this domain in the function of GluD2 (Lalouette et al, 1998; Matsuda & Yuzaki, 2002; Wang et al, 2003). Furthermore, a *specific* role for the ATD of GluD2 in PF-PC synaptogenesis was confirmed using a transgenic rescue approach. This involved injection of a modified Sindbis virus carrying the gene for either wild-type GluD2 or a GluD2 mutant lacking the ATD (GluD2 ΔATD) into the subarachnoid supracerebellar space of GluD2 KO mice; in the case of wild-type injection, this rescued the aberrant PF-PC synapse formation and the motor-dyscoordination, ataxic phenotype, whereas in the GluD2 ΔATD instance the phenotype was not rescued, strongly linking the synaptogenic activity of GluD2 to the ATD (Kakegawa et al, 2009). This requirement of the ATD for the synaptogenic activity of GluD2 was also confirmed *in vitro*; HEK cells expressing wild-type GluD2 were able to induce synapses with co-cultered cerebellar neurons, however if the GluD2 ATD was exchanged with the ATD of GluA1 this synaptogenic activity was lost (Uemura & Mishina, 2008). Also, when the GluD2 ATD alone was expressed as a fusion protein

connected to the immunoglobulin constant region, and then bound to protein A-conjugated beads; these beads were able to induce pre-synaptic differentiations in co-cultured cerebellar neurons, hence demonstrating that the GluD2ATD alone is sufficient for the synaptogenic activity of GluD2 (Uemura & Mishina, 2008).

Another noteworthy GluD2 mutant is found in the Lurcher mouse. This mouse was first discovered at the MRC Radiobiological research unit at Harwell in 1954 as a neurological mutant characterised by a wobbly, lurching, ataxic gait. This phenotype was caused by a spontaneously occurring Alanine 654 to Threonine mutation at the top of the pre-LBC S2 TM helix. The effect of the mutation is to render GluD2 as a constitutively leaky cation channel which leads to Purkinje cell death; this degeneration of the cerebellum manifests itself as the uncoordinated phenotype (Vogel et al, 2007). Thus, the Lurcher mouse provides another convincing example of how GluD2 dysfunction can have drastic consequences on motor skills, strongly implicating GluD2 in the control of motor coordination. Intriguingly, mutations of GluD1 in the same TM helix where the Lurcher mutation occurs also lead to spontaneously open channels and similar characteristics to the GluD2 Lurcher mutant (Yadav et al, 2011).

In summary, the Delta iGluRs are involved in regulating synapse formation and function in different parts of the brain. The effect on synapse formation in Delta iGluR KO mice results in several striking cognitive and behavioural phenotypes, linking these proteins to a potential involvement in the molecular mechanisms behind these complicated behaviours. Furthermore, the ATD of the Delta iGluRs is crucial to their synaptogenic activity, highlighting the importance of this domain.

1.5.3 GluD2 and LTD

One of the key features of GluD2 KO mice is their impaired cerebellar LTD and motor learning abilities, linking GluD2 to the molecular mechanisms behind LTD at the PF-PC synapse (Kashiwabuchi et al, 1995).

The intracellular CTD of GluD2 has been shown to be crucial for the involvement of GluD2 in LTD. For example, the impaired LTD seen in GluD2 KO mice was rescued when a virus carrying a wild-type GluD2 gene was introduced into the cerebellum of KO mice, but this was not the case when a virus carrying a mutant, encoding a GluD2 lacking the last seven amino acids of the C-terminal tail ($GluD2_{\Delta CT7}$) was introduced (Kohda et al, 2007). Concurring with this, expression of $GluD2_{\Delta CT7}$ rescued the ataxic phenotype and morphological abnormalities of the cerebellum typical of the GluD2 KO mouse, but did not affect the impaired motor learning abilities of the KO; that is performance in the eyeblink conditioning test was not improved by expression of $GluD2_{\Delta CT7}$ (Kakegawa et al, 2008). This last section of the C-terminal tail of GluD2 includes a PDZ-binding motif and is known to bind several different intracellular proteins such as PSD93 (Roche et al, 1999), PTPMEG (Hironaka et al, 2000), S-SCAM (Yap et al, 2003) and Delphilin (Miyagi et al, 2002). When peptides that disrupted the interaction between the CTD of GluD2 and the intracellular proteins PSD-93, PTPMEG and S-SCAM were introduced into the Purkinje cells, LTD was also abrogated (Kohda et al, 2007). Thus the essential presence of the C-terminal tail of GluD2 in mediating its role in LTD is likely to be due to involvement in linking GluD2 to several intracellular signalling and scaffolding proteins and the PSD.

D-Serine binding to the LBC of GluD2 (See Section 1.5.1) is also a mechanism by which GluD2 is involved in cerebellar LTD. D-Serine is present at high concentrations (10^{-3} M) in the forebrain and is

reported to regulate synaptic plasticity by activating NMDA iGluRs (Henneberger et al, 2010; Oliet & Mothet, 2009). D-Serine is also secreted in the cerebellum at high concentrations during the early postnatal period but the action of D-Amino Acid Oxidase (DAAO), the expression of which is initiated in postnatal week 3, reduces the amount of D-Serine in the mature cerebellum (Wang & Zhu, 2003). Application of D-Serine to GluD2 expressed in a transgenic rescue approach, i.e. in a KO background, rapidly induced LTD; conversely the same thing did not happen upon D-Serine application to a mutant of GluD2 with a disrupted D-Serine binding site (Kakegawa et al, 2011). Disruption of the D-Serine binding site also negatively affected motor coordination in immature mice. Moreover, the PDZ-motif contained in the most C-terminal part of the CTD was necessary for D-serine induced LTD as was the action of PKC (Kakegawa et al, 2011). Taken together this suggests a mechanism for D-Serine induced LTD whereby ligand binding to the LBC induces a conformational change in GluD2 and since the CTD and intracellular binding partners are necessary components, the conformational change is transmitted across the membrane to induce LTD mediated by the PKC signalling cascade (Kakegawa et al, 2011). Indeed there is evidence from other sources that supports the idea that GluD2 functions in a 'non-ionotropic' mode (Kakegawa et al, 2007).

1.5.4 Links to Human Disease

GluD1 KO mice exhibit a number of phenotypes that resemble human neurological disorders such as depression and bipolar disorder (See Section 1.5.2). Genome-wide association studies provide evidence that the GRID1 gene – which encodes GluD1 – is a candidate for several debilitating conditions such as schizophrenia, depression and bipolar disorder (Fallin et al, 2005; Guo et al, 2007; Orsetti et al, 2008; Treutlein et al, 2009; Venken et al, 2008; Zhu et al, 2009). GRID1 has also been strongly associated with ASDs through copy number variation studies (Glessner et al, 2009; Smith et al, 2009). Furthermore, the chromosomal location of the GRID1 gene, 10q22-q23, is a site

commonly linked with cognitive and behavioural defects (Balciuniene et al, 2007; van Bon et al, 2011).

Phenotypes displayed in KO mice hint at a role in motor coordination for GluD2 (See Section 1.5.2). Indeed several clinical studies have highlighted a role for GluD2 in a number of motor disorders. For example, autoantibodies against GluD2 have been found in a number of cases of cerebellitis, cerebellar ataxia, chronic myoclonia, and encephalitis, the main symptom of which is uncoordinated motor control (Fukuoka et al, 2012; Ichikawa et al, 2009; Kubota & Takahashi, 2008; Matsuo et al, 2007; Shiihara et al, 2007; Shimokaze et al, 2007; Sugiyama et al, 2004; Tomioka et al, 2008; Usui et al, 2011).

The role of the Delta iGluRs in such prevalent and debilitating neurological conditions, as well their involvement in the cellular and molecular mechanisms behind information storage and correct neural wiring in different parts of the brain, underscores the importance and medical relevance of the Delta iGluRs.

1.6 Cbln1

1.6.1 C1q Family and the Cbln Subfamily

The C1q superfamily is composed of more than 30 human proteins which are related due to the presence of a globular C1q domain. The archetypal member, C1q, is the target recognition protein of the classical complement pathway and thus a prominent component of the immune response (Kishore & Reid, 2000). The C1q domain of C1q acts as the ligand recognition domain; for example

in the classical complement pathway C1q binds to the FC region of pathogen attached antibodies via the C1q domain (Kishore & Reid, 2000). Structurally the C1q domain consists of a ten-stranded β-sandwich fold with a jelly-roll, TNF-like topology (Ghai et al, 2007). Other C1q containing proteins are involved in a wide range of processes including immunity, cell-matrix adhesion, metabolite homeostasis and neuronal functions (Ghai et al, 2007).

The Cbln subfamily is comprised of Cbln1, Cbln2, Cbln3 and Cbln4. Each member of the Cbln subfamily is a secreted glycoprotein with an identical domain structure and there is strong homology between the family members, with 57-79 % sequence similarity to each other (Yuzaki, 2008). Cbln1 is expressed in a number of brain regions including predominantly the cerebellar granule cells, though it is also expressed in other parts of the brain (Miura et al, 2006). Cbln1 was first identified by virtue of it containing the naturally occurring 16 amino acid peptide Cerebellin (Slemmon et al, 1984), hence Cbln1 was give the name Cerebellin 1 precursor protein (Urade et al, 1991). Each Cbln1 subunit is only 193 amino acids in length and after cleavage of the signal peptide each subunit contains a ~37 amino acid N-terminal extension followed by the C1q domain (Figure 1.9). It is well established that C1q domains are trimeric (Ghai et al, 2007) and it is thought that Cbln1 is arranged as a hexamer, in a dimer of trimers arrangement, where trimer dimerization is mediated by a Cys-knot domain produced by disulphide bonds formed between two Cysteine residues in the N-terminal extension of each subunit (Urade et al, 1991; Yuzaki, 2008).

Figure 1.9: Cbln1. *A schematic representing the domain composition of a single Cbln1 highlighting the putative sites of N-linked glycosylation and important Cysteine residues thought to control the oligomeric state of Cbln1 (Yuzaki, 2008).*

The other Cbln family members Cbln2, Cbln3 and Cbln4 are expressed in many different regions of the brain with distinct spatial and developmental patterns (Miura et al, 2006). Cbln2-4 have an equivalent subunit architecture to Cbln1 and there is evidence from yeast two-hybrid experiments that heteromers between Cbln1 and Cbln3 exist, meaning a wider range of heteromerizations involving the Cbln family may be possible (Pang et al, 2000). Furthermore, it has been suggested that heteromerization between Cbln1 and Cbln3 is absolutely necessary for Cbln3 secretion from cells, providing further evidence for inter-Cbln subunit oligomerization (Bao et al, 2006). As different Cbln members were shown to have independent targets, and potentially functions, it has been suggested that this heteromerization of Cbln proteins might be crucial for their regulation, since subunit composition was found to affect the affinity for a different signalling pathways (Wei et al, 2012). Thus further investigation is necessary to understand the molecular details and functional significance of these Cbln heteromeric complexes.

1.6.2 Cbln1 Function

Fascinatingly, Cbln1 KO mice display very similar behavioural, anatomical and physiological phenotypes as GluD2 KO Mice (See Section 1.5.3), that is: ataxia, aberrant PF-PC and CF-PC synapse formation, a mis-match in the length of pre-and post-synaptic zones plus impaired LTD and motor learning (Hirai et al, 2005). This phenotypic overlap of the relevant KO mice led to the suggestion that Cbln1 and GluD2 may participate in the same signalling pathway, perhaps by way of a direct interaction; this suggestion was questioned, however, due to expression patterns of GluD2 and Cbln1 that did not fully overlap (Matsuda & Yuzaki, 2012). Nonetheless, antigen unmasking revealed that Cbln1 was indeed enriched at the PF-PC synapse, the specific site of GluD2 expression (Miura et al, 2009). Evidence for a direct interaction between Cbln1 and GluD2 came from two separate studies using different techniques, for example one group used Surface Plasmon Resonance techniques and the other used cell based assays – both investigations established that Cbln1 interacts specifically with the ATD of GluD2 (Matsuda et al, 2010; Uemura et al, 2010). This discovery was interesting as it provided a possible explanation to the evidence that the ATD was essential for the synaptogenic activity of GluD2 (See Section 1.5.2) (Uemura & Mishina, 2008).

The Cbln1-GluD2 interaction was shown to act as a bidirectional synaptic organiser; *in vitro* heterologous cells expressing GluD2 were able to induce pre-synaptic differentiation in cerebellar granule cells from Cbln1 KO mice *only* when recombinant Cbln1 was exogenously applied, providing evidence for retrograde signalling (Matsuda et al, 2010). Moreover, beads coated in Cbln1 were able to induce clustering of PSD proteins in HEK 293 cells ectopically expressing GluD2 and PSD proteins such as shank and PSD-93, providing evidence for anterograde signalling (Matsuda et al, 2010). Additionally, when recombinant Cbln1 was injected into the supracerebellar space of Cbln1 KO mice, the ultrastructure and functions of the PF-PC synapse were restored (Matsuda et al, 2010; Matsuda & Yuzaki, 2012). Hence, Cbln1 and GluD2 are involved in a direct interaction that is

essential for establishing and organising the morphology and function of the PF-PC synapse, and disruptions to this interaction lead to deficiencies in motor learning and motor coordination (Matsuda & Yuzaki, 2012).

A clinical example of the importance of Cbln1 comes from a case of a child with partial trisomy of a section of Chromosome 16, resulting in a duplication of the CBLN1 gene, as well as gene ZNF423. The symptoms presented by this case were intellectual disability, language dyspraxia, microcephaly and mild dysmorphisms (Zerem et al, 2011). A possible explanation for the abnormalities seen in this case could be that over-expression of Cbln1 leads to aberrant synapse formation in the cerebellum resulting in functional abnormalities. A number of additional cases of duplications in the same region of chromosome 16 have been described, resulting in similar symptoms, without linkage to specific genes, so there is a possibility that CBLN1 was involved in these cases (Zerem et al, 2011). These examples underline the potential medical relevance of Cbln1.

1.7 Neurexins

1.7.1 The Neurexin Family

Neurexins were first discovered as the receptor for α-Latrotoxin, a component of black widow spider venom (Davletov et al, 1995; Ushkaryov et al, 1992). The Neurexins are a family of pre-synaptic Type-I membrane proteins encoded by three genes: NRXN1-3. Two promoters at each NRXN gene produce transcripts for longer α-Neurexin and a shorter β-Neurexin, yielding six primary transcripts (Missler & Sudhof, 1998). This variability of Neurexin isoforms is enhanced by the existence of multiple sites of alternative splicing – potentially producing more than a thousand different Neurexin variants (Missler & Sudhof, 1998).

Alpha-Neurexins have a large extracellular domain composed of three repeating units and an O-linked glycosylation rich region. The repeating unit is formed by two LamininA/Neurexin/Sex hormone-binding globulin (LNS) domains intercalated by an Epidermal Growth Factor-like (EGF) domain (Missler & Sudhof, 1998). Beta-Neurexin extracellular regions are comprised of just a single LNS domain followed by an area of O-linked glycosylation. All neurexins have a single transmembrane region followed by a short intracellular C-terminal tail that contains protein interaction modules such as PDZ-binding motifs. The transmembrane and C-terminal domains of α- and β-Neurexins are identical (Figure 1.10) (Missler & Sudhof, 1998).

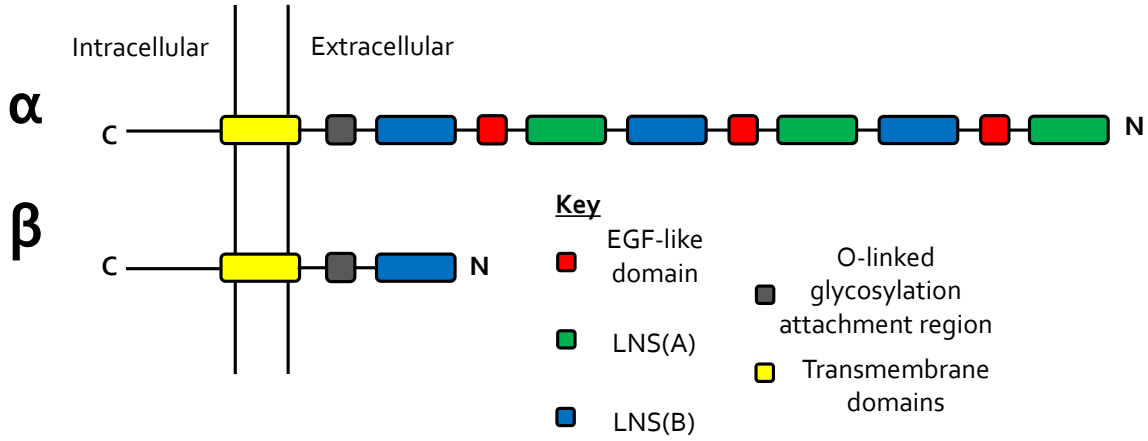

Figure 1.10: Neurexins. Schematic representation of the domain organisation of the Neurexin protein family.

Several crystal structures of different isoforms of Neurexins have been published (Arac et al, 2007; Chen et al, 2011; Chen et al, 2008; Fabrichny et al, 2007; Koehnke et al, 2008; Koehnke et al, 2010; Leone et al, 2010; Miller et al, 2011; Rudenko et al, 1999; Sheckler et al, 2006; Shen et al, 2008; Tanaka et al, 2011); for example *apo* and in complex with Neuroligin (See Section 1.7.2), non-glycosylated and glycosylated – dependent upon the expression system used. All the structures confirm that the LNS domain is composed of two seven-stranded β-sheets that form a lectin-like

fold. Of note is that splice sites are located on the periphery of the domain (Dean & Dresbach, 2006). Intriguingly, there is a marked difference between the secondary structure adopted for the sequence inserted in isoforms of Neurexin containing Splice Site 4 (SS4) (Figure 1.11). In a structure of nonglycosylated β-Neurexin + SS4, expressed in *E. coli*, the SS4 insert takes an α-helical conformation, whereas in a structure of glycosylated β-Neurexin + SS4, produced in human embryonic kidney (HEK) cells, the SS4 insert forms a β-strand that is incorporated into a β-sheet (Koehnke et al, 2010; Shen et al, 2008). This is of note as the splice site variations are thought to regulate protein interaction through discriminating between potential protein partners (Missler & Sudhof, 1998).

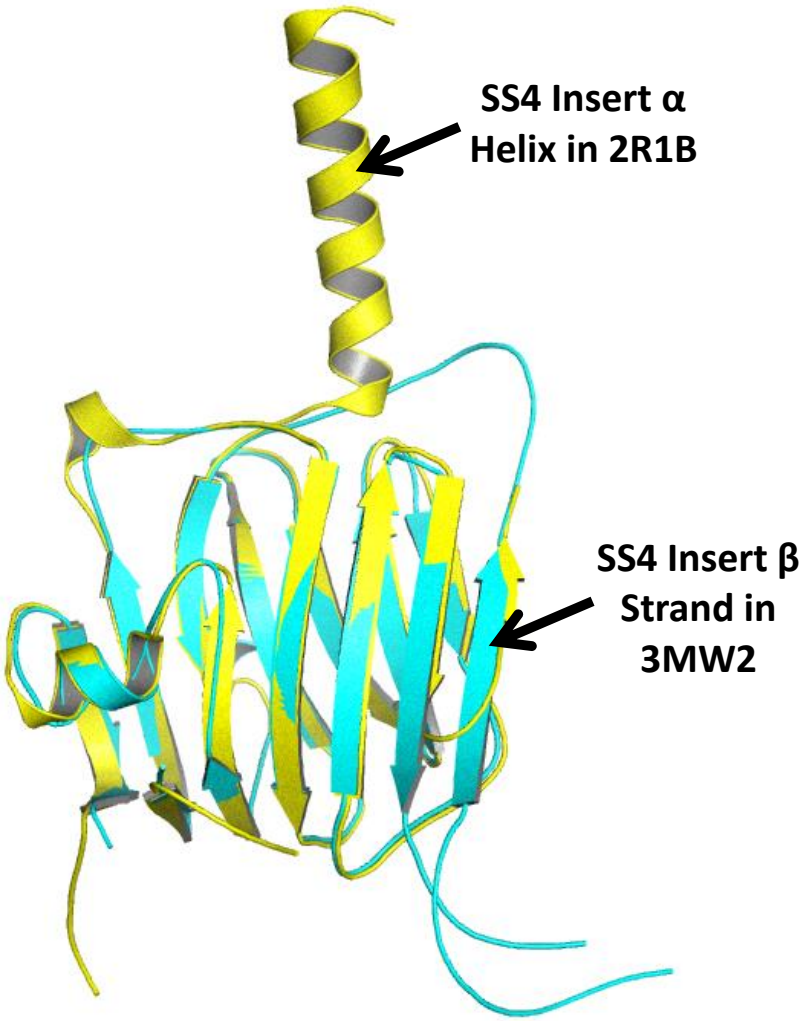

***Figure 1.11:* β-*Neurexin1 + SS4*.** *A cartoon representation of the secondary structural components of two separate crystals structures of* β-*Neurexin1 + SS4. A non-glycosylated form (2R1B, (Shen et al, 2008)), shown in yellow, is superimposed onto a glycosylated form (3MW2, (Koehnke et al, 2010)), shown in cyan. The differing secondary structure adopted by the SS4 insert in each structure is highlighted.*

1.7.2 Neurexin and Neuroligin

Neurexins have a role in synaptic cell-adhesion through their well characterised trans-synaptic interaction with Neuroligins (Bottos et al, 2011; Dean & Dresbach, 2006). Neuroligins are a family of five genes that code for Type-I post-synaptic membrane proteins containing a large extracellular Cholinesterase-like domain. Neuroligins form homomultimers through the association of the Cholinesterase-like domain, which is important for Neuroligin function (Bottos et al, 2011). Much is known about the molecular basis for the interaction between Neurexins and Neuroligins, indeed there have been extensive biochemical and biophysical studies including a handful of crystal structures of the complex between different Neurexin and Neuroligin isoforms (Arac et al, 2007; Chen et al, 2008; Fabrichny et al, 2007; Leone et al, 2010). For example it is known that the Neurexin-Neuroligin interaction is Ca^{2+}-dependent (Comoletti et al, 2003); moreover Neuroligin binds *specifically* to a Neurexin variant that lacks splice site 4 (SS4) because the position of this insert is proximal to the binding interface, and thus SS4 inclusion would occlude binding (Arac et al, 2007; Bottos et al, 2011; Chen et al, 2008; Dean & Dresbach, 2006; Fabrichny et al, 2007; Leone et al, 2010). The function of the Neurexin-Neuroligin complex is thought to regulate synapse maturation (Bottos et al, 2011; Sudhof, 2008).

1.7.3 Neurexin and Disease

There have been consistent observations linking mutations in Neurexin genes with ASDs. Precisely, seven point mutations, four large-scale deletion events and two translocation events in the NRXN1 gene have been identified in patients with autism (Feng et al, 2006; Kim et al, 2008; Marshall et al, 2008; Szatmari et al, 2007; Yan et al, 2008; Zahir et al, 2008). Furthermore, mutations in Neuroligin genes have also been linked to autism, providing strong evidence that Neurexins and Neurexin-containing protein complexes are involved in the molecular malfunctions behind ASDs (Sudhof, 2008). Moreover, deletions in the NRXN1 gene have been observed in families with schizophrenia

(Kirov et al, 2008; Walsh et al, 2008), plus linkage studies have connected the NRXN3 gene to different types of addiction (Hishimoto et al, 2007; Lachman et al, 2007). Taken together this evidence highlights the importance of Neurexins as decidedly important, medically relevant molecules.

1.7.4 Neurexin as a Pre-Synaptic receptor for Cbln1

In addition to the well characterised interaction with Neuroligins, it is now clear that Neurexins also bind to the secreted Cbln family of proteins (See Section 1.6) (Joo et al, 2011; Uemura & Mishina, 2008; Yasumura et al, 2012). A direct interaction between Cbln1 and Neurexins was first demonstrated using cell-based immunofluorescence binding assays as well as Surface Plasmon Resonance and co-immunoprecipitation techniques. These investigations revealed that Cbln1 interacted specifically with Neurexin isoforms that contained the splice site 4 insert, in an inverse manner to Neuroligins (See Section 1.7.2) (Uemura et al, 2010). Furthermore, it has subsequently been confirmed that in addition to Cbln1, other members of the Cbln family, Cbln2 and Cbln4 have the ability to bind to Neurexin variants that contain splice site 4, albeit with varying affinities (Joo et al, 2011; Matsuda & Yuzaki, 2011). Hence this data confirmed that Neurexins, containing splice site 4, are a pre-synaptic receptor for Cbln proteins. It is particularly interesting that Cbln proteins bind specifically Neurexins that contain splice site 4, and in light of the alternative secondary structure displayed by this insert (See Section 1.7.1), one key question is: how does the splice site 4 insert play such a key role in mediating the interaction with Cbln family proteins?

1.8 Aims

As discussed above, the trans-synaptic triad of Neurexin, Cbln and Delta iGluR is involved in the formation of correct neural circuitry; aberrations in this multi-protein complex lead to numerous prominent phenotypes in mouse model systems and furthermore, individual members of said trans-synaptic complexes have been implicated in a wide-range of neurological and neuropsychiatric disorders, emphasising their importance as molecular targets of study. The broad aims of this project are to use X-ray crystallography along with complimentary biophysical techniques to understand the molecular minutiae of Delta iGluR containing trans-synaptic ternary protein complexes. This general aim can be split into four targets that are roughly equivalent to chapters 3-6: i) understanding the molecular architecture of Delta iGluR ATDs, where there is currently no information; ii) exploring the organisation of the wider domain arrangement of Delta iGluR subunits; iii) investigating the structural details of Cbln proteins; and iv) probing the molecular basis for the component interactions of the aforementioned Neurexin-Cbln-Delta iGluR trans-synaptic triad. In all cases, where possible, the objective is to combine structural characterisation with functional experiments to attempt to illuminate molecular mechanisms behind biological function.

Chapter 2:

General Materials and Methods

2.1 Molecular Biology

2.1.1 cDNAs and Expression Vectors

cDNA encoding mouse GluD1 (Grid1, Genbank accession NM_008166.2) was kindly donated by Prof. Michisuke Yuzaki (Keio University, Japan). cDNA clones coding for human GluD2 (GRID2, Genbank entry BC099653, Image clone 40008397), human Cbln1 (CBLN1, GenBank entry BC093692, Image clone 7939537) were purchased from SourceBioscience (Cambride, UK). A template construct designed for human β-Neurexin1 (Genbank, NM_138735.2) LNS domain (H85-V295), including splice site 4, was synthesised by Eurofins MWG operon. Mutant constructs of mouse Cbln1 (Genbank, NM_019626.3) listed in Appendix 8.1 were generously provided by Prof. Michisuke Yuzaki (Keio University, Japan). Template constructs of CB50, CB52 and CB54 (Listed in Appendix 8.1), human Cbln1 mutants were synthesised by Eurofins MWG Operon.

The pHLsec vector suite was used for transient expression in mammalian cell lines (See Appendix 8.3) (Aricescu et al, 2006). This plasmid series contains all the required genetic elements for bacteria-based molecular cloning as well as for high-level overexpression of recombinant proteins in mammalian cells. These vectors have the same multiple cloning site and typically the EcoRI, AgeI and KpnI sites were exploited for molecular cloning. If the EcoRI site was used the native signal sequence was required, whereas if the AgeI site was utilized a vector-based secretion signal was employed. In pHLsec, a His_6 tag is encoded directly 3′ of the KpnI site, whilst the pHLsec Avitag3 vector encodes a biotin ligase (BirA) recognition site, followed by a His_6 tag, proximately 3′ of the KpnI site. Moreover, the pHLsec FC vector codes for an IgG1 hinge and Fc region and a His6 tag immediately 3′ of the KpnI site. The pHLsec mVenus vector was created by Amber Clayton (STRUBI) and when expressed includes a 3C protease cleavage site followed by amino acids 1-239 of mono Venus (Genbank DQ092360) and a most C-terminal His_6 tag, all of which is encoded directly 3′

of the KpnI site. The pHLsec 1D4 vector was made by Nikos Mitakidis (STRUBI) and encodes a TETSQVAPA 1D4 epitope tag in the equivalent position to the His_6 tag in pHLsec. The 1D4 vector can be employed to purify recombinant proteins by immuno-affinity chromatography.

2.1.2 Construct Design

Several factors were considered when designing constructs and numerous bioinformatics tools were employed to aid this process. Domain boundaries were delineated using existing structural knowledge for target proteins, and their orthologues, contained in the protein data bank (PDB) (Berman et al, 2000) and using domain boundary prediction software such as HHpred (Soding et al, 2005). Other considerations taken into account were: disorder prediction using RONN (Yang et al, 2005), sites of N-linked glycosylation (NetNGlyc 1.0 Server) and the sites of signal sequence cleavage using the SignalP 4.0 server (Petersen et al, 2011). The specific details of all the constructs made for this thesis are detailed in Appendix 8.1 and the individual results sections, chapters 3-6.

2.1.3 Polymerase Chain Reaction

Polymerase Chain reaction (PCR) allows the amplification of a specific target segment of DNA through a series of synthetic reactions. Essential requirements for successful PCR include a template of target DNA, a thermostable DNA polymerase that is not denatured at temperatures required for DNA melting, two oligonucleotides that flank a target segment of DNA and are complimentary to opposite strands – known as primers – and an excess of the four dNTPs. The amplification process involves repeating cycles of DNA denaturation at a high temperature followed by cooling, to allow primer annealing, and then incubation at an optimal temperature for the DNA polymerase, allowing extension of new DNA strands (Mullis & Faloona, 1987).

Primers were designed using bioinformatics tools such as those included in the Java Molecular Biology Directory (www.bioinformatics.org/JaMBW/). Considerations taken when designing primers included: i) The requirements for and of specific restriction endonucleases to allow correct digestion and insertion of amplified cDNAs into destination vectors; ii) A sequence complimentary to the target sequence and strand of template DNA; iii) A melting temperature of around 60-62 °C; and iv) A GC content of around 60 %. Specific details of all the primers mentioned in this thesis are listed in Appendix 8.1. Primers were purchased from Eurofins MWG Operon. A typical reaction would include the components detailed in Table 2.1 and reaction cycle parameters listed in Table 2.2.

Component	Volume / µl
Primer 1	1
Primer 2	1
Template DNA	1
Pyrobest™ DNA Polymerase *(Takara)*	0.5
10 x reaction buffer for Pyrobest™ DNA Polymerase *(Takara)*	5
dNTPs *(Takara)*	4
dH_2O	37.5

Table 2.1: *Typical PCR reaction components.*

Stage	Temperature / °C	Time / s
Melting	96	120
Melting	96	50
Annealing	55	50
Polymerisation	72	60 / kb
Polymerisation	72	600
Storage	4	∞

x 30

Table 2.2: *Typical PCR thermocycler parameters.*

2.1.4 Oligonucleotide-Mediated Mutagenesis

For introducing point mutations into DNA sequences, or for joining non-contiguous DNA sequences, an oligonucleotide-mediated approach was taken. This approach involved designing two overlapping primers for the site of mutagenesis or joining, one forward and one reverse. The overlapping core of said primers was designed to consist of roughly 20 bases and with a melting temperature of 60-62 °C. These overlapping primers were used in conjunction with 5′ and 3′ primers for the target sequence of interest in a two-step PCR process. The first set of PCRs involved two separate reactions: one reaction using the 5′ oligonucleotide of the target sequence and the reverse primer of the overlapping segment, and a second reaction with the forward primer of the overlapping segment and the 3′ oligonucleotide of the target sequence. These reactions used the same reaction components and thermocycler parameters described in Tables 2.1 and 2.2. The two separate cDNA fragments (A and B) produced by this first set of PCRs were then purified using agarose gel purification as described in section 2.1.4.1. The A and B cDNA fragments were then simultaneously spliced into a single fragment and this fragment amplified, through a second round of PCR as detailed in Tables 2.3 and 2.4. A select list of primers used in this thesis is contained in Appendix 8.1.

Component	Volume / µl
Fragment A	3
Fragment B	3
Primer 1 *(Not added to initial reaction mix, see Table 2.1.4)*	1
Primer 2 *(Not added to initial reaction mix, see Table 2.1.4)*	1
Pyrobest™ DNA Polymerase *(Takara)*	0.5
10 x reaction buffer for Pyrobest™ DNA Polymerase *(Takara)*	5
dNTPs *(Takara)*	4
dH_2O	32.5

Table 2.3: *Typical reaction components for the second round of PCR in oligonucleotide mediated mutagenesis.*

Temperature / °C	Time / s	
96	120	
96	50	x 3
55	50	
72	60 / kb	
Add Primer 1 and 2 to the reaction mix		
96	120	
96	50	x 30
55	50	
72	60 / kb	
72	600	
4	∞	

Table 2.4: *Typical thermocycler parameters for the second round of PCR in oligonucleotide mediated mutagenesis.*

2.1.5 DNA Purification Techniques

2.1.5.1 Agarose Gel Purification

One method of purifying oligonucleotides from primers and enzymes, post PCR for example, is to separate an oligonucleotide mixture using agarose gel electrophoresis (See Section 2.2.1) and then extract the target oligonucleotide directly from the agarose gel. This process is indeed essential for oligonucleotide-mediated mutagenesis (See Section 2.1.3) and during molecular cloning after target sequence and destination vector digestion (See Section 2.1.5). In brief, the process involved: performing agarose gel electrophoresis (See Section 2.2.1), followed by excision of the target band from the agarose gel using a scalpel. A Qiagen gel purification kit was then used to extract target cDNA. This process was followed as described in the manufacturer's instructions and included: three gel volumes of high salt-containing solubilisation and DNA binding buffer QG – which includes a pH indicator, as correct pH is essential for binding to the silica membrane – was added to the

excised gel fragment, this mixture was incubated at 50 °C for 10 min to melt the agarose gel, one gel volume of isopropanol was added, this mixture was then passed through a QIAquick spin column – which adsorbs DNA at high salt concentrations – the column was then washed with 750 µL of an ethanol containing buffer PE to remove any residual salts before target cDNA was eluted from the column using 30 µL of a low-salt containing buffer such as 10 mM Tris (pH 8). All steps involved centrifugation of QIAquick spin columns at roughly 13, 000 g.

2.1.5.2 PCR Purification

PCR purification provides a quicker but less stringent technique for purifying oligonucleotides; for example this technique was often applied during molecular cloning, at the stage between PCR and digestion with restriction endonucleases (See Section 2.1.5). PCR purification relies upon the same mechanism as agarose gel purification, i.e. adsorption of cDNA to a silica membrane, however with a modified protocol. For example, a PCR purification kit was used (Qiagen), the process of which involved: five times sample volume of PB, high-salt binding buffer, was added to the oligonucleotide sample, this was then applied to a QIAquick column, which was then washed with ethanol containing PE buffer before purified DNA was eluted in a low-salt elution buffer such as 10 mM Tris (pH 8). Protocols were followed as described in the manufacturer's instructions; each step relied upon centrifugation at roughly 13, 000 g.

2.1.5.3 Plasmid Purification using Alkaline Lysis

Alkaline Lysis allows extraction of plasmid DNA from a bacterial cell culture. The steps include cell growth and harvesting, cell re-suspension, cell lysis, neutralization and DNA cleaning/concentration (Birnboim & Doly, 1979).

In the first step, cell growth and harvesting, a bacterial culture was grown at 37 °C overnight, the scale of which was determined by the required yield of DNA. Cell harvesting was carried out by centrifugation at 6,000 g for 10 min. Cell re-suspension was performed in the presence of EDTA and RNAse A. RNAse A is an enzyme that degrades cellular RNA and was included to prevent sample contamination. EDTA chelates divalent cations that are essential for DNAse activity and thus was included to maintain the integrity of target plasmid DNA. Cell lysis was achieved with a solution that contains NaOH and SDS. SDS is a detergent that solubilizes the bacterial cell membrane and denatures cellular proteins. The presence of NaOH in the cell lysis buffer was an essential component of the alkaline lysis technique as this denatured the hydrogen bonding network between the two strands of DNA converting double-stranded DNA into single-stranded DNA. In the next step, neutralization, a solution was added to neutralize the pH, for example potassium acetate. This was another important and selective part of the process as neutralizing the pH allows hydrogen bonding between DNA bases to be re-established, which is possible for small circular plasmid DNA but impossible for long stretches of genomic DNA. The double-stranded plasmid DNA is highly soluble in this solution whereas single-stranded genomic DNA and denatured proteins form an insoluble precipitate. This precipitate was removed from the solution through centrifugation at 13, 000 g; this forms part of the DNA cleaning/concentration stage. Another round of cleaning as well as DNA concentration was achieved by adsorbing plasmid DNA, contained in a high molarity salt solution, onto a silica matrix.

Depending on required yield of DNA various kits supplied by Qiagen were utilized. For example: for yields of ~25 µg a Miniprep kit was used, for a yield of ~500 µg a Maxiprep kit was exploited, yields of ~3 mg required a Megaprep kit, and for yields of ~15 mg a Gigaprep kit was needed. The specific details of each protocol were followed from the manufacturers' manual.

2.1.6 Molecular Cloning

Following PCR (Section 2.1.2 and 2.1.3) the target sequence was digested with specific restriction endonucleases as designed in the primers (Section 2.1.2). All restriction endonucleases were purchased from New England Biolabs; the protocols for their use alone or in combination were followed according to the manufacturers' instructions. The minute details of molecular cloning of each construct described in this thesis are detailed in Appendix 8.1. Destination plasmids for target sequences were often from the pHLsec vector series (Appendix 8.3) (Aricescu et al, 2006) since this set of vectors is particularly well designed for the application of transient mammalian expression used in this thesis. Thus it was necessary to digest destination vectors with complimentary enzymes to those used for the target sequences, further details in Appendix 8.1. Generally, restriction endonuclease reactions were incubated for between 2-4 hours at the temperature required by the restriction endonuclease used.

Following digestion, target cDNA fragments and digested destination plasmids were purified using agarose gel purification (See Section 2.1.5.1). Ligation of the target cDNA sequence into the destination plasmid was performed using a Quick Ligation Kit (New England Biolabs). Reactions were incubated at 25 °C for ten minutes and following this incubated on ice for ten minutes. A typical reaction mix is detailed in Table 2.5. Library Efficiency DH5α cells (Invitrogen) were transformed with DNA from the ligation mix using the following standard protocol: 1 µL ligation mix was incubated with 35 µL of Library Efficiency DH5α cells on ice for 30 min, then incubated at 42 °C for 45 s and following this 80 µL of SOC (Super Optimal Medium with Catabolite repression) medium (Invitrogen) was added and the mix incubated at 37 °C, with shaking, for 60 min before the mixture was transferred and spread onto an LB-Agar plate containing 100 µg/mL of Ampicillin (Melford) then incubated at 37 °C for ~15 hours. A number of colonies for each ligation reaction were used to inoculate 3 mL LB + Ampicillin which was then incubated at 37 °C, with shaking, for

roughly 15 hours. These transgenic bacterial cell cultures were then used to prepare recombinant plasmids via alkaline lysis-based kits (Qiagen, See Section 2.1.5.3). Following this, 1 µg of purified plasmid was digested with appropriate restriction enzymes at recommended conditions for approximately 1 hour to check if an insert of correct size had been ligated into the purified plasmid. To achieve this, digests were analysed using agarose gel electrophoresis (See Section 2.2.1). Final verification of the correctness of recombinant plasmids was achieved through DNA sequencing (SourceBioscience, Department of Biochemistry University of Oxford). External sequencing primers used for DNA constructs listed in this thesis are as follows: pHLsec_fwd gctggttgttgtgctgtctcatc, pHLsec_rev caccagccaccaccttctgatag, and pHLsec_Venus_rev gccctggaacagcacctccag, N.B. all primers are written 5′ to 3′.

Component	Volume / µL
Restriction Enzyme Digested Target Insert	7.5
Destination Vector Digested with Complimentary Restriction Enzymes	2.5
2x QuickLigase Reaction Buffer	10
QuickLigase	1

Table 2.5: *Typical reaction components for Ligation reactions.*

2.2 Electrophoresis and Western Blot

2.2.1 Agarose Gel Electrophoresis

Agarose gel electrophoresis (AGE) is a simple and common method for separating and analysing DNA. DNA samples are applied to an agarose polysaccharide gel matrix and an electric current is applied across the gel, whereupon DNA will travel through the gel towards the anode due to the inherent attraction of the DNA molecule to this particular electrode. Separation of DNA molecules is dependent on size; smaller molecules will migrate much more easily and quickly through the gel matrix than larger molecules so when the same current is applied to both samples, over the same

period of time, in the same agarose matrix, a smaller DNA molecule will travel further than a larger one. This technique also relies upon DNA intercalating molecules for visualization under UV irradiation.

For all work done in this thesis: the agarose gel composition is as defined in the individual results sections; the AGE running buffer was Tris-Acetate-EDTA (TAE) Buffer; the intercalating DNA stain used was SYBR® Safe (Invitrogen); the DNA loading buffer was 15 % Ficoll 400 with bromophenol blue; the AGE running equipment used was a RunOne™ Electrophoresis cell (Embi Tec); and a constant 100 mV was typically applied across the agarose gel.

2.2.2 Sodium Dodecyl Sulphate-Polyacrylamide Gel Electrophoresis

Sodium dodecyl sulphate-Polyacrylamide gel electrophoresis (SDS-PAGE) is a technique for analysis of protein samples. In a similar manner to AGE (Section 2.2.1), the technique relies upon a molecular sieve and an applied electric field to separate proteins by size. In this case the molecular sieve is formed from the polymerization of acrylamide, forming a matrix that protein samples pass through. Samples are introduced to the matrix using an SDS-containing loading buffer; this is vital for the technique as the dodecyl sulphate ions interpolate with protein molecules contained in the sample, coating the proteins with negative charge, hence when a current is applied across the gel, SDS-coated protein molecules are attracted to and migrate towards the anode. Again, in an analogous situation to AGE, smaller molecules migrate faster through the polyacrylamide matrix than larger proteins, thus in the same gel, when the same current is applied, over the same period of time, a smaller protein would move further through the gel than a larger protein. As a method of visualization of protein samples, after the application of an electric field to separate protein

molecules by size, the gel is stained using a Coomassie-derived dye which non-specifically stains protein molecules.

SDS-PAGE gel compositions are noted in the results section, archetypally a constant 180 V were applied for a variable amount of time, Novex Minicell (Invitrogen) gel running apparatus was used, BenchMark™ and BenchMark Prestained™ (Invitrogen) protein standards were used and SimplyBlue™ SafeStain (Invitrogen) was applied.

2.2.3 Western Blot

Western blot is a more *specific* technique for analysing protein samples than SDS-PAGE. In western blot, after running an SDS-PAGE gel (See Section 2.2.2), instead of staining the gel with Coomassie dye, the separated protein samples are transferred onto a membrane which is then probed with an epitope-specific primary antibody, followed by a secondary antibody targeting the Fc region of the primary antibody. The purpose of the secondary antibody is to amplify the primary signal and also to provide a means of detection. One of the most common methods of detection is to use a secondary antibody that is conjugated to Horseradish Peroxidase; for example, when used with appropriate reagents, this enzyme oxidises a substrate which then reacts with peroxidase, under alkaline conditions, to produce an excited molecule that will emit a sustained, high intensity chemiluminescence signal that can be detected using autoradiography film.

For the work described here, initial SDS-PAGE was performed as described in Section 2.2.2. Following this, sample transfer onto Amersham ECL Hybond nitrocellulose membrane (GE Healthcare) was performed using either semi-dry (Trans-Blot SD, Biorad) or wet (XCell SureLock

Mini-Cell, Invitrogen) western blotting transfer apparatus. NuPAGE® Transfer buffer (Novex), with 10 % (v/v) methanol, was used for western blotting. Membranes were then blocked in 5 % Marvel Milk Powder containing PBS (MPBS) for either 1 hour at room temperature or overnight at 4 °C. Primary antibody incubation was performed for 1 hour at room temperature using either a mouse IgG1 penta-His antibody (Qiagen) with a working dilution of 1:1000 in MPBS, or a mouse IgG1 anti-HA antibody (Sigma) with a working dilution of 1:2000 in MPBS or an anti-1D4 antibody (University of British Colombia) with a 1:2000 working dilution in MPBS. Membranes were then washed with 0.1 % Tween 20 PBS solution (TPBS) before incubation with a HRP-conjugated donkey anti-mouse-Fc antibody (Sigma) with a working dilution of 1:2000 in MPBS. Membranes were then washed extensively in TPBS and PBS before 1 min incubation with ECL Amersham western blotting detection reagents (GE Healthcare), followed by exposure of autoradiography film (Hyperfilm ECL, GE Healthcare) to the membrane in the dark for varying and defined amounts of time. Film was developed using a Xograph Compact X4.

2.3 Mammalian Cell Culture

2.3.1 Cell Lines

Mammalian cell expression systems are particularly relevant when studying eukaryotic proteins where numerous post-translational modifications are an essential component of the function and regulation of the eukaryotic proteome. In the realm of structural biology it is often necessary to quickly modify expression constructs for target proteins as iterative rounds of refinement are frequently necessary to find an optimal protein construct for expression, purification and crystallization. Hence, due to this potentially rapid turnaround in construct requirements, the lengthy process involved in producing stably expressing mammalian cell lines is not amenable to the modern structural biology pipeline. In contrast to this however, the use of transient transfection

and expression of target proteins in mammalian cells is a much quicker and more flexible approach and is thus more relevant to the study of eukaryotic protein structure.

Human Embryonic Kidney (HEK) 293T, and HEK 293 GNTI- (293S) (See section 2.4.3) were the primary expression cell lines used for the production of all recombinant proteins described in this thesis. Cultured cells were maintained in 10 % media (Dulbecco's Modified Eagle's Medium (DMEM, PAA), supplemented with L-glutamine, non-essential amino-acids (NEAA, PAA) and 10 % fetal bovine serum (FBS, Gibco) at 37 ^{o}C and 5 % CO_2. Cell density was monitored regularly and cultures were typically passaged when cells were roughly 95 % confluent. Passage protocols involved: old media was discarded, cells were washed with a flask-appropriate volume of PBS (PAA), adherent cells were detached using Trypsin-EDTA (Gibco), and an appropriate volume of 10 % media was added to create a cell suspension. This cell suspension was then used to seed new flasks or plates with the desired cell density. The recent introduction of a CompacT SelecT cell culture robot (TAP) meant that in practice I could employ this system to automate the process of cell passage using barcoded flasks (BD Falcon) (Zhao et al, 2011).

2.3.2 Small-Scale Expression Trial

One of the crucial requirements of using transient mammalian expression for the study of extracellular proteins or protein domains is that the proteins travel through the cellular secretory pathway, post-expression, and are secreted into the culture medium. This requirement for secretion of target proteins acts as a level of quality control ensuring that all material available for purification is correctly folded and has a similar level of post-translational modification. Thus it was essential to test all new expression constructs, described in this thesis, in small-scale trials for the ability to encode proteins that could ultimately be secreted from mammalian cells.

In brief, circa 3 x 10^5 HEK 293T cells suspended in 10 % media were seeded into 6-well plates (Greiner). Once seeded with cells, plates were incubated at 37 ^{o}C and 5 % CO_2 until the cell density reached 95 % confluent, at which point cells were ready for transfection. Four micro-grams of plasmid DNA was diluted in 250 µL of SFM (DMEM supplemented with NEAA and L-glutamine) to prepare solution A. Solution B, containing 8 µL of Lipofectamine 2000 transfection reagent (Invitrogen) diluted in 250 µL of SFM, was prepared in parallel. Solutions A and B were then gently mixed and incubated at room temperature for 20 mins. During the incubation period the media maintaining HEK 293T cells prepared for small-scale transfection was exchanged for 1.5 mL of 2 % media (DMEM supplemented with NEAA, L-glutamine and 2 % FBS). After the 20 min incubation period the solution A-B mix was added to the appropriate wells and the plates were incubated at 37 ^{o}C, 5 % CO_2. After ~72 hours the cell media and cells were collected for analysis. Cell media was centrifuged at ~13, 000 g to remove cell debris and cells were resuspended in 1 mL PBS, then 10 µL of each sample was prepared in SDS-loading buffer, this was boiled for 10 min and a Western blot was undertaken (See section 2.2.3).

In certain cases where expression and/or secretion levels were weak, pharmacological manipulation of the cellular expression machinery was attempted. Valproic acid (VPA) and sodium butyrate (NaBu) are histone deacetylase inhibitors that have been shown to enhance recombinant expression of transiently transfected mammalian cells in some cases (Backliwal et al, 2008; Wulhfard et al, 2010). Hence, for some low-expressing constructs, various concentrations of VPA and NaBu were added to cells at the time of transfection to test empirically if there was an enhancement in the levels of expression and secretion.

2.3.3 Large-Scale Transient Transfection of Cells

Once the construct boundaries and conditions that permit reasonable expression and secretion from mammalian cells were delineated, the next stage was to use a greater number of cells to produce a large quantity of target protein. Adherent HEK 293T or 293S cells were cultured in expanded surface polystyrene roller bottles (2125 cm^2, Greiner Bio-one) at 37 ^{o}C until roughly 95 % confluent. Typically 12 roller bottles would be transfected in one batch and before the transfection reagents were added the culture medium in each bottle would be replaced with 200 mL of 2% media. A transfection cocktail consisting of the following components would be prepared, with the quantities given as amount per bottle: 0.5 mg of chloroform-extracted DNA, 1 mg of 25 kDa branched polyethylenimine (PEI, Aldrich) transfection reagent and 50 mL of SFM. After the transfection cocktail was prepared, it was incubated at room temperature for ten minutes before it was decanted into each roller bottle. Also at the time of transfection, pharmacological agents controlling processes such as N-linked glycan formation (See Section 2.4.3), for instance kifunensine, or expression levels (See Section 2.3.2), for example VPA, were added to the culture medium at appropriate concentrations. Roller bottles were then incubated at 37 ^{o}C for a period of time until the media is harvested (See section 2.4.1).

2.4 Protein Purification

2.4.1 Sample Preparation

Seven to fourteen day post-transfection conditioned media, containing secreted target proteins, was decanted from the culture flask and subjected to centrifugation at 6, 000 g for 25 min, to remove cell debris, before being filtered through a 0.22 µm sterile filter (Millipore). In the next stage of preparation, a QuixStand^{TM} Benchtop system (Watson Marlow, GE Healthcare) was used to exchange conditioned media against 2 L of IMAC buffer, 10 mM Tris (pH 8), 500 mM NaCl. The

QuixStand system utilizes a column of material with a defined molecular weight cut-off, hence when a sample is passed over the column at high pressure, any molecules smaller than the molecular weight cut-off are forced out of the sample.

2.4.2 Immobilized-Metal Affinity Chromatography

Immobilized-metal affinity chromatography (IMAC) relies on the ability of amino-acids, such as Histidine and Cysteine, to co-ordinate certain transition metal atoms such as Zn^{2+}, Cu^{2+}, Ni^{2+} and Co^{2+}. The use of a stable matrix, such as nitrilotriacetic acid (NTA), which chelates metal ions, and genetic modification of DNA sequences to produce recombinant proteins with poly-histidine tags has transformed IMAC into the most widely used affinity chromatography technique for protein purification (Block et al, 2009)

After sample preparation (Section 2.4.1) buffer-exchanged conditioned media was loaded onto a HisTrap™ (GE Healthcare) column using a peristaltic pump at between 1-3 mL/min. The loaded HisTrap column was then transferred to an Akta FPLC system (GE Healthcare) pre-equilibrated with two buffers, one in each pump: Buffer A contained 20 mM Tris (pH 8), 500 mM NaCl; Buffer B contained 40 mM Tris (pH 8), 500 mM NaCl, 500 mM Imidazole. Imidazole is a small organic molecule that can outcompete the His_6 tag the coordinate metal ions. With this set-up it was possible to wash the loaded HisTrap column with low concentrations (5-50 mM) of imidazole, to remove impurities from the sample, and monitor protein elution via the UV280 absorbance. When this technique was coupled with SDS-PAGE analysis of fractions, the optimal concentration of imidazole required to remove all impurities was delineated, typically 50 mM Imidazole. Once all impurities were removed, the target protein was eluted from the HisTrap column with 250 mM imidazole containing buffer, in the smallest possible volume.

2.4.3 Protein Deglycosylation

N-linked glycosylation sites are post-translational modifications on the extracellular domains of protein molecules which are often crucial for the correct folding of glycoproteins (Moremen et al, 2012; Schwarz & Aebi, 2011). The inherent structural heterogeneity of these carbohydrate moieties can be unhelpful to the investigation of protein structure by way of protein crystallography, as heterogeneity can hinder the development of a repeating lattice required in crystal formation. Owing to this, it is often necessary to manipulate the pathway that produces N-linked carbohydrate moieties to yield a more homogeneous sample. One method of achieving this is by using an N-acetylglucosaminyltransferase I deficient ($GnTI^-$) mutant HEK cell line, HEK 293S cells, which produces a less complex and heterogeneous $Man_5GlcNAc_2$ sugar pattern (Reeves et al, 2002). An alternative strategy is to add kifunensine (Toronto Research Chemicals), an α-mannosidase I inhibitor, to a final concentration of 5 µM in the media of the cultured cells at the time of transfection; this produces N-linked carbohydrates with a predominantly $Man_9GlcNAc_2$ structure (Chang et al, 2007). Once a target recombinant protein has been expressed using the transient mammalian system, using either a drug or mutant cell-line, the N-linked glycans can be trimmed further using an enzyme. Endoglycosidase H (EndoH) is an enzyme that cleaves glycans between the two GlcNAc residues of the di-*N*-acetylchitobiose core, leaving a single GlcNAc at each site of N-linked glycosylation. Such enzymatic treatment can lead to a much more homogeneous sample which can aid the process of crystallization (Chang et al, 2007).

Typically, a deglycosylation time-course experiment was carried out on a sample of protein, for example 1 µg of recombinant EndoH (Produced in STRUBI) was added to 100 µg of test protein, and this mixture was then incubated at either 37 ^{o}C or room temperature for a period of time and

samples were taken at various intervals for analysis via SDS-PAGE (See Section 2.2.2). In general, when treating a large-scale protein sample with EndoH before crystallization, between 1-10 µg recombinant EndoH was added to the batch of protein and this was incubated at either 37 °C for 1-2 hours or room temperature for roughly 15 hours. Following treatment with EndoH, samples were often exposed to SEC (See Section 2.4.4) to re-purify the target recombinant protein.

2.4.4 Size Exclusion Chromatography

Size-exclusion chromatography (SEC) separates macromolecules based on hydrodynamic radius. This is achieved through the use of a SEC column which consists of a matrix of beads with a defined pore size, for example sephadex 200, packed in a mobile phase known as the running buffer. Hence, when a mixed molecular sample is applied to an SEC column a larger protein would be less likely to penetrate the pores and thus elute earlier, whereas a smaller protein would be likely to penetrate the pores and thus be retarded and elute later.

All SEC performed for this thesis was done using an AKTA series FPLC (GE Healthcare) and was typically performed using a self-packed s200 16/60 or 10/30 in 10 mM HEPES (pH 7.5), 150 mM NaCl, unless stated otherwise in the individual results sections. During SEC, eluate fractions were collected and these samples were analysed using SDS-PAGE (See Section 2.2.2) to identify the appropriate fractions.

2.4.5 Fluorescence Size Exclusion Chromatography

One of the challenges of working with intact membrane proteins is extracting them from cell membranes in a stable form. One of the parameters that can influence extraction and stabilization

of membrane-bound proteins is the type of detergent employed. Fluorescence size exclusion chromatography (FSEC) is a technique that allows the screening of many detergents to gauge their effects on extraction and stability in small-scale (Kawate & Gouaux, 2006). By tagging a target protein with a fluorescent molecule there are two advantages: i) the fluorescent signal that is measured is *specific* for the target protein, and ii) the fluorescence is a means of *amplifying* the signal from the target protein, meaning that different parameters can be screened in small-scale. Coupling of the extraction of a fluorescently tagged target protein to SEC provides the means of assessing protein stability since SEC delivers data regarding the oligomeric state of a protein in a sample and whether or not it is aggregated.

Regarding the specifics of the method: in brief, a single small-scale six-well dish was transfected (See Section 2.3.2) for each construct for a complete detergent screen. After ~72 hour incubation at 37 °C, the media was discarded, the cells in each well resuspended in 1 mL PBS and cells transfected with the same construct were pooled. The pooled cells were then centrifuged at low speed to yield a cell pellet. This cell pellet was then resuspended in 5.6 mL of 25 mM Tris (pH 7.2), 250 mM NaCl and protease inhibitors (Sigma) and aliquoted into 14 times 400 µL fractions. To these 400 µL aliquots, 100 µL of detergent solution was added to the final concentrations listed in Table 2.6. Once the detergents were added, samples were incubated at 4 °C for one hour to allow extraction. Following this, samples were ultra-centrifuged at 55, 000 g for 1 hr at 4 °C. Samples were then loaded into a Prominence automated UFLC system (Shimadzu) with a TSKgel SuperSW3000 (TSOH Bioscince) equilibrated with 10 mM Hepes pH 7.5, 500 mM NacL, 0.03 % DDM.

Name of Detergent	Final Detergent Concentration (w/v)
Lysofos-choline 12 (LC12, Anatrace)	1 %
Dodecyldimethylamineoxide (LDAO, Anatrace)	1 %
N-dodecyl-b-d-maltoside (DDM, Anatrace)	1 %
N-decyl-b-d-maltoside (DM, Anatrace)	1 %
N-nonyl-b-d-glucoside (ng, Anatace)	2 %
C8E4 (Anatrace)	2 %
C10E5 (Anatrace)	1 %
Cymal-6 (Anatrace)	2 %
Fos-choline-12 (Anatrace)	1 %
N-octyl-b-d-glucoside (b-OG, Anatrace)	2 %
CHAPS	2 %
Triton X-100	1 %
Tween 20	1 %

Table 2.6: Detergents: The range of detergents used to screen for extraction of membrane-bound protein constructs

2.4.6 Immuno-Affinity Chromatography

One of the drawbacks of IMAC is that often impurities will co-purify with your target protein which can cause severe problems when attempting to purify a target recombinant protein to high levels, which is a necessity in protein crystallography. This problem is often exacerbated when the target construct is expressed at low-levels. When aiming to purify recombinant membrane-bound constructs, once an optimal detergent has been suggested by FSEC (See Section 2.4.5), IMAC is particularly unfavourable due to the requirement of solubilizing the entire membrane component of the transgenic cells, increasing the likelihood of problems due to impurities. Furthermore, it is expected that membrane-bound constructs will be expressed at comparatively low levels due to the limitation that cell membranes have a certain capacity, intensifying the difficulties of using IMAC to purify membrane-bound constructs. Hence a different approach was taken when attempting to purify membrane-bound constructs, this approach was immuno-affinity chromatography (IAC).

IAC provides a more *specific* method of purifying recombinant proteins from cell lysates. This technique exploits an epitope tag that is engineered onto the target protein of choice; this antigen is recognised by a specific monoclonal antibody which is chemically fixed to a stable matrix. Thus, cell lysates can be applied to beads coated in a specific antibody and only the proteins that are tagged with the antigen that said antibody recognises should bind to the beads unambiguously; following this, a peptide that covers the specific epitope can be used to elute the target protein from the antibody beads at high purity.

The IAC used for this thesis employed a TETSQVAPA, or 1D4 C-terminal tag (Wong et al, 2009) engineered onto the C-terminus of target proteins. To allow this, DNA for target proteins was cloned into a modified form of pHLsec (See Section 2.1.1), pHLsec 1D4, that encodes the TETSQVAPA epitope 3' of the DNA insert of choice. To allow the use of this epitope tag it is necessary to couple the 1D4 antibody to a stable matrix; this was done using the following protocol: 1 g cyanogen bromide-activated sepharose (GE Healthcare), was washed with 1 mM HCl, and then washed with 0.1 M $NaHCO_3$, 0.5 M NaCl, pH 8.5, before the beads were incubated overnight at 4 ^{o}C with 14 mg of 1D4 antibody (University of British Colombia) dissolved in 0.1 M $NaHCO_3$, 0.5 M NaCl, pH 8.5. Following the overnight antibody incubation beads were incubated with at room temperature for 2 hours with 0.2 M Glycine (pH 8), and then washed with low and high pH buffers before being stored in a PBS azide solution at 4 ^{o}C until they were used.

To allow purification of 1D4 tagged recombinant proteins, 12 roller bottles of HEK 293T cells were transfected (See Section 2.3.3) with DNA constructs contained in the pHLsec 1D4 vector and cells were incubated at 37 ^{o}C for ~72 hours. After this incubation period, the maintenance media was

discarded and the cells were harvested from roller bottles using PBS to resuspend cells from the plasticware surface. Following resuspension, cells were pelleted using centrifugation at low speed. This cell pellet was then resuspended in 150 mL of 10 mM HEPES (pH 7.2), 500 mM NaCl plus protease inhibitors (Sigma) and the cells were disrupted at 4 °C and 30, 000 psi using a French Press (Constant Systems Cell Disruptor). The detergent N-dodecyl-b-d-maltoside (DDM), dissolved in 10 mM HEPES (pH 7.2), 500 mM NaCl, was then added to the cell lysate to a final concentration of 1.5 % (w/v) and the cell lysate-detergent mixture was incubated at 4 °C for 2 hours to allow the extraction of the target membrane-bound protein. After incubation the mixture was applied to ultracentrifugation at 50, 000 g for 2 hours at 4 °C. Then, previously prepared and buffer equilibrated 1D4 antibody-conjugated cyanogen bromide beads were added to the post ultracentrifugation supernatant and this was incubated at 4 °C for 2 hours. Following this, beads were collected on a column, the flow-through collected and stored and the beads were washed with 4 column volumes of binding buffer: 10 mM HEPES (pH 7.2), 500 mM NaCl, 0.003 % (w/v) DDM. The target membrane protein was then eluted from the 1D4 beads in numerous fractions using a 150 µM solution of TETSQVAPA peptide (GenScript) in 10 mM HEPES (pH 7.2), 500 mM NaCl, 0.03 % DDM.

2.5 Protein Crystallization

2.5.1 Screening

The aim of crystallization is to coax purified protein samples into a solid form, and specifically to prompt the formation of a regular, repeating array that constitutes a crystal lattice, which can then be used for diffraction experiments. Sitting drop vapour diffusion is one of the most commonly used methods for protein crystallization. In this technique a *drop* is formed when a protein stock solution is mixed 1:1 with a precipitant containing *reservoir* solution. This drop sits on a stage and

equilibrates against a much larger volume reservoir solution in a closed system. The consequence of this is the concentration of precipitant in the drop is roughly half of that in the reservoir and thus, in the closed system, water will diffuse from the drop into the reservoir. Diffusion of water into the reservoir results in the concentration of protein and precipitant in the drop to increase. The objective here is that the protein and precipitant concentrations rise in such a manner that spontaneous nucleation occurs. If this is the case, the concentration of protein in the drop will decrease and this allows the growth of protein crystals. The interactions that hold together protein crystals are non-covalent in character and many different factors can influence crystal formation, for example: pH, type of precipitant, type of additive and temperature. Hence when conducting crystallization trials it is important to screen as many conditions as possible, often a sparse matrix of crystallization solutions approach is undertaken.

Specifically in this thesis, appropriate SEC peak fractions (See Section 2.4.4) were pooled and concentrated using centrifugation concentrators (Amicon Ultra, Millipore) at 3,000 g. The protein concentration used to set-up crystallization trials with each unique sample was delineated using a pre-crystallization test PCT™ (Hampton Research), following the manufacturer's instructions. A Cartesian technologies pipetting robot was used to set-up vapour diffusion crystallization trials consisting of 100 nL protein plus 100 nL reservoir sitting drops in a 96-well plate (Greiner) (Walter et al, 2005). Initial crystallization trials were conducted at both 20.5 ^{o}C and 4 ^{o}C; plates were stored either in a 20.5 ^{o}C TAP Homebase storage vault and imaged via a Veeco visualization system (Mayo et al, 2005) or left to equilibrate in the cold room before storage and imaging in a 4 ^{o}C Formulatrix Rock Imager 1000. Inspection of crystallization trials was usually performed using the web-based application xtalPiMS (Daniel et al, 2011). Initial crystallization trials were conducted with the screens listed in Table 2.7.

Masterblock	Commercial Screen	Wells	Manufacturer
Block 1	Crystal Screen	A1-D12	Hampton Research
	Crystal Screen 2	E1-H12	Hampton Research
Block 2	Wizard 1	A1-D12	Emerald Biosystems
	Wizard 2	E1-H12	Emerald Biosystems
Block 3	PEG/Ion Screen	A1-D12	Hampton Research
	PEG 6000 Grid Screen	E1-F12	Hampton Research
	Ammonium Sulphate Grid Screen	G1-H12	Hampton Research
Block 4	Natrix Screen	A1-D12	Hampton Research
	Crystal Screen Cryo	E1-H12	Hampton Research
Block 5	PEG/LiCl Grid Screen	A1-B12	Hampton Research
	NaCl Grid Screen	C1-D12	Hampton Research
	MPD Grid Screen	E1-F12	Hampton Research
	Quik Screen	G1-H12	Hampton Research
Index	Index Screen	A1-H12	Hampton Research
SaltRX	SaltRX Screen	A1-H12	Hampton Research
PACT	PACT Premier	A1-H12	Molecular Dimensions
PEGRx	PEGRx Screen	A1-H12	Hampton Research
Morpheus	Morpheus Screen	A1-H12	Molecular Dimensions
PGA	PGA Screen	A1-H12	Molecular Dimensions
Proplex	Proplex Screen	A1-H12	Molecular Dimensions

Table 2.7: The range of crystallization screens used for new protein constructs.

2.5.2 Optimization

Two optimization strategies were predominantly employed to screen around reservoir conditions that yielded initial crystallization hits. The first tactic involved varying the protein and precipitant concentrations. In brief, 3-rows of a 96-well plate were used for this optimization strategy where one row used a 1:1, a second row a 2:1 and a third row a 1:2 protein:reservoir drop ratio, and along the 12 wells of the row, the original crystallization condition was diluted from 100 % to 67 % in 3 % steps. A second approach involved using volatile and non-volatile compounds from the Hampton Research Additive screen to alter protein solubility as well as protein-protein and protein-solvent

interactions. The additive solutions were transferred to the crystallization plate by the pipetting robot (Cartesian technologies) as an extra step to the normal procedure, whereby 100 nL of non-volatile reagents were pipetted directly onto the 100 nL protein-100 nL reservoir sitting droplets, whereas for volatile compounds an aliquot of 20 µL was dispensed into the reservoir (Walter et al, 2005).

In a limited number of cases where very small crystals and needle clusters were observed, addition of glycerol 1-10 % to the protein sample solution prior to crystallization was attempted with the aim of preventing excess nucleation. Another approach taken in this scenario was micro-seeding, the protocols of which are described in (Walter et al, 2008).

The final individual crystallization solutions which yielded good quality crystals that provided useful diffraction data for data processing are described in the relevant results sections (See Chapters 3-6).

2.5.3 Reductive Lysine Methylation

Reductive lysine methylation was used as a strategy to optimize crystallization of target protein constructs when poorly diffracting crystals were obtained through other strategies outlined in Sections 2.5.1-2. The formation of a well-ordered crystal lattice can be inhibited by the flexibility of solvent exposed side chains. As an approach to counteract this, shotgun chemical modification of surface exposed lysine amino groups can radically reduce surface entropy properties of target proteins and thus potentially aid crystallization. Furthermore, the formation of di-methyl tertiary amino groups at the terminus of surface exposed lysine side-chains can also enhance crystallization, through the formation of hydrophobic interactions with neighbouring molecules in the crystal.

This procedure was performed in the late steps of purification, after IMAC and SEC (See Sections 2.4.2 and 2.4.3). Sample protein concentration was typically less than 0.5 mg/mL and buffer was 10 mM HEPES (pH7.5), 150 mM NaCl. The reducing agent, 20 mM dimethylamine borane complex (ABC, Fluka) and the methyl source, 40 mM formaldehyde (Fluka), were added to the protein sample and the reaction incubated at 4 °C for 2 hours. The concentration of reducing agent and methyl source was then doubled and the incubation at 4 °C continued for a further 2 hours. The reagents were supplemented further to reach 60 mM ABC and 120 mM formaldehyde before being incubated at 4 °C for roughly 15 hours. After this final incubation period, precipitate was removed from the solution using centrifugation at 13,000 g before the sample was applied to SEC in a 10 mM Tris (pH 7.5), 150 mM NaCl running buffer; the use of a Tris-based buffer was important as it quenches the reaction and SEC was helpful to remove the excess reagents through buffer exchange. The lysine-methylated protein was then concentrated and used in the standard crystallization trials (See Section 2.5.1) (Walter et al, 2006).

2.6 Data Collection and Structure Solution

2.6.1 Crystal Mounting and Cryo-Protection

To reduce the adverse effects of radiation damage on a test crystal, and to permit the collection of a complete dataset, diffraction experiments are routinely performed under cryogenic conditions, roughly 100 K. Cryo-crystallography can have additional benefits since the low temperature will reduce thermal vibrations and could force flexible sections of protein molecules to rest into a specific conformation; these effects could ultimately lead to higher resolution data and subsequently a more accurate structural model. To prevent the drying out and disintegration of

protein crystals, it is essential that they are maintained in the mother liquor during crystal mounting and data collection. Upon flash cooling however, without protection, the mother liquor surrounding the crystal would form crystalline ice which is deleterious to the diffraction quality of the crystal. Hence it is necessary to use a cryo-protectant to allow the vitrification of the mother liquor which is much more conducive to diffraction experiments.

Glycerol, at 25-30 % and 30 % ethylene glycol were routinely used as cryo-protectants for all crystals, unless there was a cryo-protectant present in the original crystallization solution, in which case no further additive was required. Where the addition of a cryo-protectant was needed, the cryo-solution was added directly on top of the drop so that as the crystal was picked it would pass through the cryo-solution. Crystals were picked from the drop using either CryoLoops™ (Hampton Research) or LithoLoops (Molecular Dimensions); the loop size was chosen so that is was roughly similar to that of the crystal. After the introduction of a suitable cryo-protectant and the successful picking of an individual crystal, it was flash frozen in liquid nitrogen where it was stored until data collection. The final individual cryo-protectants used to give useful diffraction data are listed in the relevant results sections (See Chapters 3-6).

2.6.2 Data Collection

X-ray diffraction experiments were carried out either at Diamond Light Source, Oxfordshire or at the European Synchrotron Radiation Facility (ESRF), Grenoble, France. The specific synchrotron and beamline used to collect data relevant to this thesis are listed in the crystallographic tables in the following results chapters. Data collection strategies, allowing optimal crystal orientation and the necessary crystal rotation for complete datasets, were determined using the program iMosflm (Battye et al, 2011). During data collection, the crystal was normally maintained in a nitrogen

cryostream at 100 K. However, on some occasions ice was introduced to crystals at some point during flash-freezing, transportation and mounting and hence in some cases annealing was attempted whereby the cryostream was blocked briefly to disrupt the ice.

2.6.3 Data Processing

Processing of X-ray diffraction images involves several steps: firstly data is indexed, where Miller indices are assigned to each reflection, and the unit cell dimensions are determined, as is the point group. Following this, data is integrated – where diffraction spot intensities are measured – and then merged and scaled, where various measurements of the same reflections are combined into a single dataset with a common absolute scale. Processing of diffraction data for this thesis was performed using the xia2 (Winter, 2010) auto-processing suite or HKL2000 (Otwinowski & Minor, 1997) processing software. In the situations when HKL2000 was used for data processing, the program cTruncate (French & Wilson, 1978; Padilla & Yeates, 2003) was used to convert measured intensities into structure factor amplitudes; the intensity of the measured reflection is proportional to the square of the amplitude of the structure factor. Data processing statistics were monitored and these are detailed in the relevant results chapters. This information is routinely used to ascertain the quality of the diffraction data and to determine the resolution limit; they include the following terms. R_{merge}, or the linear merging R-value is a traditional indicator assessing the quality of data, it provides a measure of the agreement of the consistency of multiple measures of the same reflection. An R_{merge} of 10 % for the entire dataset and less than 100 % for the highest resolution shell are routinely seen as being conventional. $I/\sigma I$ is the reflection intensity divided by the standard deviation averaged for a defined set of reflections and is a measure of signal to noise. An I/σI of roughly 2 is conventionally taken to indicate the presence of useful signal and thus to determine the high resolution limit. However it is argued that these current standards are too conservative and result in good data being lost, producing a worse model than could potentially be

achieved. Hence a recent paper has suggested a different measure termed *CC** as a new quantity for defining the high resolution limit (Karplus & Diederichs, 2012). CC* uses the Pearson correlation coefficient to compare the association between the measured data and the model. The *completeness* is the number of unique reflections that have been measured as a percentage of the expected number. Usually a greater than 90 % completeness in the highest resolution shell and greater than 95 % completeness overall are aimed for. The *redundancy* gives a measure of the number of times each unique reflection has been measured, with a higher redundancy suggesting a greater accuracy in the intensity measurement.

2.6.4 Molecular Replacement and Model Building

During a diffraction experiment we can model X-rays as waves with the common features of wavelength and amplitude. Upon collecting diffraction images, the measure being taken is the intensity of the diffraction spots. However there is no way of measuring the phase of the waves that collide with our detector. This is known as the 'phase problem' in crystallography. To solve this problem several methods have been developed which can be split into two categories: *experimental phasing* and *molecular replacement*. For the protein structures presented in this thesis, molecular replacement was used as the sole method of generating the phase information that is required to generate electron density maps. Molecular replacement is a method of phasing that relies upon the existence of a previously solved, structurally similar model (textbooks suggest a sequence identity of ~30 % or higher as being adequate) as a search probe. In molecular replacement, the search probe is rotated and translated, in the unit cell, until the best fit is obtained between the experimentally measured diffraction data of the unknown protein, and the calculated diffraction data from the molecular replacement model.

For all molecular placement procedures used to solve the structures presented in this thesis the program Phaser (McCoy et al, 2007) was used, after an initial estimate of the number of molecules in the unit cell was obtained using the Matthews coefficient (Kantardjieff & Rupp, 2003). Both Phaser and Matthews coefficient calculations are available through the ccp4 suite (Winn et al, 2011) of programs. The individual search probes used for each structure solution are detailed in the specific results sections. Whilst using Phaser, two statistics were monitored to gain an indication of whether the molecular replacement procedure was successful. *The log-likelihood gain (LLG)* is a comparison of how much better the molecular replacement model fits the experimental data compared to a random distribution of the same atoms. The *Z-score* is the LLG minus the mean LLG for a random set of translation or rotations, divided by the root-mean square deviation of a random sample of LLG values from the mean, thus indicating the number of standard deviations the molecular replacement solution LLG is above the mean LLG of a random sample of atoms. During molecular replacement the procedure was deemed successful if the Z-score was ~7-8, or greater, and the LLG was positive and increased as Phaser progressed. The resulting electron density maps were also assessed to determine if the solution seemed reasonable, i.e. there were additional unmodelled features.

Solutions from molecular replacement were extended and the protein sequence corrected using the automatic model building program ARP/wARP (Langer et al, 2008). The enhanced model outputted from ARP/wARP was improved further using iterative rounds of real-space refinement in coot (Emsley et al, 2010) coupled with restrained refinement in programs such as Phenix (Adams et al, 2010), Buster (Smart et al, 2012) or Refmac (Murshudov et al, 1997a). Several factors were monitored during iterative rounds of refinement, with the most attention being paid to R_{work} and R_{free}. These R-factors provide an indication of the agreement between the experimental diffraction data and the crystallographic model. R_{work} is calculated for the 95 % of the reflections that are

included in refinement, whilst R_{free} is calculated using the randomly assigned 5 % of reflections that are excluded from the refinement process. Hence R_{free} is used as a validation tool and if the gap between the two R-factors deviates significantly it is an indication that bias has been introduced into the model. For the final model it is conventional to expect a gap between the R-factors of roughly 5 %. The addition of solvent molecules, glycans and other heteroatoms was performed manually in coot using the CCP4 monomer library (Winn et al, 2011) or the HIC-Up online server (Kleywegt et al, 2003). The addition of LINK entries into the pdb header specified the connection between asparagine residues and individual glycan units and allowed refinement in Buster (Blanc et al, 2004) or Refmac (Murshudov et al, 1997b).

2.6.5 Quality Control

Aside from the final R-factors and a more qualitative user assessment of the agreement between the electron density map and the model, the program MolProbity (Chen et al, 2010) was used as a final validation tool. Molprobity provides different quality control features with one of the most helpful being that it highlights any amino acids that defy theoretical sterochemical restraints; these rebel amino acids are thus known as Ramachandran outliers. The polypeptide backbone angle between the N and the Cα is known as ϕ and the angle between the Cα and the C=O is carbon is known as ψ. In a Ramachandran plot these two angles are plotted against each other and define allowed regions for the backbone conformations of each amino acid in a polypeptide chain. Hence we can compare our model with the theoretical limits in a Ramchandran plot as a mode of validation and following this, correct any outliers.

2.7 Structural Analysis

The superposition of protein domains, to compare overall architecture, was based on equivalent Cα positions and was performed using the program SHP (Stuart et al, 1979). SHP also provided a measure, the RMSD (Root Mean Square Deviation), for the average distance between equivalent Cα's. Inter-chain interface analysis was performed using the online ebiPISA server, which provided details about the buried surface area for each interaction as well as highlighting the residues that are involved in protein interfaces and the types of inter-molecular forces at play (Krissinel & Henrick, 2007). The conservation of amino acids from related proteins mapped onto a single structure was performed using the ConSURF server (Ashkenazy et al, 2010). Protein vacuum electrostatics analyses were calculated using APBS (Baker et al, 2001).

2.8 Multi-Angle Light Scattering

Multi-angle light scattering (MALS) is a technique that can be used to accurately determine the molecular mass of a species. When coupled with a fractionation technique such as SEC (See Section 2.4.4) it can be particularly useful to ascertain unambiguous information about components in a mixture. When this technique is applied in the context of protein biochemistry it can be utilized to uncover the oligomeric state of test protein constructs. This relies upon the idea that when polarized light interacts with a macromolecule in solution, this light will scatter as a result of an oscillating dipole induced on the macromolecule and the concomitant re-radiation of light which causes the scatter. The polarizability of the macromolecule is related to its refractive index, plus the intensity of the scattered light is proportional to the molar mass of the macromolecule and hence this can be exploited to delineate oligomeric state. Moreover the angular variation of the scattered light can be used to provide information about the size of the molecule.

SEC-MALS experiments were carried out using a Wyatt MALS/AFFF system (Wyatt technologies), usually in 10 mM HEPES (pH 7.5), 150 mM NaCl buffer, on a superdex s200 HR 10/30 column (Pharmica Biotech). An Agilent autosampler, pump and UV detector and a Dawn Helios II MALS detector recorded refractive index and light scattering of samples upon elution from the SEC column. Astra analysis software (Wyatt) was used for data analysis and to calculate the molar mass of eluted samples from the refractive index and the scattering measurements. MALS apparatus set-up and calibration, plus the injection of samples, were all performed by either Dr. Geoff Sutton, Dr. Charlotte Coles or Dr. Elena Seiradake (STRUBI); however analysis was performed by myself.

2.9 Surface Plasmon Resonance Macromolecular Binding Assays

2.9.1 Background

Surface Plasmon Resonance (SPR) based instruments, such as those commercialized by Biacore, employ an optical technique to measure changes in the refractive index near a sensor surface. Such changes in the sensor surface refractive index are dependent upon and relative to changes in mass at the sensor surface. An essential component of this sensor surface is a thin gold layer; resonance of delocalized electrons of said thin gold layer allows some absorption of polarized light as it reflects. The angle of incidence that results in the greatest level of absorption is proportional to the refractive index of the area within 300 nm of the surface. SPR instruments measure this angle very accurately and precisely in real-time, and a shift in the maximal absorption angle of 0.0001^{o} corresponds to 1 Resonance Unit (RU) which represents the binding of ~1 pg of protein/mm^2 of the sensor surface.

During a typical SPR experiment one molecule (the ligand) is immobilised on a sensor surface whilst another molecule (the analyte) is continuously flowed over the surface for a determined period. If the analyte binds to the ligand, the accumulation of analyte protein on the surface leads to an increase in the refractive index. Such a change is measured in real-time and the read-out of any refractive index changes are provided as Resonance Units. Notably, a background response will be subtracted from all measurements to ensure that any measured changes in refractive index are not due to differences in the running buffer and the sample buffer. Measurement of the background response involves injecting the analyte over a reference surface which has either no ligand or an unrelated ligand immobilized on the sensor surface. SPR can thus be used as a sensitive technique employed for the molecular dissection of macromolecular interactions, providing data about the specificity and kinetic parameters of such interactions.

2.9.2 Ligand Preparation

Ligand capture was used as the primary method of immobilization of the ligand onto the sensor surface. This approach involved attaching Streptavidin to the sensor surface using amine coupling, followed by the capture of biotinylated ligand proteins through the femtomolar K_d (1×10^{-14} M) of the streptavidin-biotin interaction. The reasons for this approach are as follows: (i) Owing to the virtually irreversible nature of the streptavidin-biotin interaction, once prepared the sensor surface should be extremely stable. (ii) As the ligand has been indirectly coupled to the sensor surface, the ligand is more likely to be presented to the analyte in a more consistent manner across the population of molecules. In contrast, if direct coupling of the ligand had been utilized the ligand could have potentially attached to the sensor surface in a proliferation of random orientations, some of which may have obscured the binding site. (iii) Due to the specificity of the streptavidin-biotin interaction it is not necessary to use high purity biotinylated ligand samples. Whereas due to

the non-specific nature of direct coupling it would be essential to have highly pure ligand samples, otherwise all protein impurities would be coupled to the sensor surface.

The preparation of biotinylated proteins was achieved using the following general protocol. DNA constructs for ligand proteins were inserted into the pHLsec Avitag3 vector (Appendix 8.3) (Aricescu et al, 2006) resulting in the addition of a biotin ligase (BirA) recognition site and His_6 tag at the C-terminus of expressed proteins. Ligand constructs were expressed in HEK293T cells in 2-3 wells of a 6-well dish, as described in Section 2.3.1. Conditioned media was harvested as described in Section 2.3.1 and following this diluted 1:2 with PBS (pH 8). Diluted conditioned media was incubated for ~3 hours at 4 °C with 500 µl Talon resin (Clontech) whilst rotating. After the incubation period, beads were collected on a gravity flow column and washed with ~50 mL 10 mM Tris (pH 8.0). A bead suspension (total volume 1 mL) in 10 mM Tris (pH 8.0) was transferred to an eppendorf tube followed by the addition of 15 µL of ~2 mg/mL recombinant BirA enzyme (purified in STRUBI), 100 µL Buffer A (500 mM Bicine (pH 8.3)) and 100 µL Buffer B (100 mM ATP, 100 mM Magnesium Acetate, 500 µM D-biotin). The reaction mixture was incubated at room temperature for ~3 hours with mixing. Beads were then collected on a gravity flow column and were washed with ~50 mL PBS before biotinylated protein was eluted in 7 mL of 300 mM Imidazole PBS. Buffer exchange into 10 mM HEPES (pH 8), 150 mM NaCl and concentration to ~500 µL was achieved using an Amicon Ultra centrifugal filter unit (Millipore).

2.9.3 Multi-Cycle Binding Experiments

SPR experiments were performed on either a Biacore T100 or T200 instrument using CM5 sensor chips (Biacore, GE Healthcare). CM5 chips consist of a carboxymethylated dextran matrix attached to a gold surface allowing covalent attachment of molecules via amine, thiol, aldehyde or carboxyl

groups. All experiments were performed at 25 °C in a running buffer that typically consisted of 10 mM HEPES (pH7.5), 150 mM NaCl, 2 mM $CaCl_2$, 1 mM $MgCl_2$, 0.005% Tween 20. All analytes were expressed in HEK293T cells, treated with kifunensine, and purified as described in Sections 2.4.1, 2.4.2, 2.4.4. Pre-SPR SEC of analytes used the biacore running buffer described above.

The system and chip were initially primed in running buffer (see paragraph above) before the sensor surface was normalized using the BIAnormalizing solution (Biacore). The sensor surface was then activated for amine coupling through the addition of a 1:1 mixture of 100 mM NHS (N-hydroxysuccinimide) and 400 mM EDC (1-ethyl-3(3-dimethylaminopropyl) carbodiimide (Biacore, Amine Coupling Kit) at 5 µL/min for 900 s. Application of NHS-EDC mixture triggers the activation of the dextran associated carboxymethyl groups leading to the creation of highly reactive succinimide esters which can react with amine and other nucleophilic groups on proteins. Following activation, a 0.5 mg/mL streptavidin solution in pH 5.0 acetate buffer was injected over the surface at 5 µL/min for 900 s. The low pH and low salt buffer that the streptavidin is contained in is important as it provides the correct conditions for the pre-concentration event required for amine coupling. After sufficient and equivalent levels of streptavidin have been coupled to each of the four flow cells on the sensor surface, 1 M Ethanolamine (pH 8.5) is injected over the sensor surface at 5 µL/min for 900 s. Ethanolamine deactivates any remaining unreacted succinimide groups and removes any non-covalently coupled streptavidin.

Following direct coupling of streptavidin, biotinylated proteins were gradually added to individual flow cells at a flow rate of 5 µL/min until the desired density of biotinylated proteins was reached. When trying to compare the binding of a single analyte to different ligands, flow cells were generated so that equivalent densities of different ligands were applied. When aiming to establish

analyte injection times, flow rates and regeneration procedures, test injections of the analyte were performed.

For the multi-cycle binding experiments presented in this thesis, a typical flow rate of 10-20 µL/min was used for injections and regeneration was achieved using 1-3 M $MgCl_2$ for varying lengths of time. The unique parameters of each individual SPR experiment are detailed in the individual results sections. To obtain K_d values from multi-cycle equilibrium experiments, serial two-fold dilutions of the analyte were sequentially injected. The dilutions series was designed so that, where possible, representative data points were spread along the binding curve to saturation levels. In addition, if stocks of analyte protein were sufficient, injection series were repeated twice. Furthermore, all sensorgrams presented in this thesis are reference subtracted; i.e. one flow-cell surface was left blank and any response in this flow cell is subtracted from the experimental flow cells (See section 2.9.1).

2.9.4 Data Analysis

Scrubber2 (BioLogic Software) and GraphPad Prism (GraphPad Software) were used for all data analysis. For multi-cycle equilibrium experiments a nonlinear regression was used to fit a curve to the data assuming binding was 1:1, specific and tending to a saturation point. From this curve, an equilibrium binding constant (K_d) and maximum amount of analyte that could bind to the surface (Bmax) were obtained. Excel (Microsoft) was used for the presentation of all sensorgrams.

2.10 Fluorescence-Activated Cell Sorting (FACS) Plasma Membrane Trafficking Assay

FACS allows the simultaneous measurement of several parameters of large populations of cells as well as the sorting of individual cells based on these parameters.

DNA sequences of target proteins were amplified with specific primers so that the 5′ end of the cDNA coded for a HA tag. This sequence was inserted into pHLsec (Aricescu et al, 2006) as described in 2.1.1. Constructs for FACS were expressed in HEK293T cells, confluent in 6-well dish format, as described in Section 2.3.2. Twenty four hours post-transfection, media was discarded and cells in each well were sequentially resuspended in 1 mL PBS, transferred to labelled 5 mL round-bottom tubes (BD Falcon) and then softly pelleted by centrifugation at 1,000 g. Cell were then washed with 3 mL cold PBS containing 0.05 % sodium azide (PBS-NaN_3) and following this pelleted by centrifugation at 1,000 g. This wash was repeated twice more. Cells were then incubated with primary mouse anti-HA antibody for 45 mins at 4 °C. One micro-litre of a 0.5 µg/µL anti-HA (Sigma) stock was diluted in 100 µL PBS per sample. The cells were then washed three times in PBS-NaN_3 as described above. Samples were then incubated with a donkey anti-mouse APC (Allophycocyanin)-conjugated secondary antibody (Invitrogen) for 30 mins at 4 °C in the dark before being washed with three times with PBS-NaN_3 as described above. Cells were then resuspended in PBS-NaN_3 with 2 % PFA (Paraformaldehyde). Cells were then sorted with a CyAn flow cytometer (Beckman Coulter). Thirty thousand cells were counted and APC emission measured at 675 nm after excitation with 647 nm wavelength light. For some samples, the mVenus emission at 528 nm was measured after excitation with 515 nm wavelength light. All data analysis was performed using FlowJo (Tree Star Inc.) where the live cell subset, determined by counting an untransfected sample, was extracted from the raw data.

2.11 Blue Native-Polyacylamide Gel Electrophoresis Based Oligomerization Assay

Blue native-polyacrylamide gel electrophoresis (BN-PAGE) is a similar method to SDS-PAGE (Section 2.2.2) but allows the analysis of protein samples without disrupting their native oligomeric state or protein-protein interactions (Wittig et al, 2006). To allow the separation of native protein complexes under the application of a current, BN-PAGE utilizes coomassie G-250 as a charge-shift molecule, i.e. it binds to the protein complex and covers it in negative charge without denaturing it. Whereas in SDS-PAGE, SDS acts as the charge-shift molecule but simultaneously denatures any protein complexes and their components.

Expression constructs encoding the target proteins for oligomerization analysis were used to transfect HEK 293T cells as described in Section 2.3.2. After a 72 hour 37 ^{o}C incubation period the maintenance media was discarded and the cells were resuspended in 1 mL PBS. A sample was then incubated with either 1 % DDM or 1 % DMNG (decyl maltose neopentyl glycol) for 45 min at 4 ^{o}C. Following extraction, samples were spun at 16, 000 g at 4 ^{o}C. This supernatant was then used to prepare the BN-PAGE samples in NativePAGE™ Sample buffer (Novex) and NativePAGE™ 5 % G-250 sample additive following the manufacturer's instructions. A NativePAGE™ 3-12 % Bis-Tris (Novex) gel was then loaded with samples, the supplied cathode and anode buffers (Novex) were added and a constant 150 V was applied following the instructions of the manufacturer. The gel was then blotted onto a PVDF (Polyvinylidene fluoride) membrane; this membrane was then blocked and probed with an anti-HA primary and an appropriate secondary antibody, followed by ECL, film exposure and development, as described in Section 2.2.3.

2.12 Figures

Structure-based sequence alignments were prepared in Multalin (Corpet, 1988), manually edited based on SHP structural superpositions (Stuart et al, 1979), and then formatted using ESPript and Corel Draw (Corel Corporation). Secondary structural elements were determined using DSSP (Kabsch & Sander, 1983). Figures of protein structures were prepared using Pymol (The PyMOL Molecular Graphics System, Version 1.5.0.4 Schrödinger, LLC.) and images of electron density were made using coot (Emsley et al, 2010). Chromatography profiles were prepared in Microsoft Excel (Microsoft). SPR analysis was performed using Scrubber2 (BioLogic Software), sensorgram figures were made in Microsoft Excel (Microsoft) and Binding curves in either SigmaPlot (Systat Software) or GraphPad Prism (GraphPad Software). FACS figures were prepared in FlowJo (TreeStar Inc.). Other Figures were created using Adobe Photoshop (Adobe Systems), Corel Draw (Corel Corporation) or Microsoft Powerpoint (Microsoft).

Chapter 3:

Crystal Structures of the Delta iGluR ATDs

3.1 Abstract

Ionotropic glutamate receptors have a modular domain architecture and much is known about the structural details of iGluR LBCs. An increasing number of crystal structures of iGluR ATDs have become available since 2009; however, no structural details have been reported for the Delta-subtype iGluR ATDs. In this chapter crystal structures for the GluD1 ATD, at 2.25 Å, and the GluD2 ATD, at 1.8 Å are presented. These share a venus flytrap protein fold and a common dimerization interface with non-NMDA iGluRs. Structural comparisons with all the previously published iGluR ATDs revealed a series of Delta-iGluR specific features, which may play an important role in GluD1 and GluD2 functions.

3.2 Introduction and Aims

As discussed in Section 1.3, ionotropic glutamate receptors (iGluRs), an 18 gene product superfamily of ligand-gated cation channels, play an important role in excitatory neurotransmission and synaptic plasticity events, the molecular phenomena thought to underlie learning and memory (Dingledine et al, 1999). iGluRs have a modular domain architecture (See Section 1.3.2) consisting of the extracellular amino-terminal domain (ATD), the extracellular ligand-binding core (LBC), three membrane spanning helices and a re-entrant P-loop forming the transmembrane domain (TMD) and an intracellular C-terminal domain (CTD) (Traynelis et al, 2010). Extensive structural studies of the LBC from a range of iGluRs – including LBCs from each iGluR sub-family, i.e. AMPA (Armstrong & Gouaux, 2000), NMDA (Furukawa et al, 2005), Kainate (Mayer, 2005) and Delta (Naur et al, 2007) – have been carried out previously. These studies have revealed the molecular basis for ligand-binding in each sub-family as well as a prototypical molecular mechanism for channel opening and desensitization (Traynelis et al, 2010). An increasing number of crystal structures have been

reported for several iGluR ATDs, a list of the published iGluR ATDs at the time of writing is contained in table 3.1.

iGluR Sub-Family	Description of Structure	Resolution / Å	Space Group (Unit Cell Dimensions / Å, °)	Number of Molecules in ASU	PDB Code	Citation
AMPA	Rat GluA1 ATD homomer	2.50	P 2_1 2_1 2_1 (a=92.6, b=94.4, c=186.4, α=β=γ=90)	4	3SAJ	(Yao et al, 2011)
AMPA	Human GluA2 ATD homodimer	1.80	I 2 2 2 (a=51.0, b=122.5, c=138.9, α=β=γ=90)	1	2WJW	(Clayton et al, 2009)
AMPA	Human GluA2 ATD homotetramer	4.10	P 4_3 2_1 2 (a=224.3, b=224.3, c=77.0, α=β=γ=90)	3	2WJX	(Clayton et al, 2009)
AMPA	Rat GluA2 ATD homodimer	2.33	P 2_1 2_1 2 (a=64.0, b=323.0, c=61.4, α=β=γ=90)	3	3H5V	(Jin et al, 2009)
AMPA	Rat GluA2 ATD homodimer	2.69	P 2_1 2_1 2_1 (a=85.9, b=96.4, c=108.5, α=β=γ=90)	2	3H5W	(Jin et al, 2009)
AMPA	Rat GluA2 ATD homodimer	1.75	P 2_1 2_1 2_1 (a=82.5, b=93.7, c=101.5, α=β=γ=90)	2	3HSY	(Rossmann et al, 2011)
AMPA	Rat GluA2 ATD Interface Mutant N54A	1.95	P 2_1 2_1 2_1 (a=82.3, b=92.6, c=102.5, α=β=γ=90)	2	3O2J	(Rossmann et al, 2011)
AMPA	Rat GluA2 ATD Interface Mutant T78A	3.20	P 2_1 2_1 2_1 (a=64.2, b=120.2, c=360.8, α=β=γ=90)	6	3N6V	(Rossmann et al, 2011)
AMPA	Rat GluA3 ATD homodimer	2.20	P 2_1 2_1 2_1 (a=98.8, b=130.9, c=131.1, α=β=γ=90)	4	3O21	(Sukumaran et al, 2011)
AMPA	Rat GluA3 ATD homomer	4.20	P 2_1 2_1 2_1 (a=111.0, b=128.0, c=130.1, α=β=γ=90)	4	3P3W	(Sukumaran et al, 2011)
Kainate	Rat GluK2 ATD homodimer	2.90	P 6_1 (a=177.3, b=177.3, c=81.2, α=β=90, γ=120)	2	3H6H	(Kumar et al, 2009)
Kainate	Rat GluK2 ATD homodimer	2.70	P 6_1 (a=172.1, b=172.1, c=111.6, α=β=90, γ=120)	2	3H6G	(Kumar et al, 2009)
Kainate	Rat GluK3 ATD homodimer	2.75	P 6_1 (a=171.2, b=171.2, c=68.2, α=β=90, γ=120)	2	3OLZ	(Kumar & Mayer, 2010)
Kainate	Rat GluK5 ATD homodimer	1.68	C 2 (a=109.3, b=65.6, c=113.8, α=γ=90, β=95.7)	2	3OM1	(Kumar & Mayer, 2010)
Kainate	Rat GluK5 ATD homodimer	1.40	C 2 2 2_1 (a=66.3, b=102.0, c=116.2, α=β=γ=90)	1	3OMo	(Kumar & Mayer, 2010)
Kainate	Rat GluK2-GluK5 heterodimer	2.91	P 2_1 2_1 2_1 (a=65.6, b=139.6, c=195.4, α=β=γ=90)	4	3QLU	(Kumar et al, 2011)
Kainate	Rat GluK2-GluK5 heterotetramer	3.94	C 2 (a=366.6, b=109.2, c=155.5, α=γ=90, β=97.5)	10	3QLV	(Kumar et al, 2011)
Kainate	Rat GluK2 ATD glycan wedge homodimer	2.99	I 4 (a=191.8, b=191.8, c=47.0, α=β=γ=90)	2	3QLT	(Kumar et al, 2011)
NMDA	Rat GluN1 ATD homomer	3.40	P 3_1 2 1 (a=164.7, b=164.7, c=147.3, α=β=90, γ=120)	3	3Q41	(Farina et al, 2011)
NMDA	Rat GluN2B Zinc-bound monomer	3.21	P 3_1 2 1 (a=143.4, b=143.4, c=88.5, α=β=90, γ=120)	1	3JPY	(Karakas et al, 2009)
NMDA	Xenopus laevis GluN1 ATD homodimer	2.00	P 2_1 2_1 2_1 (a=47.3, b=92.8, c=210.0, α=β=γ=90)	2	3QEK	(Karakas et al, 2011)
NMDA	Heterotetrameric complex of Xenopus laevis GluN1 ATD and Rat GluN2B ATD in complex with Ifenprodil	2.60	C 2 (a=268.0, b=60.9, c=144.9, α=γ=90, β=116.5)	4	3QEL	(Karakas et al, 2011)
NMDA	Heterotetrameric complex of Xenopus laevis GluN1 ATD and Rat GluN2B ATD in complex with Ro 25-6981	3.00	C 2 (a=268.0, b=61.3, c=144.4, α=γ=90, β=116.3)	4	3QEM	(Karakas et al, 2011)

Table 3.1: Structural Data of iGluR ATDs. *A table listing details of the iGluR ATD structures published by September 2012.*

The role of the ATD in iGluR function is still not completely understood; although there is clear evidence for its involvement in regulating iGluR subunit assembly, controlling ion channel open probability (Gielen et al, 2009) and, in the case of NMDA receptors, binding of allosteric modulators such as ifenprodil (Traynelis et al, 2010) and zinc (Sensi et al, 2009). The ATD is also a known protein binding domain, interacting with other extra-cellular, synaptic proteins; for example the neuronal pentraxins are known to bind to AMPA ATDs (O'Brien et al, 1999; Sia et al, 2007).

As demonstrated by Table 3.1, there is a gap in the structural knowledge of iGluR ATDs; there is no published crystal structure for the Delta iGluR sub-family. The Delta iGluR ATDs have known interaction partners, the Cbln family of secreted glycoproteins (Matsuda et al, 2010; Ryu et al, 2012; Uemura et al, 2010). Through the ATD interaction with Cbln family members, Delta iGluRs form part of a trans-synaptic bridge with pre-synaptic Neurexin (Schmid & Hollmann, 2010). This Trans-synaptic complex is crucial for correct synaptogenesis and synapse function in the cerebellum and furthermore, disruption of this complex leads to deficiencies in motor coordination and motor learning (Yuzaki, 2009).

Thus the aim of this chapter was to complete the structural picture of the iGluR ATDs through analysis of the Delta iGluR ATDs using X-ray crystallography. Furthermore, since Delta iGluRs have not been reported to demonstrate ion channel conductance, unlike the other members of the iGluR superfamily (Traynelis et al, 2010), an additional aim was to reveal any unique features of Delta iGluR ATDs which may provide a molecular explanation to this enigma by answering the questions: i) What are the unique structural features of iGluR ATDs and ii) What structural characteristics are common to all iGluR ATDs?

3.3 GluD2 ATD Constructs and Expression Trials

Several constructs of the GluD2 ATD were designed with the aim of optimizing the level of expression and secretion from HEK 293T cells. GD1-6 (See Appendix 8.1) were designed with different secretion signals – native and pHLsec-derived – and C-terminal construct end-points; the different construct C-termini were based on: sites of predicted N-linked glycosylation, i.e. N426; sequence alignment with the C-terminus of the published GluA2 ATD crystal structure (Clayton et al, 2009); and the N-terminus of the published GluD2 LBC crystal structure (Naur et al, 2007). All molecular cloning was performed as described in Section 2.1 and Appendix 8.1.

Small-scale trials were performed as described in Section 2.3.2 to test for expression and secretion of GD1-6 in HEK cells. Western blot analysis of transfected cells and conditioned media revealed that all constructs were expressed and secreted with similar efficiency (Figure 3.1A). Construct GD6 was chosen as a candidate for large-scale expression due to this construct encoding entirety of the GluD2 ATD.

3.4 Large-Scale Expression and Purification of GluD2 ATD

HEK 293S cells, cultured in roller bottles, were transfected with GD6 expression plasmid as described in Section 2.3.3. Conditioned media was then exchanged into IMAC buffer, before the recombinant protein was subject to purification by IMAC (Figure 3.1B). A small sample of GD6 was then used in a time-course deglycosylation experiment to test protein stability upon deglycosylation (See Section 2.4.3). Treatment of the sample with EndoH was successful in that N-

linked glycans were cleaved, and deglycosylation did not affect protein stability (Figure 3.1C); hence the remainder of the GD6 sample was subjected to EndoH treatment before being applied to a final round of SEC (Figure 3.1D). Sample analysis was performed using SDS-PAGE (See Section 2.2.2) which indicated that greater than 95 % purity was achieved (Figure 3.1D).

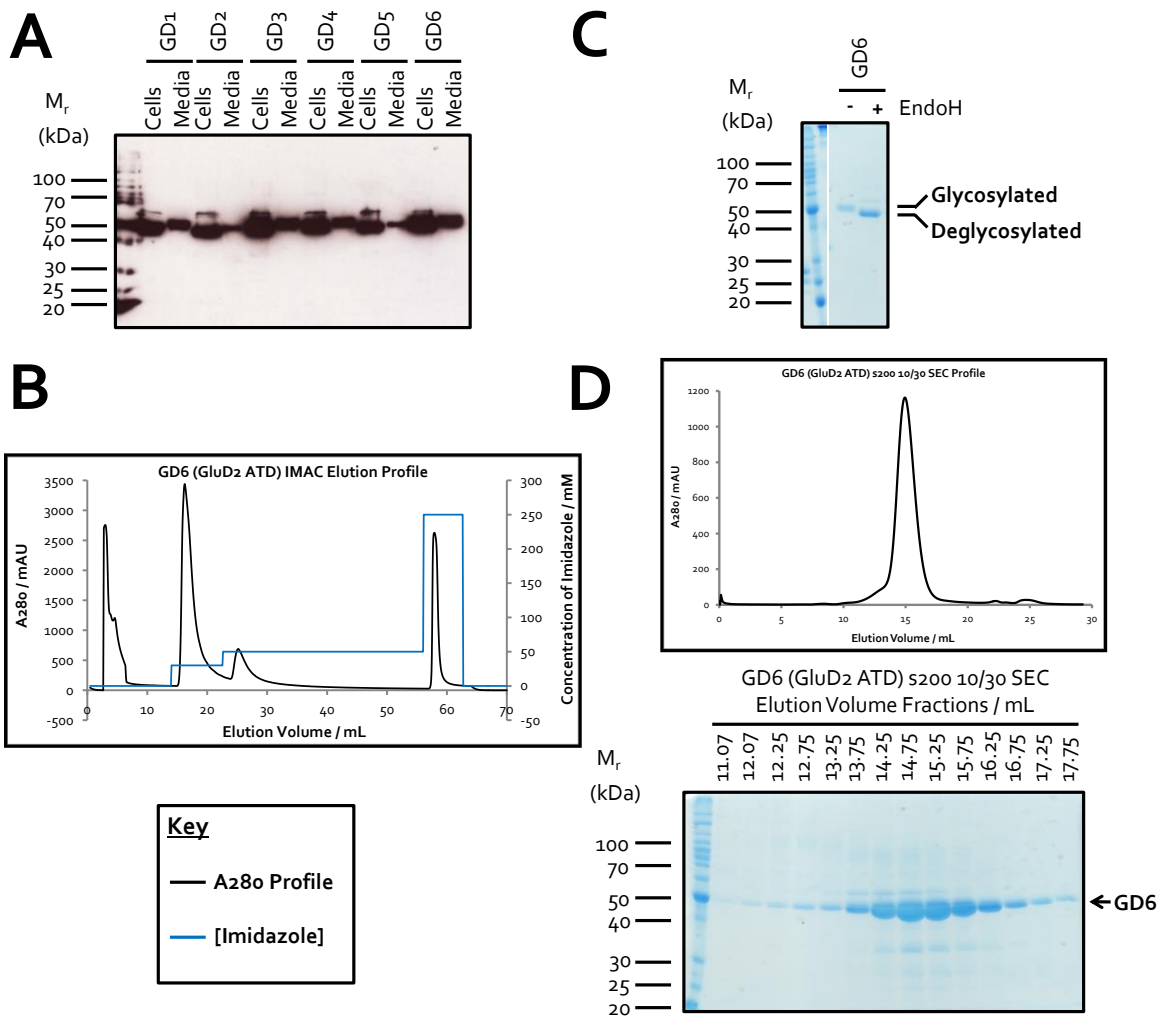

Figure 3.1: Expression and Purification of GluD2 ATD. ***A:*** *Anti-His tag Western blot analysis of a GluD2 ATD construct expression trial.* ***B:*** *GD6 (GluD2 ATD) IMAC elution profile monitoring A280 and Imidazole concentration versus elution volume.* ***C:*** *12 % SDS-PAGE analysis of deglycosylation trial of construct GD6.* ***D:*** ***Top image*** *– construct GD6 (GluD2 ATD) SEC elution profile, monitoring A280 versus elution volume from an s200 10/30 column.* ***Bottom image*** *– 12 % SDS-PAGE analysis of construct GD6 (GluD2 ATD) SEC fractions.*

3.5 GluD2 ATD Crystallization and Structure Determination

Deglycosylated GD6 sample was then concentrated using ultrafiltration and sitting drop vapour diffusion crystallization trials were set-up using a protein concentration of 8.7 mg/mL following a pre-crystallization test (See Section 2.5). GD6 crystals which grew in a final condition of 20 % (w/v) Polyethylene Glycol 1000, 0.2 M Calcium Acetate, 0.1 M Imidazole pH 8.0 and 0.4 M NDSB-221 (Figure 3.2A) diffracted with observable spots to ~1.8 Å (Figure 3.2B) at the I04 beamline (Diamond Light Source). This crystal was cryo-protected with 30 % (v/v) ethylene glycol. Diffraction images were indexed to space group I222, $\alpha = \beta = \gamma = 90^{\circ}$, a = 45.1 Å, b =79.1 Å, c = 246.6 Å (Table 3.2). This data was phased using the two lobes of the ATD of GluK2 – which has ~23 % sequence identity to GluD2 – (PDB code 3H6G (Kumar et al, 2009) as individual search probes for molecular replacement (See Section 2.6.4). The model was built and refined from electron density as described in Section 2.6.3-2.6.5. A representative 2Fo-Fc electron density map is displayed in Figure 3.2C, data processing and refinement statistics are listed in Table 3.2.

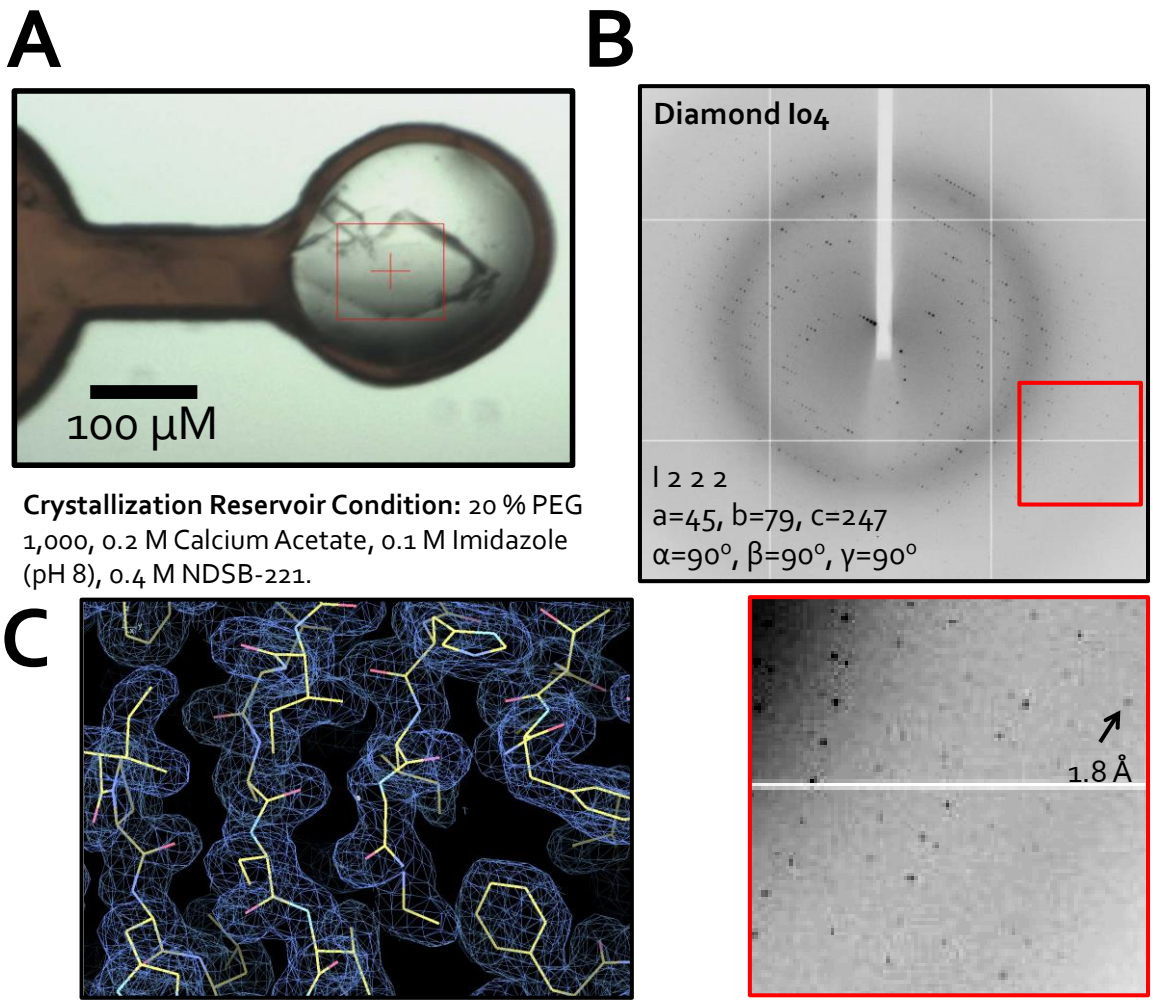

Figure 3.2: GluD2 ATD Crystallization, Diffraction Experiments and Electron density. ***A:*** *An image displaying a mounted crystal of GluD2 ATD, which grew in a reservoir condition containing 20 % (w/v) PEG 1,000, 0.2 M calcium acetate, 0.1 M imidazole (pH 8.0), 0.4 M NDSB-221.* ***B:*** *Images displaying X-ray diffraction from the crystal exhibited in* ***A****. Images were indexed to space group I 2 2 2 with unit cell dimensions a = 45.1 Å, b =79.1 Å, c = 246.6 Å, α = β = γ = 90°.* ***C:*** *A Representative 2Fo-Fc electron density map, contoured at 1 σ, calculated to 1.8 Å.*

DATA COLLECTION		
Beamline	Diamond I04	
Resolution	50.0-1.8 (1.9-1.8)	
Space group	I222	
Cell dimensions	[Å]	[°]
	a = 83.5 b = 83.5 c = 50.6	α = 90 β = 90 γ= 90
Wavelength [Å]	1.00000	
Unique reflections	41572 (5555)	
Completeness [%]	100 (100)	
R_{merge} [%][a]	8.4 (61.4)	
I/σI	18.9 (3.5)	
Redundancy	12.2 (10.3)	
REFINEMENT		
Resolution range [Å]	50.0-1.8 (1.85-1.80)	
Number of reflections	39498 (2663)	
R_{factor} [%)][c]	18.8 (25.8)	
R_{free} [%] [d]	22.1 (29.1)	
No. of atoms (Protein/NAG/EG/Ca/Water)	3122/0/4/2/209	
B factors [Å^2] (Protein/Water)	38/0/40/40/39	
R.M.S.D. bonds [Å]	0.020	
R.M.S.D. angles [°]	1.95	
Ramachandran statistics[d] Favoured [%] Disallowed [%]	 99.0 0.0	

Table 3.2: GluD2 ATD Crystallographic Statistics. *A table listing the data collection and refinement statistics for the crystal structure of GluD2 ATD.* R.M.S.D. stands for root mean square deviation from ideal geometry. Numbers in parentheses refer to the appropriate outer shell.

[a] $R_{merge} = \Sigma_{hkl} \Sigma_i |I(hkl;i) - \langle I(hkl) \rangle| / \Sigma_{hkl} \Sigma_i I(hkl;i)$, where $I(hkl;i)$ is the intensity of an individual measurement and $\langle I(hkl) \rangle$ is the average intensity from multiple observations.

[b] $R_{factor} = \Sigma_{hkl} ||F_{obs}| - k|F_{calc}|| / \Sigma_{hkl} |F_{obs}|$.

[c] R_{free} equals the *R*-factor against 5% of the data removed prior to refinement.

[d] Calculated using MolProbity (Davis et al, 2007).

The model for the GluD2 ATD (Figure 3.3) contains 395 amino acids, with one molecule per asymmetric unit; the regions Q292-I294, N404-R411 and the region C-terminal of L429 were disordered and thus omitted (Figure 3.3). The GluD2 ATD has a bilobal venus flytrap fold where each lobe consists of a characteristic type I bPBP αβ fold with a central β-sheet surrounded by α-helices, similar to ATDs of the other iGluR superfamily (See Table 3.1), the metabotropic glutamate receptor ecto-domain (Kunishima et al, 2000) and the LIVBP (Sack et al, 1989). The GluD2 ATD is a homodimer mediated by both R1-R1 and R2-R2 interlobal interfaces (Figure 3.3C). The R1-R1 interface consists of 26 amino acids contributed from each subunit, involved in Van der Waal's contacts, 7 salt bridges and 6 hydrogen bonds (Figure 3.3D). The R2-R2 interface is composed of 22 residues per monomer involved in Van der Waal's forces, one salt bridge and three hydrogen bonds. Amino acids mediating R2-R2 salt bridges and hydrogen bonds are labelled in Figure 3.3E. Further analysis of the GluD2 ATD and ATD interface is detailed in Section 3.8.

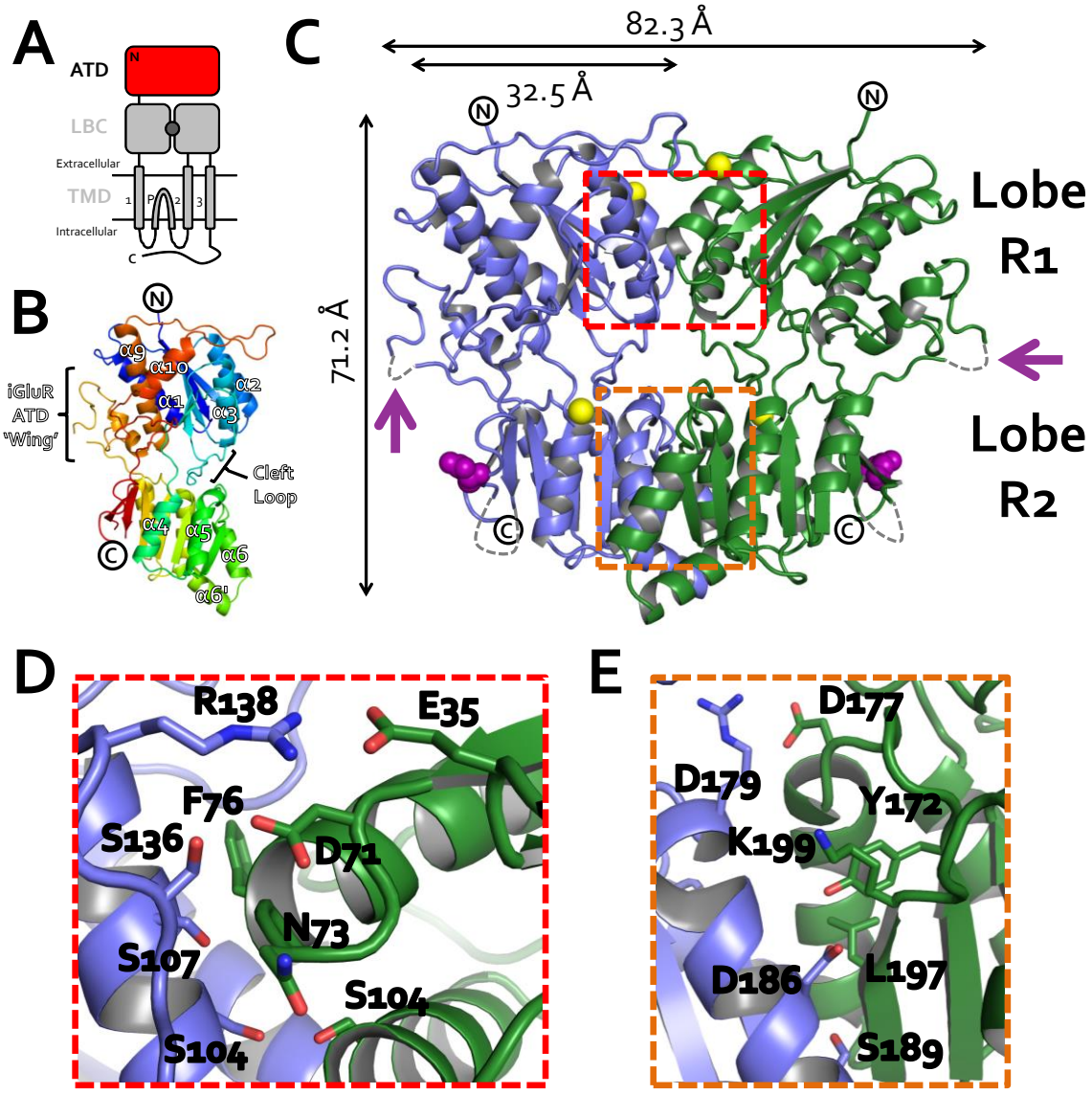

Figure 3.3: The Crystal Structure of GluD2 ATD. ***A:*** *A schematic depicting the domain composition of an iGluR subunit, highlighting the ATD.* ***B:*** *Rainbow cartoon representation of the GluD2 ATD structure. Helices are labelled as described in Figure 3.8.* ***C:*** *Cartoon representation of the GluD2 ATD homodimer, each monomer is related by a crystallographic two-fold axis, dimensions are labelled. Putative sites of N-linked glycosylation are labelled with either a purple arrow or purple spheres. Yellow spheres depict calcium ions. Residues involved in R1-R1 and R2-R2 interface salt bridges and hydrogen bonds are highlighted and labelled in* ***D*** *and* ***E****, respectively.*

3.6 Construct Design, Expression and Purification of GluD1 ATD

Domain boundaries for the expression construct of GluD1 ATD were based on those used in the GD6 construct due to the ~62 % sequence identity (See Appendix 8.1). Small-scale expression trials (Section 2.3.2) confirmed that recombinant protein was produced and secreted from mammalian cells (Figure 3.4A). Large-scale transfection of HEK 293S cells was carried out as described in Section 2.3.3 and the conditioned media was prepared and applied to IMAC (Figure 3.4B) as described in Section 2.4.1-2.4.2. GluD1 ATD sample was then treated with EndoH endoglycosidase before being applied to SEC (See Sections 2.4.3-2.4.4). SDS-PAGE analysis confirmed the success of protein deglycosylation and highlighted that greater than 95 % purity was achieved (Figure 3.4C).

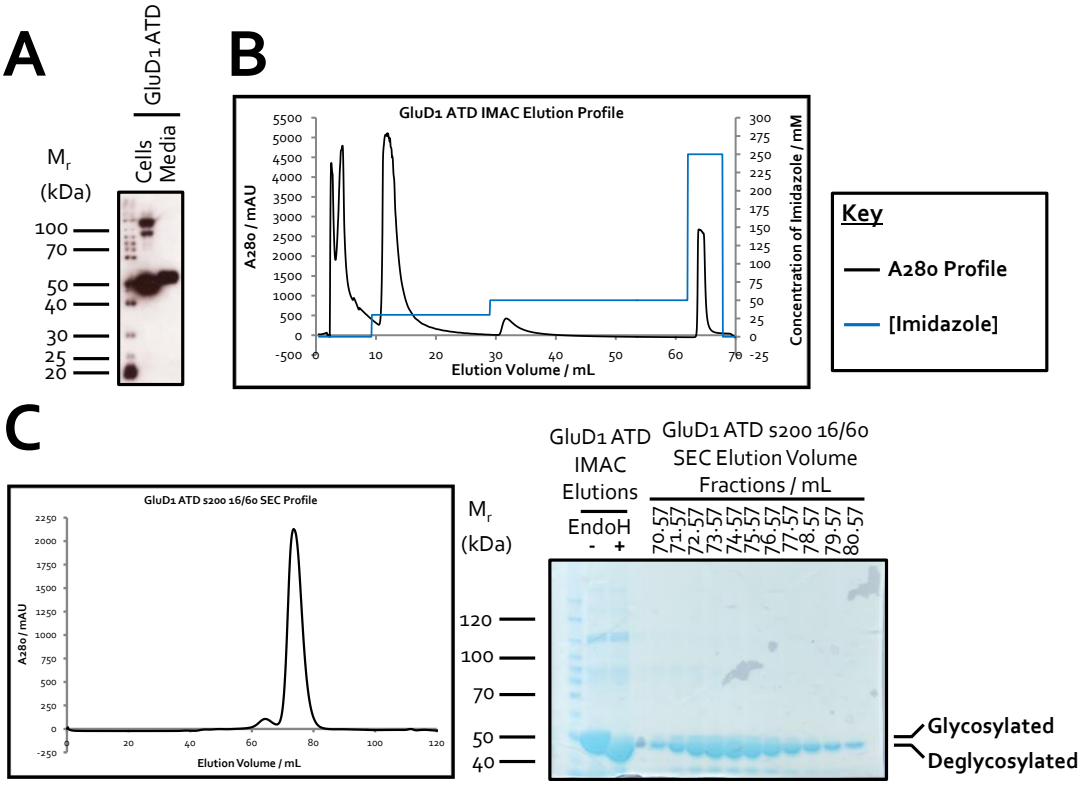

Figure 3.4: Expression and Purification of GluD1 ATD. ***A:*** *Anti-His tag Western blot analysis of a GluD1 ATD construct expression trial.* ***B:*** *GluD1 ATD IMAC elution profile monitoring A280 and Imidazole concentration versus elution volume.* ***C: Left image*** *– GluD1 ATD SEC elution profile, monitoring A280 versus elution volume from an S200 10/30 column.* ***Right image*** *– 12 % SDS-PAGE analysis of GluD1 ATD of deglycosylation SEC fractions.*

3.7 Crystallization and Structure Determination of GluD1 ATD

The recombinant GluD1 ATD sample was concentrated using ultrafiltration before a pre-crystallization test was undertaken. Sitting drop vapour diffusion crystallization trials were set-up with a protein concentration of 10.3 mg/mL (See Section 2.5). GluD1 ATD crystals which grew in 0.1 M MES/Imidazole (pH 6.5), 10 % (w/v) PEG 8,000, 20 % (w/v) Ethylene glycol, 0.02 M 1,6-hexanediol, 0.02 M (*RS*)-1,2-propanediol, 0.02 M 1-butanol, 0.02 M 2-propanol, 0.02 M 1,4-butanediol, 0.02 M 1,3-propanediol (Figure 3.5A), from well D2 of the Morpheus screen, diffracted with observable spots to ~2.3 Å (Figure 3.5B) at beamline I04-1 (Diamond Light Source). This crystal was cryo-protected with 30 % (v/v) ethylene glycol. Diffraction images were indexed to space group P 3_2 2 1, $\alpha = \beta = 90^{\circ}$, $\gamma = 120^{\circ}$, a = 128.5 Å, b = 128.5 Å, c = 153.2 Å (Table 3.3). Phases were obtained by molecular replacement (See Section 2.6.4), where the GluD2 ATD structure (See Section 3.5) was used as a search probe. A model was built into the resultant electron density and this was refined as described in Sections 2.6.3-2.6.5. Data processing and refinement statistics are displayed in Table 3.3 and representative 2Fo-Fc electron density is exhibited in Figure 3.5C.

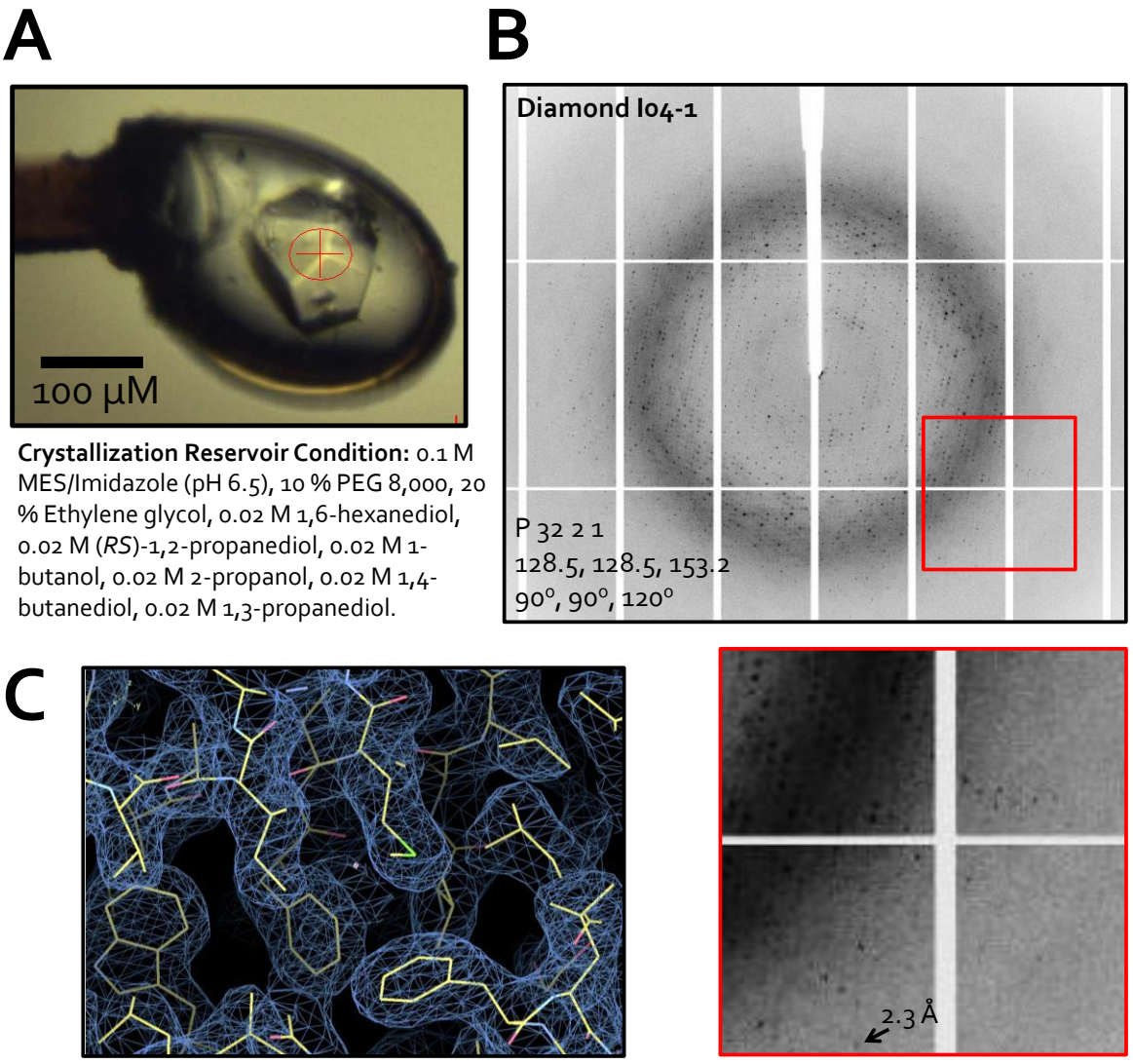

Crystallization Reservoir Condition: 0.1 M MES/Imidazole (pH 6.5), 10 % PEG 8,000, 20 % Ethylene glycol, 0.02 M 1,6-hexanediol, 0.02 M (*RS*)-1,2-propanediol, 0.02 M 1-butanol, 0.02 M 2-propanol, 0.02 M 1,4-butanediol, 0.02 M 1,3-propanediol.

Figure 3.5: GluD1 ATD Crystallization, Diffraction Experiments and Electron density. ***A:*** *An image displaying a mounted crystal of GluD1 ATD, which grew in a reservoir condition containing: 0.1 M MES/imidazole (pH 6.5), 10 % PEG 8,000, 20 % ethylene glycol, 0.02 M 1,6-hexanediol, 0.02 M (RS)-1,2-propanediol, 0.02 M 1-butanol, 0.02 M 2-propanol, 0.02 M 1,4-butanediol, 0.02M 1,3-propanediol.* ***B:*** *Images displaying X-ray diffraction from the crystal exhibited in* ***A****. Images were indexed to space group* $P3_2\,2\,1$ *with unit cell dimensions a = 128.5 Å, b =128.5 Å, c = 153.2 Å,* $\alpha = \beta = 90^{o}$, $\gamma = 120^{o}$. ***C:*** *A representative electron 2Fo-Fc density map, contoured at 1 σ, calculated to 2.25 Å.*

DATA COLLECTION		
Beamline	Diamond Io4-1	
Resolution	31.5-2.25 (2.31-2.25)	
Space group	$P3_221$	
Cell dimensions	[Å]	[°]
	a = 128.5 b = 128.5 c = 153.3	α = 90 β = 90 γ= 90
Wavelength [Å]	0.91730	
Unique reflections	69628 (5057)	
Completeness [%]	99.9 (100.0)	
R_{merge} [%][a]	6.4 (97.5)	
I/σI	16.9 (2.1)	
Redundancy	9.5 (9.2)	
REFINEMENT		
Resolution range [Å]	50.0-2.25 (2.31-2.25)	
Number of reflections	69445 (5020)	
R_{factor} [%)][c]	18.9 (23.3)	
R_{free} [%] [d]	22.0 (26.1)	
No. of atoms (Protein/NAG/EG/Ca/Water)	9099/42/80/0/198	
B factors [Å^2] (Protein/Water)	70/88/64/0/59	
R.M.S.D. bonds [Å]	0.10	
R.M.S.D. angles [°]	1.12	
Ramachandran statistics[d] Favoured [%] Disallowed [%]	 97.8 0.1	

Table 3.2: GluD1 ATD Crystallographic Statistics. *A table listing the data collection and refinement statistics for the crystal structure of Glu1 ATD.* R.M.S.D. stands for root mean square deviation from ideal geometry. Numbers in parentheses refer to the appropriate outer shell.

[a] $R_{merge} = \Sigma_{hkl} \Sigma_i |I(hkl;i) - \langle I(hkl) \rangle| / \Sigma_{hkl} \Sigma_i I(hkl;i)$, where $I(hkl;i)$ is the intensity of an individual measurement and $\langle I(hkl) \rangle$ is the average intensity from multiple observations.

[b] $R_{factor} = \Sigma_{hkl} ||F_{obs}| - k|F_{calc}|| / \Sigma_{hkl} |F_{obs}|$.

[c] R_{free} equals the *R*-factor against 5% of the data removed prior to refinement.

[d] Calculated using MolProbity (Davis et al, 2007).

Three molecules of the GluD1 ATD are present in each asymmetric unit; hence there is some variability in the amino acids described by each chain due to the different crystal packing arrangement and resultant levels of order in each molecule. Chain A contains 404 amino acids and is the most ordered chain of the asymmetric unit. Chain B contains 382 amino acids; the regions between amino acids D52-Q56, D290-H299, T400-F405 and the region C-terminal of S424 were disordered and thus omitted from the model. Chain C was the most disordered hence only 377 amino acids were built and electron density for the region N200-T211 is particularly weak and so a poly-alanine chain has been built as a model for the polypeptide chain. Additionally, the regions between D52-S57, M212-R225, A288-N291, and Y401-G406 are disordered and omitted completely from the model. Electron density for sites of N-linked glycosylation are visible and ordered at positions N200 and N422 in chain A, as well as N200 of chain B (Figure 3.6C).

The overall shape of the GluD1 ATD is similar to GluD2 ATD (Section 3.5) and the other iGluR ATDs (Table3.1), in that it has a bilobal, R1 and R2, venus flytrap fold (Figure 3.6). GluD1 ATD dimerization is mediated by R1-R1 and R2-R2 interactions (Figure 3.6C). The R1-R1 interface contains 23 amino acids from each molecule which mediate Van der Waal's contacts, two salt bridges and four hydrogen bonds. Residues involved in R1-R1 salt bridges and hydrogen bonds are labelled in Figure 3.6D. The R2-R2 interface also consists of 23 amino acids per molecule and the interaction involves three salt bridges, four hydrogen bonds and Van der Waal's forces. Amino acids mediating R2-R2 salt bridges and hydrogen bonds are labelled in Figure 3.6E. Further analysis of the GluD1 ATD and ATD interface is detailed in Section 3.8.

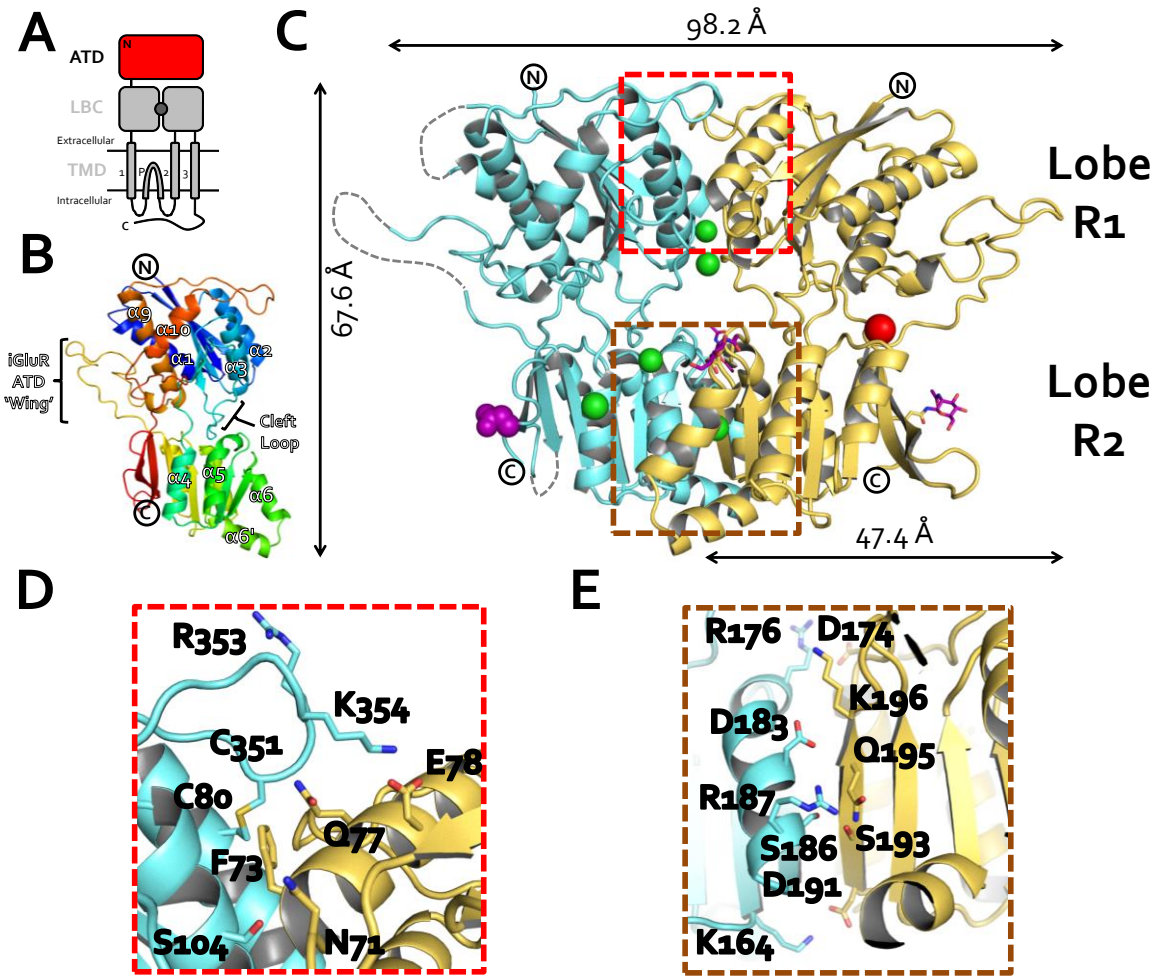

Figure 3.6: The Crystal Structure of GluD1 ATD. ***A:*** *A schematic depicting the domain composition of an iGluR subunit, highlighting the ATD.* ***B:*** *Rainbow cartoon representation of the GluD1 ATD structure. Helices are labelled as described in Figure 3.8.* ***C:*** *Cartoon representation of the GluD1 ATD homodimer, dimensions are labelled. Sites of N-linked glycosylation are labelled with either in purple sticks or purple spheres. Green spheres depict chloride ions and the red sphere represents a sodium ion. Residues involved in R1-R1 and R2-R2 interface salt bridges and hydrogen bonds are highlighted and labelled in* ***D*** *and* ***E****, respectively.*

3.8 Structural Analysis of the Delta iGluR ATDs

The global structural similarity between the GluD2 ATD and the GluD1 ATD is very close (Figure 3.7), with an RMSD of 1.32 Å for 218 equivalent Cα positions in the R1 lobe, representing 94 % of

GluD2 ATD R1 and 93 % of GluD1 ATD R1, and an RMSD of 0.79 Å for 162 equivalent Cα positions in the R2 lobe, representing 100 % of GluD2 ATD R2 and 95 % of GluD1 ATD R2 (Table 3.3).

Comparing the Delta-iGluR ATDs with ATDs of the other members of the iGluR superfamily, the closest homology is seen with non-NMDA iGluR ATDS, i.e. members of the Kainate subfamily. For example, an RMSD of 1.75 Å is observed when comparing the R1 lobes of GluD2 ATD and GluK2 ATD, for 196 equivalent Cα positions, representing 84 % of the GluD2 ATD R1 and 89 % of the GluK2 ATD R1 (Table 3.3). Additionally, there is an RMSD of 1.90 Å between the R2 lobes of GluD2 ATD and GluK2 ATD, for 142 equivalent Cα positions covering 88 % of GluD2 ATD R2 and GluK2 ATD R2 (Table 3.3).

ATDs from members of the NMDA iGluR subfamily demonstrate the least homology to the Delta-iGluR subfamily ATDs. For instance, an RMSD of 2.30 Å is observed between the R1 lobes of GluD2 ATD and GluN2B ATD, for 157 equivalent Cα positions covering 67 % of GluD2 ATD R1 and 85 % of GluN2B ATD R1 (Table 3.3). Furthermore, there is an RMSD of 2.26 Å between the R2 lobes of GluD2 ATD and GluN2B ATD, for 139 corresponding Cα positions representing 86 % of the GluD2 ATD R2 and 82 % of the GluN2B ATD R2 (Table 3.3).

Reference Molecule	Molecule Used for Comparison (PDB ID)	Lobe	RMSD / Å	Number of Equivalent Residues	Percentage of Equivalences in Reference Molecule / %	Percentage of Equivalences in Comparison Molecule / %
GluD2 ATD (This Thesis Section 3.5)	GluD1 ATD (This Thesis Section 3.7)	R1	1.32	218	94	93
		R2	0.79	162	100	95
	GluA1 (PDB: 3SAJ)	R1	1.86	187	80	87
		R2	2.28	131	81	85
	GluA2 (PDB: 2WJW)	R1	1.84	187	80	89
		R2	2.06	143	88	86
	GluA3 (PDB: 3O21)	R1	1.87	187	80	86
		R2	1.99	142	88	91
	GluK2 (PDB: 3H6G)	R1	1.75	196	84	89
		R2	1.90	142	88	90
	GluK3 (PDB: 3OLZ)	R1	1.73	197	85	91
		R2	2.10	139	86	90
	GluK5 (PDB: 3OM0)	R1	1.88	196	84	83
		R2	1.98	129	80	80
	GluN1 (PDB: 3QEL)	R1	1.94	174	75	92
		R2	2.25	131	81	79
	GluN2B (PDB: 3QEL)	R1	2.30	157	67	85
		R2	2.26	139	86	82

Table 3.3: iGluR ATD Homology Analysis. *A table containing statistics from the structural comparison of the known structures of iGluR ATDs. Each individual lobe of the venus flytrap architecture from the listed iGluR ATDs were aligned separately using the program SHP (Stuart et al, 1979).*

Through superposition of the iGluR ATD crystal structures (Figure 3.7) and using a structure-based sequence alignment (Figure 3.8), a number of iGluR-Delta specific features were observed in both GluD1 and GluD2 ATDs. For example the inter-lobal ATD cleft, which has been the centre of some debate regarding its potential as a binding site for allosteric ligands in non-NMDA receptors (Clayton et al, 2009; Kumar et al, 2009; Mayer, 2011; Sukumaran et al, 2011), is occupied by a Delta-iGluR specific ATD 'Cleft-Loop' (Figure 3.7 A-B, Figure 3.8). B-factor analysis of the Delta-iGluR 'Cleft-Loop' demonstrates that this feature is well ordered (Figure 3.7 E-F), indeed it is held in place by a disulphide bond between C131 from the 'Cleft-Loop' and C99 from the α3 helix in the case of GluD2 (Figures 3.7B and 3.8). The presence of the 'Cleft-Loop' has two important implications,

firstly the iGluR-Delta ATDs are more rigid molecules, compared to other iGluR ATDs, and secondly it is very unlikely the GluD1 and GluD2 ATDs inter-lobal cleft will bind ligands.

A second iGluR-Delta specific feature is the presence of a α6′ helix; an additional helix in the R2 lobe, relative to other iGluR ATDs (Figure 3.7 A, D, G-H, and Figure 3.8). Superposition of the Delta-iGluR ATDs with the GluA2 ATD (2WJW, (Clayton et al, 2009)) demonstrates that the Delta-iGluR ATD venus flytrap fold has a more open conformation than the GluA2 ATD (Figure 3.7A) due to the combined effects of the 'Cleft-Loop' and the α6′ helix. For example, a superposition based on the R1 lobes of GluA2 ATD and GluD2 ATD reveals that there is a clear 10 Å displacement of the R2 lobe of GluD2 ATD (Figure 3.7A). A potential consequence of this could be that there are more extensive ATD-LBC interactions in the Delta-iGluRs compared to the other iGluRs, which could be functionally significant.

The crystal structures of the GluD2 ATD and the GluD1 ATD also provide further evidence for the structural heterogeneity of the iGluR ATD 'Wing' (Figure 3.7A, C, and Figure 3.8). This is clearly the most variable region of the iGluR ATDs and it is attractive to speculate that this region of iGluR ATDs could determine sub-type specific functional properties of iGluRs, for example binding to specific protein interaction partners. However this is yet to be investigated, but the iGluR ATD wing could be an intriguing target for functional experiments.

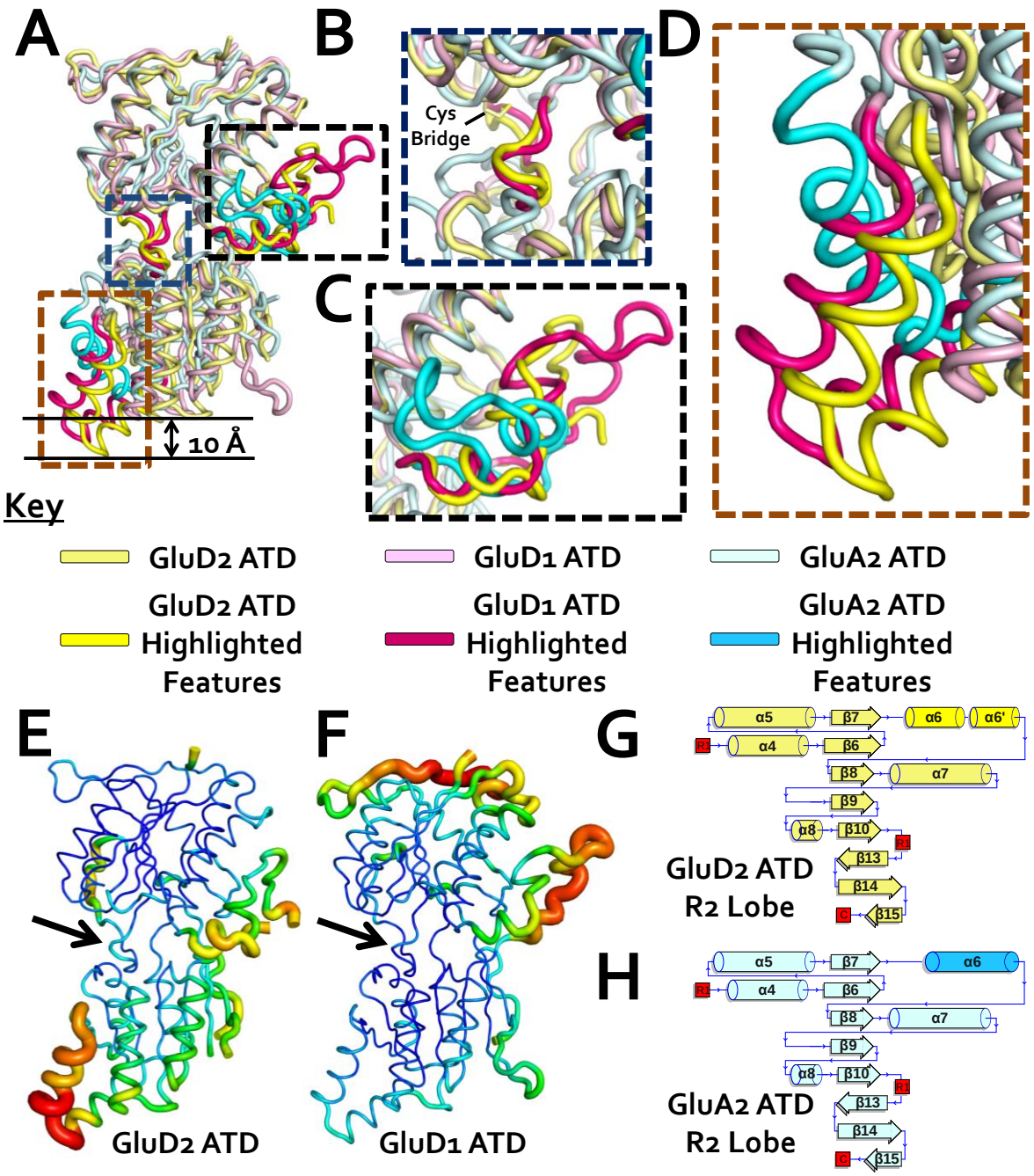

Figure 3.7: Structural Comparison of the Delta-iGluR ATDs with Other iGluR ATDs. ***A:*** *A structural superposition of the GluD2 ATD, with GluD1 ATD and the GluA2 ATD (2WJW, (Clayton et al, 2009)). Structures were aligned onto the R1 lobes using the program SHP (Stuart et al, 1979). Interesting features are highlighted with coloured boxes.* ***B:*** *Close-up view of the Delta-iGluR Cleft loop.* ***C:*** *Close-up view of the iGluR ATD 'Wing'.* ***D:*** *Close-up view of the iGluR-Delta specific α6' and α6 R2 helices compared to the GluA2 α6 helix.* ***E-F:*** *GluD2 ATD (**E**) and GluD1 ATD (**F**) coloured by B-factor (blue = low, red = high). The iGluR-Delta cleft loop is highlighted with arrows.* ***G-H:*** *Schematics depicting the secondary structural elements of GluD2 ATD R2 lobe (**G**) and GluA2 ATD R2 lobe (**H**). The differences in the α6 helices are highlighted.*

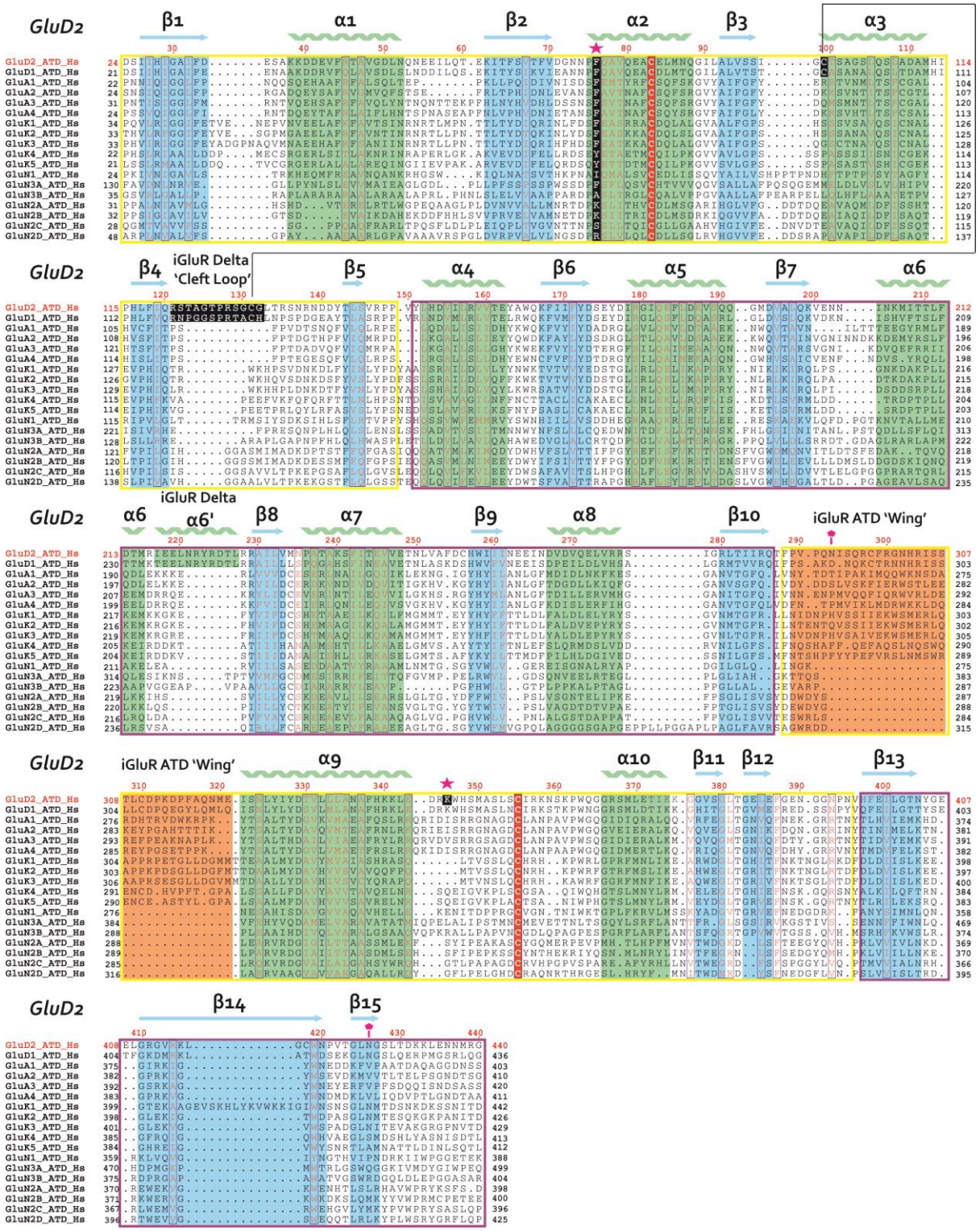

Figure 3.8: Structure-Based Sequence Alignment of the iGluR ATDs.

Figure 3.8: Structure-Based Sequence Alignment of the iGluR ATDs. *Secondary structural elements are labelled, as is the iGluR-Delta 'Cleft Loop' and the iGluR 'Wing'. Amino acids which form the R1 lobe are highlighted with a yellow box and residues which constitute the R2 lobe are highlighted with a purple box. Important residues discussed in the text of this thesis are highlighted with a pink star and putative sites of N-linked glycosylation in GluD2 are labelled with a pink pentagon on a pink rectangle. The following NCBI reference entry codes were used to obtain the sequences used for the alignment: GluD2, NP_001501.2; GluD1, NP_060021.1; GluA1, NP_000818.2; GluA2, NP_001077088.1; GluA3, NP_015564.4; GluA4, NP_000820.3; GluK1, NP_000821.1; GluK2, NP_068775.1; GluK3, NP_000822.2; GluK4, NP_055434.2; GluK5, NP_002079.3; GluN1, NP_000823.4; GluN2A, NP_000824.1; GluN2B, NP_000825.2; GluN2C, NP_000826.2; GluN2D, NP_000827.2; GluN3A, NP_597702.2; and GluN3B, NP_619635.1.*

The sizes of the Delta iGluR ATD dimerization interfaces are slightly larger than those of other non-NMDA receptors (Figure 3.9). The NMDA ATD interface was not considered as an alternative mode of interaction, that is mediated by the R1 lobes only, is present in NMDA subtype ATDs (Karakas et al, 2011). The mean size of the non-NMDA receptor ATD dimerization interface is 1523.6 Å^2 of buried surface area, with a range from 1405.3 Å^2 to 1621.5 Å^2 (Figure 3.9). The equivalent interfaces of GluD2 ATD and GluD1 ATD rank at the upper end of this scale, measuring 1620.7 Å^2 (Figure 3.9B) and 1621.5 Å^2 (Figure 3.9B) of buried surface area respectively.

Electrostatic potentials of the non-NMDA iGluR ATD interfaces, calculated using APBS (Baker et al, 2001), demonstrate that the interface is generally not highly charged, exemplifying the extensive Van der Waal's contacts at each interface (Figure 3.10).

Sequence conservation of the non-NMDA iGluRs ATDs (Figure 3.11), calculated using the ConSURF server (Ashkenazy et al, 2010), reveals that the ATD interface is well conserved, particularly the R1-R1 interface (Figure 3.11D). Precisely, the residues equivalent to GluD2 F76 and S107 are highly conserved across the non-NMDA iGluR ATDs (Figure 3.9 and Figure 3.11D). This is interesting

because in GluD2 ATD these two residues are involved in interface mediating hydrogen bonds (Figure 3.3), as are the equivalent residues in GluD1 ATD (Figure 3.6) and GluA2 ATD (Clayton et al, 2009). Furthermore, the conservation of the R1 interface Phe76, highlighted in Figure 3.11D, is interesting as mutation of the equivalent residue in the GluA2 ATD, to an aspartate, renders the normally dimeric GluA2 ATD a monomer (Clayton et al, 2009).

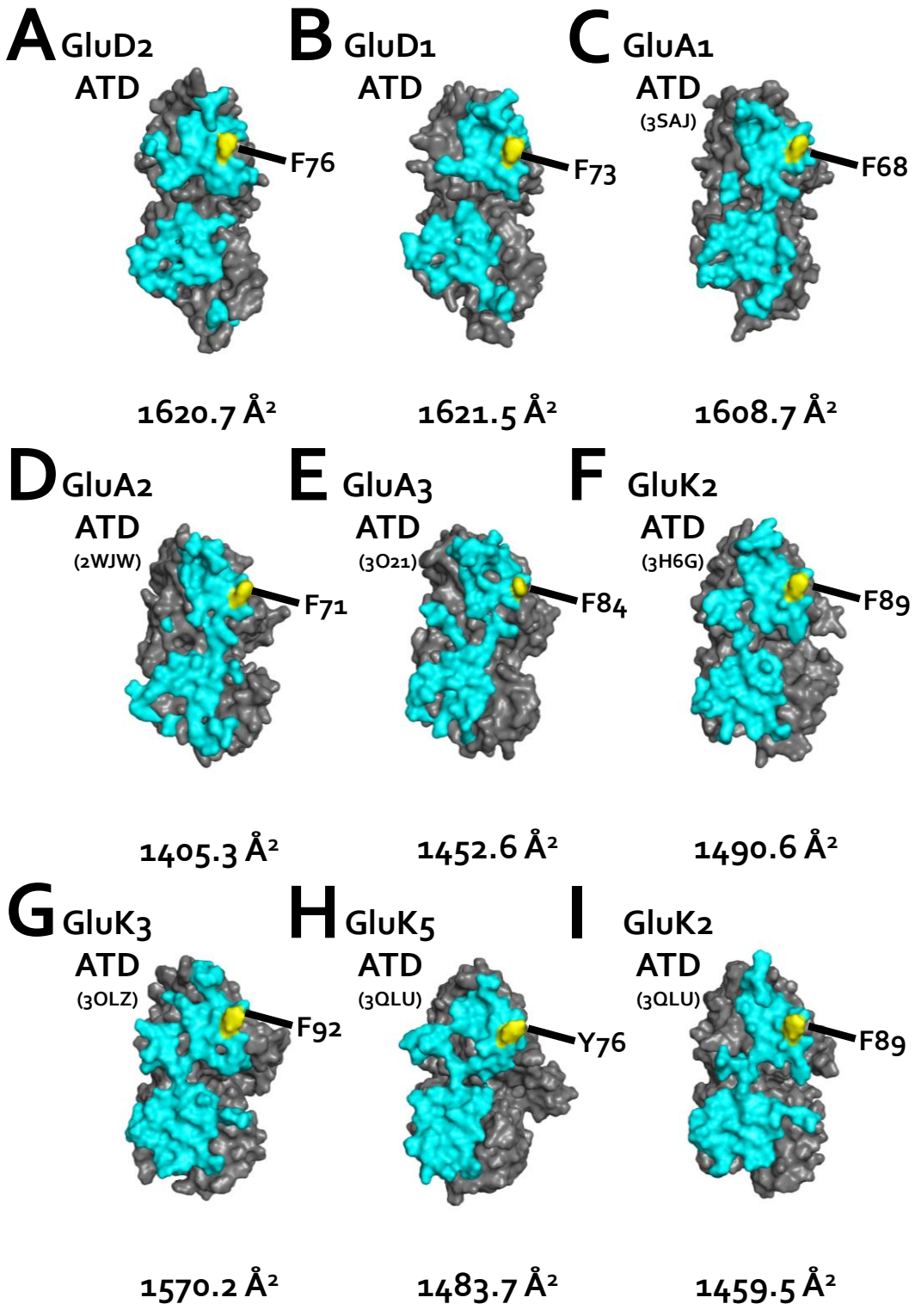

Figure 3.9: Non-NMDA iGluR ATD Dimerization Interface Residues: A-I: *Surface representation of the structures of non-NMDA iGluR ATDs, viewed into the surface of the interface. The iGluR subunit is detailed and PDB code is listed in brackets. Interface residues are highlighted in blue and yellow and the buried surface area for each interface is labelled.*

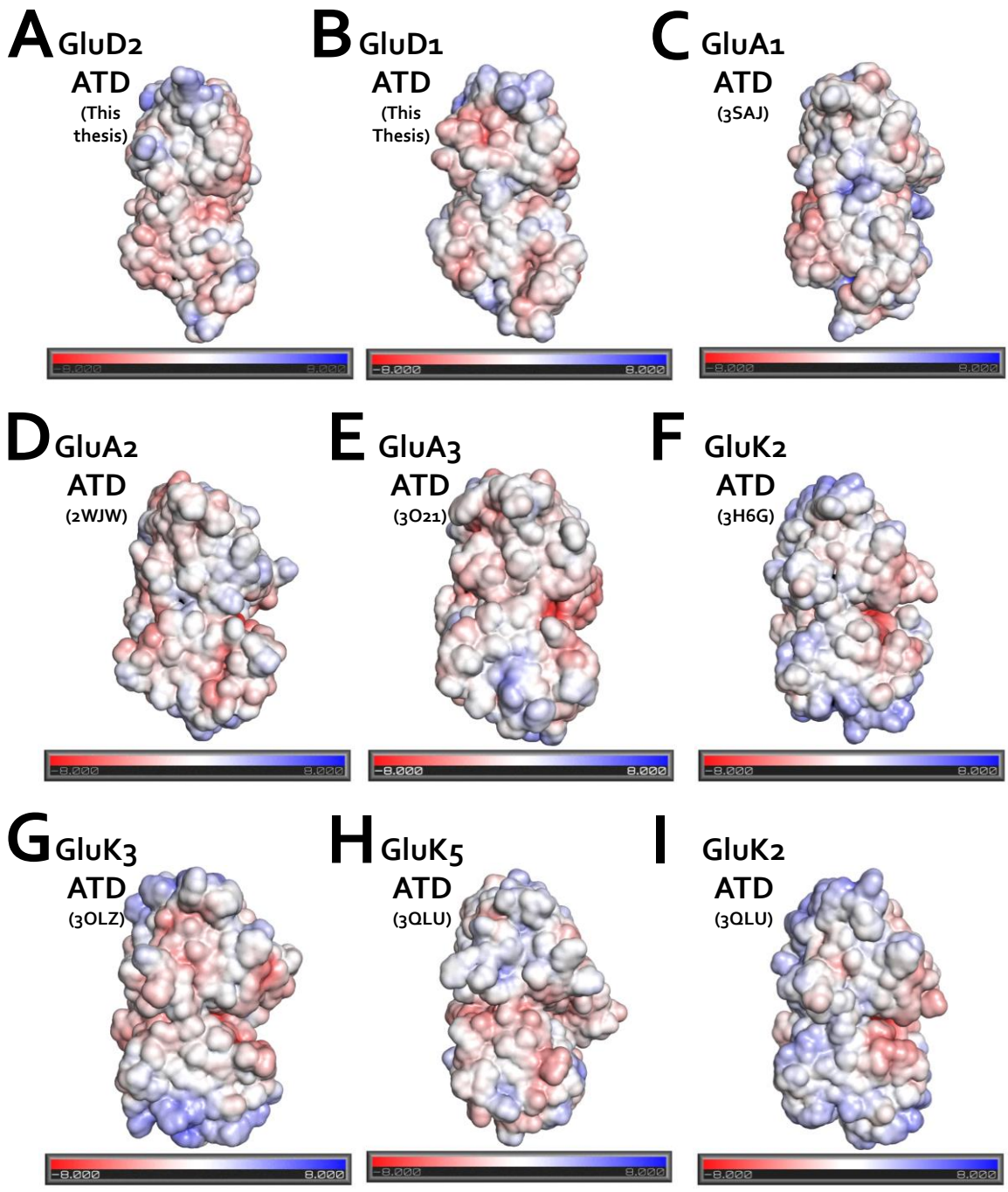

Figure 3.10: Non-NMDA iGluR ATD Dimerization Interface Electrostatic Potentials: A-I: *Surface representation of the vacuum electrostatic potential, calculated using APBS (Baker et al, 2001), of non-NMDA iGluR ATDs, viewed into the interface surface. The iGluR subunit and PDB code is listed. Blue indicates positive charge; white indicates neutral charge and red indicates negative charge. The units of electrostatic charge are in kTe-1 (k = Boltzmann constant, T = Temperature and e is the charge of an electron).*

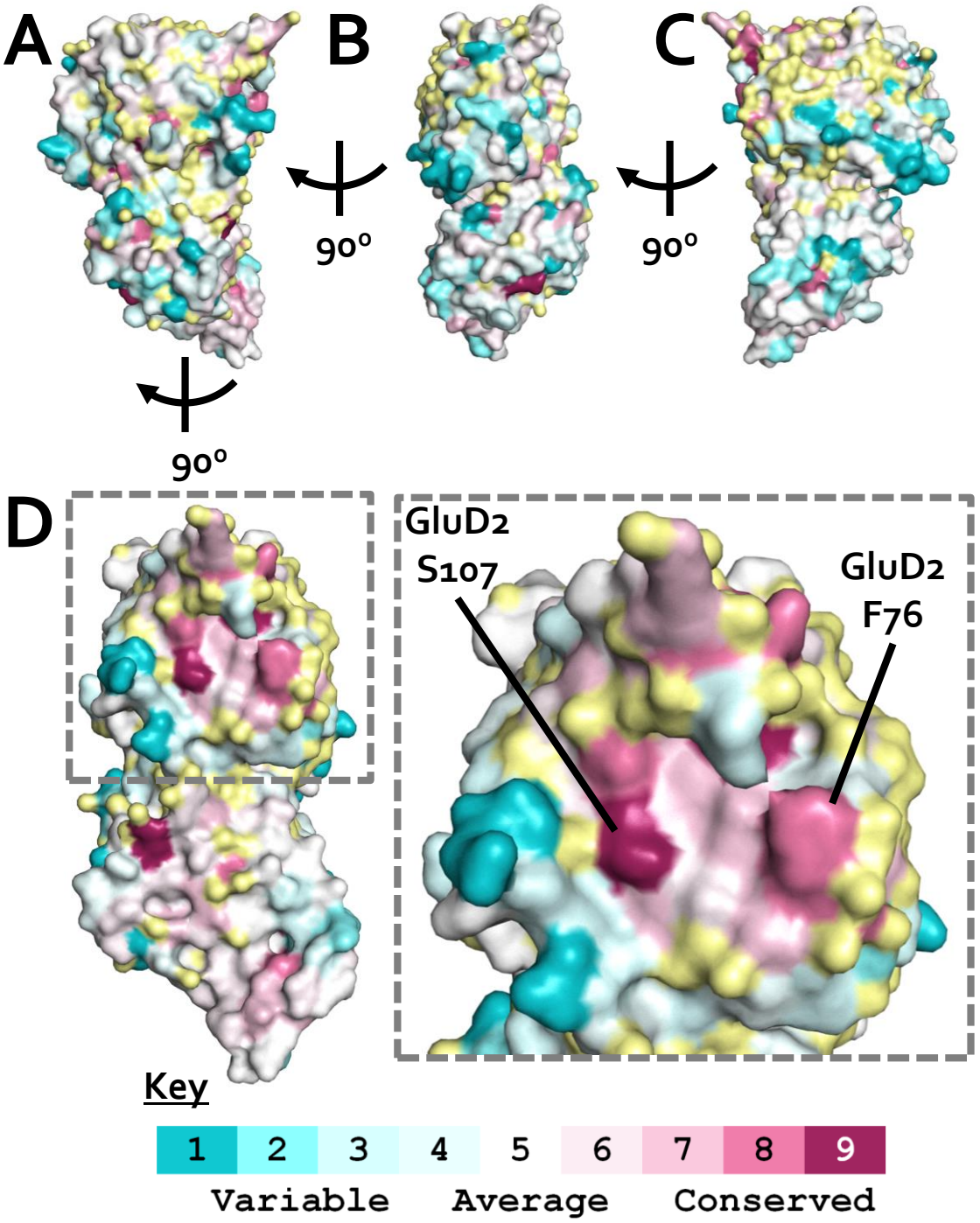

Figure 3.11: Sequence Conservation of Non-NMDA iGluR ATDs. ***A-D:*** *Sequence conservation of the non-NMDA receptor iGluR ATDs plotted onto the structure of the GluD2 ATD, rotations around this plot are depicted. Sequence conservation was calculated using the ConSURF server (Ashkenazy et al, 2010).* ***B*** *is a view of the conservation of the ATD 'Wing' (Figure 3.3, 3.6 and 3.8) and* ***D*** *is a view of the conservation of the ATD interface. Highly conserved GluD2 residues in the R1-R1 interface are labelled.*

Hence taken together this analysis provides evidence for a similar size (Figure 3.9), electrostatic potential (Figure 3.10), residue content and mode of binding (Figure 3.10) of the dimer interface of the non-NMDA iGluR ATDs.

3.9 Summary and Future Directions

In summary, parameters for the recombinant expression and purification of GluD1 (Section 3.6) and GluD2 ATDs (Section 3.3-3.4) from mammalian cells have been established. This led to the successful crystallization and the structure determination of both GluD1 ATD (Section 3.7) and GluD2 ATD (Section 3.5) at 2.25 Å and 1.8 Å respectively. Models built from obtained electron density confirmed the overall bilobal venus flytrap fold of the Delta-iGluR ATDs (Figure 3.3 and 3.6), analogous to the known ATD structures from other members of the iGluR superfamily (Table 3.1). Homology analysis of the iGluR ATDs revealed the GluD1 and GluD2 had the closest similarity to the non-NMDA iGluR ATDs (Table 3.3). The interface between the Delta-iGluR ATDs was found to be above average for the non-NMDA ATDs (Figure 3.9), however the conservation of residues in the ATD interface was found to be high, particularly in the R1-R1 interface (Figure 3.11D). The electrostatic potential of the non-NMDA iGluR interface is generally neutral (Figure 3.10) indicating a high level of Van der Waal's interaction. The conservation of the equivalent residues to GluD2 F76 and S107 (Figure 3.11D) – which are involved in R1-R1 inter-molecular hydrogen bonds (Figures 3.3 and 3.6) – in conjunction with published data showing the importance the equivalent residue to GluD2 F76 in GluA2 for ATD dimerization (Clayton et al, 2009), highlights the common mode of interaction at the non-NMDA iGluR ATD interface.

Conversely, comparison of structure of GluD1 and GluD2 ATDs with other members of the iGluR superfamily draws attention to some iGluR-Delta specific ATD features such as the 'Cleft-Loop' (Figure 3.7B) and the R2 α6' helix (Figure 3.7D). The combined effect of these features is the perceived open conformation of the ATD flytrap in comparison to other iGluR ATDs (Figure 3.7A), suggesting that more extensive ATD-LBC interactions could be present in iGluR-Delta ATDs relative to other member of the iGluR superfamily. Furthermore, the models for the Delta-iGluR ATDs add to the existing knowledge of the structural heterogeneity of the iGluR ATD 'Wing' (Figures 3.7C and 3.11B), implying this feature could play a role in iGluR subtype-specific functions.

The natural follow-up work from these results would be to: i) Use functional studies to test some of the general and Delta-iGluR specific features highlighted in this Chapter, i.e. the non-NMDA iGluR ATD interface, the 'Cleft-Loop' and iGluR ATD 'Wing'; ii) Investigate the wider structural details of Delta iGluRs to provide more information about additional subfamily specific features which may explain the molecular mechanisms behind their unique functional roles (Yuzaki, 2012); and iii) Use the protocols established in this chapter for the production of Delta-iGluR ATDs to investigate their reported interactions with members of the Cbln family of secreted glycoproteins (Matsuda et al, 2010; Ryu et al, 2012; Uemura et al, 2010). Work towards the aims described in points i, ii and iii is described in Chapters 4, 5 and 6 respectively.

Chapter 4:

Characterisation of the Role of the ATD Interface in GluD2 Function

4.1 Abstract

GluD2, a member of the iGluR superfamily, plays a crucial role in mediating D-Serine-dependent LTD in the immature cerebellum (Kakegawa et al, 2011), however little is known about the molecular mechanism behind the transmission and induction of the relevant signals. In this chapter, the structure of the GluD2 ATD and the analysis of the iGluR ATD dimerization interface (Chapter 3) were used to create a point mutant that disrupted the GluD2 ATD interface. Subsequent characterisation shows that this point mutation did not affect the overall tetrameric assembly of GluD2, the total protein expression level, its ability to traffic to the plasma membrane or to interact with an extracellular partner protein Cbln1. One specific functional effect however, which was tested in collaboration with the laboratory of Prof. M. Yuzaki, Keio University Japan, was the impairment of D-serine dependent LTD in mice expressing the mutant form of GluD2. Assimilating this data into a putative mechanism led to the hypothesis that the GluD2 ATD interface acts as a hinge point to allow the transmission of the D-Serine signal and subsequent LTD.

4.2 Introduction and Aims

Ionotropic glutamate receptors have a modular domain architecture; the extracellular region of iGluR subunits consists of the ATD and the LBC (See Section 1.3.2) (Traynelis et al, 2010). Extensive pharmacological studies have uncovered much about the function of the LBC and this information combined with structural studies of the isolated LBC have revealed a molecular mechanism for activation and desensitization of the iGluR channels (Sun et al, 2002; Traynelis et al, 2010). However, a consensus on the set of functions performed by the ATD is yet to be reached.

For example there is evidence that the ATD determines the strict subfamily specific assembly of iGluRs (Ayalon et al, 2005; Leuschner & Hoch, 1999; Meddows et al, 2001). Moreover, it has been demonstrated that the ATD has a role in modulating the ion channel activity of iGluRs, influencing channel open probability (Gielen et al, 2009) , the kinetics of deactivation and desensitization as well as mediating the subtype-specific potency of agonist binding (Yuan et al, 2009). Additionally, in NMDA receptors the ATD is known to be the site for the binding of allosteric modulators such as zinc and ifenprodil (Karakas et al, 2009; Karakas et al, 2011; Sensi et al, 2009). The iGluR ATD is also known to be the site of interaction with various synaptic partner proteins; examples include the Cbln proteins which interact with the ATDs of the Delta subtype iGluRs (Matsuda et al, 2010; Uemura et al, 2010; Yasumura et al, 2012), N-cadherins and neuronal pentraxins which interact with AMPA subtype ATDs (O'Brien et al, 1999; Saglietti et al, 2007; Sia et al, 2007), and EphB that has been postulated to interact with NMDA ATDs (Dalva et al, 2000; Takasu et al, 2002). Taken together, this evidence points to an idea that the iGluR ATD is a multi-functional domain; perhaps a point of convergence for several different modulatory inputs.

The iGluR subunit GluD2 is crucial for the manifestation of LTD at the PF-PC synapse in the cerebellum (Kashiwabuchi et al, 1995). D-Serine is a ligand for GluD2 and binds to the LBC with an affinity of 1 mM (Naur et al, 2007). Binding of D-serine to GluD2 in the immature cerebellum plays a role in mediating LTD at the PF-PC synapse and a concomitant role in motor coordination and learning (Kakegawa et al, 2011). There is evidence that the molecular mechanism which facilitates the effects of D-serine binding to GluD2 involves the GluD2 CTD, which includes binding sites for PDZ-containing proteins, and protein kinase C (PKC); suggesting that a global conformational change in the GluD2 receptor takes place and this is transmitted across the membrane, affecting binding to PDZ-containing intracellular partners such as PSD93, PTPMEG, S-SCAM and delphilin, after which the signalling pathways converge on PKC (Kakegawa et al, 2011). However direct

structural evidence for such a conformational change remains unavailable, hence further investigation into the molecular basis for GluD2 mediated, D-serine induced LTD is required.

The aim of this chapter was to use the structural information and iGluR ATD interface analysis, presented in Chapter 3, as a tool to investigate the function of the GluD2 ATD. Specifically, the GluD2 ATD dimerization interface was targeted to understand the effects of ATD oligomerization on the actions of GluD2.

4.3 Expression and Purification of GluD2 F76D

Based upon the structures of GluD2 and GluD1 ATDs and the analysis of the iGluR ATD interfaces that were presented in Chapter 3, phenylalanine 76 (Figure 4.1A) was chosen as a candidate for mutation to disrupt the GluD2 ATD interface. The hypothesis that mutating this residue, to a charged residue like aspartate, would disrupt the ATD interface was based upon its sequence conservation in all the known non-NMDA iGluR ATD structures (Figure 3.8), its involvement in an interface mediating hydrogen bond (Figure 3.3), as well as the evidence that an equivalent mutation in the GluA2 ATD abolished protein dimerization (Clayton et al, 2009). Hence oligonucleotide-mediated mutagenesis was used to introduce a mutation to encode an aspartate at position 76 in the GD6 construct. Details of the cloning of GluD2 ATD F76D are contained in Section 2.1 and Appendix 8.1. This construct was then tested for expression and secretion from HEK 293T cells, following the protocol described in Section 2.3.2; additionally the ability of two histone deacetylase inhibitors, valproic acid and sodium butyrate, to enhance the levels of expression and secretion was also tested. The GluD2 ATD F76D construct was found to be expressed and secreted from HEK cells (Figure 4.1B) and furthermore 4 mM valproic acid was found to enhance expression and secretion of

this construct relative to the scenario with no additive (Figure 4.1C). However sodium butyrate seemed to have little effect on the level of expression and secretion (Figure 4.1C).

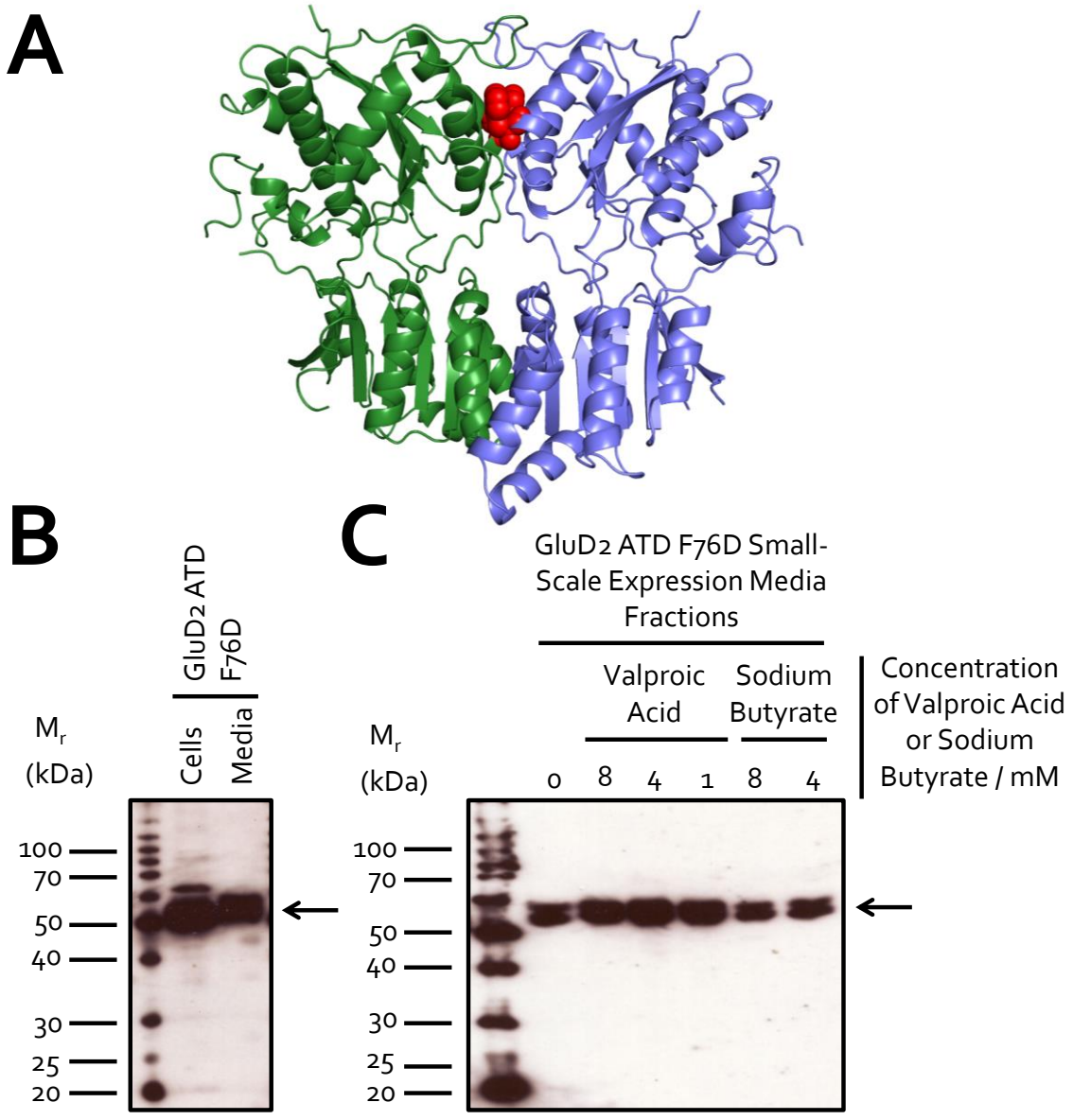

Figure 4.1: Expression Trials of construct GluD2 ATD F76D. ***A:*** *Structural cartoon representation of the GluD2ATD structure (Chapter 3), highlighting Phenylalanine 76 in red spheres.* ***B:*** *Anti-His western blot analysis of a small-scale expression trial of GluD2 ATD F76D. The arrow highlights the band that corresponds to GluD2 ATD F76D.* ***C:*** *Anti-His western blot analysis of a small-scale expression trial assessing the effect of histone deacetylase inhibitors on the expression and secretion of GluD2 ATD F76D. The arrow points out the double band that corresponds to GluD2 ATD F76D glycoforms.*

This GluD2 ATD F76D construct was then used to transfect HEK293T cells, cultured in roller bottles, as described in Section 2.3.3. Valproic acid, at a final concentration of 4 mM, was also added at the time of transfection. This conditioned media was then processed and applied to IMAC, as described in Section 2.4.1-2 (Figure 4.2B) followed by an additional stage of purification, SEC (Figure 4.2B). SDS-PAGE analysis of SEC fractions revealed that the GluD2 ATD F76D was purified to >99 % (Figure 4.2C).

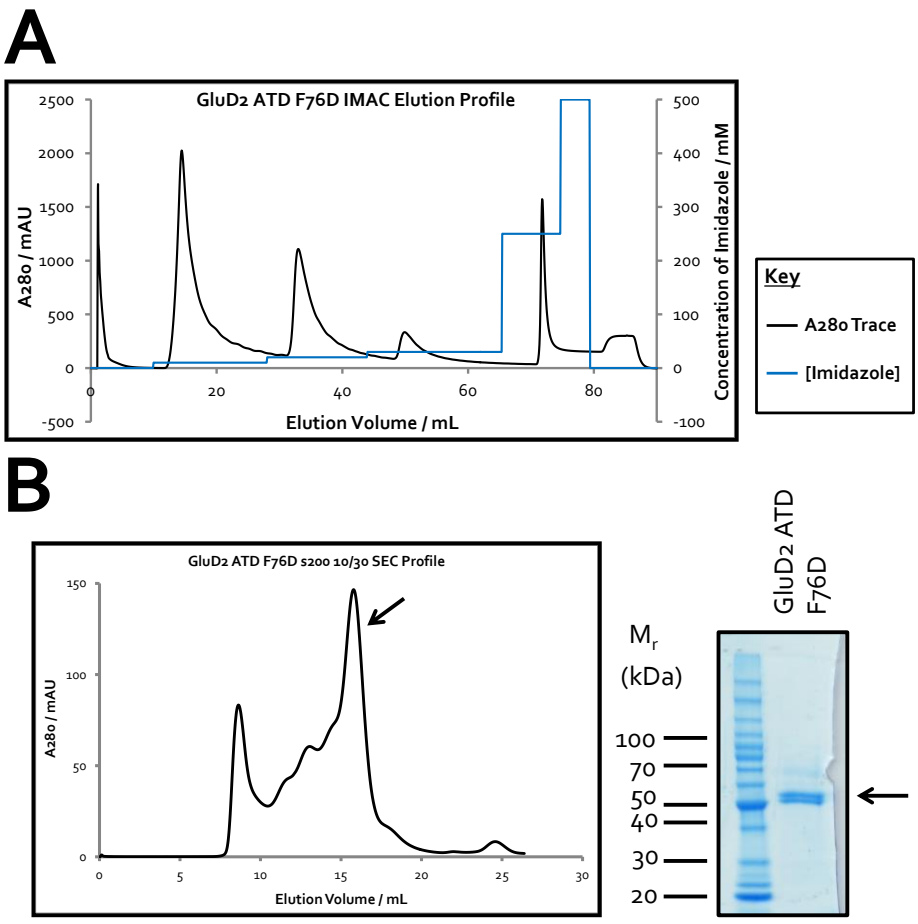

Figure 4.2: Purification of Recombinant GluD2 ATD F76D. A: *A profile displaying the IMAC purification of GluD2 ATD F76D, A280 absorbance and concentration of imidazole are plotted against elution volume.* ***B: Left Image:*** *Elution profile for the SEC of GluD2 ATD F76D, monitoring A280 absorbance versus elution volume. The arrow highlights the peak that corresponds to GluD2 ATD F76D, other peaks represent IMAC impurities.* ***Right Image:*** *Coomassie-stained SDS-PAGE analysis of the peak pooled peak fractions from the SEC of GluD2 ATD F76D. The arrow draws attention to the double band for GluD2 ATD F76D glycoforms.*

4.4 F76D Mutation Disrupts the Integrity of the GluD2 ATD Interface, But Not the Overall Assembly or Expression of GluD2

Following the establishment of the successful expression and purification of the GluD2 ATD F76D construct, this recombinant protein could be used for various analyses. The first goal was to verify that the F76D mutation did indeed disrupt the integrity of the GluD2 ATD dimer interface, as was the case for the equivalent mutation in GluA2 (Clayton et al, 2009). MALS was chosen as a technique to measure oligomeric state. Samples of GluD2 ATD, GluD1 ATD and GluD2 ATD F76D were all investigated using MALS; the concentration of each sample under analysis was standardised, i.e. all were tested at 1 mg/mL. Analysis of the samples via MALS proved that the F76D mutation in GluD2 was successful in perturbing the ATD interface; GluD2 ATD (90.6 kDa) and GluD1 ATD (91.2 kDa) were found to be dimeric, whereas GluD2 ATD F76D (46.5 kDa) was measured to be monomeric under the conditions tested (Figure 4.3).

A

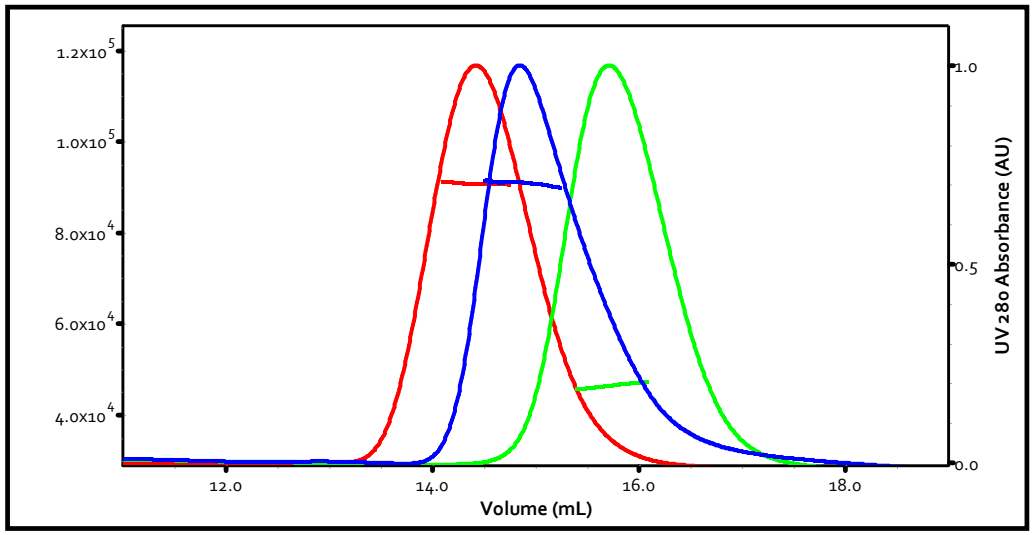

Key

GluD2 ATD **GluD1 ATD** **GluD2 ATD F76D**

B

Sample	Measured Molar Mass (kDa)	Molecular Weight of a Single Subunit (kDa)	Measured Molar Mass/Single Subunit Molecular Weight	Oligomeric State of Sample
GluD2 ATD	90.6	47.0	1.93	Dimer
GluD1 ATD	91.2	46.9	1.94	Dimer
GluD2 ATD F76D	46.5	47.0	0.99	Monomer

Figure 4.3: Analysis of the oligomeric state of Delta iGluR ATDs. ***A:*** *MALS analysis of the oligomeric state of Delta iGluR ATDs, displaying measured molar mass and UV 280 absorbance versus elution volume.* ***B:*** *A Table displaying oligomer calculations using the data obtained from MALS.*

After establishing that the F76D mutation disrupts the ATD interface of GluD2 (Figure 4.3), the next property to test was how this point mutation effected the global oligomeric state of full-length GluD2. To test this, full-length constructs of GluD2, i.e. D24-I1007, were created, one wild-type and one with the F76D mutation. Both constructs were engineered to encode N-terminal HA-tags.

Additionally an N-terminally tagged HA construct of GluD2 without an ATD, GluD2 ΔATD, was designed to test the effects of removing the ATD on the oligomerization state of GluD2.

Since these expression constructs all encoded intact transmembrane proteins, there would be considerable technical challenges to produce these samples in high enough quantity and purity to allow analysis by MALS. To investigate the effects of the mutation and truncation on the global oligomeric state of GluD2, BN-PAGE on crude cellular extracts from transiently transfected mammalian cells, utilizing the engineered N-terminal HA-tag for western blot, was used.

BN-PAGE (Section 2.11) followed by anti-HA western blot analysis of cellular extracts expressing the GluD2 transmembrane constructs demonstrated the molecular weight of wild-type GluD2 to be ~450 kDa, i.e. a tetramer, GluD2 F76D to be ~480 kDa, i.e. a tetramer, and GluD2 ΔATD to be ~250 kDa, again a tetramer (Figure 4.4). A construct of full-length GluA2 Flop Q isoform, encoding N25-I883 with an N-terminal HA-tag (produced by Amber Clayton, STRUBI) was also included for BN-PAGE analysis as a control, since this had previously been shown to be tetrameric using both BN-PAGE (Kim et al, 2010) and crystallography (Sobolevsky et al, 2009). The GluA2 construct was found to be ~400 kDa, thus a tetramer (Figure 4.4), hence validating the execution of the technique.

A

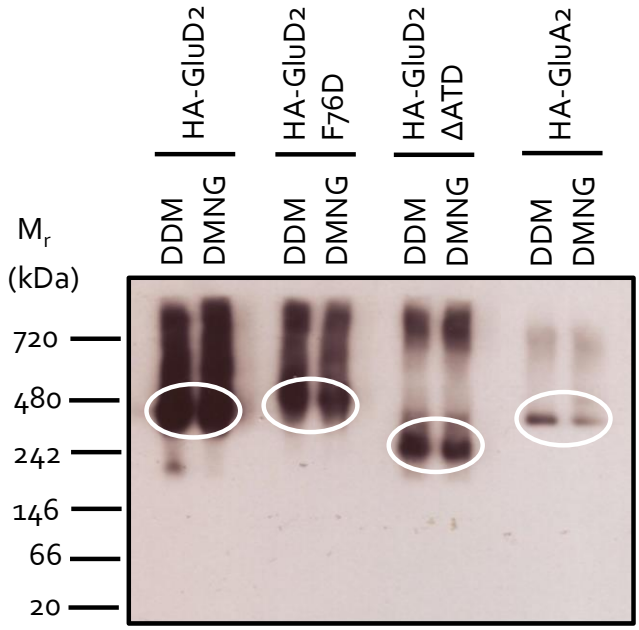

B

Sample	BN-PAGE Estimate of Molecular Weight (kDa)	Molecular Weight of a Single Subunit (kDa)	Molecular Weight Estimate/Single Subunit Molecular Weight	Oligomeric State of Sample
HA-GluD2	~450	111.4	~4.04	Tetramer
HA-GluD1 F76D	~480	111.4	~4.31	Tetramer
HA-GluD2 ΔATD	~250	64.9	~3.85	Tetramer
HA-GluA2	~400	97.0	~4.12	Tetramer

Figure 4.4: Analysis of the oligomeric state of GluD2 transmembrane constructs. ***A:*** *3-12 % BN-PAGE followed by anti-HA western blot analysis of the oligomeric state of various transmembrane constructs of GluD2. The white ellipses highlight the appropriate band. The detergent used to aid loading of the samples is detailed above the blot. DDM stands for n-Dodecyl-ß-maltoside and DMNG notates Decyl maltose neopentyl glycol.* ***B:*** *Table of analysis using the data obtained from BN-PAGE displayed in* ***A****.*

The BN-PAGE results presented in Figure 4.4 indicate that the F76D mutation does not significantly affect the total expression level of GluD2, relative to wild-type, although the ATD truncation seems to diminish the expression level. To investigate this further, SDS-PAGE followed by anti-HA western blot on total cell extracts of transiently transfected mammalian cells was used to evaluate

the effects of the mutation and truncation on total expression levels. Non-native SDS-PAGE corroborated the inference from BN-PAGE that the GluD2 F76D mutation did not adversely affect total cell expression, additionally excision of the ATD resulted in a slight reduction in the level of total expression of GluD2 (Figure 4.5).

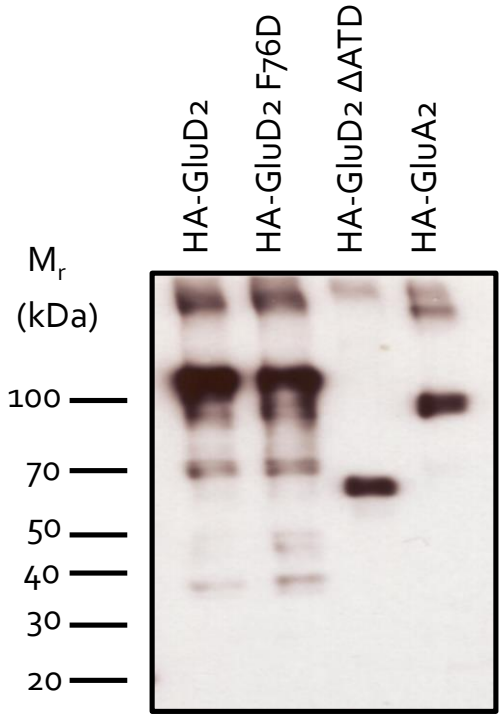

Figure 4.5: Assessing the effects of mutation and truncation on the expression of GluD2 from HEK 293T cells. *An anti-HA western blot of total cellular extracts from HEK 293T cells transiently expressing either HA-GluD2, HA-GluD2 F76D, HA-GluD2ΔATD, HA-GluA2.*

4.5 Monomerization of GluD2 ATD Does Not Effect Binding To Cbln1

Following the confirmation that the F76D mutation successfully disrupted the GluD2 ATD interface, this recombinant protein could be used as a tool to dissect the function of GluD2. As the GluD2 ATD is the known binding site for Cbln1 (Matsuda et al, 2010; Uemura et al, 2010) the first question to answer was: Does monomerization of GluD2 ATD affect the interaction with Cbln1? To answer

this question SPR analysis was performed using Cbln1 constructs as ligands and GluD2 ATD constructs as analytes. GluD2 ATD was prepared as described in Section 3.4 and GluD2 ATD F76D was produced as described in Section 4.3. The Cbln1 ligand was prepared as described in Chapter 5. The regeneration protocol established for this interaction was a 30 s injection of 1 M $MgCl_2$. Multi-cycle equilibrium binding SPR experiments with this arrangement showed that the F76D mutation did not affect the binding affinity of GluD2 to Cbln1 (Figure 4.6). The interaction between GluD2 ATD and Cbln1 was calculated to 19.72 ± 1.03 μM (Figure 4.6A) and comparably the interaction between GluD2 ATD F76D and Cbln1 was calculated to 24.26 ± 4.28 μM (Figure 4.6B). There was a reduction in the observed B_{max} between experiments using GluD2 ATD (Figure 4.6A) and GluD2 ATD F76D (Figure 4.6B) which can be rationalized by the reduced mass of the analyte in the case of GluD2 ATD F76D. From this, it is possible to infer that monomerization of the GluD2 ATD does not inhibit binding to Cbln1, hence the Cbln1 binding site is not formed upon dimerization but each monomeric ATD has the ability to interact with Cbln1.

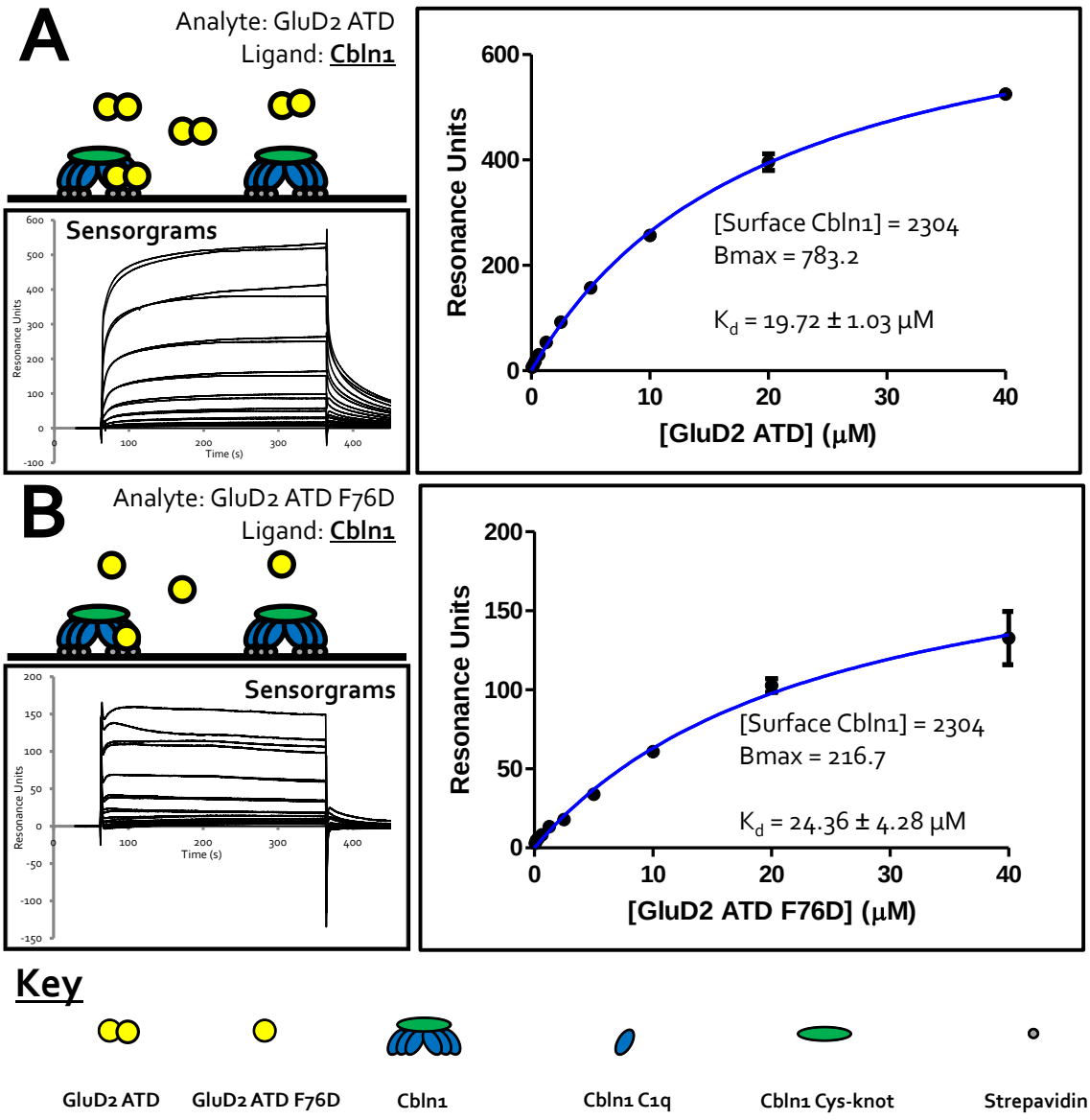

Figure 4.6: SPR Binding Studies of the Interaction between Cbln1 and GluD2 ATD and GluD2 ATD F76D. A: Top Left Image of each Panel A-B: *A schematic representing the experimental set-up to study the interaction between Cbln1 and either full-length GluD2 ATD in* ***A****, or GluD2 ATD F76D in* ***B****.* ***Bottom left of each Panel A-B:*** *Experimental, reference-subtracted sensorgrams displaying real-time binding and unbinding of the analyte to the ligand.* ***Right Image of each Panel A-B:*** *Binding curve for the interaction under test. The amount of ligand coupled to the chip, the binding curve-derived Bmax and K_d are listed.*

To verify this conclusion the SPR studies were repeated in the inverse orientation, i.e. with GluD2 constructs as the ligands and with Cbln1 as the analyte. To allow the execution of this the GluD2

ATD and GluD2 ATD F76D were transferred into the pHLsec-Avitag3 vector as described in Section 2.1 and Appendix 8.1. The Cbln1 analyte was prepared as described in Section 6.4. Multi-cycle equilibrium SPR using this alternative arrangement confirmed the conclusion taken from Figure 4.6 that perturbation of the GluD2 ATD interface does not adversely disturb the interaction with Cbln1 (Figure 4.7). In this orientation the interaction between Cbln1 and GluD2 ATD was measured at 2.23 ± 0.47 μM (Figure 4.7A) and the interaction between Cbln1 and calculated to 3.62 ± 0.76 μM (Figure 4.7B). The discrepancy between the calculated values in Figure 4.6 and 4.7 may be a result of the differing avidity effects in each orientation that the SPR experiments were conducted; i.e. Cbln1 is predicted to be a dimer of trimers (Bao et al, 2005), and each subunit may harbour a binding for GluD2 ATD, whereas GluD2 ATD is dimeric (Figure 4.3). After establishing that F76D mutation disrupts the integrity of the GluD2 ATD interface but not the ability of GluD2 ATD to interact with Cbln1, this information could be used as an investigative tool to unpick the function of GluD2 ATD; i.e. investigate the functional effects of ATD disruption without also disrupting the formation of the trans-synaptic complex.

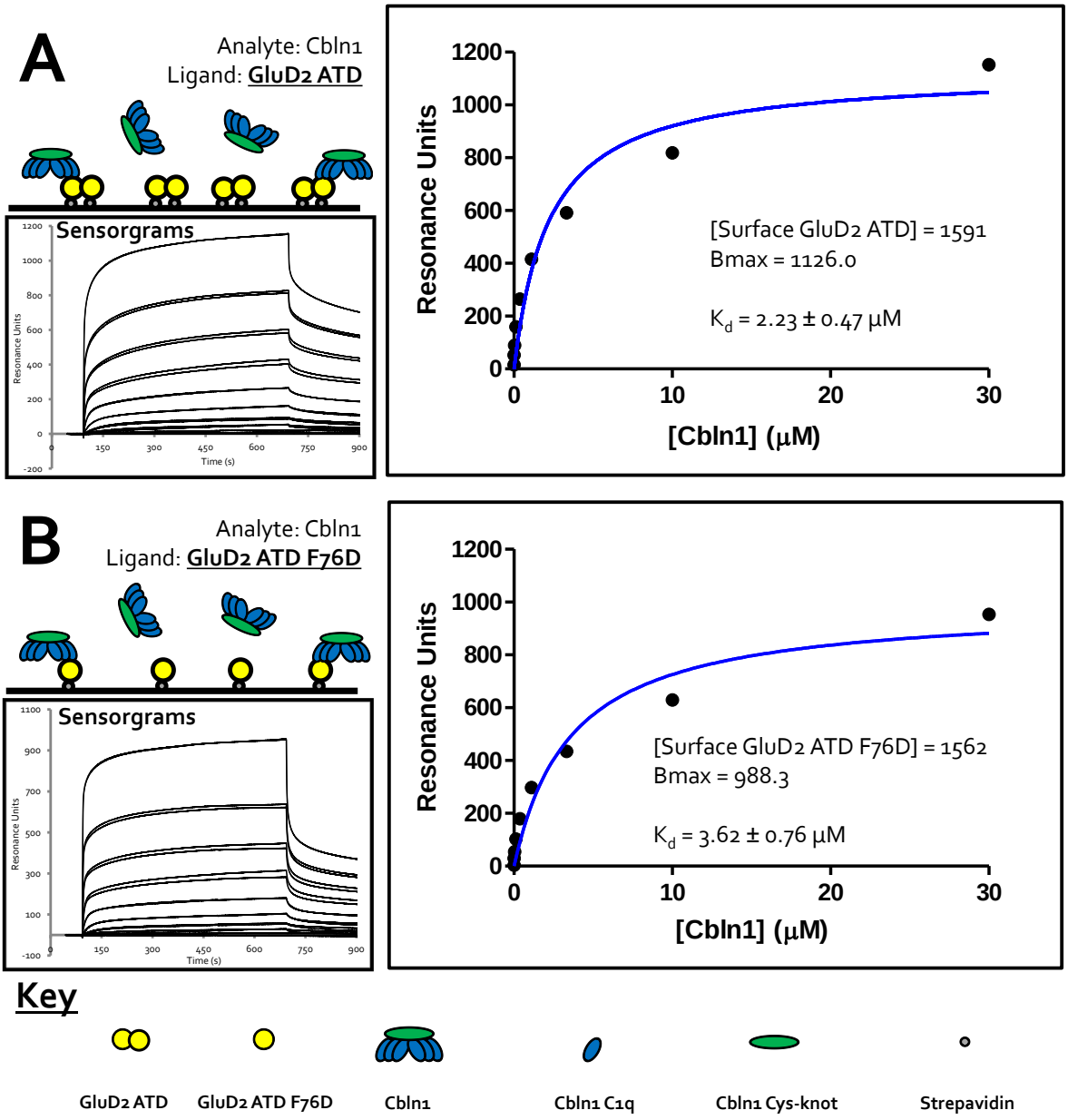

Figure 4.7: SPR Binding Studies of the Interaction between Cbln1 and GluD2 ATD and GluD2 ATD F76D in the Inverse Orientation. A: Top Left Image of each Panel A-B: *A schematic representing the experimental set-up to study the interaction between Cbln1 and either full-length GluD2 ATD in* ***A****, or GluD2 ATD F76D in* ***B****.* ***Bottom left of each Panel A-B:*** *Experimental, reference-subtracted sensorgrams displaying real-time binding and unbinding of the analyte to the ligand.* ***Right Image of each Panel A-B:*** *Binding curve for the interaction under test. The amount of ligand coupled to the chip, the binding curve-derived Bmax and K_d are listed.*

4.6 F76D Mutation Does Not Effect Plasma Membrane Trafficking

A FACS based plasma membrane trafficking assay was used to ascertain if the GluD2 F76D mutation had an effect on trafficking of GluD2 to the plasma membrane. This was carried out using transmembrane N-terminal (extracellular) HA-tagged constructs (Section 4.4), as described in Section 2.10. This assay showed that the amount of fluorescence detected on the cell surface, measured for the same number of counted cells, was roughly equivalent for both GluD2 and GluD2 F76D, indicating a comparable amount of anti-HA primary and fluorescent secondary antibodies had bound to the surface of the counted cells, and hence that the expression of GluD2 and GluD2 F76D must be equally similar (Figure 4.8). Additionally, this effect was tuneable, in that when expression constructs were diluted ten-fold with a 'dummy plasmid' both GluD2 and GluD2 F76D surface trafficking levels were reduced by a comparable amount (Figure 4.8). Surprisingly, the removal of the ATD seemed to enhance the surface trafficking of GluD2 ΔATD (Figure 4.8). When this data is combined with that presented in Figure 4.5 that the overall expression of GluD2 ΔATD is reduced, relative to wild-type, this suggests that although removal of the ATD reduces total expression levels, the protein that is produced is more efficiently trafficked to the cell surface. An explanation may be that a greater level of total expression of GluD2 and GluD2 F76D may in fact overwhelm the secretory machinery, reducing the efficiency of trafficking, whereas in the scenario with GluD2 ΔATD a lower level of total expression allows more effective trafficking. A further possibility is that in the GluD2 ΔATD case, the HA epitope may just be more accessible. Nevertheless, Figure 4.8 provides firm evidence for the idea that oligomerization of the GluD2 ATD is not necessary for plasma membrane trafficking.

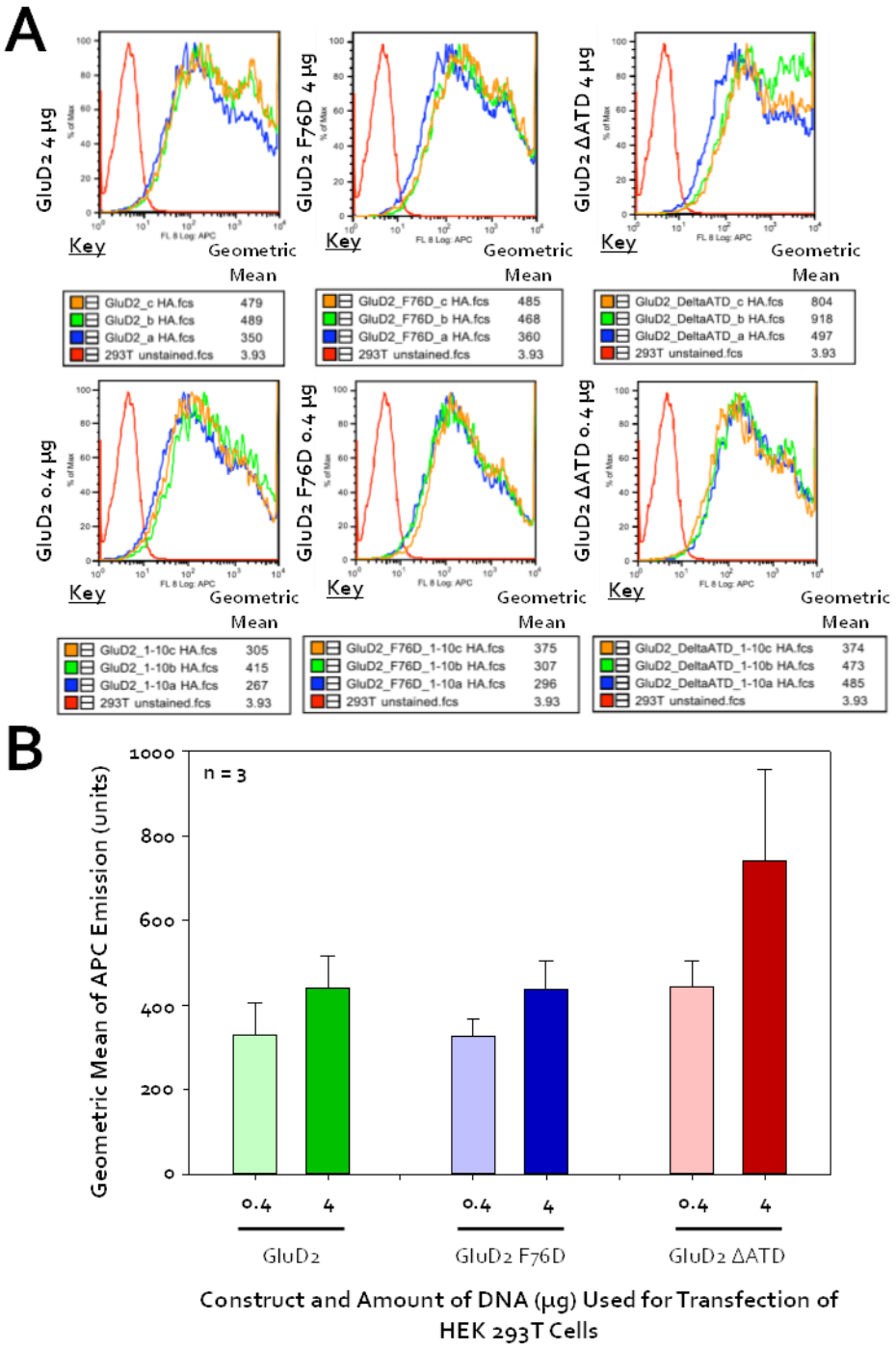

Figure 4.8: FACS-Based Plasma Membrane Trafficking Assay to Assess the Effects of Disruption of the ATD Interface on GluD2 cell surface trafficking. ***A:*** *Population charts displaying reference subtracted geometric mean of APC emission of live cell subset from the 30,000 cells counted and sorted using FACS. For each construct, cell counts were performed in triplicate on three separately prepared samples. The geometric mean for the fluorescence data was calculated for each cell count and is displayed in the key.* ***B:*** *A bar chart displaying geometric mean of fluorescence for each construct and transfection level. Error bars representing one standard deviation are shown.*

4.7 Functional Effects of GluD2 F76D Mutation

To test the effects of the GluD2 F76D mutation on D-Serine induced LTD, the constructs encoding full-length N-terminally HA-tagged GluD2 and GluD2 F76D (Section 4.4) were sent to collaborators in the laboratory of Professor Michisuke Yuzaki, Keio University, Japan. The Yuzaki lab has access to a GluD2 KO mouse and have previously utilized a transgenic rescue approach in this mouse to identify and characterise D-Serine-dependent LTD in the immature cerebellum (Kakegawa et al, 2011). Our collaborators used the GluD2 and F76D constructs (Section 4.4) in transgenic rescue experiments and performed various forms of analysis. The most striking finding was that immature mice expressing the F76D mutant demonstrated deficient D-Serine induced LTD (Figure 4.9). This suggests that the integrity of the ATD interface is crucial for the mechanism behind transmitting the signal resulting from D-Serine binding to GluD2. Furthermore, this implies an inter-domain synergistic mechanism whereby the contacts made by ATDs from different subunits are necessary to allow a global conformational change that initiates the specific signals resulting in LTD, perhaps by acting as a molecular hinge point.

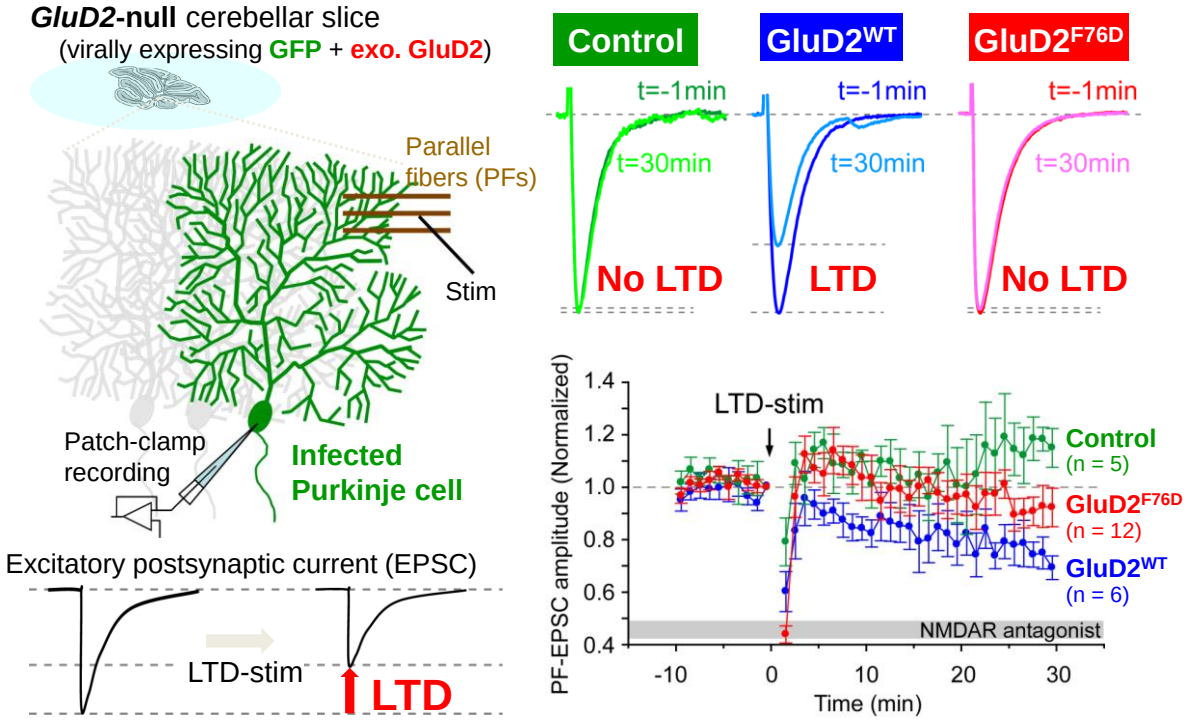

Figure 4.9: D-Ser-dependent long-term depression (LTD) in immature cerebellar slices is impaired in Purkinje cells expressing GluD2 F76D. A: Left Panel*, schematic representing the experimental set-up for recordings from Purkinje cells expressing either GluD2 or GluD2 F76D.* ***Right Panel:*** *Patch clamp recordings of EPSC (Excitatory Post-Synaptic Current) before and after stimulus of LTD from immature cerebellar slices transgenically modified with GluD2, GluD2 F76D or a control. Figure provided by Prof. M. Yuzaki, Keio University, Japan.*

4.8 Summary and Future Directions

Mutation of GluD2 phenylalanine 76 to a charged residue, aspartate, was found to disrupt the interface of the isolated GluD2 ATD (Figure 4.3). When this mutation is introduced into the full-length version of the receptor, the overall tetrameric state of GluD2 is not affected (Figure 4.4), suggesting this mutation simply perturbs the native arrangement of the ATD layer rather than the overall receptor assembly. Moreover, the GluD2 F76D mutation did not significantly diminish the expression of the GluD2 in a heterologous expression system (Figure 4.5), abrogate binding to the extracellular partner protein Cbln1 (Figure 4.6 and 4.7) or affect the level of trafficking to the plasma

membrane (Figure 4.8); thereby signifying that the general assembly of the GluD2 ATD layer is not involved in these functions. One effect of the F76D mutation in full-length GluD2 is that, within a physiological context, i.e. in transgenic rescued mice, D-Serine-dependent LTD is impaired (Figure 4.9). D-Serine is a ligand for GluD2 and ligand binding leads to closure of the LBC cleft (Naur et al, 2007), which is typical for protein domains with venus flytrap architecture (Mayer, 2006). A consequence of D-Serine binding to GluD2 is induction of LTD in the immature cerebellum, which is dependent on the C-terminus of GluD2, leading to a suggestion that the signal is transmitted across the cell membrane through a non-ionotropic mechanism (Kakegawa et al, 2011). The new data presented in this chapter, regarding the necessity of the integrity of the ATD interface for the induction of D-Serine-dependent LTD, leads to a hypothesis for the molecular mechanism behind this process where the GluD2 ATD acts as a hinge point, allowing the transduction of the D-Serine signal across the plasma membrane initiating the signalling pathways that culminate in endocytosis of AMPA receptors (Figure 4.10). Thus we can propose a new function of the iGluR ATD as a signal transduction module; evidence in this chapter points to a hypothesis that dimerization of ATDs in tetrameric GluD2 is crucial for the global structural changes that occur upon ligand binding and the concomitant signal transduction. However, it is also important to note that at the same PF-PC synapse there is a D-Serine and ATD-independent, yet CTD-dependent form of LTD in the adult cerebellum (Kohda et al, 2007), suggesting alternative mechanisms for the action of GluD2 may exist.

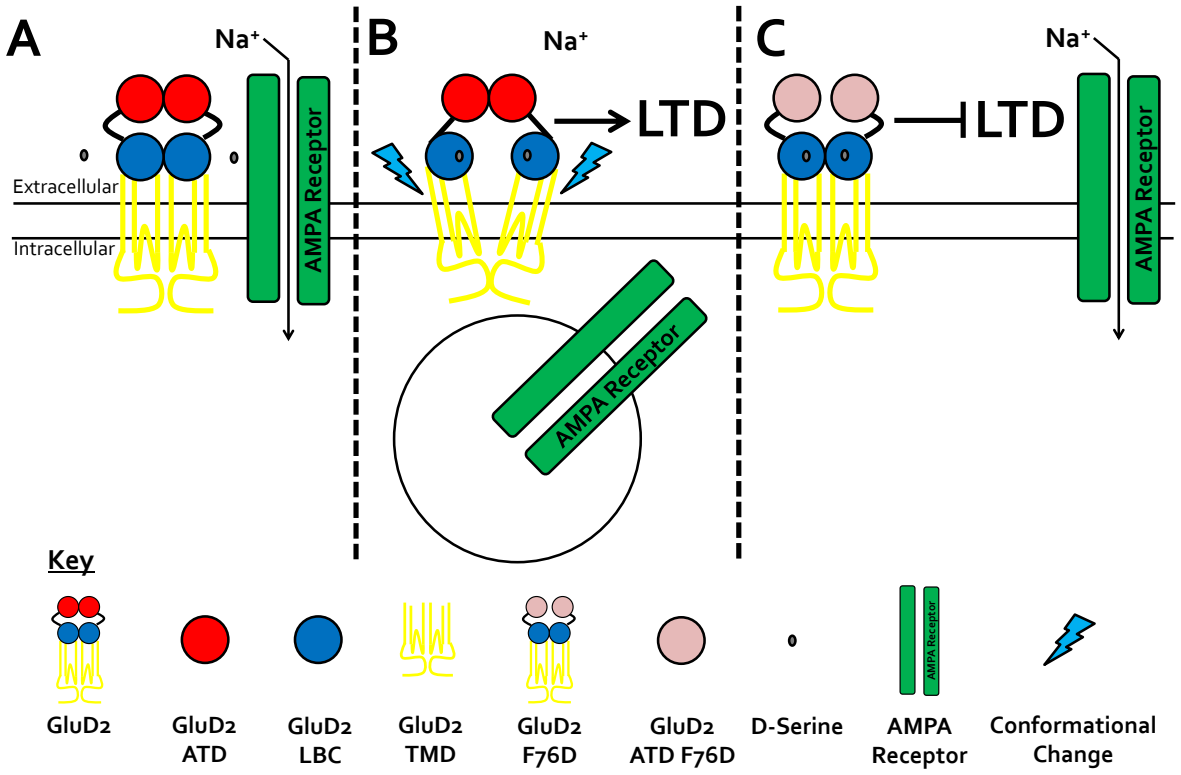

Figure 4.10: Proposed Mechanism for the Hinge Action of the GluD2 ATD in the Transduction of D-Serine-Dependent LTD is in Immature Cerebellum. ***A:*** *Schematic showing GluD2 in the inactive apo state, and AMPA receptors present at the cell surface allowing the conductance of cations and post-synaptic cell depolarization.* ***B:*** *Schematic showing GluD2 in the ligand bound active state, having undergone some sort of conformational change that is dependent on the ATD interface, perhaps acting as a hinge point. The conformational change is highlighted by the light blue lightning bolts and results in AMPA receptor endocytosis and LTD.* ***C:*** *A schematic representing the case for GluD2 F76D where the GluD2 dimer interface is disrupted meaning the hinge point crucial for the transduction of the initial D-Serine signal cannot operate correctly meaning the onset of LTD is inhibited.*

One way to unequivocally prove this mechanism suggested in Figure 4.10 would be to obtain structural snapshots of either the GluD2 extracellular domain or the full-length, transmembrane spanning GluD2 in various conformations equivalent to the *apo* inactive state and the active D-Serine bound state. X-ray crystallography would provide the richest source of information along such a line of study and efforts in this direction are detailed in Chapter 5. Single particle EM could also be employed as a technique to investigate these hypothetical conformational changes;

however such changes would have to be quite substantial to be noticeable using this technique considering the resolution limitations of EM. Additionally another line of study, following the findings presented in this chapter, would be to explore the consequences of the F76D mutation on whole animal behaviour since LTD has been described as the cellular substrate of motor control and learning (Ito, 1989) and the common consequence of disrupting cerebellar LTD is an impairment in these motor behaviours and functions (Kakegawa et al, 2011; Kashiwabuchi et al, 1995).

Chapter 5:

Probing the Domain Organisation of GluD2

5.1 Abstract

The delta-iGluRs, GluD1 and GluD2 are irregular members of the iGluR superfamily as their mode of function is thought not to involve the flow of ions through their putative pore. To investigate whether these differences were a result of structural variances in the iGluR ecto-domains, a construct of GluD2 ecto-domain was produced and this was used for crystallization trials. After several rounds of optimization, including protein methylation, crystals which diffracted to ~4 Å were obtained and this data led to a partly refined model for the GluD2 ecto-domain. However, the domain arrangement seen in this model was rationalized as an artefact. The assembly of the GluD2 ecto-domain was investigated further using targeted cysteine mutatgenesis and this led to a symmetric dimer model, as a nucleus for the assembly of the GluD2 ecto-domain. Finally, steps were taken to initiate a project targeting the structural characterisation of the full-length transmembrane GluD2.

5.2 Introduction and Aims

The Delta iGluRs are the most enigmatic subfamily of iGluRs as a result of the observations that, despite a high sequence homology to other iGluRs – particularly in the pore-lining M3 helix (Sobolevsky et al, 2009) of the TMD (Figure 5.1) – the Delta iGluRs do not form functional glutamate-gated ion channels when expressed alone or in combination with other iGluRs in heterologous cells, nor do they bind glutamate or glutamate analogs (Araki et al, 1993; Lomeli et al, 1993). Hence for a long time they were known as 'orphan receptors' (Yuzaki, 2003). D-serine has subsequently been demonstrated as the ligand for GluD2, however application of D-serine to wild-type GluD2 does not induce ion flux through the membrane-spanning protein (Naur et al, 2007).

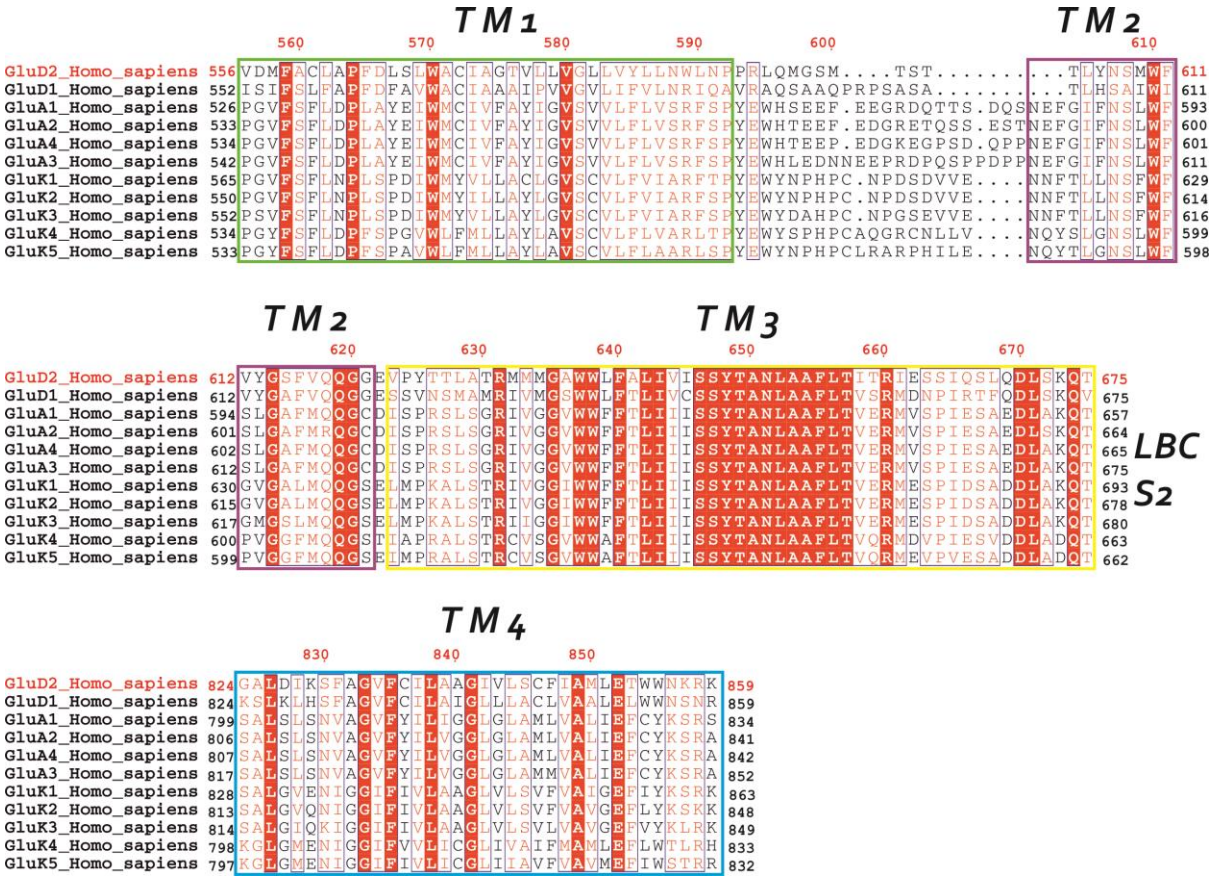

Figure 5.1: The iGluR Transmembrane Domain. *A multiple sequence alignment of the transmembrane domains of non-NMDA iGluRs. The green box highlights TM1, the purple box TM2, the yellow box TM3 and the blue box TM4. The following NCBI reference entry codes were used to obtain the sequences used for the alignment: GluD2, NP_001501.2; GluD1, NP_060021.1; GluA1, NP_000818.2; GluA2, NP_001077088.1; GluA3, NP_015564.4; GluA4, NP_000820.3; GluK1, NP_000821.1; GluK2, NP_068775.1; GluK3, NP_000822.2; GluK4, NP_055434.2; GluK5, NP_002079.3.*

In addition to the high sequence similarity of the GluD2 pore-lining TMD M3 helix to other iGluRs (Figure 5.1), another piece of evidence supporting the idea that the GluD2 TMD has inherent biophysical properties to permit ion flux is the existence of the gain of function Lurcher mutant (See Section 1.4.2). The Lurcher mutant mice have a spontaneous Ala654Thr mutation (Zuo et al, 1997) that produces a distinguishing uncoordinated phenotype (Vogel et al, 2007). The molecular result of this mutation is that GluD2 becomes constitutively leaky to cations, indicating that under the appropriate circumstances the GluD2 TMD has the ability to allow ion flow (Zuo et al, 1997).

Furthermore, molecular grafting experiments revealed that the GluD2 TMD can be fully functional when the LBC core is replaced with those of AMPA or Kainate receptors (Schmid et al, 2009). The implication from this is that the puzzling functional aspects of GluD2, relative to other iGluRs, may be owing to different structural features or domain organisation outside of the TMD; however this remains to be investigated.

Moreover, following the observation that the phenotypes of GluD2 null mice can be rescued by the transgenic introduction of a version of GluD2 where the putative channel pore is disrupted, it has been suggested that GluD2 functions in a 'non-ionotropic' mode (Kakegawa et al, 2007). An effective method to provide incontrovertible evidence to support this notion would be obtain crystal structures of GluD2 in different conformations representing alternative states of activation, if this were possible, in an analogous manner to that performed for G protein-coupled receptors (GPCRs) (Chung et al, 2011; Standfuss et al, 2011).

Each iGluR subunit has a modular domain architecture comprising the extracellular ATD and LBC, a TMD and a CTD (Traynelis et al, 2010). The most informative piece of evidence regarding the extracellular domain organisation of iGluRs comes from the crystal structure of a transmembrane construct of the rat GluA2 homotetramer (Sobolevsky et al, 2009). This result indicated a tiered arrangement of the ATD, LBD and TMD as well as a subunit crossover, whereby the individual subunit interactions in each tier are non-equivalent leading to an ecto-domain twist (Mayer, 2011; Sobolevsky et al, 2009). Furthermore in the GluA2 homotetramer crystal structure, two alternative subunit conformations provide an insight into the extent and dynamics of ATD-LBC interactions. However, as a means to reach the 3.6 Å data, some construct engineering was required to yield suitably diffracting crystals; for example, part of this protein engineering involved excising some

amino-acids from the ATD-LBC linker (Sobolevsky et al, 2009), ultimately meaning it is difficult to draw valid conclusions regarding ATD-LBC interactions from this data. Thus it is essential to obtain crystal structures of other iGluR ecto-domains or intact transmembrane constructs, with sequences closer to wild-type, so as to assess the universality of the of the subunit crossover seen in the GluA2 homotetramer as well as to characterise the level of ATD-LBC interactions of the various iGluRs in different states.

The aims of this chapter were ambitious and technically challenging. Since very little structural detail is known about the communication between the ATD and LBD in iGluRs, a primary aim was to use a soluble construct of the GluD2 ecto-domain as a prototypical example to investigate a full-length iGluR ecto-domain. Furthermore, a soluble construct based approach could be used to understand the structural differences between Delta and other iGluRs. Also, an additional aim was to take the initial steps towards crystallography of membrane spanning GluD2, following the notion that until a complete view of the global structural characteristics of the Delta-iGluRs is known, only then will it be possible to explain the anomalies of the Delta-iGluRs, in comparison to other iGluRs, and truly understand their function.

5.3 GluD2 Ecto-Domain Constructs

A construct of the GluD2 ecto-domain was designed using the domain boundaries of the published GluD2 LBC (Naur et al, 2007) as a guide for the s1 s2 boundaries. Since the iGluR LBC is formed from non-contiguous amino acid sequences an oligonucleotide-mediated PCR approach (See Section 2.1.3) was taken (Figure 5.2A). Construct GD13, the GluD2 ecto-domain, is composed of amino acids Asp24-Arg551 plus Ser664-Leu812, joined by a Gly-Thr linker; Appendix 8.1 includes

details regarding the primers and production of this construct. The point mutant constructs described in this chapter were also all created using an oligonucleotide-mediated approach (See Section 2.1.3). Constructs were cloned as described in the appropriate parts of Section 2.1 and Appendix 8.1.

5.4 Expresssion, Purification and Crystallization of the GluD2 Ecto-Domain Construct

Small-scale expression trials in HEK cells (Section 2.3.2) confirmed that the GluD2 Ecto-domain construct was expressed and secreted from mammalian cells (Figure 5.2A). HEK 293T cells were then transfected with construct GD13 in large-scale. The recombinant protein was purified from conditioned media using IMAC (Figure 5.2B) before a deglycosylation trial confirmed that EndoH treatment successfully cleaved N-Linked glycans and did not affect protein solubility (Figure 5.2C). A final round of SEC followed by SDS-PAGE analysis of fractions confirmed that greater than 95 % purity was achieved (Figure 5.2D).

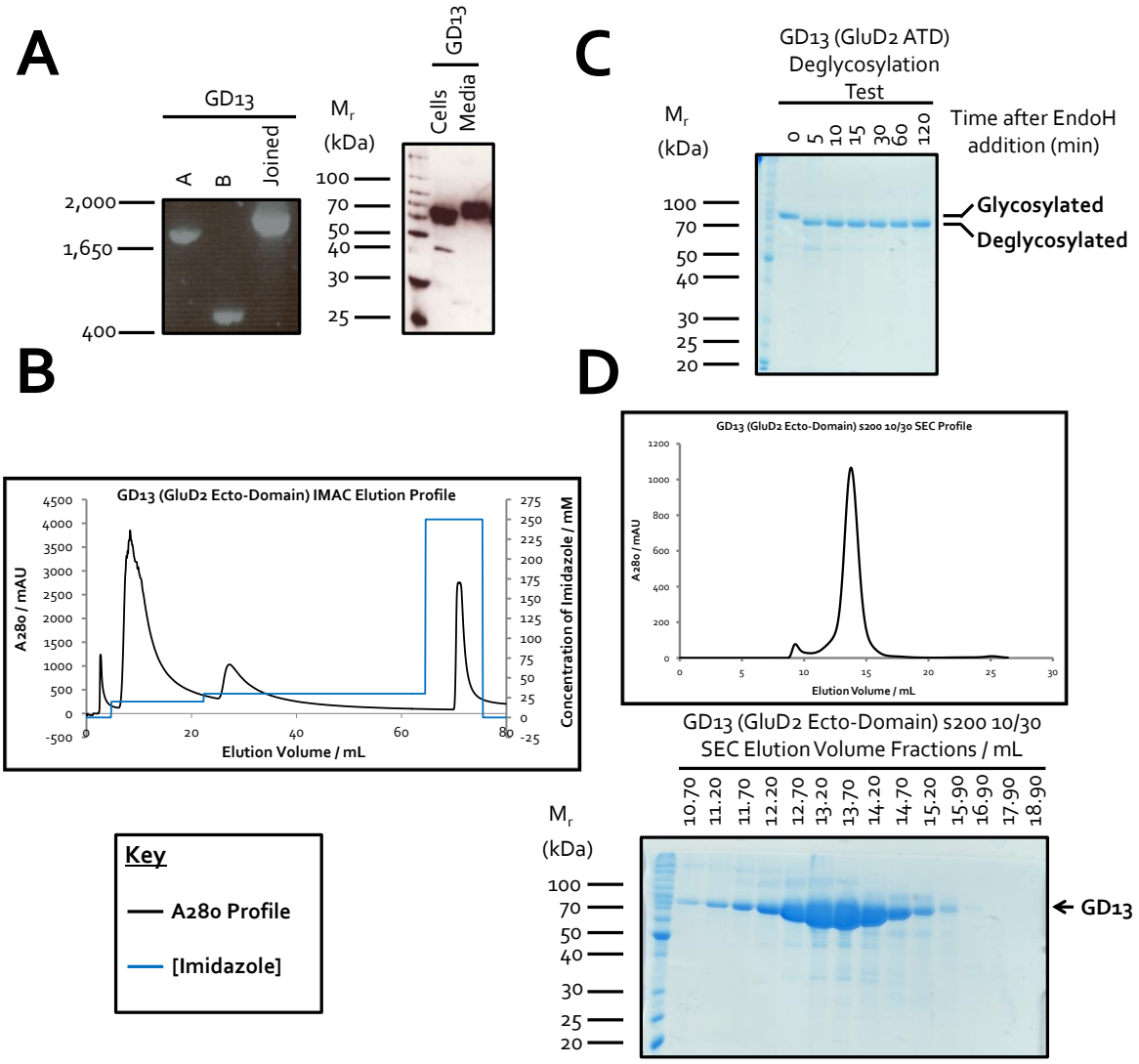

Figure 5.2: Expression and Purification of GluD2 Ecto-Domain. A: Left Image: *1 % agarose gel analysis of PCR products during the cloning of GD13.* ***Right Image:*** *Anti-His tag Western blot analysis of a GluD2 Ecto-Domain construct (GD13) expression trial.* ***B:*** *GD13 (GluD2 Ecto-domain) representative IMAC elution profile monitoring A280 and Imidazole concentration versus elution volume.* ***C:*** *10 % SDS-PAGE analysis of deglycosylation trial of construct GD13.* ***D: Top image*** *– GluD2 Ecto-domain SEC elution profile, monitoring A280 versus elution volume from an s200 10/30 column.* ***Bottom image*** *– 10 % SDS-PAGE analysis of construct GD13 SEC fractions.*

Sitting-drop vapour diffusion crystallization trials were initiated using GD13 purified protein at 5 mg/mL. The GluD2 ecto-domain construct crystallized in numerous conditions. Crystals were screened for diffraction quality using synchrotron source X-rays, however crystal diffraction was

generally to quite low resolution, i.e. between 9-10 Å. A crystal which grew in a reservoir condition containing 0.88 M MES (pH 6.0), 0.7 M ammonium sulphate, with a drop ratio of 2:1 protein:reservoir (Figure 5.3A), diffracted to better than 8 Å at the I03 beamline, Diamond Light Source (Figure 5.3B).

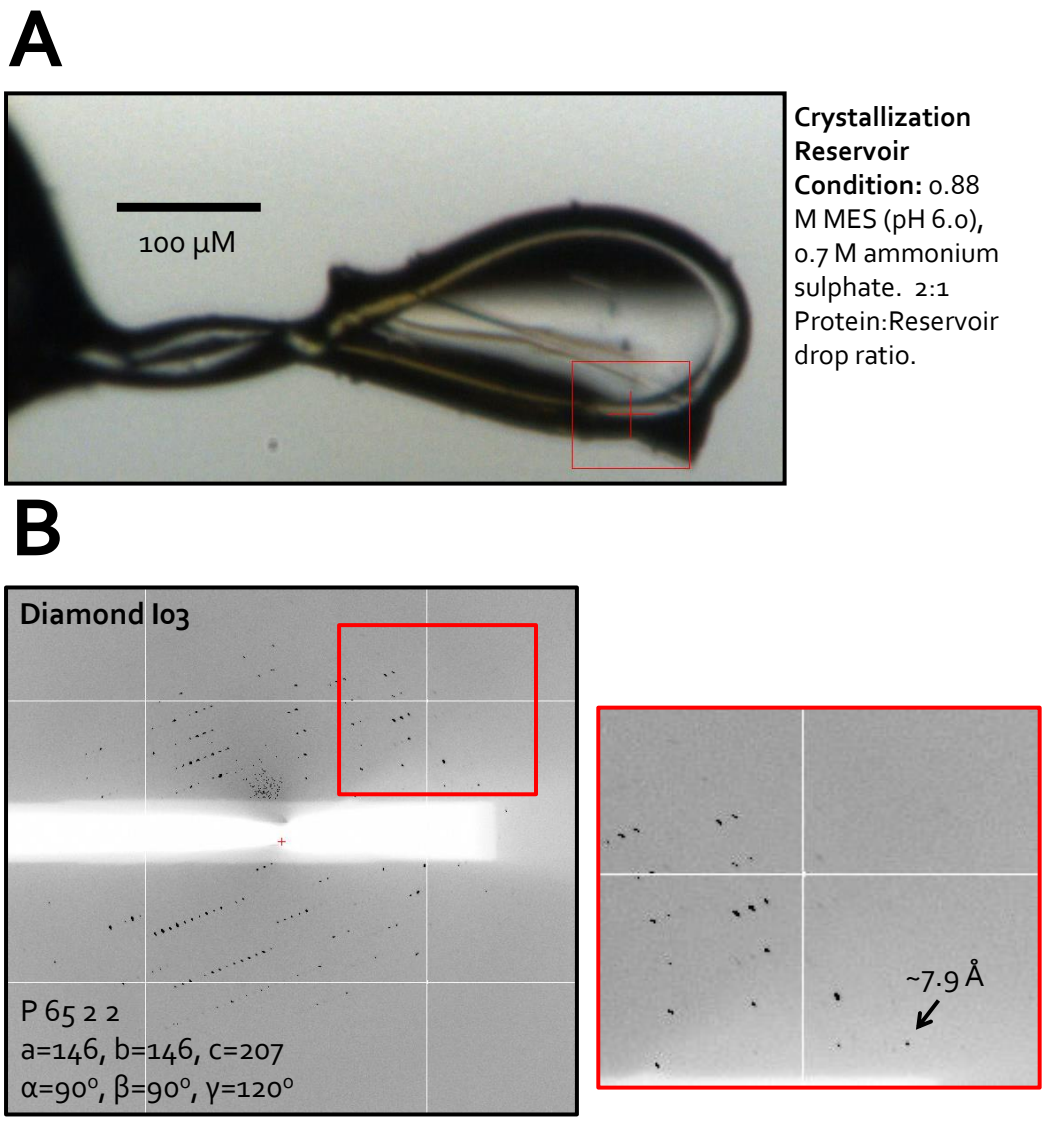

Figure 5.3: Crystallization and Diffraction Experiments of GluD2 Ecto-domain. ***A:*** *An image displaying a mounted GluD2 ecto-domain construct (GD13) crystal that grew in the condition 0.88 M MES (pH 6.0), 0.7 M ammounium sulphate in a 2:1 protein:reservoir drop ratio.* ***B:*** *An image displaying the diffraction pattern obtained from the crystal displayed in* ***A****. Reflections were observable to better than 8 Å at Diamond I03, Oxfordshire. The diffraction images were indexed to space group P* 6_5 *2 2 with unit cell dimensions of a = b = 146 Å, c = 207 Å,* $\alpha = \beta = 90^{o}$, $\gamma = 120^{o}$.

5.5 Methylation and Crystal Optimization of the GluD2 Ecto-Domain

Protein methylation was attempted as a strategy for optimizing GD13 crystals that diffracted to low resolution. Methylation was performed as described in Section 2.5.3; following this, methylated protein was re-purified by SEC (Figure 5.4A) and sitting-drop vapour diffusion crystallization trials were set-up at 4.2 mg/mL. Methylated GD13 crystallized in numerous conditions. After optimization, crystals that grew in the reservoir condition containing 0.1 M citric acid (pH 5.0), 5 % (w/v) polyethylene glycol 6000, 6 % (w/v) D-Galactose (Figure 5.4B) diffracted with observable reflections to ~4 Å (Figure 5.4C) at beamline I04-1, Diamond Light Source. A complete diffraction data-set was measured for this crystal obtained from methylated protein and the processing of this data is discussed in Section 5.6. Data collection statistics are detailed in Table5.1.

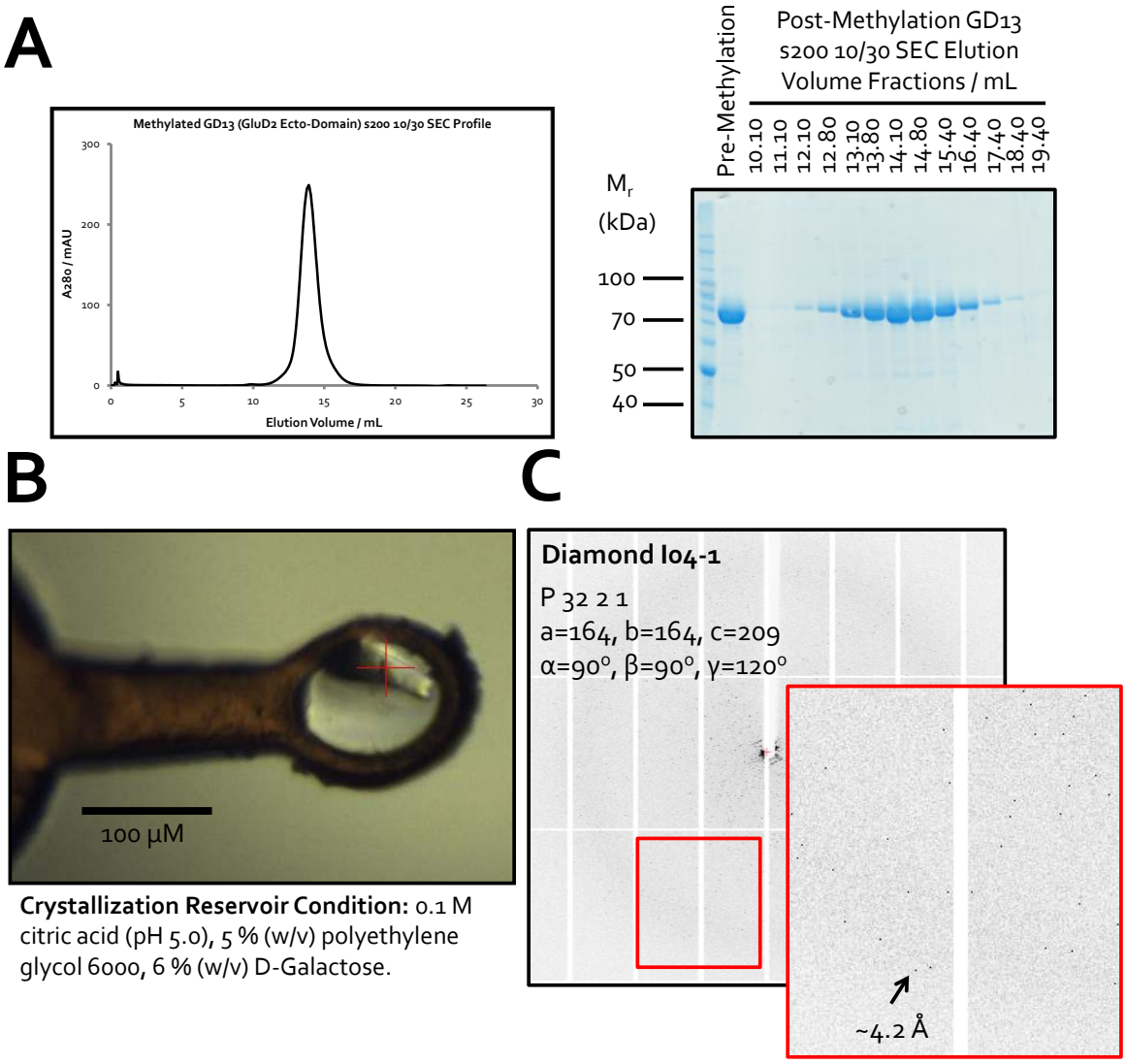

Crystallization Reservoir Condition: 0.1 M citric acid (pH 5.0), 5 % (w/v) polyethylene glycol 6000, 6 % (w/v) D-Galactose.

Figure 5.4: Methylation of GluD2 Ecto-Domain and Crystallization and Diffraction Experiments of Methylated GD13. A: Left image: *SEC profile of GD13 post-methylation, monitoring A280 versus elution volume from an s200 10/30 column.* ***Right image:*** *SDS-PAGE analysis of elution fractions from post-methylation SEC.* ***B:*** *An image displaying a mounted crystal of methylated GluD2 ecto-domain construct GD13. The crystal grew in the condition 0.1 M citric acid (pH 5.0), 5 % (w/v) polyethylene glycol 6000, 6 % (w/v) D-galactose with a 1:1 protein:reservoir drop ratio.* ***C:*** *An image displaying the diffraction pattern obtained from the crystal displayed in* ***B****. Reflections were observable to ~4 Å at beamline I04-1, Diamond Light Source. The diffraction images were indexed to space group P 3_2 2 1 with unit cell dimensions of a = b = 164 Å, c = 209 Å, α = β = 90°, γ = 120°.*

DATA COLLECTION		
Beamline	I04-1	
Resolution	142.2-4.1 (4.2-4.1)	
Space group	P 3_2 2 1	
Cell dimensions	[Å]	[°]
	a = 164.2 b = 164.2 c = 208.8	α = 90 β = 90 γ = 120
Wavelength [Å]	0.91730	
Unique reflections	26021 (1879)	
Completeness [%]	99.8 (99.8)	
R_{merge} [%][a]	25.3 (91.4)	
I/σI	9.3 (2.7)	
Redundancy	11.0 (11.0)	

Table 5.1: Methylated GluD2 Ecto-Domain Data Collection Statistics. *A table listing the data collection statistics for diffraction data collected from methylated GluD2 ecto-domain crystals.* Numbers in parentheses refer to the appropriate outer shell.

[a] $R_{merge} = \Sigma_{hkl} \Sigma_i |I(hkl;i) - \langle I(hkl) \rangle| / \Sigma_{hkl} \Sigma_i I(hkl;i)$, where $I(hkl;i)$ is the intensity of an individual measurement and $\langle I(hkl) \rangle$ is the average intensity from multiple observations.

5.6 Structure Determination and Features of the GluD2 Ecto-Domain

Molecular replacement using Phaser (McCoy et al, 2007) and the following search probes, GluD2 ATD (Chapter 3) and GluD2 LBC (2V3T, (Naur et al, 2007)), was attempted to phase the data-set collected from the methylated GluD2 ecto-domain crystal shown in Figure 5.4B. Sequential rounds of molecular replacement for the methylated GluD2 ecto-domain were attempted, as detailed in Table 5.2; in each sequential molecular replacement cycle the solution from the previous round was fixed, and then the additional domains were searched for. Statistics from each round of molecular

replacement are also detailed in Table 5.2. The first four rounds of molecular replacement were successful (Table 5.2), after two GluD2 ATDs and two GluD2 LBCs were placed in electron density. However initial inspection of the maps after round four revealed a significant amount of electron density which was unaccounted for (Figure 5.5). Subsequent rounds of molecular replacement, where both a GluD2 ATD monomer and GluD2 LBC monomer were used as search probes, were not successful (Table 5.2). Hence the additional electron density could not be accounted for, despite exhaustive attempts at data processing and molecular replacement, and thus it was reasoned this was a result of a crystal defect.

Round	Search Probe	Source of Search Probe	Translation function *Z*-scores	Log-likelihood gain
1	GluD2 ATD Monomer	Chapter 3	8.6	432
2	GluD2 ATD Monomer	Chapter 3	17.9	1532
3	GluD2 LBC Monomer	PDB code: 2V3T (Naur et al, 2007)	6.0	1557
4	GluD2 LBC Monomer	PDB code: 2V3T (Naur et al, 2007)	10.0	1901
5	GluD2 LBC Monomer	PDB code: 2V3T (Naur et al, 2007)	No Solution	No Solution
6	GluD2 ATD Monomer	Chapter 3	No Solution	No Solution

Table 5.2: GluD2 Ecto-Domain Molecular Replacement. *Phaser-derived (McCoy et al, 2007) statistics for sequential rounds of molecular replacement for the methylated GluD2 ecto-domain data-set.*

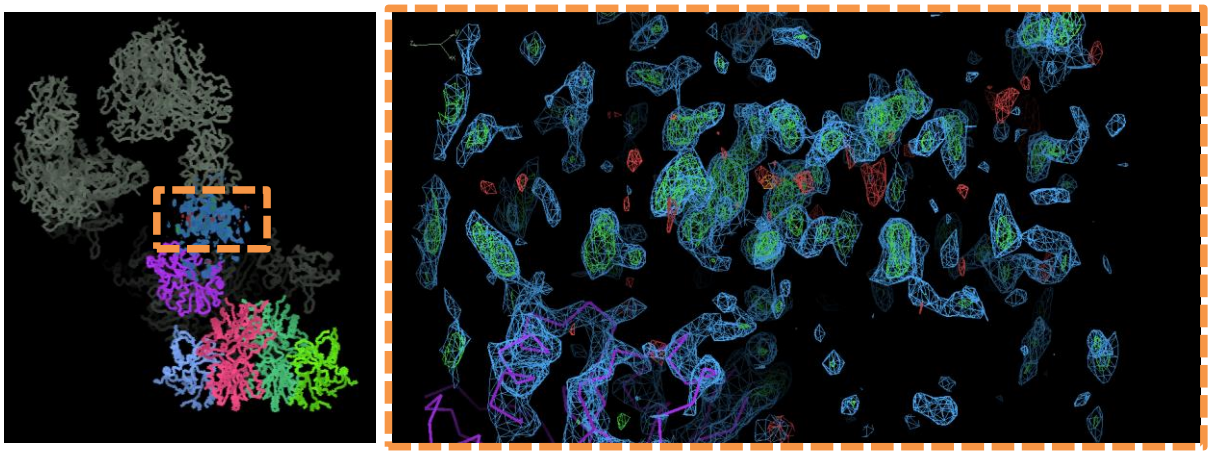

Figure 5.5: GluD2 Ecto-Domain Molecular Replacement Solution Unaccounted Electron Density. *2Fo-Fc and Fo-Fc electron density maps contoured at 1σ displaying the molecular replacement solution after molecular replacement round 4 (Table 5.2) for the GluD2 ecto-domain. Unaccounted for electron density is highlighted in the yellow box.*

Using the molecular replacement from round four it is possible to build a rigid body refined model for the domain organisation of the GluD2 ecto-domain construct (Figure 5.6A-B), R_{factor} 29.6 %, R_{free} 33.3 %. In this model there is an unexpected relative arrangement of the domains. The ATD interface is similar to that observed in the crystal structure of GluD2 ATD (Chapter 3). However the orientation of the LBCs in the GluD2 ecto-domain model is dissimilar to the crystal structure of the dimeric GluD2 LBC (2V3T (Naur et al, 2007); in the GluD2 ecto-domain model there is no LBC-LBC interface analogous to that seen in 2V3T or the full-length GluA2 homotetramer (Sobolevsky et al, 2009). This is a result of a perceived 'flipping-out' of the LBCs which may be caused by a lack of TMD tethering, allowing free movement of the flexible ATD-LBC linker (Figure 5.6A-B). To investigate the flexibility of this linker, a sample of the GluD2 ecto-domain was sent to collaborators in the laboratory of Dr. Terunaga Nakagawa (University of California, San Diego), where it was analysed using single-particle negative stain electron microscopy; class averages are displayed in Figure 5.6C. The class averages clearly demonstrate the LBCs have multiple conformations relative to the rigid ATDs, suggesting the ATD-LBC linker possesses inherent structural flexibility (Figure

5.6C). Hence the implication is that the proposed model for the GluD2 ecto-domain is likely to be an artefact, either of construct design or of crystallization. It could be that due to the low affinity (K_d ~6,000 μM) of the iGluR LBC dimer (Sun et al, 2002) relative to the iGluR ATD (K_d ~4.3 μM) dimer (Clayton et al, 2009), that during crystallization an energetically more favourable but physiologically irrelevant conformation was adopted.

Despite the model for the GluD2 ecto-domain being only partly refined, there is evidence to believe that it is a correct solution. Firstly, the same relative domain arrangement was observed in the molecular replacement solution obtained using the lower resolution diffraction data produced by the non-methylated GluD2 ecto-domain crystals presented in Figure 5.3 (Data not shown). Secondly, weak unbiased electron density for the linker can be observed in the electron density map when contoured at 0.4σ (Figure 5.6D). Thirdly, the C-terminus of the ATD and the N-terminus of the LBC are within ~26.6 Å which could be reasonably bridged by the 12 amino acids which are absent from the sequence in this model.

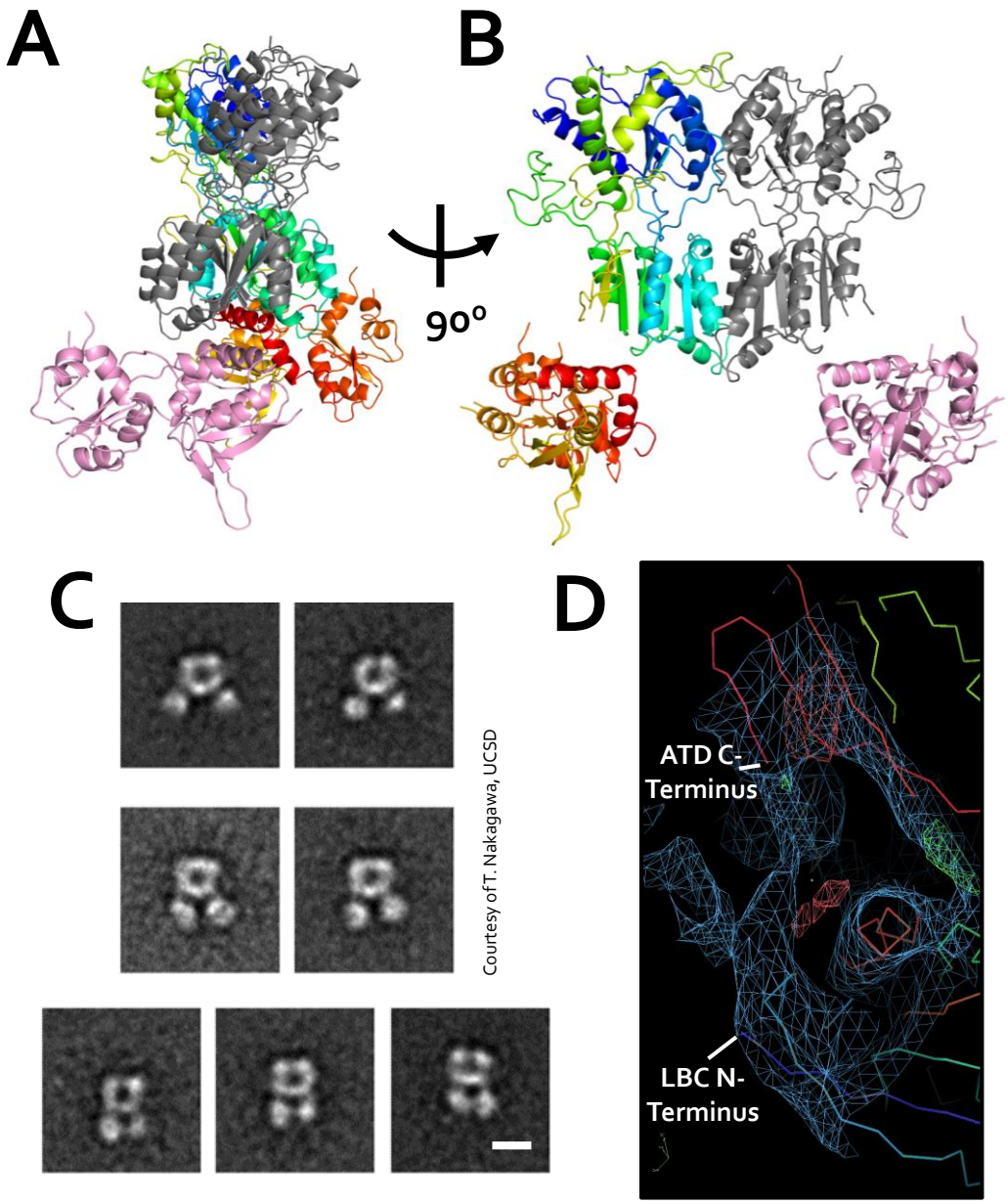

Figure 5.6: A Model of the GluD2 Ecto-Domain. A-B: *cartoon structural representation of the proposed model of the GluD2 ecto-domain implied from molecular replacement of data collected from crystals formed from methylated GluD2 ecto-domain recombinant protein (Figure 5.4). One chain is coloured as a chainbow, from blue at the N-terminus to red at the C-terminus. A second chain is coloured to highlight the two different domains, grey is the ATD and pink the LBC.* ***C:*** *Single-particle negative stain EM class averages of the GluD2 ecto-domain recombinant protein. EM analysis was performed by collaborators in the laboratory of Dr. Terunaga Nakagawa, University of California, San Diego, on samples that were prepared by myself. The scale-bar represents ~75 Å.* ***D:*** *2Fo-Fc and Fo-Fc electron density maps contoured at 0.4σ highlighting the ATD-LBC linker. The C-terminus of the ATD and N-terminus of the LBC are labelled.*

5.7 Assessing the Likelihood of Subunit Crossover in the GluD2 Ecto-Domain

When comparing the domain organisation of the GluD2 ecto-domain construct presented in Section 5.6, with the ecto-domain of the intact transmembrane rat GluA2 homotetramer (Sobolevsky et al, 2009)(See Section 1.3.3) there are clear differences: i) The oligomeric state: the GluD2 ecto-domain construct crystal structure appears arranged as a dimer, whereas the nearly full-length GluA2 crystal structure is tetrameric; ii) Subunit crossover resulting in an ecto-domain twist which is apparent in the transmembrane rat GluA2 crystal structure but not in the GluD2 ecto-domain construct. These differences may be a result of crystal packing, or could be due to features of the artificial ecto-domain construct, i.e. a lack of the TMD. Equally the differences could be due to inherent structural variances between GluA2 and GluD2. To test the likelihood of an ecto-domain twist in GluD2, attempts were made to engineer tetramerization in the GluD2 ecto-domain construct, with the hypothesis being that if one of these methods did result in an altered oligomeric state then it provided support to the suggestion of subunit crossover in GluD2.

Two strategies were employed to induce tetramerization: point mutation and fusion to a protein partner. In the first strategy, point mutation, the published structure of the GluD2 LBC (2V3T) (Naur et al, 2007) was used to pin-point residues in the LBC interface that could be mutated to cysteine to introduce disulphide bonds that would lock together to LBCs at their interface with the intention of mediating tetramerization, based on the assumption that GluD2 has the same subunit arrangement and ecto-domain twist as the GluA2 model (Sobolevsky et al, 2009). The LBC interface residues that were targeted for mutation are illustrated in Figure 5.7. GluD2 T538 was targeted for mutation to cysteine as a distance of 6.4 Å was measured between the Cα's of equivalent amino acids in the partner LBCs. Also, E790 and P528 comprised a second set of targets for mutation to cysteine as a

distance of 5.7 Å was measured between the Cα of a glutamate residue of one chain and the Cα of a proline residue of the partner chain. This double mutation would putatively lead to two disulphide bonds being introduced. In the second strategy, use of a fusion partner, the GluD2 ecto-domain was fused to the hinge and Fc region of an IgGγ1 antibody using the pHLsec Fc vector (Aricescu et al, 2006). The Fc and hinge of an Ig antibody is dimeric and thus it was thought that in combination with the high affinity ATD dimer that this format may allow the necessary balance between restraint and flexibility to produce tetramerization.

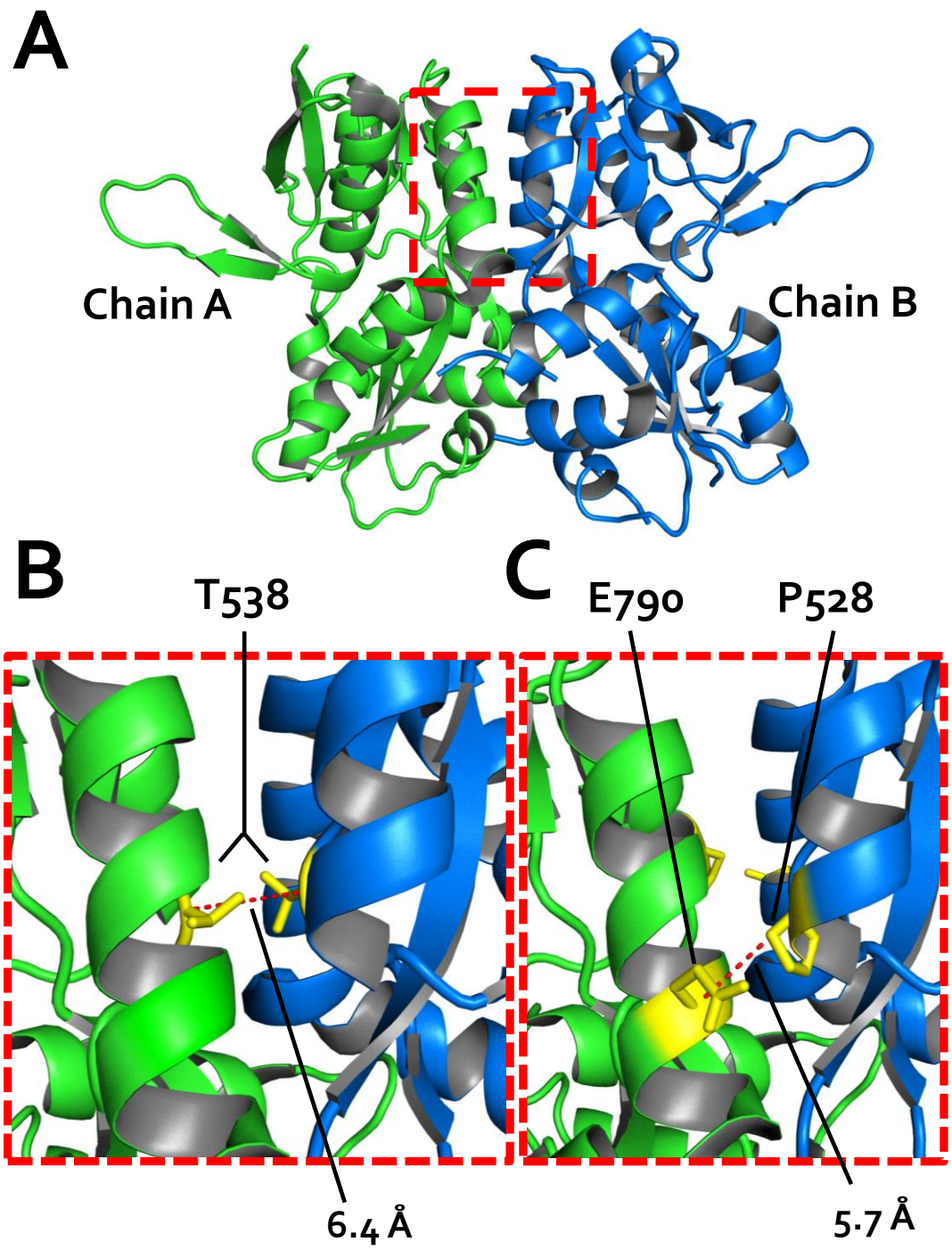

Figure 5.7: GluD2 LBC interface mutations. A: *Cartoon representation of the GluD2 LBC crystal structure (2V3T) (Naur et al, 2007), chain A is depicted in green and chain B is represented in blue.* ***B:*** *Close-up view of GluD2 T538, one of the targets for mutation to cysteine in an attempt to induce tetramerization. Relevant amino acids are labelled as is the bond distance.* ***C:*** *Close-up view of GluD2 P528 and E790, a second pair of targets for mutation to cysteine and induction of tetramerization. Relevant amino acids are labelled as is the bond distance.*

The cysteine point mutations were introduced into the GluD2 ecto-domain construct using oligonucleotide-mediated mutagenesis, further details in Section 2.1.3 and Appendix 8.1. Specifics of the production of GluD2 ecto-domain Fc construct are also contained in Appendix 8.1. Expression constructs were tested in small-scale expression trials (Section 2.3.2) and all were found to be expressed and secreted from transiently transfected mammalian cells (Figure 5.8A). These modified ecto-domain constructs were all then transfected in HEK 293T cells in large-scale (Section 2.3.3) and purified in an analogous manner to GD13 (See Section 5.4). All modified ecto-domain constructs were purified to monodispersity and greater than ~95 % purity (Figure 5.8B-D).

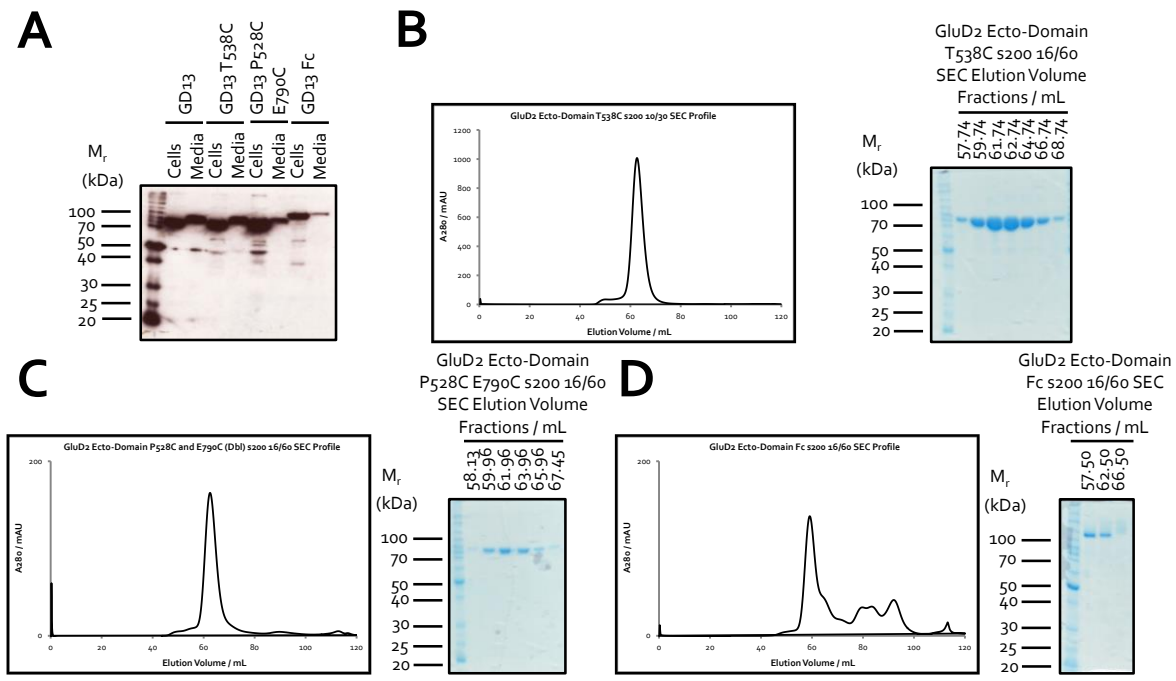

Figure 5.8: Expression and Purification of GluD2 Modified Ecto-Domain constructs. ***A:*** *Anti-His tag Western blot analysis of modified GluD2 Ecto-Domain constructs expression trial.* ***B: Left image*** *– GluD2 Ecto-domain T538C SEC elution profile, monitoring A280 versus elution volume from a superdex 200 10/30 column.* ***Right image*** *– SDS-PAGE analysis of GD13 T538C SEC fractions.* ***C: Left image*** *– GluD2 Ecto-domain P528C E790C SEC elution profile, monitoring A280 versus elution volume from a superdex 200 10/30 column.* ***Right image*** *– SDS-PAGE analysis of GD13 P528C E790C SEC fractions.* ***C: Left image*** *– GluD2 Ecto-domain GD13 Fc SEC elution profile, monitoring A280 versus elution volume from a superdex 200 10/30 column.* ***Right image*** *– SDS-PAGE analysis of GD13 Fc SEC fractions.*

MALS (Section 2.8) was used as a tool for analysing the oligomeric state of the modified ecto-domain recombinant protein samples. As an index for comparison, the oligomeric state of the original GluD2 ecto-domain construct, GD13, was determined; the indication from the crystal structure of GD13 was that this protein construct was dimeric and this was corroborated by MALS analysis (Figure 5.9A-B). When analysing the modified ecto-domain constructs, the hypothesis was that if one of the strategies, particularly LBC-interface point mutation, induced tetramerization this would provide evidence for subunit crossover in the GluD2 ecto-domain in an equivalent manner to GluA2.

The first mutant tested was GD13 T538C which MALS analysis showed to be dimeric (Figure 5.9A-B). Examination of GD13 T538C by western blot under reducing and non-reducing conditions suggested that despite the introduction of a cysteine at the LBC interface, no inter-subunit disulphide bond formation was apparent, as indicated by the lack of gel shift for this sample in Figure 5.9C. Perhaps the ~6.4 Å distance between the equivalent residue in each subunit, T538 (Figure 5.7B) was too great and steric clashes may have prevented disulphide bond formation.

A second mutant, GD13 P528C E790C was also found to exist as a dimer using MALS analysis (Figure 5.9A-B). However, analysis of this sample by western blot under reducing and non-reducing conditions clearly demonstrated the successful introduction of inter-subunit disulphide bonds as a result of the double cysteine mutation, signified by the band shift of the reduced sample relative to the non-reduced equivalent (Figure 5.9C). The evidence for successful tethering of the LBC interface in combination with the dimeric state of the GD13 P528C E790C mutant supports a null hypothesis regarding GluD2 ecto-domain subunit crossover.

Further evidence against an ecto-domain twist in GluD2 comes from the GD13 Fc construct. Analysis of this construct by western blot in the presence and absence of reducing agent indicated the existence of inter-chain disulphide bonds (Figure 5.9C); this would be expected since the antibody hinge region, which is encoded in the pHLsec Fc vector, contains two inter-subunit disulphide bonds (Janeway et al, 2001). Despite the introduction of inter-chain tethering disulphide bonds, investigation of the oligomeric state of GD13 Fc using MALS revealed a dimeric organisation (Figure 5.9A-B).

A

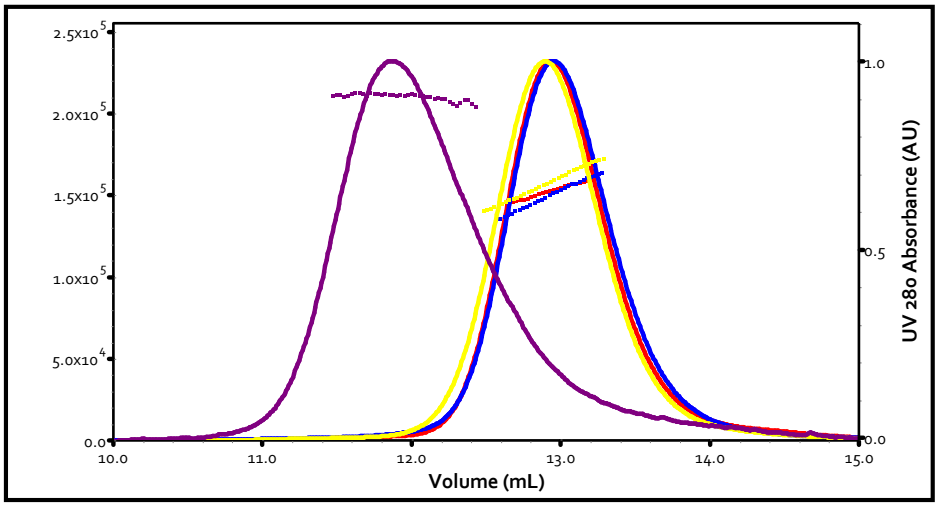

Key

GD13 — GD13 T538C — GD13 P528C E790C — GD13 Fc

B

Sample	Measured Molar Mass (kDa)	Molecular Weight of a Single Subunit (kDa)	Measured Molar Mass/Single Subunit Molecular Weight	Oligomeric State of Sample
GD13	153.5	78.2	1.96	Dimer
GD13 T538C	151.5	78.2	1.94	Dimer
GD13 P528C E790C	156.2	78.2	2.00	Dimer
GD13 Fc	210.4	104.8	2.01	Dimer

C

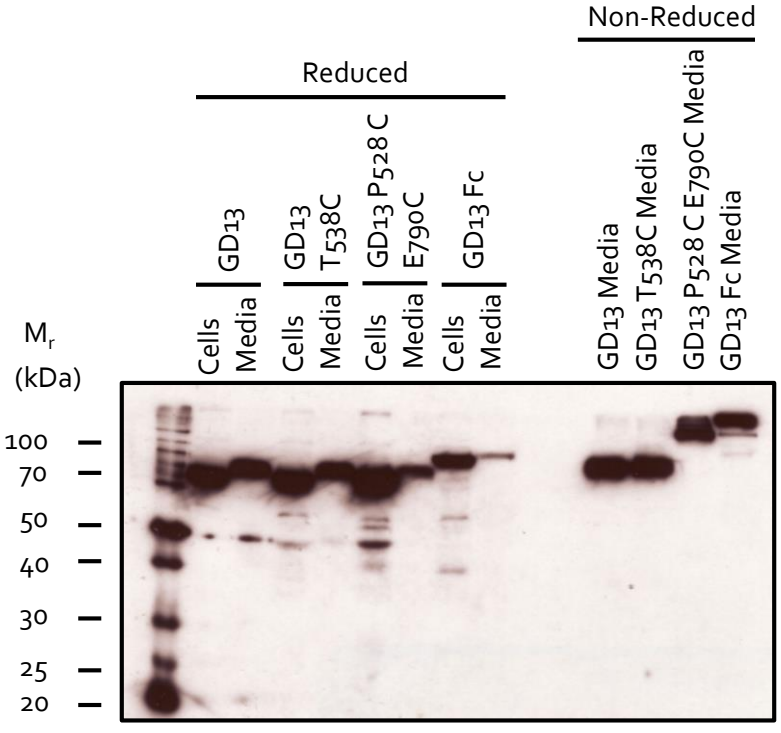

Figure 5.9: Analysis of the GluD2 Modified Ecto-Domain Constructs. A: *MALS profile displaying measured molecular mass and A280 versus elution volume. The GD13 construct profile is displayed in red, GD13 T538C is in blue, GD13 P528C E790C in yellow and GD13 Fc in purple.* ***B:*** *A table listing the measured molecular mass, determined using MALS, and calculations of sample oligoeric states.* ***C:*** *An anti-His western blot examining small-scale transfected GluD2 modified ecto-domain samples, analysed under reducing and non-reducing conditions.*

Hence, taken together this provides evidence against subunit crossover in the GluD2 ecto-domain, in the absence of the TMD, as the data in the Figure 5.9 points to the formation of a symmetric dimer (Figure 5.10A). Since native GluD2 is a tetramer (Section 4.5, Figure 4.4), two models for the relative domain arrangement of GluD2 ATD and LBCs can be proposed based on this (Figure 5.10). In both the square and oblong models (Figure 5.10B-C) the ATD and LBC of one subunit interact with the equivalent domain from the same partner subunit, forming a symmetric dimer (Figure 5.10A). Tetramerization is then mediated by alternative modes, by symmetric contacts in the square model (Figure 5.10B) and asymmetric interactions in the oblong model (Figure 5.10C). Such dissimilarity between the arrangement of subunits in the GluA2 crystal structure and the models proposed here for GluD2 could provide a molecular explanation for the discrepancies between the GluD2 and the other members of the iGluR superfamily, discussed in Section 5.2. However an argument against such models would be that they are based on experiments using an artificial ecto-domain construct where the LBC s1 and s2 are joined by a short GT linker, rather than the TMD, which may impose non-natural restraints upon the molecule, consequently raising doubt about the physiological relevance of the ecto-domain construct. The premier method of providing irrefutable evidence regarding the structural characteristics of the GluD2 ecto-domain would be through a high resolution crystal structure, thus steps were taken to initiate a crystallography project targeting an intact transmembrane construct of GluD2 (Section 5.8-5.9).

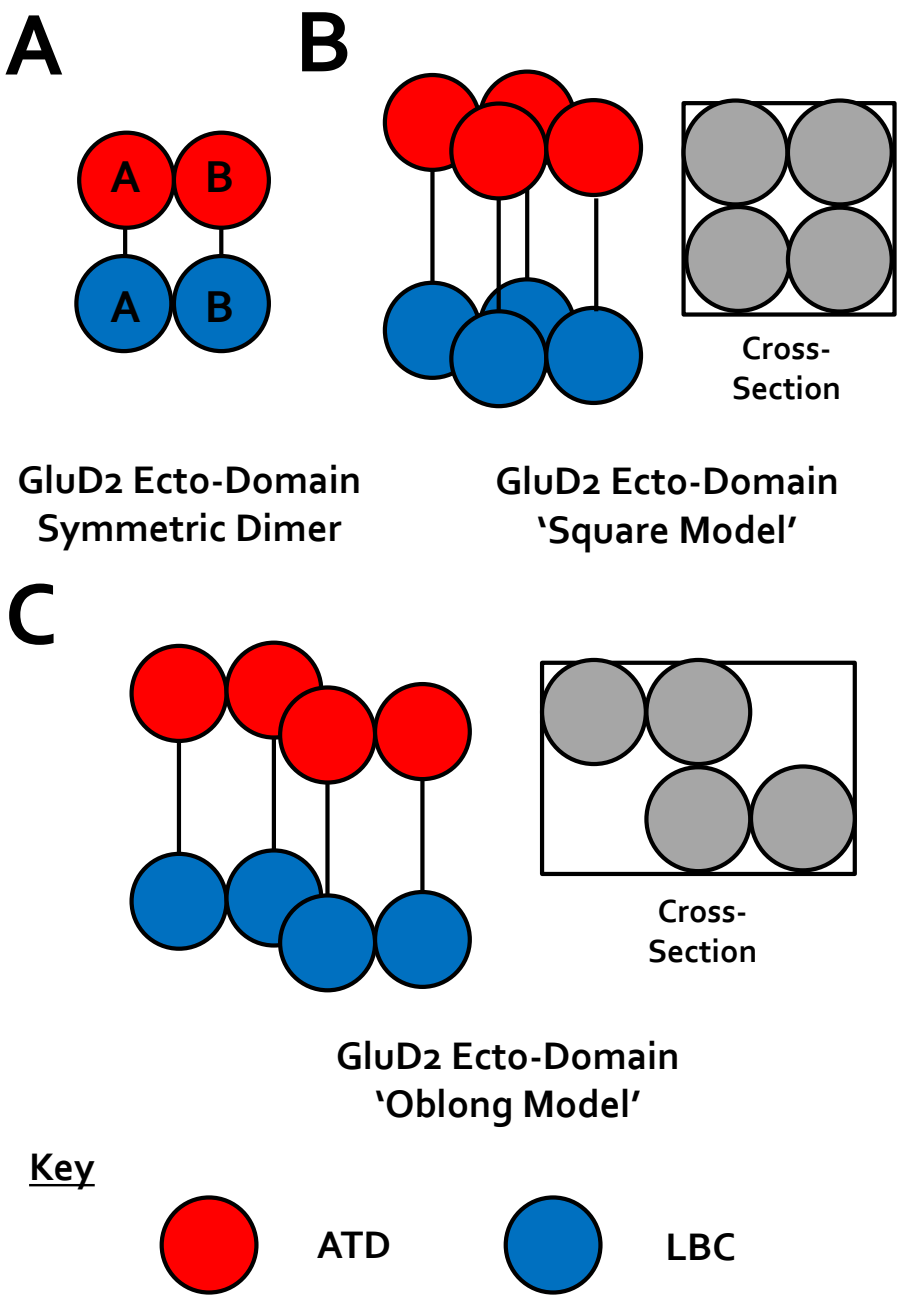

Figure 5.10: Models for the GluD2 Ecto-Domain. ***A:*** *Schematic representation of the GluD2 symmetric dimer ecto-domain model proposed as a result of oligomeric analysis of tethered ecto-domain constructs, showing that the ATD and LBC of one chain, A, both interact with the equivalent domain of a second chain B .* ***B:*** *'Square Model' of the GluD2 ecto-domain where the symmetric dimer in* ***A*** *is developed to a tetramer via symmetric interactions between two symmetric dimers.* ***C:*** *'Oblong Model' of the GluD2 ecto-domain where a tetramer is formed by asymmetric interactions between two symmetric dimers.*

5.8 Screening of Membrane Spanning GluD2 Constructs

Crystallographic study of membrane bound proteins requires their extraction from cellular membranes in a soluble, stable form. Due to the hydrophobic nature of the membrane interacting segments of the protein it is necessary to use amphipathic molecules such as detergents to maintain their solubility. However, some detergents can hamper the stability of the protein molecules and can disrupt their native oligomeric state and thus it is necessary to test several detergents for their ability to both extract and conserve the form of the target protein. Furthermore, an approach that enhances the probability of crystallization is to engineer a target protein so that any unstructured parts of a polypeptide chain are removed since flexible sections of amino acids are likely to block crystal lattice formation. As a result of this, three transmembrane constructs of GluD2 were designed and produced: GD28 comprised full-length GluD2 E24-I1007 with and N-terminal HA tag and a C-terminal mVenus tag, GD30 covered amino acids E24-E867 with a C-terminal mVenus tag, and GD35 encoded E24-E867 with an N-terminal HA tag and a C-terminal mVenus tag. Thus GD30 and GD35 did not include 140 amino acids of the mainly unstructured C-terminal tail of GluD2, and were deemed to be more likely to crystallize. These constructs were produced as described in Section 2.1 and Appendix 8.1.

Initially a FACS based approach (Section 2.10) was used to test the total expression, targeting a intracellular mVenus tag, and cell surface trafficking, utilizing an extracellular N-terminal HA tag, of these TM constructs. An N-terminally tagged construct of GluA2 and a C-terminally tagged construct of CD45 (both created by Amber Clayton, STRUBI) were included for FACS analysis as positive and negative controls when different fluorescence emission wavelengths were measured. Both GD28 and GD35 were found to be expressed and present at the cell surface at equivalent levels and comparable to positive controls (Figure 5.11A). Furthermore construct GD30 was found to be expressed (Figure 5.11A) and since this construct did not have a HA tag cell surface trafficking could

not be tested. However since GD30 and GD35 had the same N- and C-terminal boundaries, and GD35 was found to traffic to the cell surface, it was assumed that GD30 would have the same trafficking properties.

Following this, FSEC (Section 2.4.5) was used to investigate the ability of various detergents to extract GD28 and GD30, from cell membranes, and maintain their native oligomeric state. Figure 5.11B depicts the FSEC profile of a selection of detergent extractions of GD30. There is a prominent triplet of peaks in the FSEC profile which were rationalized into three groups: the DDM and CHAPS group representing a GluD2 tetramer, the TX100 and DM group denoting a GluD2 dimer and the FC12 peak representing a GluD2 monomer. Nevertheless, it is often difficult to define the oligomeric state of a protein using FSEC in the presence of a detergent as it can be challenging to estimate the size of the detergent micelle around the membrane protein and this can vary from one detergent to another. However it is clear from Figure 5.11B that a number of detergents were successful in solubilizing GD30 subunits and a number of candidates were available for testing in larger-scale.

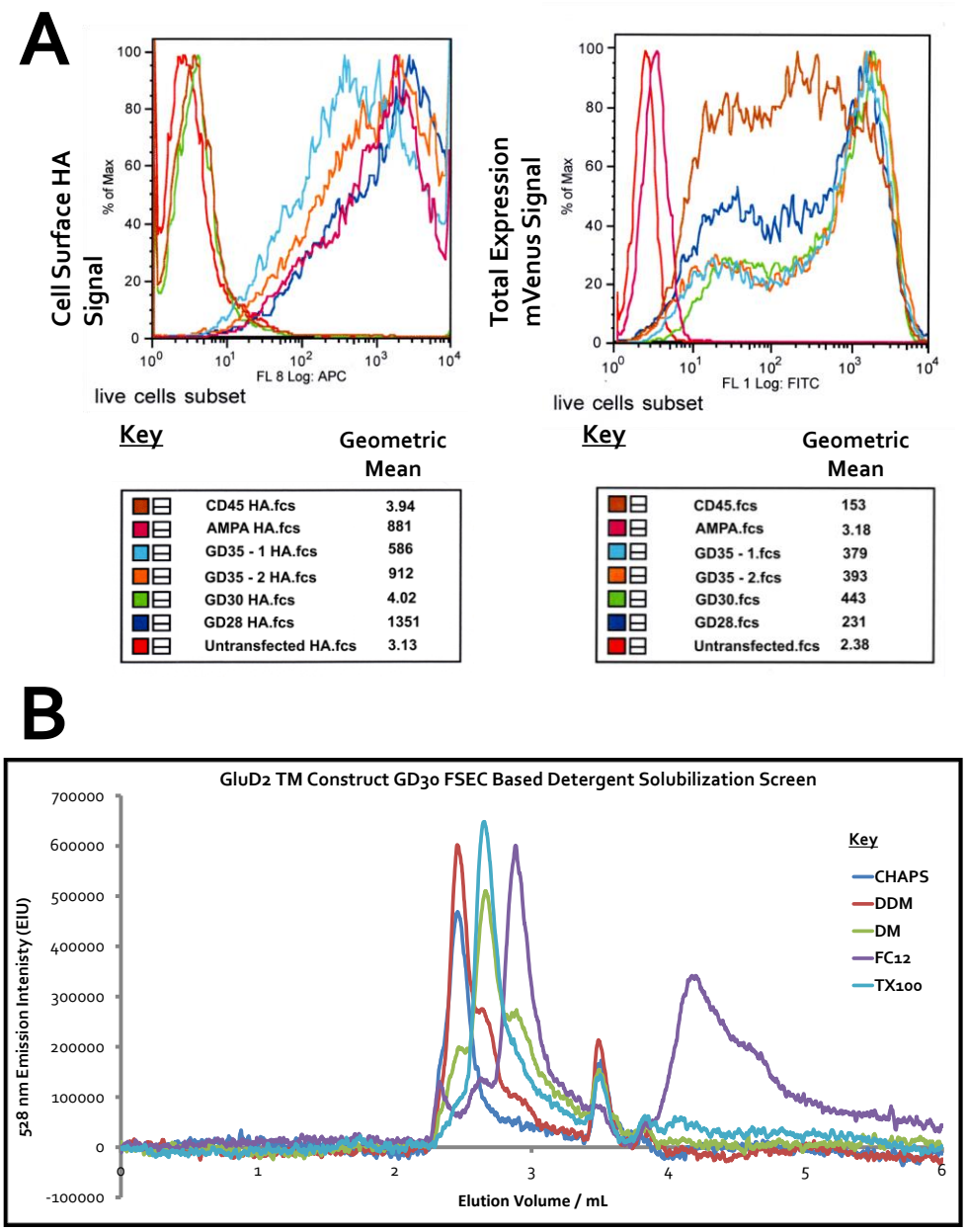

Figure 5.11: Plasma Membrane Trafficking and Solubilisation Assays of GluD2 Transmembrane Constructs. ***A:*** *Population charts displaying fluorescence data for the 30,000 cells counted and sorted using FACS. The geometric mean for the fluorescence data was calculated for each cell count and is displayed in the key.* ***Left Image:*** *Fluorescence charts measured from cells fixed and probed with an Anti-HA antibody targeted against cell surface recombinantly expressed proteins.* ***Right Image:*** *Fluoresence data from intracellular mVenus tags engineered onto the C-terminus of recombinantly expressed proteins.* ***B:*** *FSEC profiles following the solubilisation of an C-terminally tagged mVenus transmembrane construct of GluD2. The detergents used for solubilisation are listed and the profile monitors 528 nm emission spectrum versus elution volume.*

5.9 IAC Purification of Transmembrane GluD2: A Step Towards Membrane Protein Crystallography

After proving that extraction of GD30 was both possible and successful in small-scale using fluorescence based techniques, a new construct was created based on GD30, i.e. covering amino acids E24-E867 of GluD2, but with a 1D4 tag to allow immuno-affinity chromatography (Wong et al, 2009). This DNA construct was termed GD31; further details about the construct are in Appendix 8.3. HEK293T, cultured in 12 roller bottles, were then transfected with GD31 expression construct (Section 2.3.3) and following a ~72 hour, 37 ^{o}C incubation period the transfected cells were harvested, solubilized and the lysate subjected to IAC purification as described in Section 2.4.6. DDM was chosen as the detergent used for solubilisation of GD31 as FSEC demonstrated that this detergent successfully solubilized GluD2 (Figure 5.11), and DDM was used for the crystal structure of the GluA2 homotetramer (Sobolevsky et al, 2009). SDS-PAGE and western blot analysis of IAC elution fractions revealed that the target protein was purified to high levels (Figure 5.12A-B) though the yield was quite low, i.e. barely detectable by Coomassie stained SDS-PAGE (Figure 5.12A). Furthermore, western blot examination of the IAC beads, after the final elution was performed revealed that a significant amount of target protein remained bound to the beads (Figure 5.12B). This could be a result of denatured target protein aggregating on the beads or it could be due to a sub-optimal elution strategy. Hence, further work must be undertaken to improve the yield of an intact membrane-bound GluD2 construct to allow the complete structural characterisation of this molecule; this approach is undoubtedly the next logical step in trying to understand the intricacies of this enigmatic receptor.

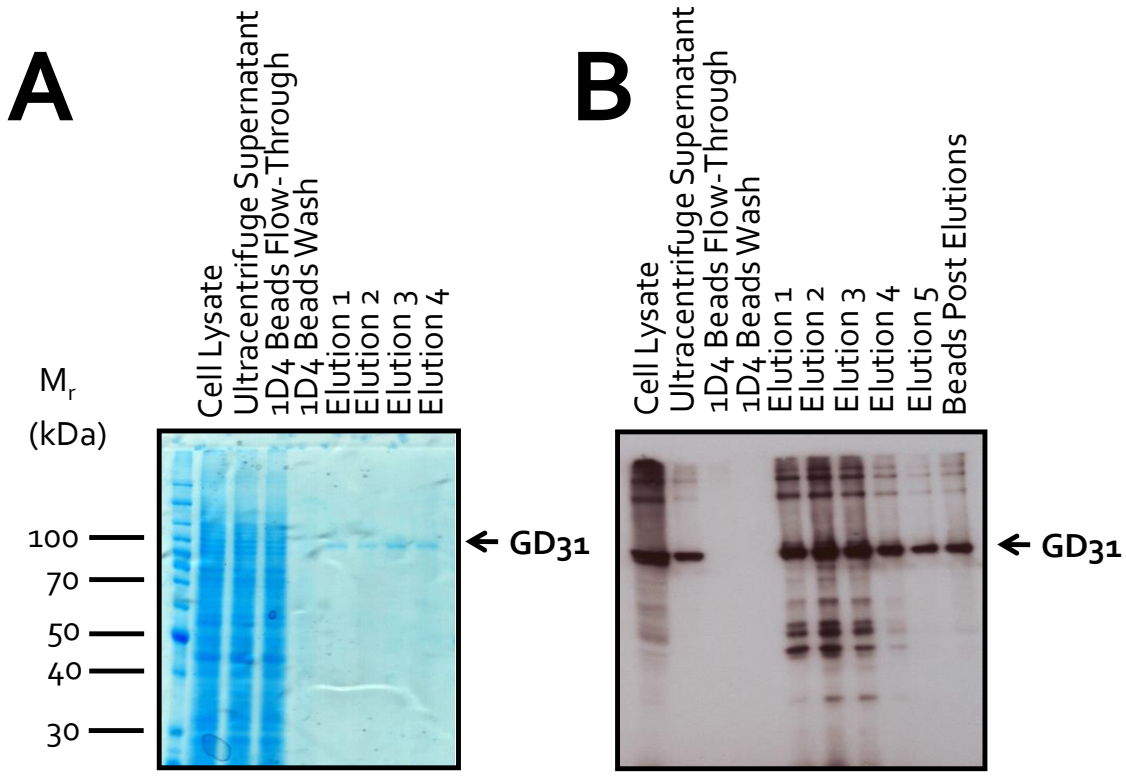

Figure 5.12: Purification of a GluD2 Membrane Protein Construct. A: *10 % SDS-PAGE analysis of the various stages of an IAC purification of a 1D4-tagged transmembrane construct of GluD2.* ***B:*** *Anti-1D4 western blot examination of the various stages of the same IAC purification of a 1D4-tagged transmembrane construct of GluD2.*

5.10 Discussion and Future Work

In summary, a construct for the GluD2 ecto-domain was designed to investigate the differences between GluD2 and other iGluRs. Protocols for the production and purification of this construct were established (Figure 5.2). This reagent was used to initiate crystallization trials, which yielded several hits. However, when these crystals were used in diffraction experiments they were found to diffract to a low resolution limit (Figure 5.3). Crystals were then optimized using a methylation protocol and crystals obtained from methylated protein diffracted to ~4 Å (Figure 5.4). A complete solution could not be obtained by molecular replacement (Table 5.2, Figure 5.5), and a partly refined model was produced (Figure 5.6). However the relative domain orientations in this model were

reasoned to be an artefact of either construct design or crystallization. Following this, mutants of the GluD2 ecto-domain were designed and produced to investigate the probability of a subunit crossover in the GluD2 ecto-domain (Figure 5.8); the results provided some evidence against a GluD2 ecto-domain twist (Figure 5.9). This led to a model for the arrangement of the GluD2 ecto-domain based upon a symmetric dimer (Figure 5.10). Undoubtedly the next necessary steps to understand the architecture and molecular mechanisms of GluD2 will require a high resolution transmembrane protein crystal structure. Therefore, initial steps were taken to establish the protocols for the purification of a membrane-bound construct of GluD2 (Figure 5.12). Structural studies on the intact GluD2 receptor appear to be essential to understand its subunit architecture. However, intact membrane protein crystallography is still an actively developing discipline and numerous significant technical hurdles would need to be negotiated to reach such a goal. Nevertheless, the protocols established in Section 5.10 provide a sound basis for the future trajectory of for the structural characterization of full-length GluD2. Furthermore, additional techniques such as single-particle electron microscopy should be investigated to glean structural information for GluD2. Certainly structural biology provides the clearest evidence to understand how proteins function at atomic resolution, and hence multiple transmembrane structures of GluD2 in different forms would aid the understanding of the role of GluD2 in motor control and motor information storage as well provide the potential for rational drug design targeting GluD2 or related proteins.

Chapter 6:

Structural Investigation of Cbln1 and Molecular Dissection of a Trans-Synaptic Complex

6.1 Summary

A ternary protein complex between Neurexin, Cbln1 and GluD2 bridges the synaptic cleft between parallel fibres and Purkinje cells in the cerebellum. This complex is both crucial for the formation of this synapse and for its functional properties, such as long-term depression of synaptic signalling and the control of motor skills and learning (Schmid & Hollmann, 2010). In this chapter, the molecular details of this trans-synaptic complex were investigated. This led to the 2.4 Å crystal structure of the Cbln1 C1q domain, as well as the characterization of the component interactions of the trans-synaptic complex through the use of negative stain electron microscopy, surface plasmon resonance and targeted mutational analysis. Moreover, based on this evidence a model is proposed for the formation of a trans-synaptic array involving this ternary protein complex.

6.2 Introduction and Aims

Cbln1 is a secreted glycoprotein and member of the C1q family of proteins (Yuzaki, 2008). Each Cbln1 subunit is 193 amino acids in length and consists of a globular C1q domain and an N-terminal extension of ~37 amino acids (Figure 6.1A and Section 1.5.1) (Urade et al, 1991). Trimerization is a common mode of organization of C1q domains, and cross-linking experiments have established that the mature oligomeric state of Cbln1 is as a hexamer, with a putative dimer-of-trimers arrangement (Bao et al, 2005). The hexamerization is mediated through the provision of two cysteine residues from the N-terminal extension of each subunit, possibly forming a 'Cys-knot' domain (Bao et al, 2005). Whilst this information provides an idea of the domain composition of Cbln1, analysis using structural and biophysical techniques would allow a greater level of detailed knowledge concerning the assembly and function of Cbln1 to be obtained.

Cbln1 has been shown to act as an adaptor molecule forming a trans-synaptic bridge between pre-synaptic Neurexin and post-synaptic GluD2 (Matsuda et al, 2010; Uemura et al, 2010). This trans-synaptic triad is essential for correct synaptogenesis and ensuring the precise alignment of the pre- and post-synaptic zones at the PF-PC synapse in the cerebellum (Schmid & Hollmann, 2010). Furthermore, this ternary interaction is not just a structural link but is involved in signalling functions too, as evidenced by the observations that disruption of distinct components of the complex results in impaired LTD at the PF-PC synapse (Hirai et al, 2005; Kashiwabuchi et al, 1995) and that the individual proteins can induce pre- and post-synaptic specializations (Matsuda et al, 2010; Uemura et al, 2010).

One of the current suggestions regarding the molecular composition of the Neurexin-Cbln1-GluD2 trans-synaptic bridge is that Cbln1 must be in a hexameric form to interact with both Cbln1 and GluD2; based upon immunohistochemical studies with a timeric form of Cbln1 (Matsuda et al, 2010; Uemura et al, 2010). It is known that the only variants of Neurexins to interact with Cbln family members are those that include splice site 4 (Joo et al, 2011; Uemura et al, 2010). Additional current suggestions regarding the molecular basis for the Neurexin-Cbln1-GluD2 ternary protein complex is that: (i) Amino acid region Ser57-Ala60 of Cbln1 is involved in the interaction with Neurexin (Lee et al, 2012); (ii) W136 of Cbln1 is required to mediate binding to GluD2 (Lee et al, 2012); (iii) The so-called 'Flap-loop' (R345-W363) of the GluD2 ATD is the binding site for Cbln1 (Kuroyanagi & Hirano, 2010). Recently, it has been proposed that the stoichiometric ratio of the components forming the trans-synaptic bridge between monomeric Neurexin, hexameric Cbln1 and tetrameric GluD2 is 4:2:1 (Lee et al, 2012).

A principal aim of this chapter was to provide information regarding the tertiary and quaternary structure of Cbln1. Following this, a further aim was to offer an insight into the nature of the interactions holding together the PF-PC Neurxin-Cbln1-GluD2 trans-synaptic bridge.

6.3 Cbln1 Constructs and Expression Trials

Constructs of Cbln1 were designed to allow the expression of full-length protein and the isolated C1q domain. Alternative signal sequences, i.e. native versus pHLsec-derived, were tested, as were different start sites for the mature polypeptide chain, to achieve optimal domain boundaries to permit expression and secretion from mammalian cells, as well as producing recombinant protein with the highest propensity to crystallize. All molecular cloning was performed as described in Section 2.1, and a full list of details of the initial Cbln1 constructs (CB1-4) is described in Appendix 8.1. Small-scale expression trials of these initial Cbln1 constructs were performed as described in Section 2.3.2. Anti-His tag western blot of the conditioned media revealed that three out of four constructs, CB2-4, were expressed and secreted from HEK 293T cells (Figure 6.1). CB2 encoded full-length Cbln1, Q22-L193, following the pHLsec-derived signal sequence; CB3 encoded a two amino acid shorter construct than CB2, E24-L193, as this removed a putative N-Linked glycosylation site at N23; and construct CB4 encoded the C1q domain of Cbln1.

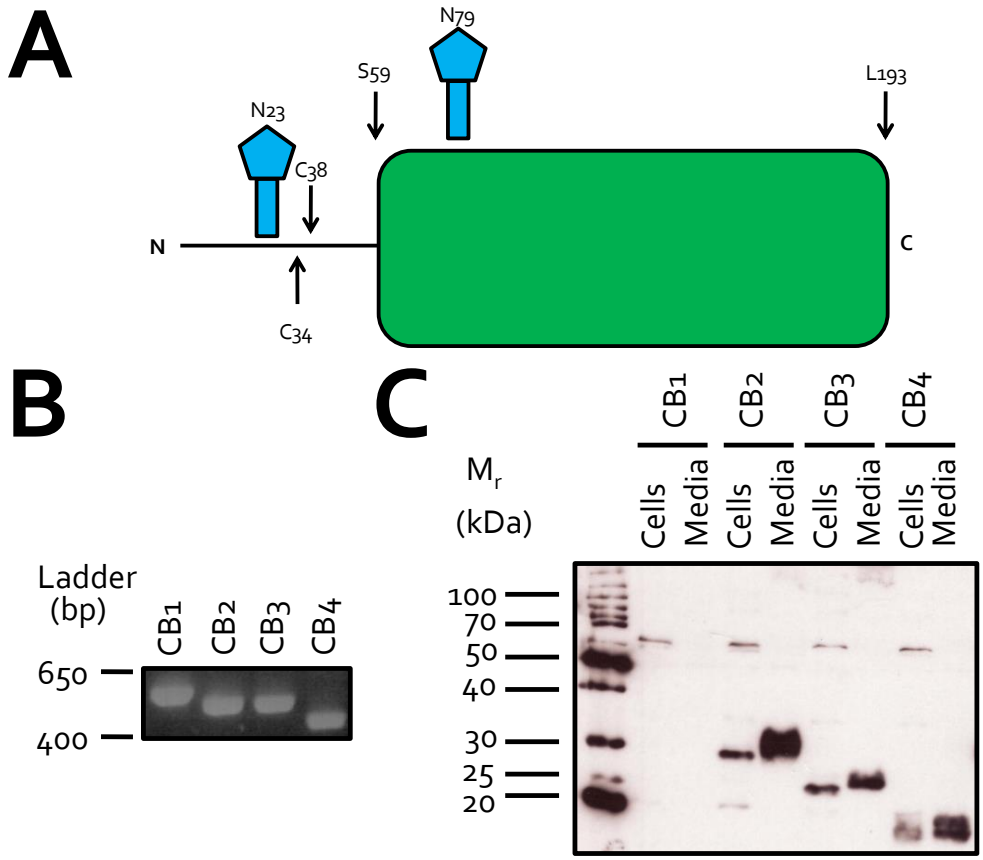

Figure 6.1: Cloning and Expression of Trials of Initial Cbln1 Constructs. ***A:*** *A schematic depicting the domain composition of a single Cbln1 subunit. Domain boundaries are highlighted, as are cysteine residues which are thought to mediate oligomerization (Bao et al, 2005). Mounted pentagons highlight sites of N-linked glycosylation.* ***B:*** *1 % agarose gel electrophoresis of initial Cbln1 constructs PCR products.* ***C:*** *Anti-His Western blot analysis of samples taken from Cbln1 construct small-scale expression trial.*

6.4 Purification of Cbln1 Constructs

Constructs CB2 and CB3 were initially targeted for large-scale expression and purification since both these constructs were found to be secreted efficiently in small-scale (Figure 6.1). HEK 293T cells, cultured in roller bottles were transfected with DNA encoding either CB2 or CB3. Conditioned media from each transfection was then harvested after a 10-14 day incubation period at 37 °C; this was then processed and applied to IMAC purification as described in Sections 2.4.1-2. Both samples

were then applied to a final purification step of SEC, as described in Section 2.4.4, and SEC fractions were then analysed using SDS-PAGE and this revealed that greater than 95 % purity was achieved for both samples (Figure 6.2A-B). Deglycosylation trials, where Endoglycosidase H was added to each sample in a time course experiment, showed that enzymatic removal of N-linked glycans severely affected the solubility of both CB_2 and CB_3 (data not shown), hence N-linked glycan removal was subsequently not attempted with these samples.

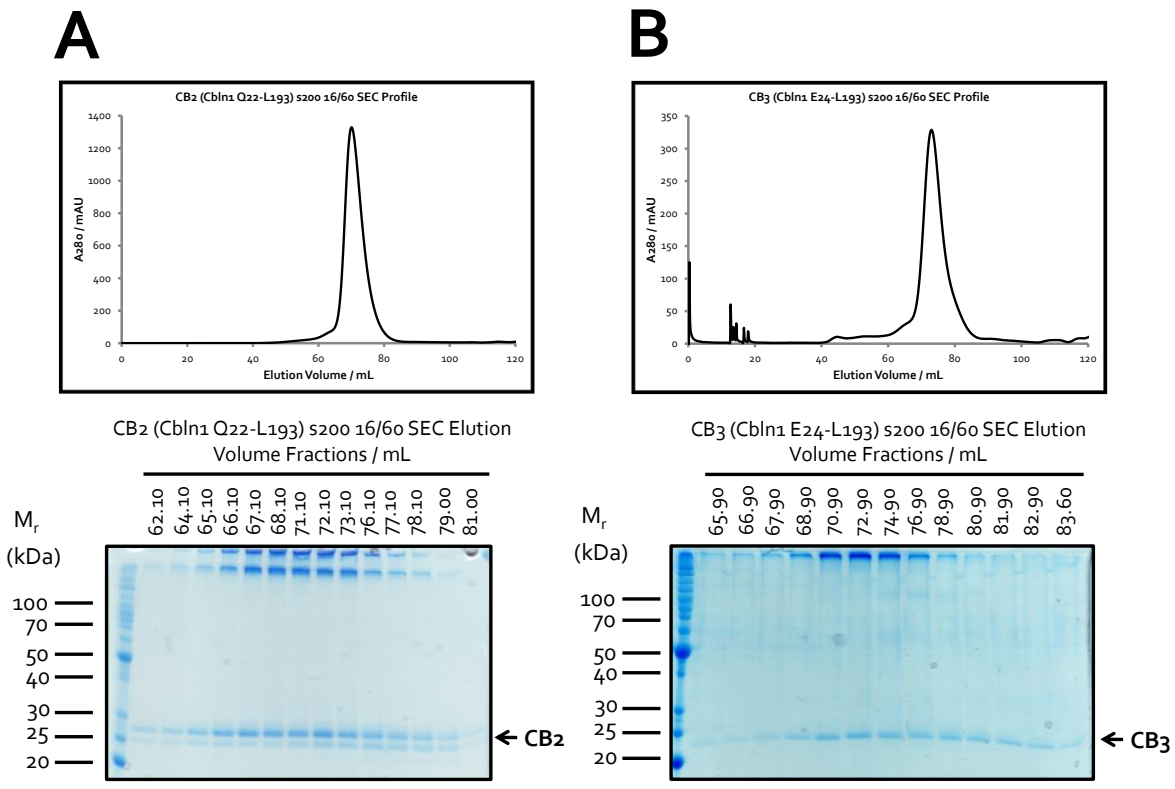

Figure 6.2: Purification of Initial Cbln1 Constructs. A: Top Image: *CB2 SEC profile, monitoring absorbance at 280 nm versus elution volume from a superdex 200 16/60 column.* ***Bottom Image:*** *Coomassie stained SDS-PAGE gel of CB2 SEC fractions; the double band represents different glycoforms.* ***B: Top Image:*** *CB3 SEC profile, displaying A280 versus elution volume from a superdex 200 16/60 column.* ***Bottom Image:*** *SDS-PAGE analysis of CB3 SEC fractions.*

6.5 Crystallization and Structure Determination of Construct CB3

Following successful purification, glycosylated CB2 and CB3 samples were then concentrated using ultrafiltration. During concentration, the lack of solubility of sample CB3 became particularly problematic, which led to the addition of 50 mM each of arginine and glutamate (Golovanov et al, 2004) to enhance solubility and allow higher protein concentrations to be achieved. Following a pre-crystallization test (Section 2.5), sitting drop vapour diffusion crystallization trials were set-up with sample concentrations as follows: ~8.7 mg/mL of CB2 and 4.8 mg/mL of CB3. Crystals of varying size and morphology grew in several conditions for both CB2 and CB3 samples.

Crystals of construct CB3 (Cbln1 E24-L193) which grew in the condition 0.2 M sodium malonate (pH 7.0), 20 % (w/v) polyethylene glycol 3350 (Figure 6.3A) yielded isomorphous diffraction and visible reflections to ~2.5 Å in X-ray experiments at beamline I04, Diamond Light Source (Figure 6.3B). Crystals were cryo-protected using 30 % ethylene glycol. These diffraction images were indexed to space group P6 with unit cell dimensions of: a = 83.5 Å, b = 83.5 Å, c = 50.6 Å, $\alpha = 90^{\circ}$, $\beta = 90^{\circ}$, $\gamma = 120^{\circ}$ (Table 6.1).

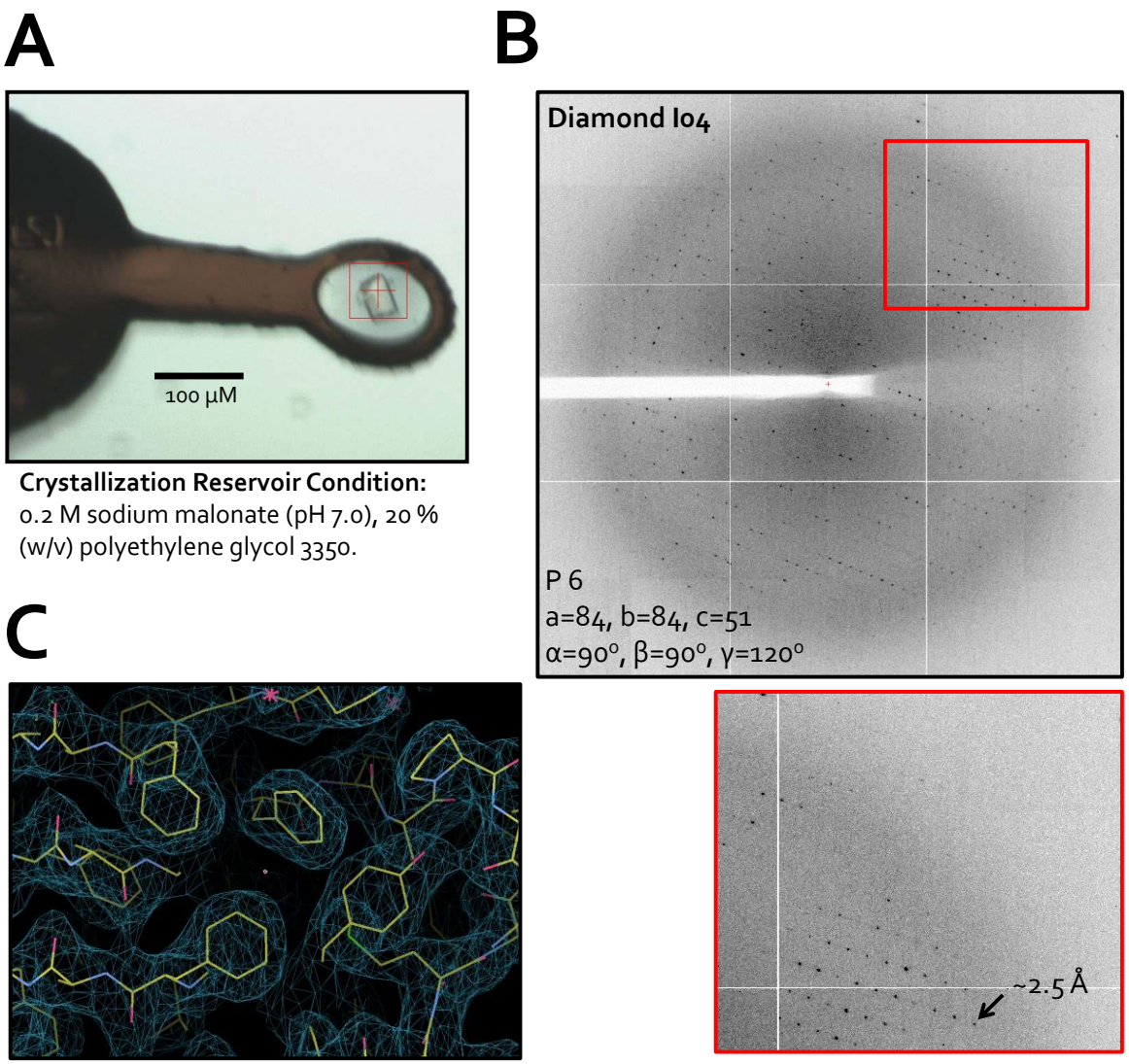

Figure 6.3: CB3 Crystallization, Diffraction Experiments and Electron density of CB3 (Cbln1 E24-L193). A: *An image displaying a mounted crystal which grew in a reservoir condition containing 0.2 M sodium malonate (pH 7.0), 20 % (w/v) polyethylene glycol 3350.* ***B:*** *Images collected during X-ray diffraction experiments using the crystal exhibited in* ***A****. Images were indexed to space group P 6 with unit cell dimensions a = b = 84 Å, c = 51 Å, α = β = 90°, γ = 120°.* ***C:*** *Representative 2Fo-Fc electron density maps, contoured at 1 σ, calculated to 2.4 Å.*

DATA COLLECTION		
Beamline	Diamond I04	
Resolution	50.0-2.4 (2.46-2.40)	
Space group	P6	
Cell dimensions	[Å]	[°]
	a = 45.1 b = 79.1 c = 246.6	α = 90 β = 90 γ= 120
Wavelength [Å]	1.0730	
Unique reflections	7973 (583)	
Completeness [%]	99.9 (100)	
R_{merge} [%][a]	10.7 (96.1)	
I/σI	13.4 (1.7)	
Redundancy	5.6 (5.6)	
REFINEMENT		
Resolution range [Å]	50.0-2.4 (2.68-2.40)	
Number of reflections	7971 (2242)	
R_{factor} [%)][c]	17.1 (20.1)	
R_{free} [%] [d]	20.5 (28.4)	
No. of atoms (Protein/NAG/EG/Ca/Water)	1081/14/0/0/38	
B factors [Å^2] (Protein/Water)	45/77/0/0/46	
R.M.S.D. bonds [Å]	0.010	
R.M.S.D. angles [°]	1.17	
Ramachandran statistics[d] Favoured [%] Disallowed [%]	 97.8 0	

Table 6.1: Cbln1 C1q Domain Crystallographic Statistics. *A table listing the data collection and refinement statistics for the crystal structure of Cbln1 C1q domain.* R.M.S.D. stands for root mean square deviation from ideal geometry. Numbers in parentheses refer to the appropriate outer shell.

[a] $R_{merge} = \Sigma_{hkl} \Sigma_i |I(hkl;i) - \langle I(hkl) \rangle| / \Sigma_{hkl} \Sigma_i I(hkl;i)$, where $I(hkl;i)$ is the intensity of an individual measurement and $\langle I(hkl) \rangle$ is the average intensity from multiple observations.

[b] $R_{factor} = \Sigma_{hkl} ||F_{obs}| - k|F_{calc}|| / \Sigma_{hkl} |F_{obs}|$.

[c] R_{free} equals the *R*-factor against 5% of the data removed prior to refinement.

[d] Calculated using MolProbity (Davis et al, 2007).

This CB_3 diffraction data was phased using the Collagen X NC1 trimer (27 % sequence similarity, PDB code 1GR3, (Bogin et al, 2002)) as a search probe in molecular replacement. This was followed by iterative rounds of model building and refinement (Table 6.1). A representative 2Fo-Fc electron density map is displayed in Figure 6.3C. This CB_3 crystal form had one molecule in the asymmetric unit and, unexpectedly, electron density could be observed for only the C1q domain of Cbln1, i.e. residues G58-L193, suggesting that the N-terminal 34 residues were absent or disordered. Inspection of the arrangement of the crystal lattice revealed that the C1q domains were arranged as trimers (Figure 6.4). Furthermore, the stacking of the layers within the crystal suggests that it is likely that a proteolytic cleavage event occurred during crystallization since it is unlikely that the Cbln1 Cys-knot domain could be accommodated between layers (Figure 6.4). Additionally, the idea that Cbln1 is a target for proteolysis is not unprecedented. It has been reported that both recombinant and native Cbln1 undergoes extensive proteolytic processing (Bao et al, 2005).

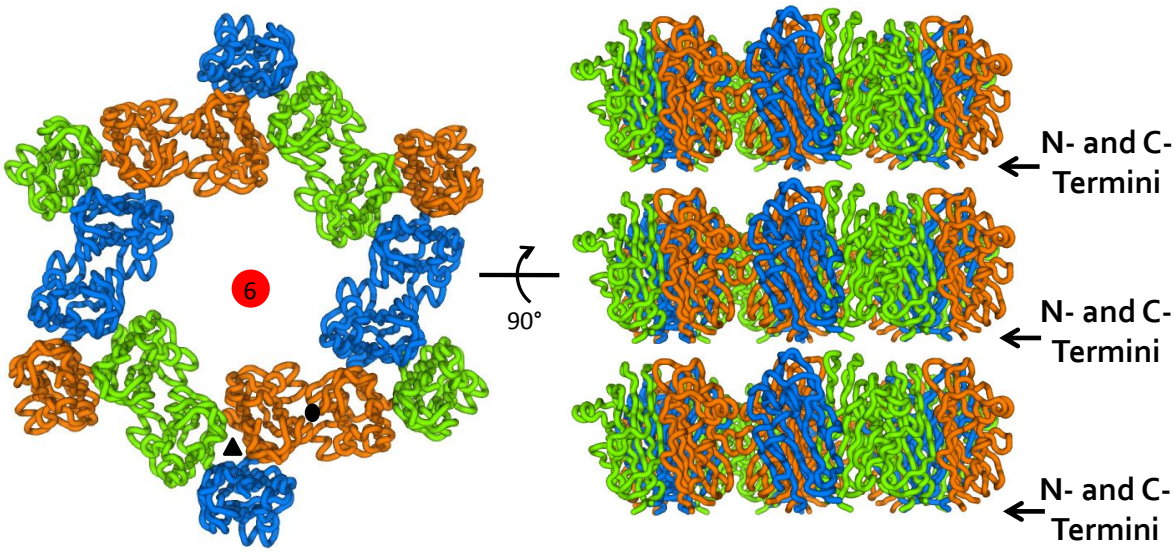

Figure 6.4: Crystal Packing in the CB_3 crystal form. A: *Cartoon representation of the crystal packing in the CB_3 crystal form, viewed from two different perpendicular orientations.* ***Left image:*** *A view of the crystal packing within in one layer of the crystal.* ***Right Image:*** *A view of the crystal packing showing the parallel layers in the CB_3 crystal form.*

6.6 Features of the Cbln1 C1q Domain

The model for the Cbln1 C1q domain contains 135 amino acids covering completely the residues G58-P192 of Cbln1 (Figure 6.5). Furthermore, a site of N-linked glycosylation is visible and ordered at position N79 (Figure 6.5C). The Cbln1 C1q domain exhibits a nine-stranded β-sandwich with a jelly-roll topology (Figure 6.5B). This is similar to the C1q domains of other proteins such as the Collagen X 1NC1 Trimer (Bogin et al, 2002) and ACRP30/adiponectin (Shapiro & Scherer, 1998), as well as tumour necrosis factor (TNF) (Eck & Sprang, 1989; Jones et al, 1989). Table 6.2 displays the statistics for structural homology analysis between Cbln1 C1q and a selection of C1q and TNF domains from other proteins. The Cbln1 C1q shows the closest structural homology to the C1q domain of ACRP30, evidenced by an RMSD of 1.62 Å, for 124 equivalent residues representing 91 % of the Cbln1 C1q and 94 % of the ACRP30 C1q domain (Table 6.2).

Structural superposition of the Cbln1 C1q with other C1q and TNF containing proteins (Figure 6.5D), along with structure-based sequence alignments (Figure 6.6), demonstrate that the Cbln1 C1q domain exhibits unique features. Specifically the insertion of a helix, α1, between the β1 and β2 sheets (Figure 6.5D-E). The α1 helix harbours an N-linked glycosylation site (Figure 6.5B). The function of this helix remains to be tested but since C1q domains are known protein-interaction domains (Ghai et al, 2007), the α1 helix and the concomitant glycan could be involved in defining the specificity for certain Cbln1 binding partners.

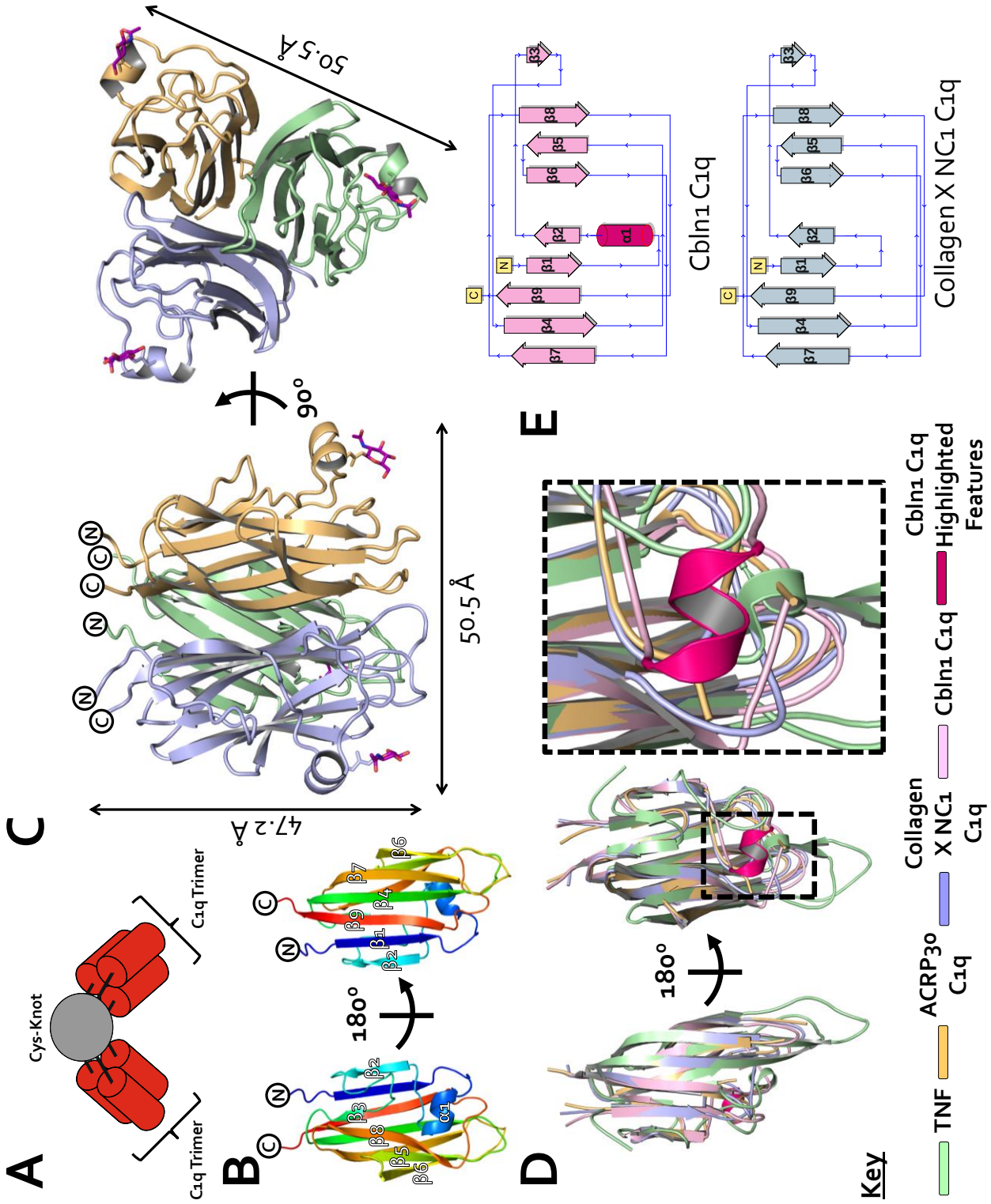

Figure 6.5: The Crystal Structure of the Cbln1 C1q Domain.

Figure 6.5: The Crystal Structure of the Cbln1 C1q Domain. A: *A schematic representing the purported hexameric structure of Cbln1 (Bao et al, 2005).* ***B:*** *Rainbow cartoon representation of the C1q domain of Cbln1. Helices and sheets are labelled as in Figure 6.6.* ***C:*** *Cartoon structural representation of the C1q domain trimer. Dimensions are labelled and sites of N-linked glycosylation are symbolised with a purple coloured stick representation.* ***D:*** *Superposition of the Cbln1 C1q (in pink and magenta) with the C1q domain from the collagen X NC1 (in blue, 1GR3 (Bogin et al, 2002)), the C1q domain from ACRP30 (in light orange, 1C28 (Shapiro & Scherer, 1998)) and TNF (in mint green, 1TNF (Eck & Sprang, 1989)). The α1 helix in Cbln1 C1q is highlighted in magenta. Superpositions were generated using the program SHP (Stuart et al, 1979).* ***E:*** *A schematic displaying the secondary structural elements in the C1q domain of Cbln1 (**Top Image**) and the C1q domain of the collagen X NC1 (**Bottom Image**, 1GR3 (Bogin et al, 2002)). The Cbln1 C1q α1 helix is highlighted in magenta.*

Reference Molecule	Molecule Used for Comparison	RMSD / Å	Number of Equivalent Residues	Percentage of Equivalences in Reference Molecule / %	Percentage of Equivalences in Comparison Molecule / %
Cbln1 C1q Domain (This Thesis, Chapter 6)	Collagen X NC1 C1q Domain (PDB: 1GR3)	1.64	124	91	94
	ACRP30 C1q Domain (PDB: 1C28)	1.62	124	91	94
	TNF (PDB: 1TNF)	2.02	115	84	76

Table 6.2: Homology Analysis of a Selection of C1q and TNF Domains. *A table containing a set of statistics from the structural comparison of a selection of C1q and TNF domains. Structures were aligned using the program SHP (Stuart et al, 1979).*

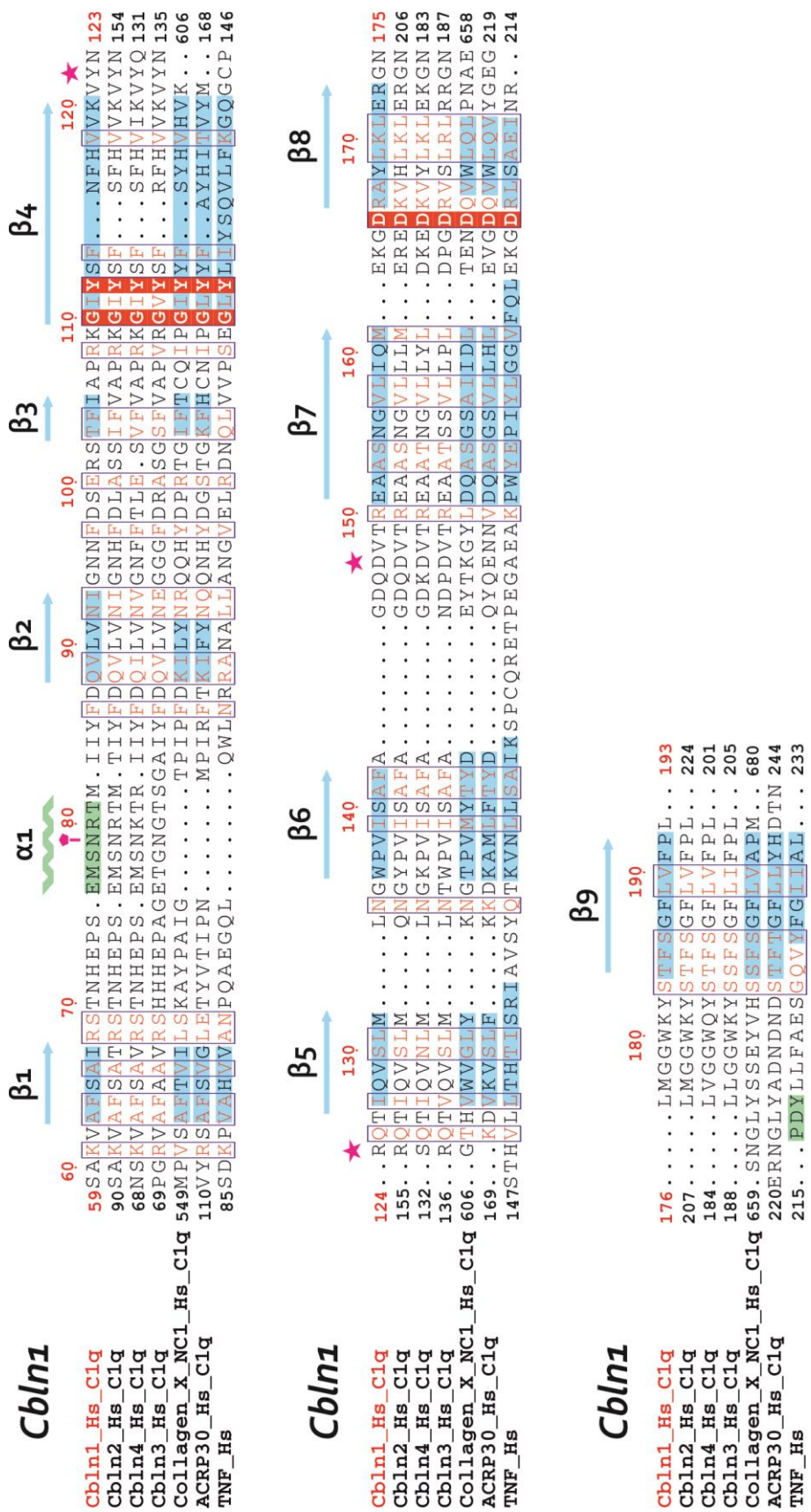

Figure 6.6: Structure-Based Sequence Alignment of the C1q and TNF domains.

Figure 6.6: Structure-Based Sequence Alignment of the C1q and TNF domains. *Secondary structural elements are labelled, as are important residues discussed in the text of this thesis, highlighted with a pink star, and putative sites of N-linked glycosylation in the Cbln1 C1q domain are labelled with a pink pentagon on a pink rectangle. The following NCBI reference entry codes were used to obtain the sequences used for the alignment: Cbln1, NP_004343.1; Cbln2, NP_872317.1; Cbln3, NP_001034860.1; Cbln4, NP_542184.1; Collagen X NC1, NP_000484.2; ACRP30, NP_001171271.1; and TNF, NP_000585.2.*

One molecule of the Cbln1 C1q is present in each asymmetric unit; however inspection of the crystal lattice suggests that the C1q domain is arranged as a crystallographic trimer (Figure 6.4). The interface between two C1q domains, at the core of the C1q trimer is 792.0 $Å^2$/subunit, consisting of 31 residues from one subunit and 26 residues from the partner subunit. The interactions at the core of the Cbln1 C1q trimer are mainly hydrophobic; however 7 hydrogen bonds also mediate the interaction. Amino acid conservation analysis demonstrates that the core of the C1q trimer (Figure 6.7A), and the bottom surface of the C1q trimer (Figure 6.7D) are both highly conserved within the Cbln family of glycoproteins. Electrostatic potential calculations of the surface charge on the Cbln1 C1q domain also exemplify the hydrophobic nature of the Cbln1 C1q Trimeric core (Figure 6.7E).

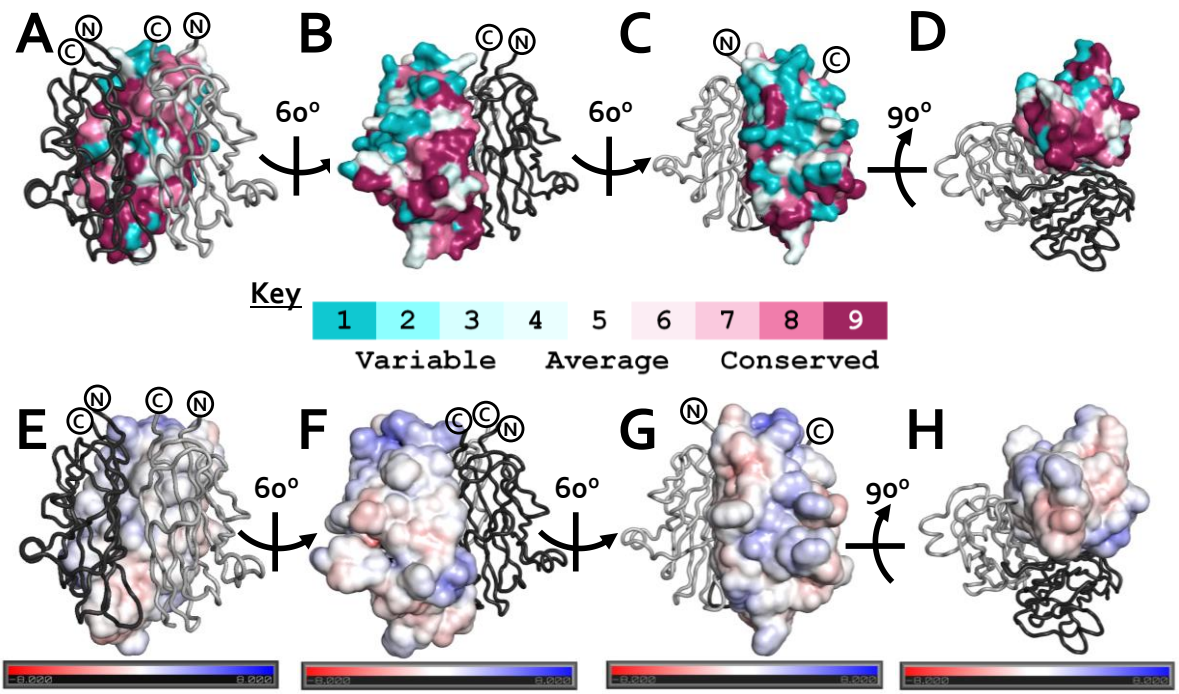

Figure 6.7: Properties of the Cbln C1q domain. A-D: *Conservation of residues in C1q domain of the Cbln family plotted onto the crystal structure of the Cbln1 C1q domain. Different views of the plot are displayed, such as the C1q trimeric interface view in* ***A****, and the C1q trimer 'tip' surface view in* ***D****. Conservation calculations were performed using the ConSURF server (Ashkenazy et al, 2010).* ***B-H:*** *Electrostatic potential of the Cbln1 C1q domain, calculations were performed using APBS (Baker et al, 2001). Various views of the electrostatic potential of the Cbln1 C1q domain are provided including the C1q trimeric interface view in* ***E****, and the C1q trimer 'tip' surface view in* ***H****. Blue indicates positive charge; white indicates neutral charge and red indicates negative charge. The units of electrostatic charge are in kTe-1 (k = Boltzmann constant, T = Temperature and e is the charge of an electron).*

6.7 Characterisation of Full-length Cbln1

The Cbln1 C1q domain is a crystallographic trimer the CB_3 crystal form (Figure 6.5A). However, a previous study that employed western blotting analysis of Cbln1 under native and reducing conditions indicated that the native oligomeric state of full-length Cbln1 is hexameric, and that this hexamerization was dependent upon inter-subunit disulphide bond formation mediated by Cys 34 and 38 (Bao et al, 2005).

To verify this conclusion, MALS was used as a more rigorous method of assessing oligomeric state of high purity recombinant protein samples. Samples of full-length Cbln1 (Q22-L193) and the Cbln1 C1q domain were prepared as described in Sections 6.3 and 6.4. In addition to this a mutant construct of Cbln1 was created by oligonucleotide-mediated mutagenesis, where Cysteine 34 and 38 were mutated to serine; a similar mutant had previously been used for functional studies (Matsuda et al, 2010; Uemura et al, 2010). This new construct termed Cbln1 CS was found to be expressed and secreted from mammalian cells (Figure 6.8A). HEK 293T cells were then transfected with this construct in large-scale, as described in Section 2.3.3. Cbln1 CS was then purified from conditioned media using IMAC and SEC, as described in Sections 2.4.1-4, to greater than 95 % purity (Figure 6.8B).

MALS analysis of Cbln1, Cbln C1q and Cbln1 CS identified that the oligomeric state of these samples were hexameric, trimeric and trimeric, respectively (Figure 6.8C). The trimeric nature of the Cbln1 C1q domain is consistent with the crystal packing observed in the CB_3 crystal form (Section 6.5-6.6). Furthermore, the oligomeric state of these samples is consistent with the PAGE observations of et al, 2005. Therefore these experiments confirm that full-length Cbln1 is hexameric in solution, and that this hexamer consists of a dimer of trimers and that higher oligomerization is dependent upon inter-subunit Cys-bridge formation involving Cysteines 34 and 38.

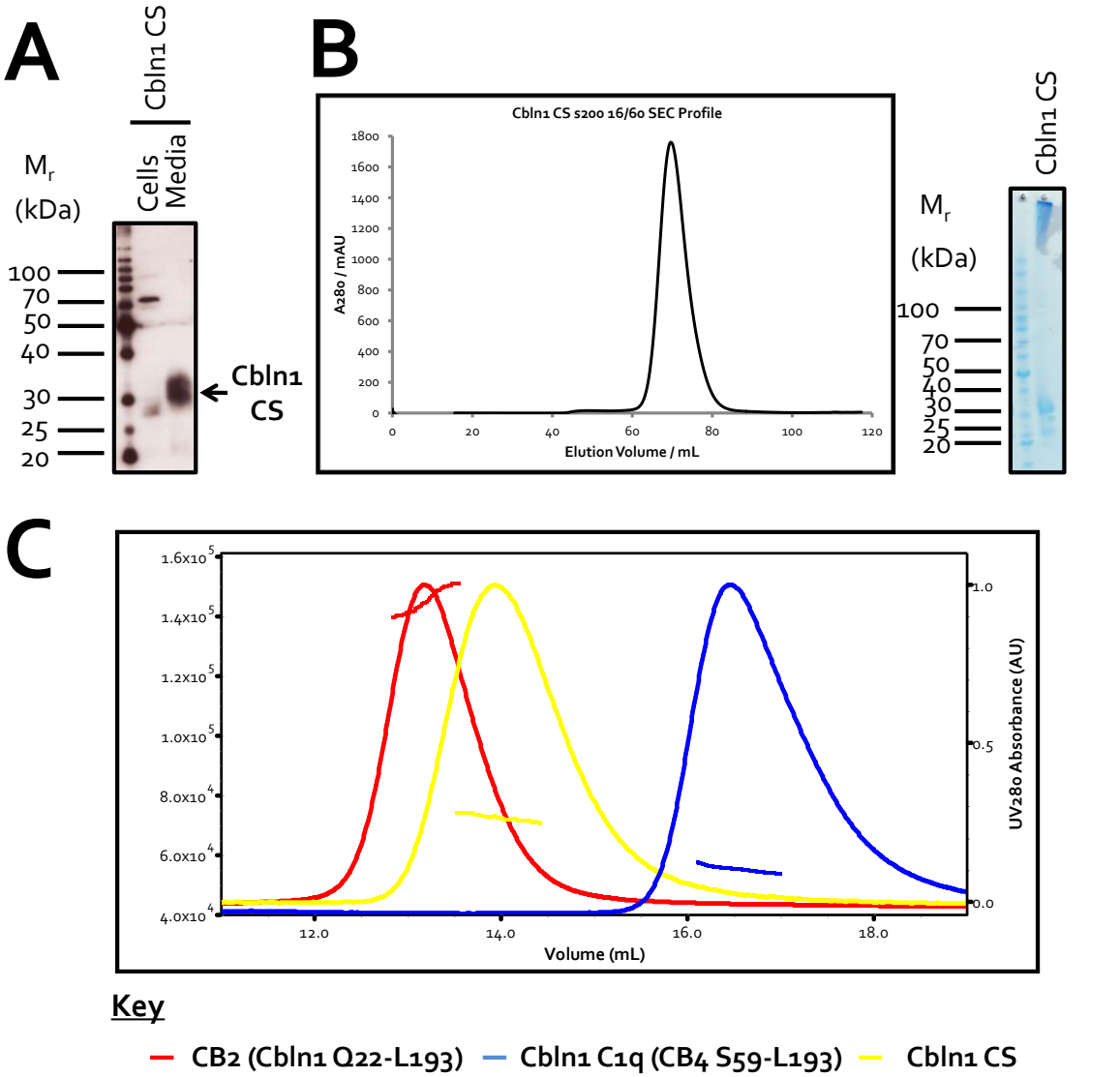

Sample	Measured Molar Mass (kDa)	Molecular Weight of a Single Subunit (kDa)	Measured Molar Mass/Single Subunit Molecular Weight	Oligomeric State of Sample
Cbln1	145.3	24.2	6.00	**Hexamer**
Cbln1 CS	72.6	24.2	3.00	**Trimer**
Cbln1 C1q	55.3	18.5	2.99	**Trimer**

Figure 6.8: Cbln1 CS Purification and MALS analysis of Cbln1. ***A:*** *Anti-His Western blot analysis of samples taken from Cbln1 CS construct small-scale expression trial.* ***B:*** *Cbln1 CS SEC profile (**Left Image**) and SDS-PAGE analysis of Cbln1 CS pooled SEC fractions (**Right Image**).* ***C:*** *MALS analysis of the oligomeric state of various constructs of Cbln1, displaying measured molar mass and UV 280 absorbance versus elution volume.*

Whilst MALS analysis provides strong evidence for the global structure and domain arrangement of Cbln1, details of the secondary and quaternary structure of the Cys-knot domain of Cbln1 remain unknown. Thus steps were taken to use X-ray crystallography to provide high resolution structural details of full-length Cbln1, by targeting mutant Cbln1 constructs that aimed to disrupt the putative enzymatic cleavage site that resulted in the crystallization of the Cbln1 C1q domain from full-length Cbln1 (Section 6.5).

Before designing cleavage site mutants, the cleavage site was first identified. The first amino acid with clear electron density in the CB_3 crystal form (Section 6.6) is G58; this suggested that a cleavage event occurred in the proximity of this amino acid. Evidence to support this assumption comes from the existence of the hexadecapeptide: cerebellin (Slemmon et al, 1984). The sequence of cerebellin, SGSALVAFSAIRSTNH, is equivalent to amino acids Ser57-His71 of Cbln1 (Figure 6.6). The cerebellin peptide is a proteolytic cleavage product of Cbln1; initially Cbln1 was known as cerebellin-precursor protein (Urade et al, 1991). Thus due to the vicinity, in the Cbln1 amino acid sequence, of the first amino acid of the cerebellin peptide and the first amino acid that there is clear electron density for in the Cbln1 C1q domain (Section 6.6), it was reasoned that the N-terminal cleavage event that results in the release of the cerebellin peptide could occur at the same site that resulted in the crystallization of the C1q domain seen in the CB_3 crystal form (Section 6.5). Additionally, it has been suggested that Cbln1 could be a substrate for TACE (TNFα converting enzyme) due to sequence similarity between Cbln1 and proTNFα at the site of TACE-mediated cleavage in proTNFα (Bao et al, 2005). The equivalent site in Cbln1 is between amino acids S54 and V55 (Figure 6.9A). Two strategies were taken in an attempt to disrupt this putative site. The first was to mutate the amino acid immediately N-terminal of the first amino acid of the cerebellin peptide, R56, to a glutamine; this construct was termed CB_9 (Figure 6.9A). The second strategy involved deleting the four amino acids that precede the first amino acids of the cerebellin peptide,

V54-G58, thereby hoping to remove putative cleavage site; this construct was named CB35 (Figure 6.9A). Both of these mutants were created using oligonucleotide-mediated mutagenesis as described in section 2.1.3. CB9 and CB35 were both expressed and secreted from mammalian cells; both could be purified in an analogous manner to CB2 and CB3, through IMAC and SEC. Figure 6.9B displays a representative CB35 SEC profile and SDS-PAGE of CB35 SEC fractions, illustrating the high level of purity achieved.

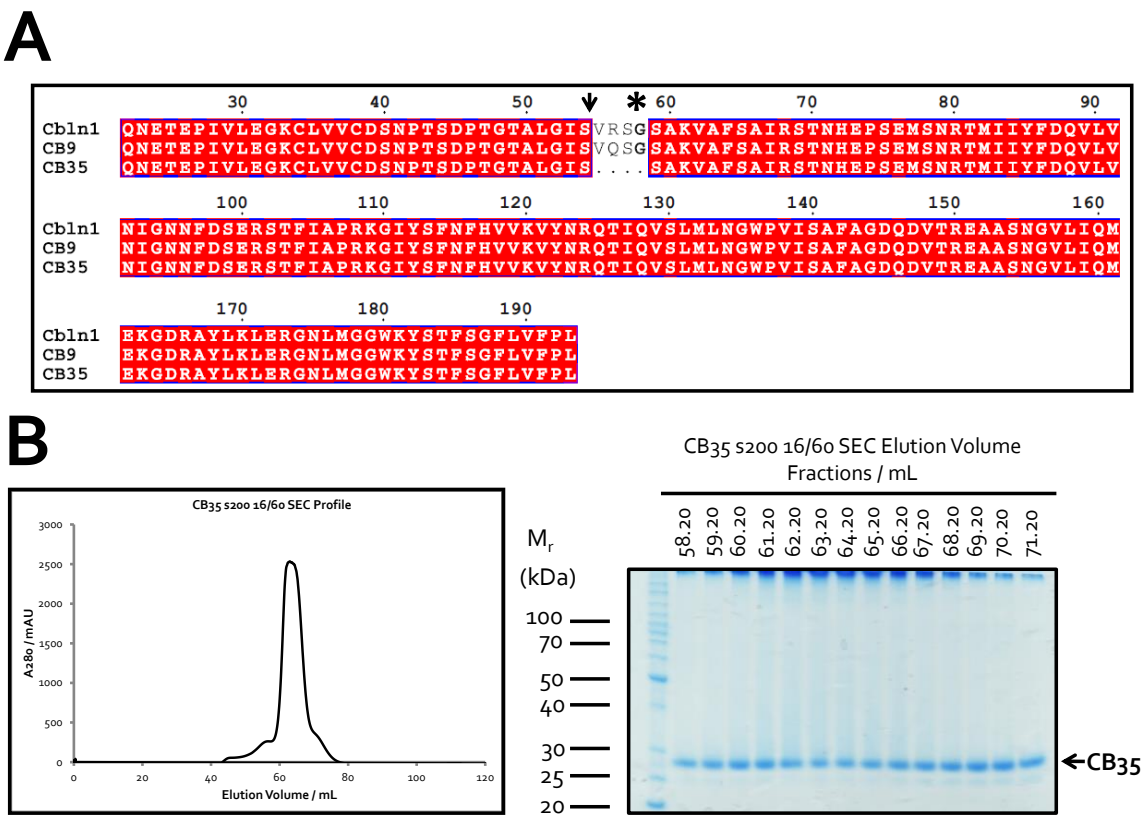

Figure 6.9: Cbln1 Cleavage Mutants. ***A:*** *Sequence alignment highlighting the difference between Cbln1 and the two versions of Cbln1 cleavage mutants, CB9 and CB35. The star (*****) highlights the first amino acid that can be observed in the Cbl1n C1q domain structure (Section 6.6). The arrow represents the position in Cbln1 that is equivalent to the TACE cleavage site in proTNFα.* ***B:*** *SEC profile and Coomassie stained SDS-PAGE gel for purification of Cbln1 cleavage mutant CB35.*

Crystallization trials were initiated with both CB9 and CB35. Both these constructs yielded positive hits in crystallization trials; however it was often the case that the crystals had the same morphology as the CB3 crystal form described in Section 6.5. Moreover when multiple CB9 and CB35 derived crystals of this morphology were tested for diffraction they were indexed to the same space group with the same unit cell dimensions as the CB3 crystal form described in Section 6.5, i.e. space group P6 with unit cell dimensions of: a =~ 84 Å, b = ~84 Å, c = ~51 Å, α = 90°, β = 90°, γ = 120°, suggesting that these crystals were formed from just the C1q domain of Cbln1 and proteolytic cleavage events had occurred.

An additional crystal form seen in the case of CB35 had an alternative morphology and was found in a reservoir condition consisting of 0.85 M HEPES (pH 7.5), 8.5 % (v/v) isopropanol, 17 % (w/v) polyethylene glycol 4000, 15 % (w/v) glycerol, 20 mM sodium bromide (Figure 6.10A). This CB35 crystal form was tested for diffraction at beamline I03 , Diamon Light Source. This CB35 crystal grew in a condition that already contained cryo-protectant; hence no further additive was required. However, due to the flat morphology of this crystal the diffraction observed was very anisotropic, with reflections to roughly 3.5 Å in one orientation but very few reflections when the crystal was rotated by 90° (Figure 6.10B). Initial indexing of these diffraction images pointed to a space group of C 2 2 2, with unit cell dimensions of a = 80 Å, b = 173 Å, c = 117 Å, α = β = γ = 90°. Structure solution by molecular replacement using the Cbln1 C1q domain (Section 6.6), revealed the position of the globular C1q trimer, but no electron density for the Cys-knot domain was observed (data not shown) despite refinement to R_{factor}/R_{free} of ~19%/22%. In this structure solution, layers of trimers are separated by ~20 Å, therefore the Cys-knot must be present, yet it is completely disordered in this crystal form, which could be a result of the presence of six glycans on the Cys-knot. Further strategies to obtain a crystal structure of full-length Cbln1 could involve truncation of the linker

between the Cys-knot and C1q domain, optimization of deglycosylation, or targeting a complex of Cbln1 with Neurexin, GluD2 or other members of the Cbln family.

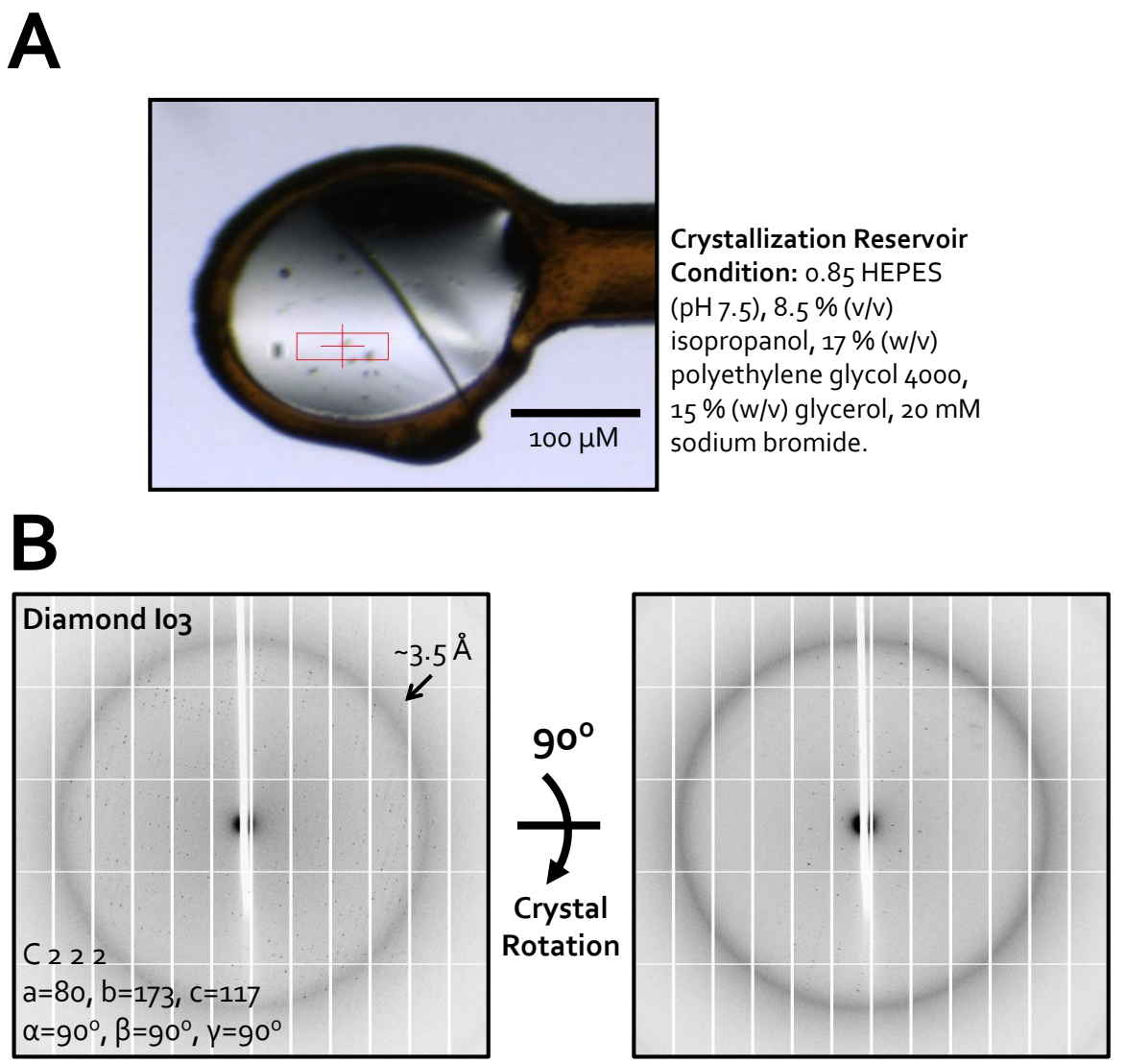

Figure 6.10: CB35 Crystal Form and Anisotropic Diffraction. ***A:*** *An image displaying a mounted crystal which grew in a reservoir condition containing 0.85 M HEPES (pH 7.5), 8.5 % (v/v) isopropanol, 17 % (w/v) polyethylene glycol 4000, 15 % (w/v) glycerol, 20 mM sodium bromide.* ***B:*** *Images from X-ray diffraction experiments performed on crystals shown in* ***A*** *at Diamond I03 beamline. Diffraction was anisotropic with diffraction ~3.5 Å in one orientation but few diffraction reflections when the crystal is rotated by 90°. The images were indexed to space group C 2 2 2, with unit cell dimensions a = 80 Å, b = 173 Å, c = 117 Å, α = β = γ = 90°.*

Due to the lack of high resolution Cbln1 data from X-ray crystallography efforts it was decided to use an alternative technique to gain a structural understanding of full-length Cbln1. To this end, a sample of full-length Cbln1 Q22-L193 (CB2), purified as described in Section 6.4, was sent to collaborators in the laboratory of Dr. Terunaga Nakagawa (University of California, San Diego) who performed single-particle negative stain electron microscopy on this sample. Single particle class averages of this Cbln1 sample revealed a structure that is consistent with the idea that Cbln1 is formed from a dimer of trimers arrangement (Figure 6.11). The class averages of Cbln1 have a 'bicycle' shape, where each C1q domain trimer forms the two wheels and the Cys-knot domain the connecting frame. The size of the C1q domain seen in the class averages is roughly ~50 Å which is consistent with the size of the C1q trimer calculated from the C1q crystal structure (Section 6.6, Figure 6.5).

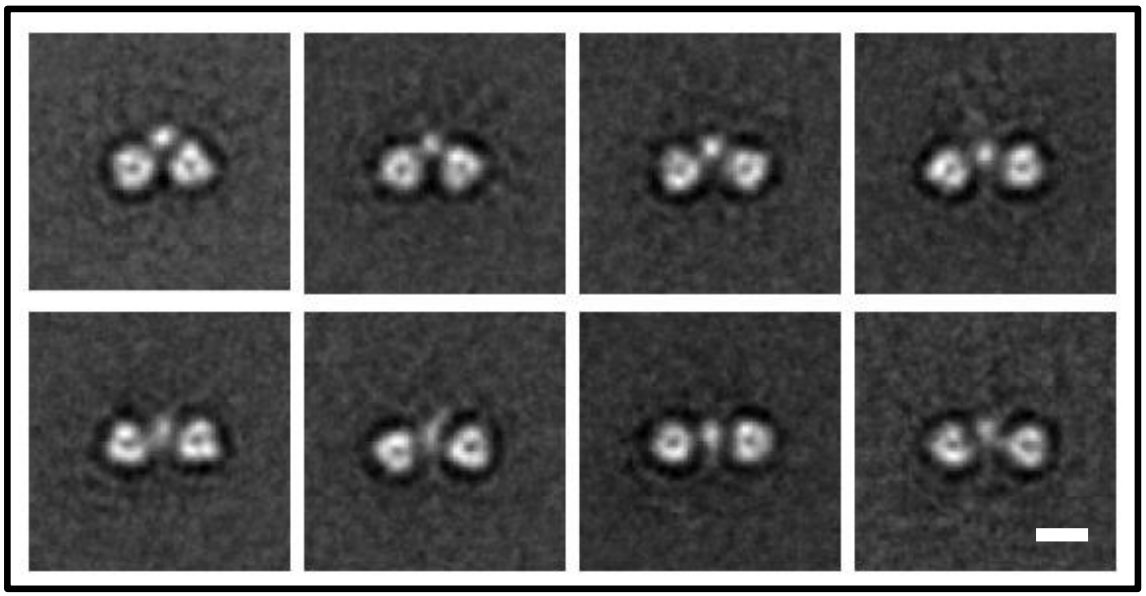

Figure 6.11: Cbln1 Single Particle Negative Stain Electron Microscopy. A: *Single particle class averages of Cbln1. These data confirm a dimer of trimers structure for Cbln1, whereby each C1q domain trimer is connected by a Cys-knot domain. The scale bar represents 50 Å. This work was carried out in the laboratory of Dr. Terunaga Nakagawa, University of California, San Diego.*

6.8 Exploring the Interaction between Cbln1 and Neurexin

The original study that discovered the interaction between Cbln1 and βNeurexin revealed that only βNeurexins containing splice site four were able to bind to Cbln1, highlighting the potential binding site (Uemura et al, 2010). This study also indicated that hexamerization of Cbln1 was required for the interaction between Cbln1 and βNeurexin. Additionally Uemura et al, 2010 used SPR and kinetic analysis to determine a binding constant (K_d) of 0.17 nM. A more recent study from the same group, which employed gel filtration, isothermal calorimetry (ITC) and immunohistochemistry confirmed that splice site four in βNeurexin is the binding site for Cbln1 (Lee et al, 2012). Furthermore this study suggested that βNeurexin and Cbln1 interact with a ratio of 2:1 and that the region Ser57-Ala60 of Cbln1 was required for the interaction with βNeurexin.

In an effort to provide more structural details regarding the interaction between Cbln1 and Neurexins a DNA construct encoding the βNeurexin1 LNS domain, including splice site four was created as described in Section 2.1 and Appendix 8.1. HEK 293T cells were then co-transfected with DNA for both βNeurexin1+SS4 and Cbln1 construct E24-L193 (CB3), using the protocol detailed in Section 2.3.3. Conditioned media containing His-tagged CB3 and βNeurexin1+SS4 was then subjected to IMAC followed by SEC. The s200 10/30 gel filtration profile of the co-purified Cbln1-Neurexin contained two distinct peaks, one with a peak at ~14 mL and one with a peak at ~17 mL (Figure 6.12A). SDS-PAGE analysis of the SEC fractions indicates that the peak that eluted at ~14 mL contained Cbln1 and βNeurexin1+SS4; also the peak that eluted at ~17 mL contained only βNeurexin1+SS4. This indicates that a stable protein complex is formed between Cbln1 and βNeurexin1+SS4, and secondly the presence of the additional Neurexin-only containing peak suggests that βNeurexin1+SS4 was expressed at higher levels than Cbln1 and presumably all the Neurexin binding sites within Cbln1 are saturated.

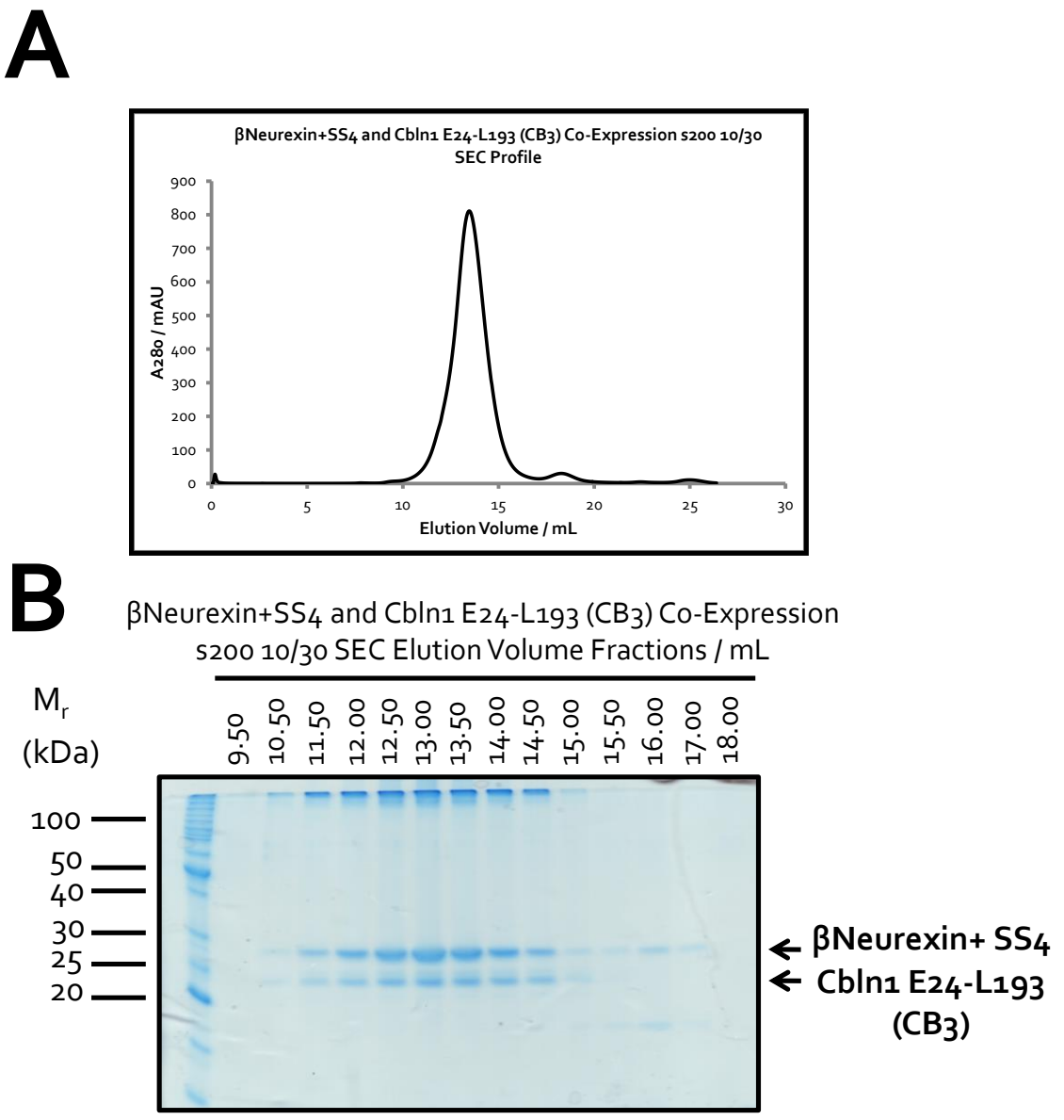

Figure 6.12: Purification of a Cbln1-Neurexin Complex. A: *Cbln1-Neurexin+SS4 co-purification SEC profile.* ***B:*** *SDS-PAGE analysis of Cbln1-Neurexin+SS4 elution fractions. The identity of each set of bands is indicated with the labelled arrows.*

Single-particle negative stain EM analysis of this Cbln1-Neurexin complex was carried out by collaborators in the laboratory of Dr. Ternunaga Nakagawa, University of California San Diego. When comparing the class averages of the Cbln1-Neurexin complex (Figure 6.13A) with the class averages of Cbln1 alone (figure 6.13B and 6.11), it is clear that extra features are present in the

Cbln1-Neurexin class averages, highlighted by the white arrows (Figure 6.13A). This extra feature is undoubtedly the βNeurexin1+SS4 LNS domain. In Section 6.7 the shape of Cbln1 seen in EM class averages was described as a 'bicycle' shape, with the C1q trimers the two wheels and the Cys-Knot domain the joining frame. In the case of the Cbln1-Neurexin class averages (Figure 6.13), the βNeurexin1+SS4 LNS domain can be styled as the 'rider' on the 'bicycle'. The major implication and conclusion from these class averages is that βNeurexin1+SS4 LNS domain interacts with the Cys-knot domain of Cbln1.

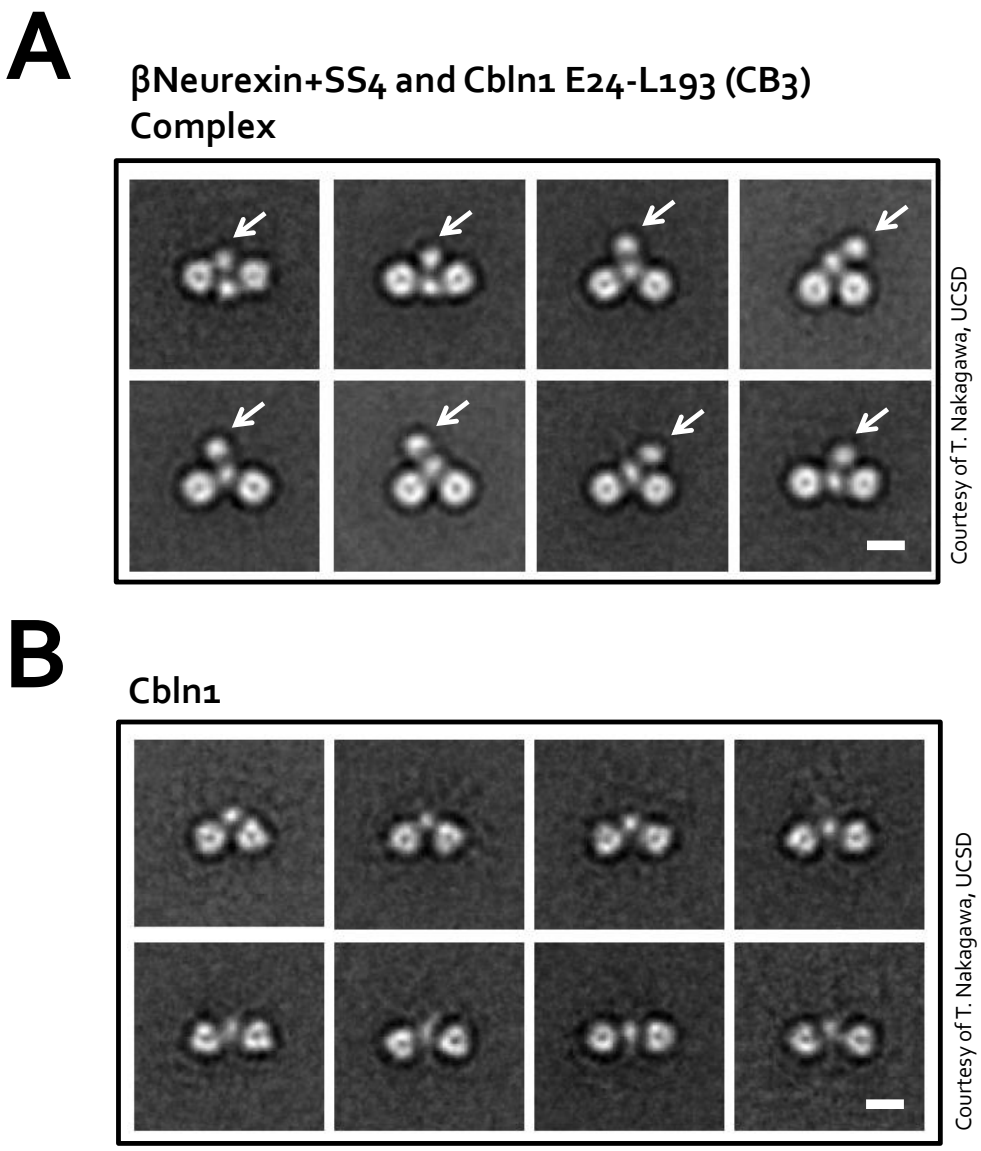

Figure 6.13: Cbln1 Single Particle Negative Stain Electron Microscopy.

Figure 6.13: Cbln1 Single Particle Negative Stain Electron Microscopy. ***A:*** *Single particle class averages of Cbln1- βNeurexin1+SS4 LNS domain. The class averages of Cbln1 alone from Section 6.7, Figure 6.11 are shown in* ***B*** *for comparison. Unique features of the Cbln1- βNeurexin1+SS4 complex are shown highlighted by the white arrows. The scale bar represents 50 Å.*

Surface plasmon resonance based techniques were chosen as the strategy to verify the inference from the class averages that Neurexin interacts with the Cys-knot domain of Cbln1. In this case, various versions of Cbln1 were chosen as ligands and the LNS domain of βNeurexin1+SS4 was chosen as the analyte. To follow this strategy, Cbln1 (Q22-L193), Cbln1 C1q (CB_4) and Cbln1 CS were cloned into pHLsec Avitag3 vector as described in Section 2.1 and Appendix 8.1. These ligand samples were then produced and biotinylated as described in Section 2.9.2. To prepare the analyte, HEK 293T cells were transfected with the construct of βNeurexin1+SS4 LNS domain described in Appendix 8.1. Conditioned media was then prepared and subjected to IMAC followed by SEC. Figure 6.14 displays a representative SEC profile and SDS-PAGE analysis of SEC fractions; greater than 99 % purity of the βNeurexin1+SS4 LNS domain was achieved.

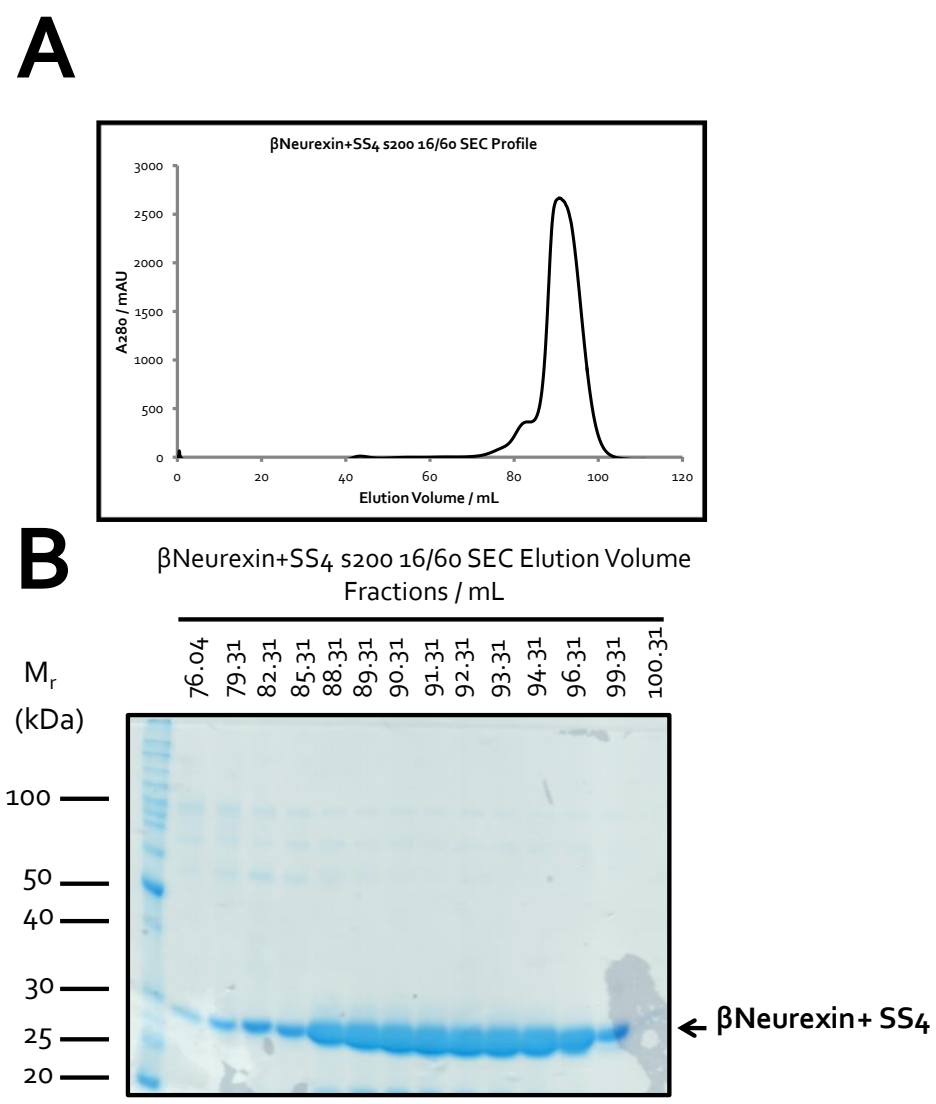

Figure 6.14: Purification of the βNeurexin1+SS4 LNS domain. A: *SEC profile from the purification of the βNeurexin1+SS4 LNS domain, monitoring A280 absorbance against elution volume through an s200 16/60 column.* ***B:*** *SDS-PAGE examination of the βNeurexin1+SS4 SEC fractions.*

Cbln1, Cbln1 C1q and Cbln1 CS ligands were indirectly immobilised onto the chip surface through ligand capture (Section 2.9.2). Following preparation of the sensor surface, conditions for regeneration of the surface were delineated; for Biacore experiments involving Cbln1 and Neurexin three injections of 3 M $MgCl_2$ over 300 s was used for regeneration. Injections of a dilution series of the βNeurexin1+SS4 LNS domain were made in duplicate and multi-cycle equilibrium binding

analysis was performed. Figure 6.15 presents the sensorgrams and binding curves for binding experiments between Neurexin and constructs of Cbln1.

SPR analysis using this system found that βNeurexin1+SS4 directly interacted with Cbln1 (Figure 6.15A), verifying previous reports (Uemura et al, 2010). The binding constant for the Cbln1-Neurexin interaction was calculated to be 137.5 ± 28.96 nM. However, Uemura et al, 2010 reported a K_d of 0.17 nM. This discrepancy in calculated binding constants could be a result of the different methods and analysis strategies applied in each study; for example Uemura et al, 2010 used kinetics analysis and a two-state reaction model to analyse their data, whereas for the data presented in Figure 6.15 a single-site binding model was applied, following the implication from the Cbln1-Neurexin class averages presented in Figure 6.13A.

Furthermore, SPR analysis showed clearly that βNeurexin1+SS4 is not able to interact with either the Cbln1 C1q domain or Cbln1 CS (Figure 6.15B-C). This corroborates the suggestion from the EM Cbln1-Neurexin class averages that Neurexin interacts with the Cys-knot domain of Cbln1 (Figure 6.13A). Furthermore since the trimeric Cbln1 CS (Figure 6.15C) is not able to interact with βNeurexin1+SS4, the implication is that hexamerization of Cbln1 is required for the interaction with Neurexin, which is in agreement with previous findings (Uemura et al, 2010).

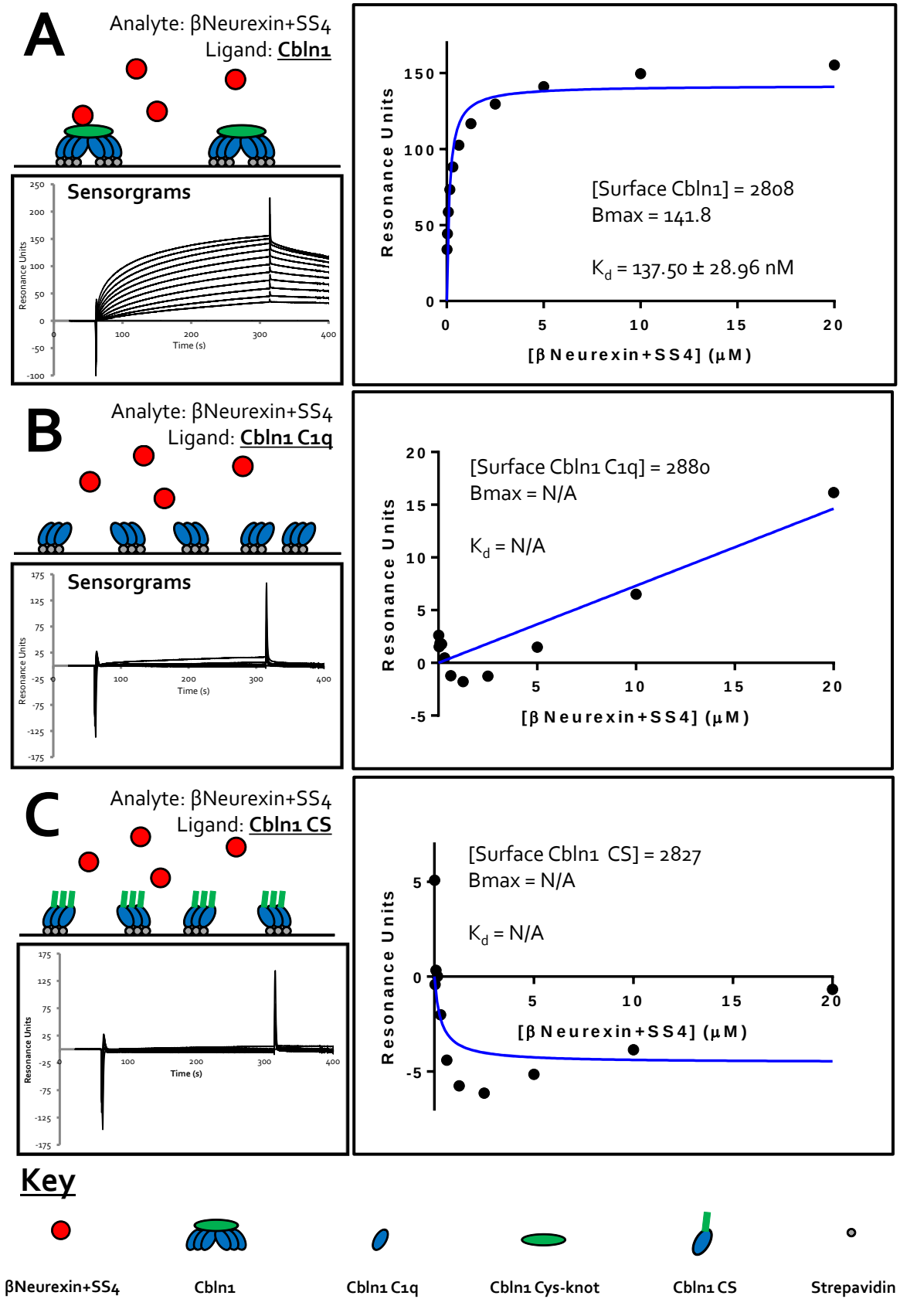

Figure 6.15: SPR Binding Studies of the Interaction between Cbln1 and βNeurexin1+SS4.

Figure 6.15: SPR Binding Studies of the Interaction between Cbln1 and βNeurexin1+SS4. Top Left Image of each Panel A-C: *A schematic representing the experimental set-up to study the interaction between βNeurexin1+SS4 and either full-length Cbln1 in* ***A****, the Cbln1 C1q domain in* ***B*** *or Cbln1 CS in* ***C****.* ***Bottom left of each Panel A-C:*** *Experimental, reference-subtracted sensorgrams displaying real-time binding and unbinding of the analyte to the ligand.* ***Right Image of each Panel A-C:*** *Binding curve for the interaction under test. The amount of ligand coupled to the chip, the binding curve-derived Bmax and K_d are listed.*

To further characterise the molecular basis for the interaction between Cbln1 and Neurexin, three deletion mutants of the N-terminal extension from each Cbn1 subunit were designed and synthesised as described in Section 2.1 and Appendix 8.1. The specific amino acids from the native Cbln1 sequence that were deleted in each mutant are detailed in Figure 6.16A. In brief: in construct CB50 amino acids 55-58 are deleted, and the following point mutations were made N41M, T43A, D45A, S59A; in construct CB52 amino acids 52-58 are deleted and the same point mutations were introduced N41M, T43A, D45A, S59A; and in construct CB54 amino acids 48-58 were deleted and the same point mutations engineered N41M, T43A, D45A, S59A. As these mutants would be used as ligands to allow SPR analysis of the effect of the mutations on binding to βNeurexin1+SS4, the deletion mutants were cloned into the pHLsec-Avitag3 vector. The Cbln1 deletion mutant ligands were expressed and biotinylated as described in Section 2.9.2; Figure 6.16B exhibits their positive expression and secretion from HEK293T cells. The sensor surface was prepared with the various ligands before a dilution series of βNeurexin1+SS4 LNS domain was flowed over the chip surface in duplicate. Multi-cycle equilibrium analysis was applied to the binding data. The regeneration procedure used in this case was three 300s injections of 3 M MgCl2.

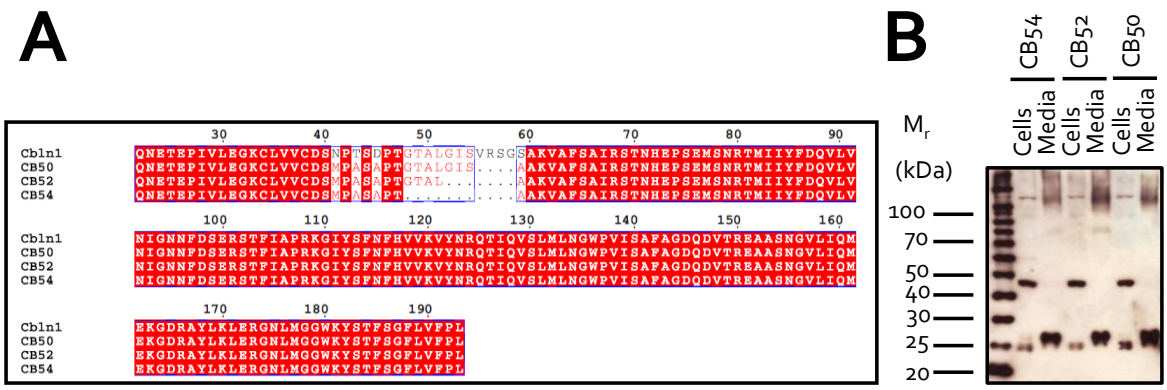

Figure 6.16: Cbln1 Deletion Mutants. ***A:*** *Sequence alignment highlighting the difference between Cbln1 and the three versions of Cbln1 deletion mutants, CB50, CB52 and CB54.* ***B:*** *Anti-His western blot of a small-scale expression trial for the three Cbln1 deletion mutants.*

SPR analysis demonstrated that all the Cbln1 deletion mutants were able to bind to the βNeurexin1+SS4 LNS domain with comparable affinities to wild-type Cbln1 (Figure 6.17). Although a 1:1 binding model does not fit the data as well as for native protein (Figure 6.15), possibly reflecting a potential impairment of binding, which could be a result of steric hindrance, for example. The indication from this is that Cbln1 amino acids G48-S59 are not required for the interaction between Cbln1 and βNeurexin1+SS4 LNS domain. Furthermore it is possible to exclude N41, T43, and D45 from the Neurexin binding site in Cbln1. Hence we can narrow the Cbln1 residues that potentially mediate the interaction with Neurexin to between E24-T47, discounting N41, T43, and D45. The conclusion from the evidence presented in Figure 6.17 is at odds with a previous study that suggested that the region between S57-A60 in Cbln1 is important in mediating binding with Neurexin (Lee et al, 2012). This discrepancy may be a result of the different techniques employed, i.e. this study employed SPR binding analysis with crystallization-grade purified protein and protein concentrations determined with a NanoDrop spectrophotometer whereas Lee et al, 2012 used SPR and 'protein concentrations were estimated by Western blotting and SDS-PAGE with Coomassie staining'.

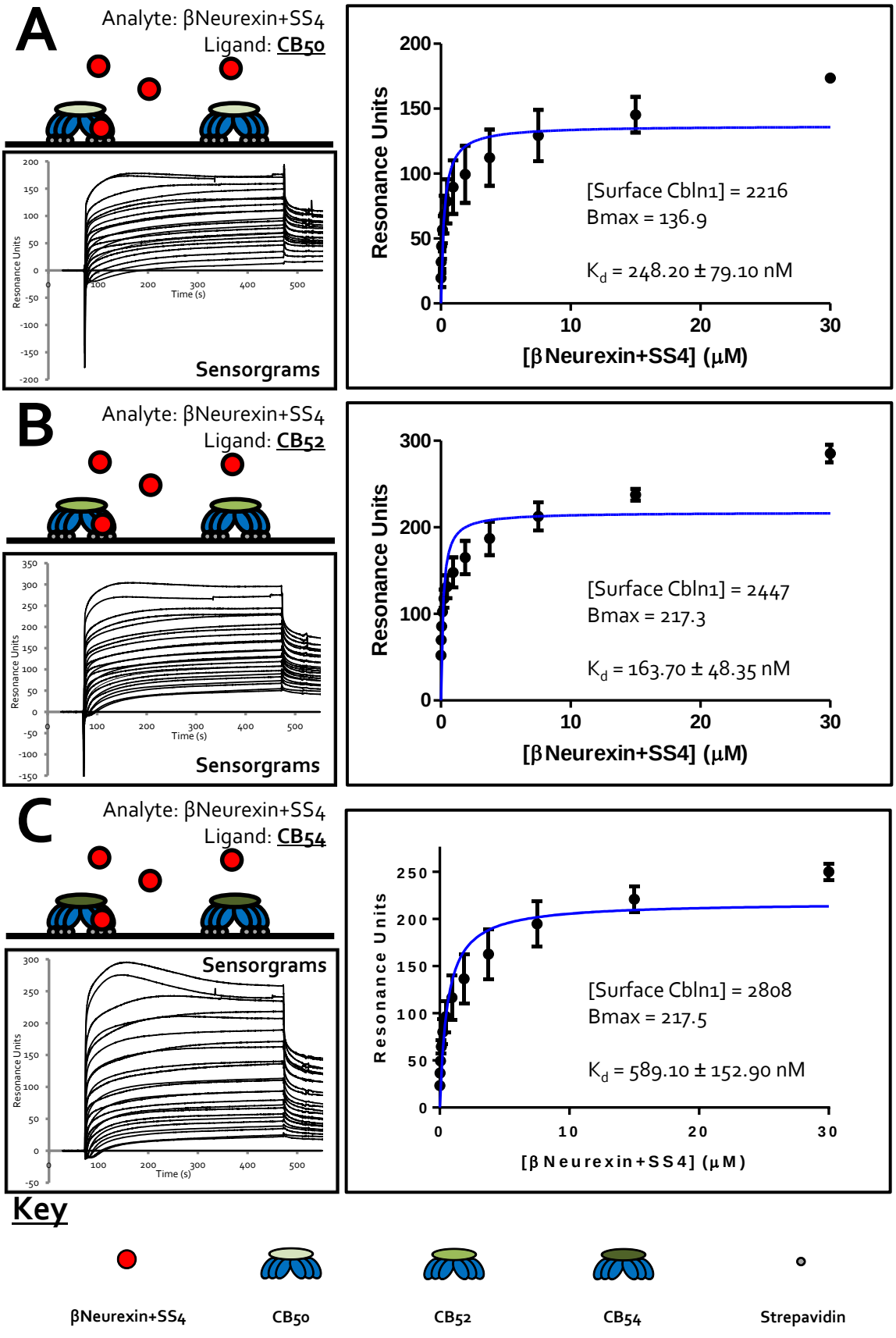

Figure 6.17: SPR Binding Studies of the Interaction between Cbln1 Deletion Mutants and βNeurexin1+SS4.

Figure 6.17: SPR Binding Studies of the Interaction between Cbln1 Deletion Mutants and βNeurexin1+SS4. ***Top Left Image of each Panel A-C:*** *A schematic representing the experimental set-up to study the interaction between βNeurexin1+SS4 and either Cbln1 construct CB50 in* ***A****, CB52in* ***B*** *or CB54 in* ***C****.* ***Bottom left of each Panel A-C:*** *Experimental, reference-subtracted sensorgrams displaying real-time binding and unbinding of the analyte to the ligand.* ***Right Image of each Panel A-C:*** *Binding curve for the interaction under test. The amount of ligand coupled to the chip, the binding curve-derived Bmax and K_d are listed.*

6.9 Investigating the Interaction between Cbln1 and GluD2

The initial study that reported the interaction between Cbln1 and GluD2 proposed that hexamerization of Cbln1 was necessary to allow the interaction, based on immunohistochemical studies (Matsuda et al, 2010). This suggested that the GluD2 binding epitope on Cbln1 was only created upon higher order oligomerization. Regarding the Cbln1 binding site in GluD2, two separate studies confirmed that the ATD of GluD2 was the domain that interacted with Cbln1 (Matsuda et al, 2010; Uemura et al, 2010). Following this, alanine scanning mutagenesis and immunohistochemistry was used to highlight that the ATD 'Flap-loop' (R345-W363) was an important region for the interaction with Cbln1 (Kuroyanagi & Hirano, 2010). Furthermore, it has been suggested that dimeric GluD2 ATD and hexameric Cbln1 interact in a 1:1 ratio, meaning that the intact transmembrane GluD2 would interact with hexameric Cbln1 with a ratio of 1:2 (Lee et al, 2012). One inference from this is that the minimal binding site for Cbln1 binding in GluD2 could be the ATD dimer. Additionally, W136 of Cbln1 has been implicated in mediating the interaction with GluD2 (Lee et al, 2012).

I intended to validate these observations using crystallization-grade purified proteins and integrate this data with the GluD2 ATD, GluD1 ATD and Cbln1 C1q structural information described earlier in this thesis (Section 3.5, 3.7 and Section 6.6). The first question was whether GluD2 ATD interacted

with the Cbln1 Cys-knot domain or the C1q domain, as both were previously suggested (Matsuda et al, 2010; Schmid & Hollmann, 2010). To answer this question, SPR studies were instigated where GluD2 ATD was the analyte and either full-length Cbln1 (Q22-L193, CB2) or the Cbln1 C1q domain (S569-L193, CB4) as the ligand immobilised on the chip. Multi-cycle equilibrium binding experiments were carried out as described in 2.9.3.

GluD2 ATD was found to interact with both full-length Cbln1 (Figure 6.18A) and the isolated Cbln1 C1q domain (Figure 6.18B). A binding constant for the interaction between GluD2 ATD and full-length Cbln1 was calculated as 19.72 ± 1.03 μM, whereas the K_d for the interaction between GluD2 ATD and the C1q domain of Cbln1 was determined as 10.18 ± 0.73 μM. This discrepancy between the two binding constants could be a result of the enhanced molecular freedom and reduced steric restraint in the C1q-only situation in comparison to full-length Cbln1. Since the oligomeric state of the isolated C1q domain is trimeric (Section 6.7, Figure 6.8), the evidence from the Biacore data presented in Figure 6.18 does not agree with a previous study that suggested that hexamerization of Cbln1 was necessary for the interaction with GluD2 ATD (Matsuda et al, 2010). However, the previous study used immunoblot and immunohistochemical studies which can often have low sensitivity, whereas SPR techniques are highly sensitive and provide real-time information regarding a test interaction, and when combined with pure protein samples can provide very reliable data. Two previous studies reported binding affinities of 167 nM (Matsuda et al, 2010) and 16.5 nM (Uemura et al, 2010) which vary by an order of magnitude, possibly reflecting the different techniques involved. Furthermore, the data presented in Figure 6.18 determines the K_d for the interaction between Cbln1 and GluD2 ATD to be between 10-20 μM. This again differs from other estimates of the affinity of the interaction, which again could be a result of different experimental approaches, perhaps in the method used to determine protein concentration. Nonetheless, if the interaction was to have a binding affinity in the low nanomolar range, this would suggest a very

strong interaction; but when Cbln1 and GluD2 ATD were co-expressed in mammalian cells, along with Neurexin, then subjected to IMAC and SEC, the proteins eluted as separate peaks in SEC, suggesting that no complex is formed (Figure 6.19). This behaviour in SEC is not characteristic of a low nanomolar affinity interaction, perhaps suggesting the estimate of Kd from Figure 6.18 is more reflective of the true affinity of the Cbln1-GluD2 ATD interaction.

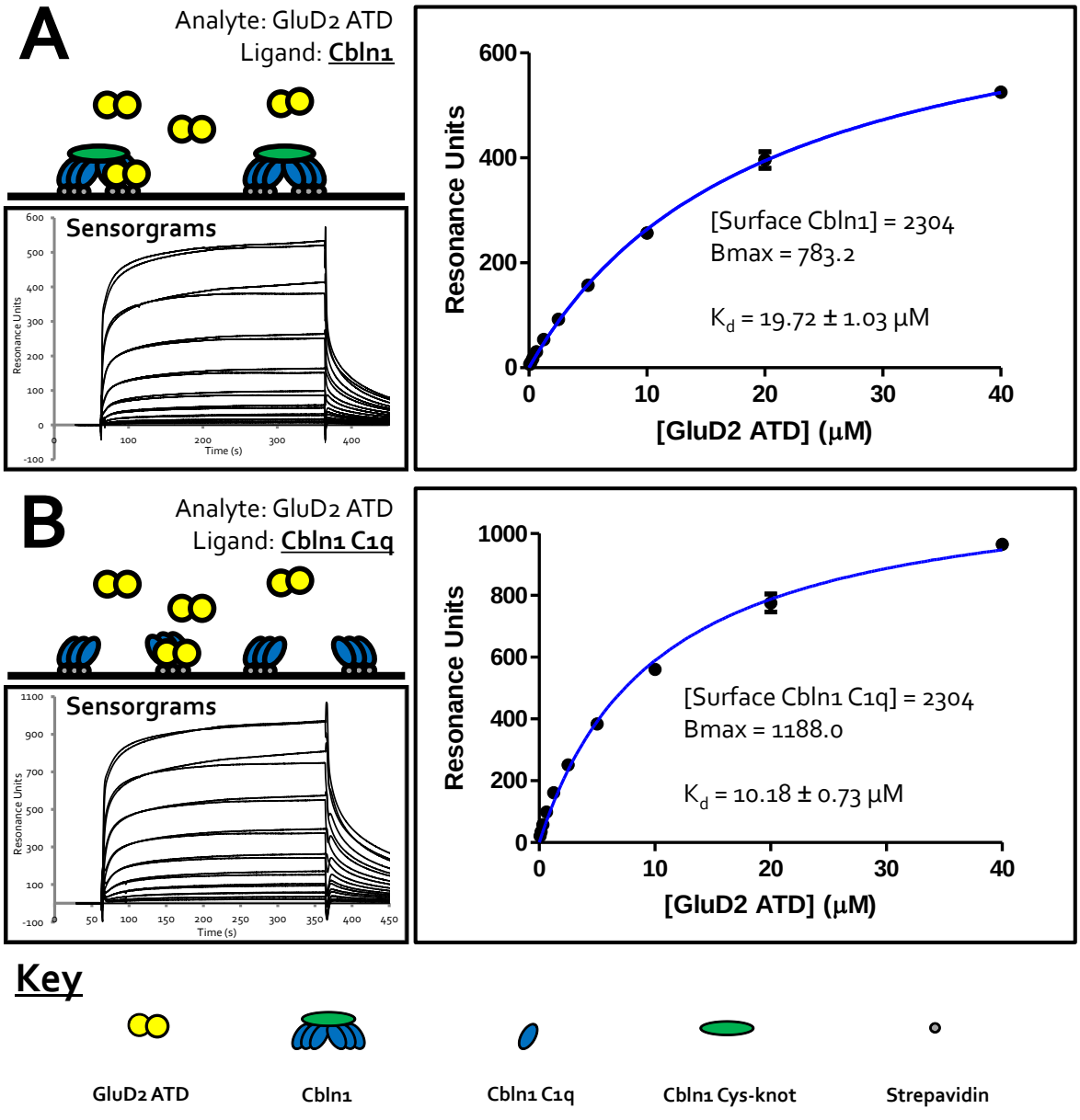

Figure 6.18: SPR Binding Studies of the Interaction between Cbln1 and GluD2 ATD.

Figure 6.18: SPR Binding Studies of the Interaction between Cbln1 and GluD2 ATD. Top Left Image of each Panel A-B: *A schematic representing the experimental set-up to study the interaction between GluD2 ATD and either full-length Cbln1 in* ***A*** *or Cbln1 C1q domain in* ***B****.* ***Bottom left of each Panel A-B:*** *Experimental, reference-subtracted sensorgrams displaying real-time binding and unbinding of the analyte to the ligand.* ***Right Image of each Panel A-C:*** *Binding curve for the interaction under test. The amount of ligand coupled to the chip, the binding curve-derived Bmax and K_d are listed.*

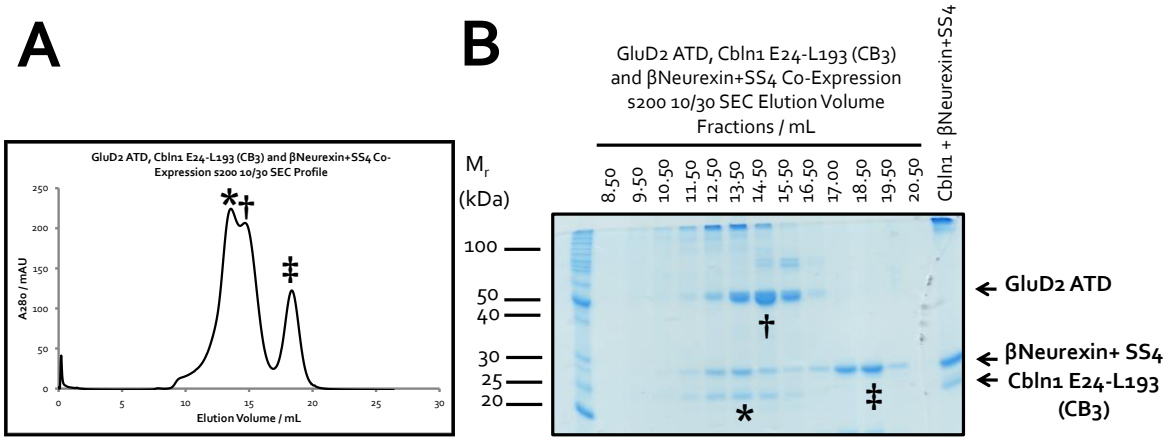

Figure 6.19: Analysis of the Neurexin-Cbln1-GluD2 ATD ternary complex through Size Exclusion Chromtography. A: *SEC profile from the co-expression and co-purification of GluD2 ATD, Cbln1 and βNeurexin+SS4.* ***B:*** *SDS-PAGE analysis of the SEC profile shown in* ***A****. * represents the Neurexin-Cbln1 complex, † highlights GluD2 ATD and ‡ Neurexin.*

Following this, the ability of GluD2 ATD F76D to bind to Cbln1 was tested. By testing this it would provide an answer to the question: Is the Cbln1 binding site in GluD2 across the ATD dimer, or is it possible for each ATD chain to independently interact with Cbln1? When using GluD2 ATD F76D (Section 4.3) in multi-cycle equilibrium SPR binding studies, it was demonstrated that monomeric GluD2 ATD was able to interact with both full-length Cbln1 and the C1q trimer. Calculated K_d values for the GluD2 ATD F76D-Cbln1 interactions – 24.36 ± 4.28 µM for GluD2 ATD F76D- full-length Cbln1 interaction (Figure 6.20A) and 24.40 ± 4.09 µM for GluD2 ATD F76D-Cbln1 C1q domain interaction (Figure 6.20B) – were comparable to that calculated for the GluD2 ATD-Full-length

Cbln1 interaction, 19.72 ± 1.03 μM (Figure 6.18A). This may be reflective of the removal of the avidity effect in the case of GluD2 ATD F76D. Hence we can now enhance a model of the Neurexin-Cbln1-GluD2 trans-synaptic complex by including the idea that the GluD2 ATD from each individual subunit has the capacity to interact with a single Cbln1 C1q trimer. However, in the formation of tans-synaptic complexes, steric restraints may prevent each individual GluD2 ATD from finding a Cbln1 binding partner.

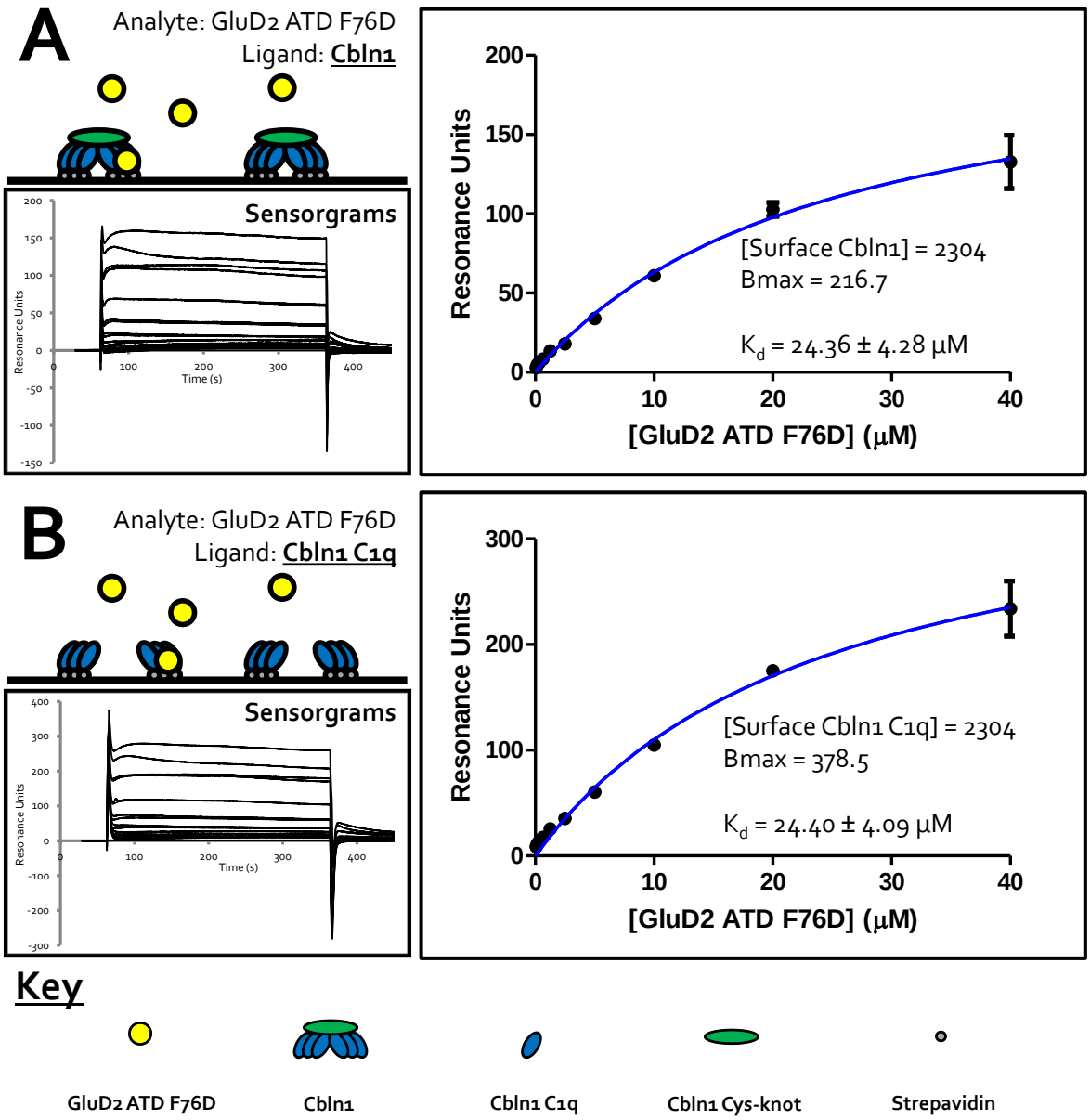

Figure 6.20: SPR Binding Studies of the Interaction between Cbln1 and GluD2 ATD F76D.

Figure 6.20: SPR Binding Studies of the Interaction between Cbln1 and GluD2 ATD F76D. Top Left Image of each Panel A-B: *A schematic representing the experimental set-up to study the interaction between GluD2 ATD F76D and either full-length Cbln1 in* ***A*** *or Cbln1 C1q domain in* ***B****.* ***Bottom left of each Panel A-B:*** *Experimental, reference-subtracted sensorgrams displaying real-time binding and unbinding of the analyte to the ligand.* ***Right Image of each Panel A-C:*** *Binding curve for the interaction under test. The amount of ligand coupled to the chip, the binding curve-derived Bmax and K_d are listed.*

A previous study highlighted GluD2 ATD 'Flap-loop', that is amino acids Arg345-Trp363, as the region in GluD2 that interacts with Cbln1 (Kuroyanagi & Hirano, 2010). The main technique used in this paper was alanine scanning mutagenesis coupled with immunohistochemistry, and one of the most intriguing findings was that one particular mutation, K346A (Figure 6.21A) seemed to enhance the interaction between GluD2 and Cbln1. In order to investigate this suggestion of enhanced binding further, and to provide additional evidence supporting the idea that the ATD 'Flap-loop' is indeed involved in mediating the interaction between Cbln1 and GluD2, SPR analysis, using GluD2 ATD K346A as the analyte, was performed. A construct of GluD2 ATD K346A was created using oligonucleotide-mediated mutagenesis, and this was used to transfect HEK 293T cells in large-scale. GluD2 ATD K346A conditioned media was then subjected to IMAC and SEC (Figure 6.21B). SDS-PAGE analysis of the purified GluD2 ATD K346A demonstrated that purity was adequate for use as an SPR analyte (Figure 6.21B).

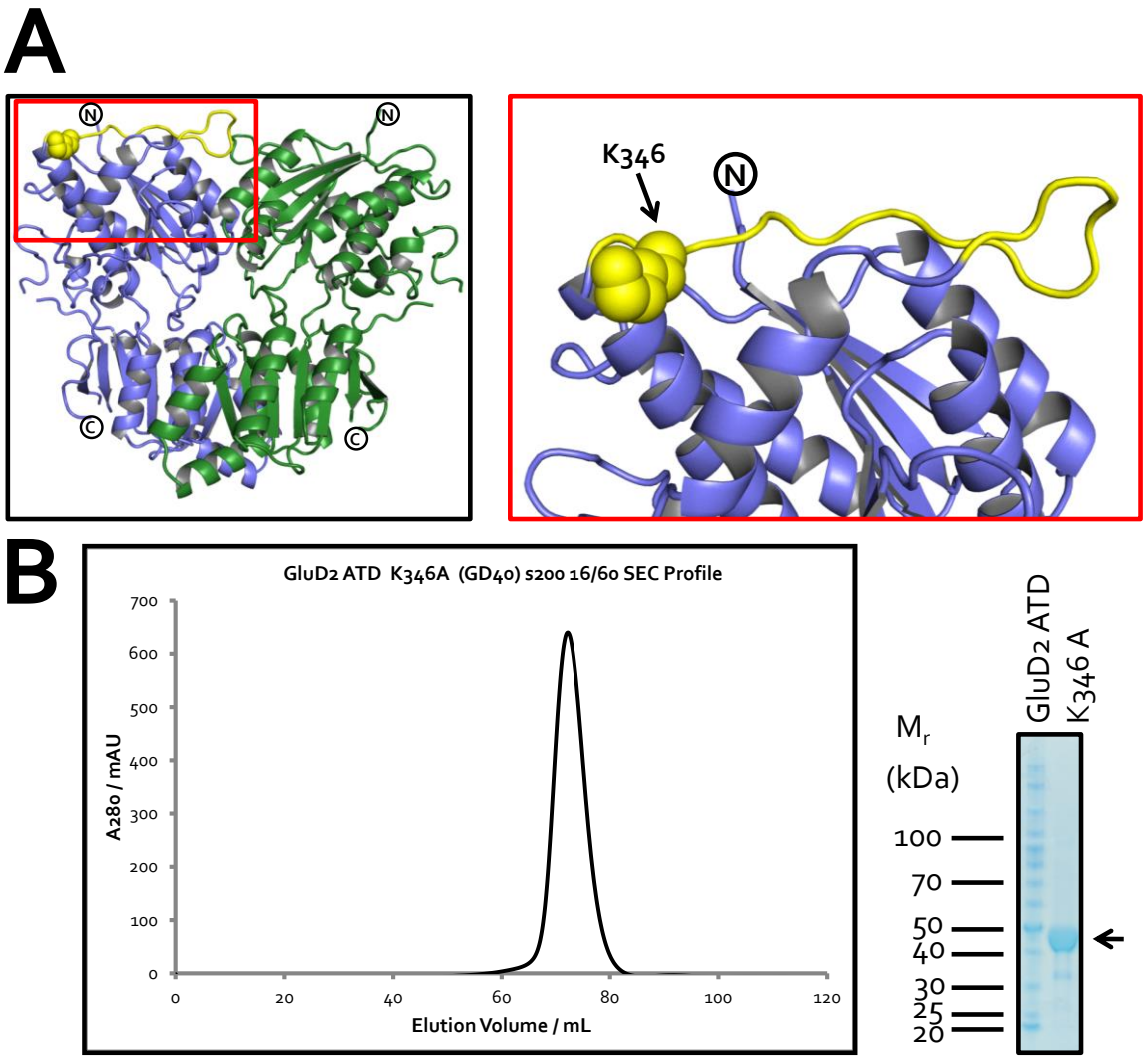

Figure 6.21: GluD2 ATD K346A. ***A:*** *Cartoon depiction of the GluD2 ATD, highlighting amino acid Lysine 346 (Labelled) and the 'Flap-loop' (Coloured n yellow).* ***B: Left Image:*** *An SEC profile from the purification of GluD2 ATD K346A.* ***Right Image:*** *SDS-PAGE analysis of the purified GluD2 ATD K346A.*

SPR analysis, using GluD2 ATD K346A as the analyte demonstrated that there was a mild enhancement in binding affinity to Cbln1 as a result of the K346A mutation, relative to wild-type GluD2 ATD. For example, the calculated K_d for K346A mutant's interaction with full-length Cbln1 was 12.19 ± 1.04 µM (Figure 6.22A), whereas the binding affinity for the interaction of wild-type GluD2 ATD with Cbln1 was calculated to 19.72 ± 1.03 µM (Figure 6.18A). In addition, the calculated

binding constant for K346A mutant's interaction with the isolated Cbln1 C1q domain was 6.61 ± 0.48 µM (Figure 6.22A), while the calculated K_d for the interaction between wild-type ATD and the isolated Cbln1 C1q domain was 10.18 ± 0.73 µM (Figure 6.18B). Thus there was a roughly two-fold augmentation in the binding properties as a consequence of the K346A mutation, which is in agreement with previous work (Kuroyanagi & Hirano, 2010). Hence, the evidence supplied in Figure 6.22 provides further support to the idea that Cbln1 interacts with the 'Flap-loop' of GluD2 ATD.

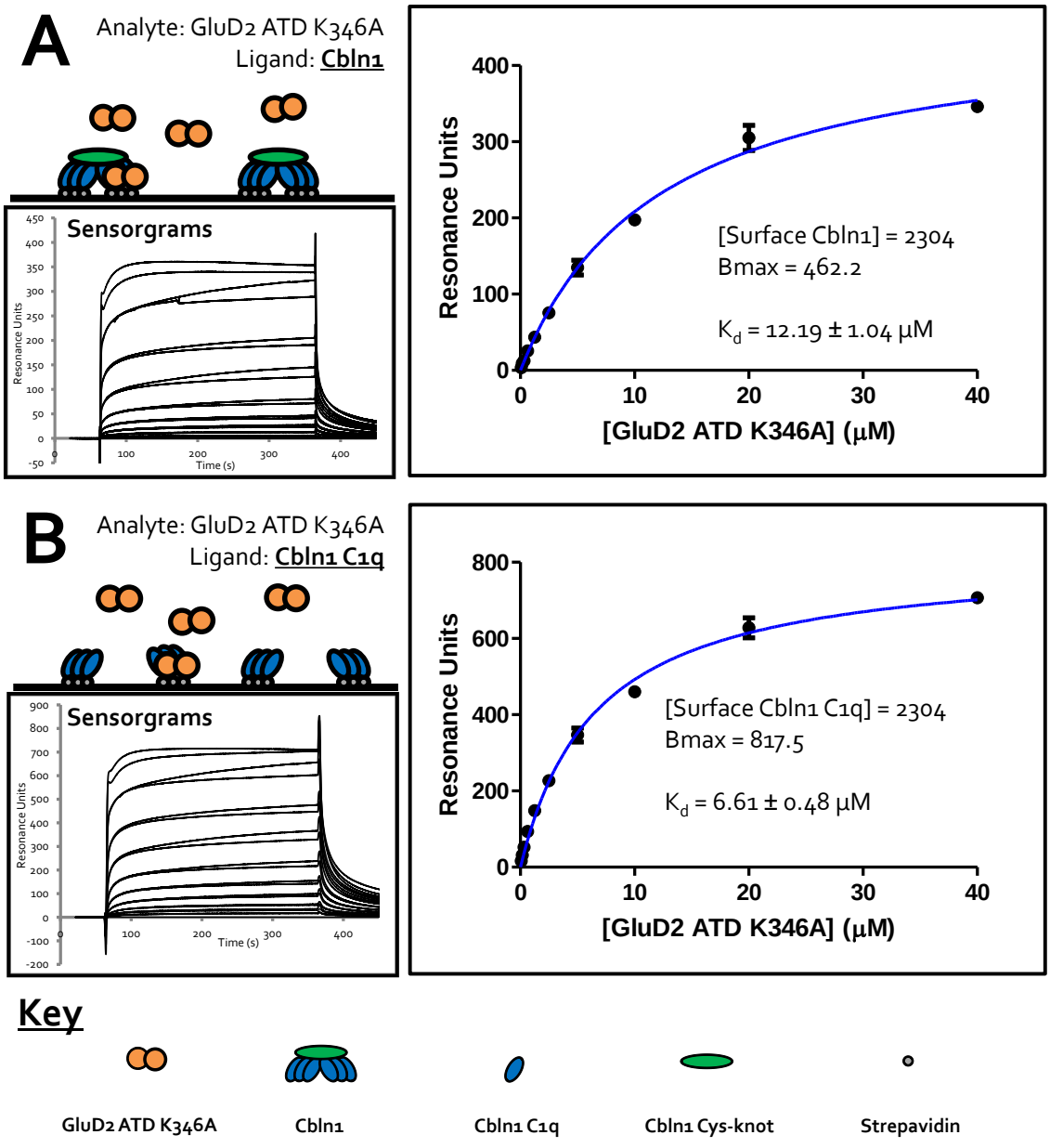

Figure 6.22: SPR Binding Studies of the Interaction between Cbln1 and GluD2 ATD K346A.

Figure 6.22: SPR Binding Studies of the Interaction between Cbln1 and GluD2 ATD K346A. Top Left Image of each Panel A-B: *A schematic representing the experimental set-up to study the interaction between GluD2 ATD K346A and either full-length Cbln1 in* ***A*** *or Cbln1 C1q domain in* ***B****.* ***Bottom left of each Panel A-B:*** *Experimental, reference-subtracted sensorgrams displaying real-time binding and unbinding of the analyte to the ligand.* ***Right Image of each Panel A-C:*** *Binding curve for the interaction under test. The amount of ligand coupled to the chip, the binding curve-derived Bmax and K_d are listed.*

Since the EM class averages of the Cbln1-Neurexin complex (Section 6.8, Figure 6.13A) suggest that the Cbln1 Cys-knot is the binding site for Neurexin, to allow the formation of a ternary trans-synaptic complex it is logical to hypothesise that the site of interaction with GluD2 is at the 'tip' of the C1q domain trimer (Figure 5.23). To test this idea, the crystal structure of the Cbln1 C1q domain (Section 6.6) was inspected to identify the amino acids that form the 'tip' of the C1q trimer. Three amino acids in particular were selected as candidates for alanine mutagenesis: Tyrosine 122, Arginine 124 and Aspartate 147 (Figure 6.23A). Two mutant expression constructs were produced using oligonucleotide-mediated mutagenesis, Cbln1 C1q D147A and Cbln1 C1q Y122A R124A, encoded in the pHLsec-Avitag3 vector; further details in Section 2.1 and Appendix 8.1. These mutant Cbln1 constructs were then tested in small-scale in HEK 293T cells; both constructs, Cbln1 C1q D147A and Cbln1 C1q Y122A R124A, were found to be expressed and secreted (Figure 6.23B).

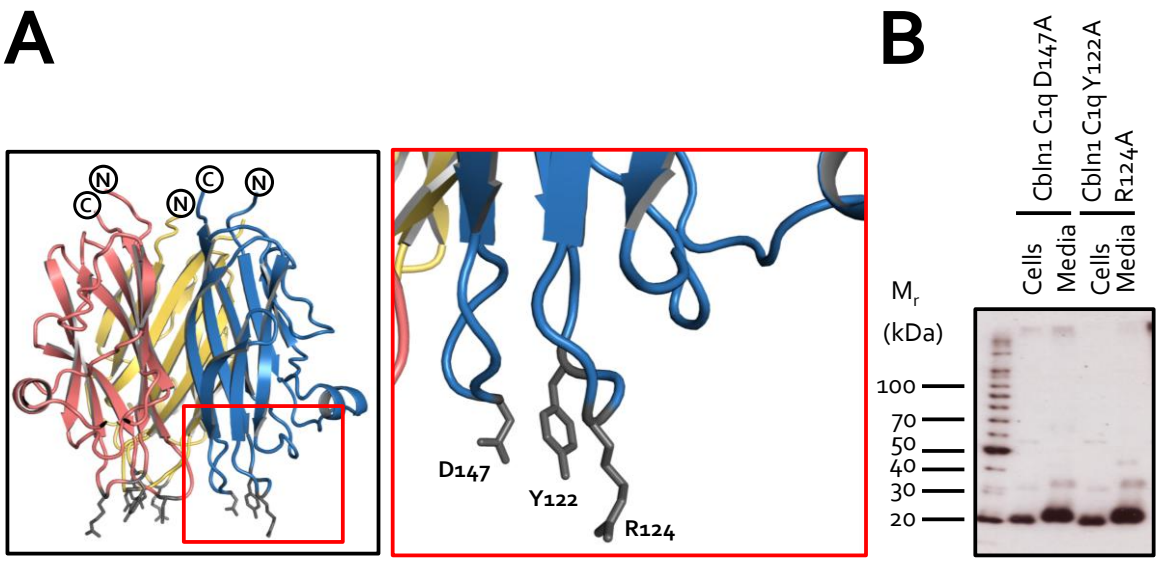

Figure 6.23: Cbln1 C1q D147A and Cbln1 Y122 R124A. ***A:*** *Cartoon depiction of the structure of the Cbln1 C1q domain, highlighting amino acids Tyrosine 122, Arginine 124 and Aspartate 147 (Labelled).* ***B:*** *Anti-His western blot analysis of a small scale expression trial of point mutant constructs of the amino acids displayed in* ***A****.*

These Cbln1 C1q point mutants were used as ligands in SPR analysis to assess the effect of the mutations on the interaction with the GluD2 ATD, the analyte, in multi-cycle equilibrium binding experiments. The D147A mutation of the Cbln1 C1q domain resulted in a roughly ten-fold reduction in the binding affinity to GluD2 ATD, i.e. the GluD2 ATD-Cbln1 C1q D147A K_d was calculated to 103.30 ± 9.98 µM (Figure 6.24B), compared to 8.56 ± 1.25 µM for the interaction between GluD2 ATD And wild-type Cbln1 C1q (Figure 6.24A). Additionally, the mutation of Y122 and R124 to Alanine resulted in the complete abolition of binding to GluD2 ATD (Figure 6.24C). Taken together, this provides strong evidence for the hypothesis that the tip of the Cbln1 C1q domain comprises part, if not all, of the site of interaction with GluD2.

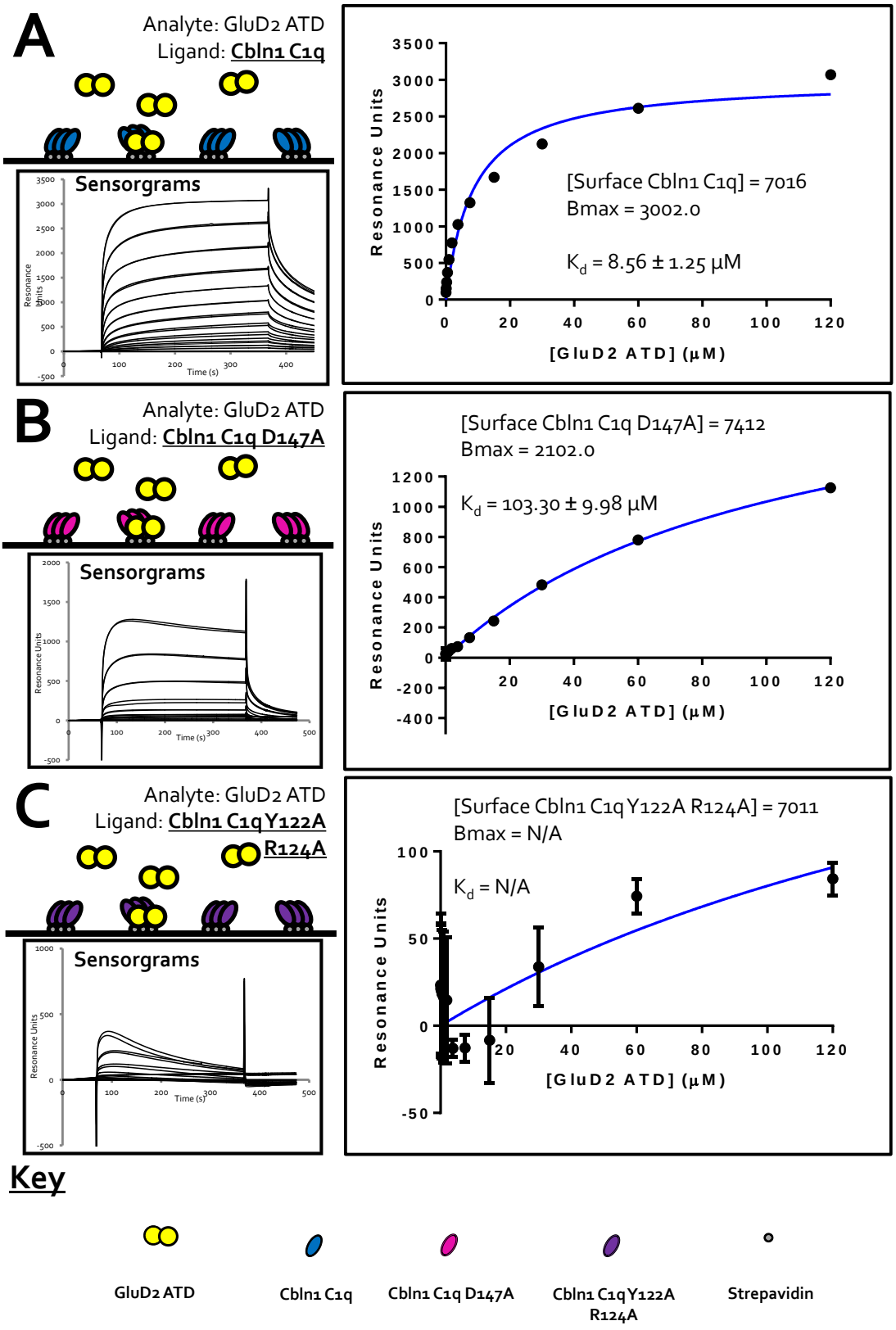

Figure 6.24: SPR Binding Studies of the Interaction between GluD2 ATD and the Cbln1 C1q Domain Mutants.

Figure 6.24: SPR Binding Studies of the Interaction between GluD2 ATD and the Cbln1 C1q Domain Mutants. A: Top Left Image of each Panel A-B: *A schematic representing the experimental set-up to study the interaction between GluD2 ATD K346A and either wild-type Cbln1 C1q in* ***A****, Cbln1 C1q D147A in* ***B*** *or Cbln1 C1q Y122A R124A in* ***C****.* ***Bottom left of each Panel A-B:*** *Experimental, reference-subtracted sensorgrams displaying real-time binding and unbinding of the analyte to the ligand.* ***Right Image of each Panel A-C:*** *Binding curve for the interaction under test. The amount of ligand coupled to the chip, the binding curve-derived Bmax and K_d are listed.*

The SPR analysis provides an insight into the molecular basis for the interaction between Cbln1 and GluD2. However, the best way to confirm such details would be to use X-ray crystallography to solve the structure of a complex between Cbln1 and GluD2. Whilst much effort was placed in this direction during the course of this DPhil, progress was limited due to a lack of high quality protein complex crystals. Since other members of the iGluR-Delta subfamily and Cbln family are known to interact (Yasumura et al, 2012), a follow-up investigation which focusses on characterising the structural details of some of these related interactions may be more conducive to study using X-ray crystallography. Indeed, SPR analysis of the interaction between GluD1 ATD and Cbln1 suggests that this interaction roughly four times stronger (4.95 ± 1.19 μM, Figure 6.25) than the interaction between GluD2 ATD and Cbln1 (19.72 ± 1.03 μM, Figure 6.18A).

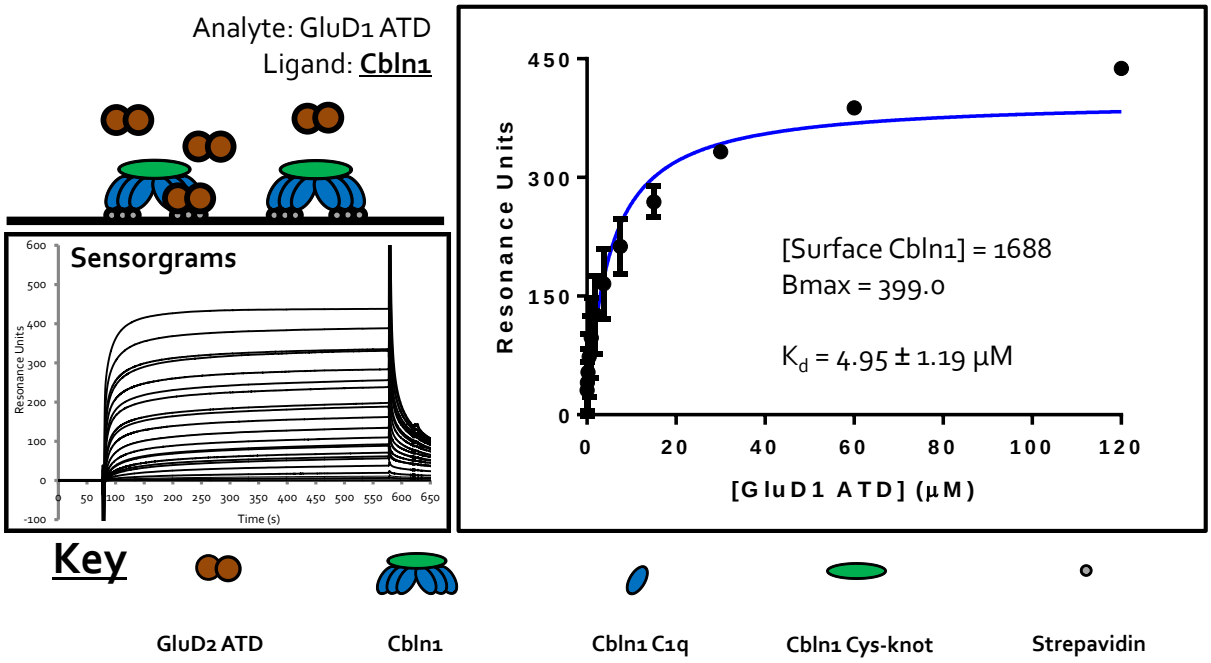

Figure 6.25: SPR Binding Studies of the Interaction between Cbln1 and GluD1 ATD. Top Left Image: *A schematic representing the experimental set-up to study the interaction between GluD1 ATD and full-length Cbln1.* ***Bottom left:*** *Experimental, reference-subtracted sensorgrams displaying real-time binding and unbinding of the analyte to the ligand.* ***Right Image:*** *Binding curve for the interaction under test. The amount of ligand coupled to the chip, the binding curve-derived Bmax and K_d are listed.*

6.10 Synopsis and Future Perspectives

To summarise, protocols for the production of various additional reagents for the characterization of the Neurexin-Cbln1-GluD2 trans-synaptic complex were established (Figure 6.2 and 6.14). Following this, a crystal structure of the Cbln1 C1q domain was solved to 2.4 Å, revealing a TNF-like jelly-roll topology, similar to other C1q and TNF domains, and the insertion of an α helix (α1) between the β1 and β2 sheets (Figure 6.5 and 6.6). Analysis of full-length Cbln1 using MALS (Figure 6.8) and single-particle negative stain EM (Figure 6.11) confirmed that Cbln1 is a disulphide mediated dimer of trimers. Significant effort was made towards the high resolution structural characterization of full-length Cbln1 using X-ray crystallography; however numerous technical

hurdles limited progress in this direction (Figure 6.9 and 6.10). Single-particle negative stain EM analysis of the complex between Cbln1 and βNeurexin1+SS4 inferred that the site of interaction with Neurexin was the Cbln1 Cys-knot domain (Figure 6.13); this was confirmed using SPR techniques (Figure 6.15). Deletion mutational analysis of Cbln1 indicated that the binding site for Neurexin in Cbln1 lies in the amino acid range E24-T43 (Figure 6.17). GluD2 ATD was found to interact with the C1q domain of Cbln1 (Figure 6.18) and the 'tip' of the C1q domain; in particular, amino acids Y122, R124 and D147 of Cbln1 were found to be crucial residues mediating the interaction with GluD2 ATD (Figure 6.23 and 6.24). Moreover, monomeric GluD2 ATD was able to bind to Cbln1 (Figure 6.20) and further evidence was provided for the idea that the 'Flap-Loop' of GluD2 and specifically K346 is involved in mediating the interaction with Cbln1 (Figure 6.22) (Kuroyanagi & Hirano, 2010). Using these molecular details and other published information, the docking program HADDOCK (de Vries et al, 2007) was used to provide a model for the mode of interaction between Cbln1 and GluD2 (Figure 6.26).

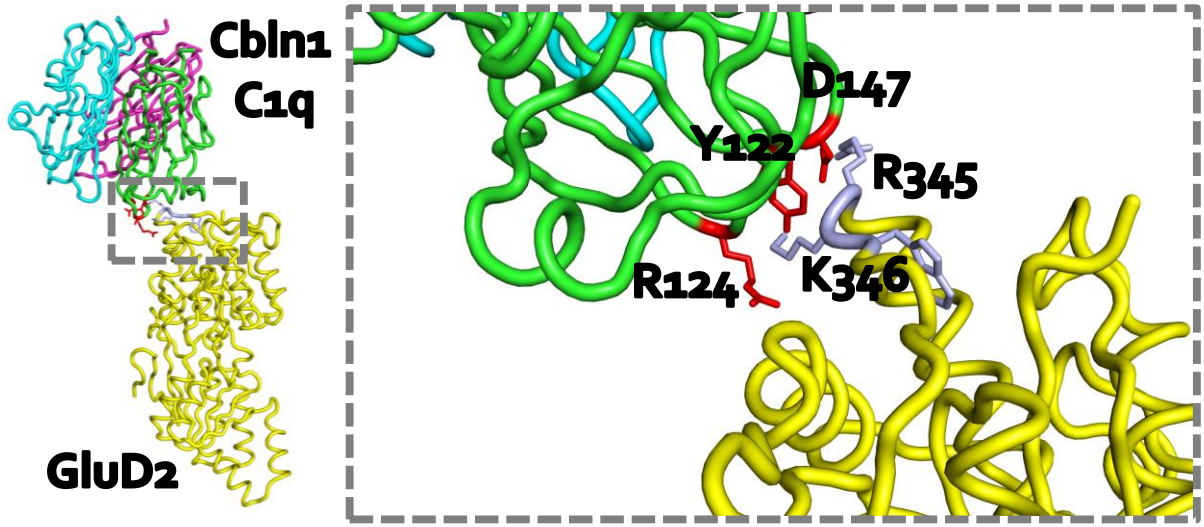

Figure 6.26: A Model for the Interaction between Cbln1 and GluD2. *Cartoon representation of the HADDOCK (de Vries et al, 2007) structural model for the interaction between GluD2 and Cbln1. Important residues are highlighted.*

Assimilating all this data together, it is possible to propose a model for the structure of the Neurexin-Cbln1-GluD2 trans-synaptic complex (Figure 6.27). In this model, one molecule of pre-synaptic Neurexin interacts with one molecule of hexameic Cbln1. The base of the Cbln1 C1q trimer has the potential to interact with monomeric GluD2 ATD; however steric restraints resulting from the oligomerization state of hexameric Cbln1 and tetrameric GluD2, may restrict the binding pattern between Cbln1 and GluD2, but also lead to the formation of a trans-synaptic protein array. The formation of such an array of proteins involving synaptic proteins is not unprecedented; the tyrosine kinase EphB and its ligand ephrin have been demonstrated to form signalling clusters (Seiradake et al, 2010), and the formation of a similar array has been observed for the Neurexin-Neuroligin complex (Tanaka et al, 2012). The model proposed in Figure 6.27 is presented as a linear model for simplicity, but it is likely that this molecular array will extend into a planar network. The upshot of the binding mode proposed in Figure 6.27 is a clustering mechanism of the Neurexin-Cbln1-GluD2 ternary trans-synaptic complex which may be crucial for the induction of the various signalling and functional events that this trans-synaptic complex is involved in, i.e. PF-PC synapse formation, LTD as well as motor control and learning (Schmid & Hollmann, 2010).

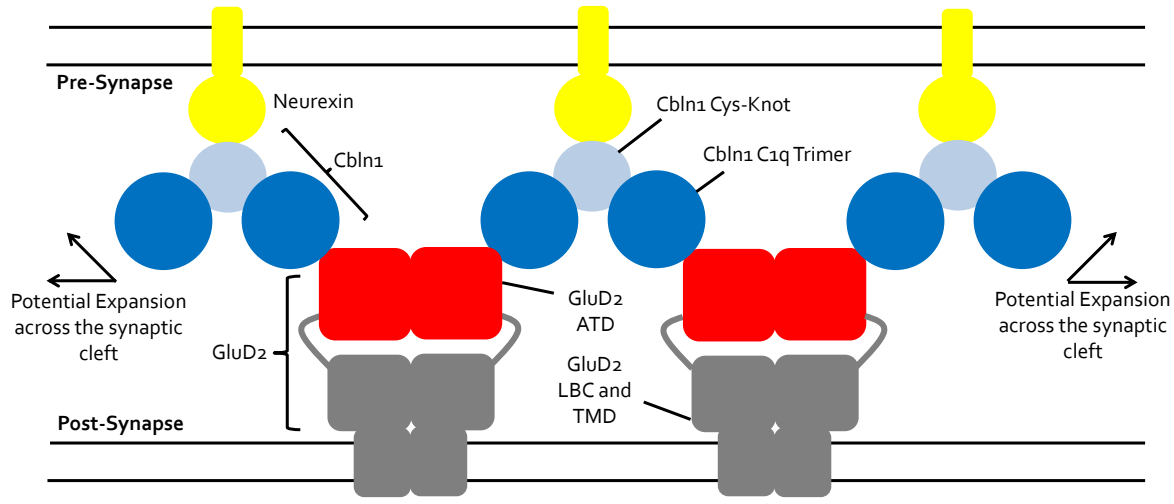

Figure 6.27: The Trans-Synaptic Triad Array Model: *A Schematic representing a model for the formation of a trans-synaptic array involving the ternary complex between pre-synaptic Neurexin, the bridging protein Cbln1 and post-synaptic GluD2.*

The model proposed in Figure 6.27 still needs confirmation through further investigation and additional data. Currently high resolution structural information is available for βNeurexin+ss4 (Koehnke et al, 2010; Shen et al, 2008), the C1q domain of Cbln1 (Section 6.6) and the ATD of GluD2 (Section 3.5). A high resolution crystal structure of full-length Cbln1, or a related Cbln, would undoubtedly aid the understanding of the trans-synaptic complex. Furthermore, a structural snapshot of the interaction between Neurexin-Cbln1 and Cbln1-GluD2, or related proteins would help to confirm or modify the binding models proposed in this chapter. Hence, these lines of investigation would certainly be the next logical next steps to investigate this trans-synaptic complex. Furthermore, the use of alternative techniques such as electron tomography (Ibiricu et al, 2011) could also be a useful method for investigating the proposed formation of trans-synaptic arrays. If such an approach were to be successful, tomography data could be combined with high resolution crystal structures and functional experiments to provide a complete understanding of the molecular details of this system and hence provide a prototypic example of the modes of interaction between iGluRs and other trans-synaptic proteins, and their biological consequences.

Chapter 7:

Further Discussion

7. Further Discussion

To enhance the understanding of the molecular details of synaptogenesis and the supra-molecular organisation of trans-synaptic proteins, a ternary complex involving pre-synaptic Neurexin, members of the Cbln family of secreted glycoproteins and post-synaptic Delta-family iGluRs was targeted for investigation (Ryu et al, 2012; Uemura et al, 2010). A version of this trans-synaptic complex containing βNeurexin1+SS4, Cbln1 and GluD2 is found exclusively at the synapses between parallel fibres and Purkinje cells in the cerebellum (Schmid & Hollmann, 2010). This triad is hugely important for the correct synaptogenesis in the cerebellum and for the normal functioning of the PF-PC synapse (Schmid & Hollmann, 2010); for example disruption of this ternary complex leads to aberrations in cerebellar LTD, as well as whole animal motor control and motor learning (Hirai et al, 2005; Kashiwabuchi et al, 1995). In the immature cerebellum, it was recently established that GluD2 is crucial for the onset of D-Serine dependent LTD, and that this has an impact on the motor learning in the preadolescent animal (Kakegawa et al, 2011). Moreover, individual members of this triad have been linked to complex neurological diseases such as motor disorders (Ichikawa et al, 2009; Kubota & Takahashi, 2008), schizophrenia (Guo et al, 2007; Treutlein et al, 2009), bipolar (Fallin et al, 2005) and autism spectrum disorders (Feng et al, 2006; Glessner et al, 2009; Marshall et al, 2008). The molecular details of the Neurexin-Cbln1-GluD2 complex are not well established and thus the proposed molecular mechanisms behind its involvement in the formation and function of this synapse are incomplete.

Work presented in this thesis led to: i) A 1.8 Å crystal structure of the GluD2 ATD (Section 3.5); ii) A 2.25 Å crystal structure of the GluD1 ATD crystal structure (Section 3.7); iii) The characterization of the GluD2 ATD interface (Section 3.8) and the functional effects of disruption of this interface (Chapter 4), resulting in a proposed molecular mechanism for the induction of D-Serine dependent LTD in the immature cerebellum (Section 4.8, Figure 4.10); iv) A 2.4 Å crystal structure of the C1q

domain of Cbln1 (Section 6.6); v) A model for the formation and clustering of the Neurexin-Cbln1-GluD2 trans-synaptic complex based on structural, biophysical and targeted mutagenesis studies (Sections 6.7-6.10); vi) A suggestion for the domain arrangement of the GluD2 ecto-domain supported by structural and mutagenesis studies (Sections 5.3-5.7); and vii) The establishment of protocols for the expression and purification of recombinant transmembrane GluD2 (Sections 5.8-5.9). Altogether these data enhance our understanding of the molecular details of this trans-synaptic triad and provides a platform for its future analysis and comprehension as a prototypical example of a trans-synaptic network.

The future trajectory of the structural analysis of this synapse-spanning complex should focus on three specific goals. Firstly the use of soluble proteins and protein domains – the expression and purification of which have been established here – to gain a crystal structure of a Neurexin-Cbln-iGluR Delta ternary complex and its component interactions; to achieve this, focus could be placed on other members of the respective families such as GluD1 and Cbln2-4 as these related proteins may prove to be more conducive to study by protein crystallographic methods. A second direction would be to continue with the effort to gain a structural insight into full-length Delta iGluRs, following the protocols established for the expression and purification of a transmembrane construct of GluD2 here. To achieve this, membrane protein crystallography should be the primary technique employed as, if successful, this would provide the most information rich data, but other techniques such as single-particle negative stain electron microscopy and solid-state NMR could be investigated as alternatives, or in a combined approach. A final suggested line of enquiry would be to investigate the proposed clustering model for the higher-order arrangement of the Neurexin-Cbln-GluD synapse-spanning triad (Figure 6.27). Relevant techniques for this investigation could include electron tomography (Ibiricu et al, 2011) and super-resolution light microscopy methods

such as stimulated emission depletion (STED) and stochastic optical reconstruction microscopy (STORM) (Huang et al, 2010).

The formation of elaborate neural networks is vital for the ability of the human brain to control a multitude of complex processes ranging from higher learning and perception to the control of motor skills and coordination. Neural network formation is dependent upon the precise connection and alignment between the billions of neurons in the brain at specialised cell junctions termed synapses. Elucidation of the molecular mechanisms behind the formation and regulation of synapses is thus essential for the complete understanding of neural wiring and higher brain functions, as well as recognising and rectifying the irregularities that result in numerous neurological and neuropsychiatric disorders such as autism spectrum disorders, schizophrenia and Alzheimer's disease. The protein content of synapses number into the thousands of individual members (Bayes et al, 2011) and synapse formation requires the synchronised formation of large assemblies of proteins and specialized membrane domains (McAllister, 2007; Waites et al, 2005). A number of trans-synaptic protein complexes have been identified as having a role in synapse formation and function including: Neurexin-Neuroligin (Graf et al, 2004), SynCAM (Biederer et al, 2002), N-cadherins (Togashi et al, 2002), SALMs (Ko et al, 2006), EphB-ephrin (Kayser et al, 2006), PTPδ-Slitrk3 (Takahashi et al, 2012) and LAR-NGL-3 (Woo et al, 2009). Whilst some details are known, a complete understanding of the molecular minutiae of these synapse-spanning complexes is not currently available and very little is known about the higher-order organisation of these trans-synaptic molecules once they are amalgamated into a trans-synaptic network of interactions (Lucic et al, 2005; Zuber et al, 2005).

A complete understanding of molecular neurobiology will not be achieved until: i) All the interactions between the thousands of individual components have been characterised and compiled into interaction super-maps; and ii) These have been combined with structural, functional and mechanistic data for the individual elements and constituent supra-molecular networks. Such an achievement, and the vast amount of work and technological advancement that would be required to reach this target, would unquestionably lead to new strategies and therapeutics for the improvement of human mental health. The work presented in this thesis, and the suggested follow-up work, would make a contribution to this ultimate goal.

Chapter 8:

Appendices

Appendix 8.1 Details of All Constructs Prepared for this Thesis

Construct Name	Parent Protein and Construct Amino Acid Boundaries	PCR Template	Primers (5′ -> 3′)	Destination Vector	Cloning Strategy
GD1	GluD2: Met1-Thr430	Human GRID2, GenBank entry BC099653, Image clone 40008397.	Fwd: cgaggaattcgccaccATGGAAGTTTTCCCCTTG CTCTTGGTTTTGTC Rev: cgcggtaccAGTCAGTGACCCATTCAGACCTGTG AC	pHLsec	PCR product digested with EcoRI and KpnI. Destination vector digested with EcoRI and KpnI.
GD2	GluD2: Met1-Asn426Gln	Human GRID2, GenBank entry BC099653, Image clone 40008397.	Fwd: cgaggaattcgccaccATGGAAGTTTTCCCCTTG CTCTTGGTTTTGTC Rev: cgcggtaccTCCACGCATGTTATTCTCCAATTTC TTGTCAG	pHLsec	PCR product digested with EcoRI and KpnI. Destination vector digested with EcoRI and KpnI.
GD3	GluD2: Met1-Gly440	Human GRID2, GenBank entry BC099653, Image clone 40008397.	Fwd: cgaggaattcgccaccATGGAAGTTTTCCCCTTG CTCTTGGTTTTGTC Rev: cgcggtaccTCCACGCATGTTATTCTCCAATTTC TTGTCAG	pHLsec	PCR product digested with EcoRI and KpnI. Destination vector digested with EcoRI and KpnI.
GD4	GluD2: Asp24-Thr430	Human GRID2, GenBank entry BC099653, Image clone 40008397.	Fwd: cgcaccggtGATTCGATCATTCACATCGGAGCAA TTTTTGATG Rev: cgcggtaccAGTCAGTGACCCATTCAGACCTGTG AC	pHLsec	PCR product digested with AgeI and KpnI. Destination vector digested with AgeI and KpnI.
GD5	GluD2: Asp24-Asn426Gln	Human GRID2, GenBank entry BC099653, Image clone 40008397.	Fwd: cgcaccggtGATTCGATCATTCACATCGGAGCAA TTTTTGATG Rev: cgcggtaccTCCACGCATGTTATTCTCCAATTTC TTGTCAG	pHLsec	PCR product digested with AgeI and KpnI. Destination vector digested with AgeI and KpnI.
GD6	GluD2: Asp24-Gly440	Human GRID2, GenBank entry	Fwd: cgcaccggtGATTCGATCATTCACATCGGAGCAA TTTTTGATG Rev: cgcggtaccTCCACGCATGTTATTCTCCAATTTC	pHLsec	PCR product digested with AgeI and KpnI. Destination

		BC099653, Image clone 40008397.	TTGTCAG		vector digested with AgeI and KpnI.
GluD1 ATD	GluD1 Asp21-Gly436	Mouse GRID1, Genbank entry NM_008166.2	Fwd: cgcaccggtGACTCCATCATCCACATCGGTGCC Rev: cgcggtacctCCTTGGAGGCGGCTGCCCATG	pHLsec	PCR product digested with AgeI and KpnI. Destination vector digested with AgeI and KpnI.
GluD2 ATD F76D, aka GD17	GluD2: Asp24-Gly440, with Phe76Asp mutation	Human GRID2, GenBank entry BC099653, Image clone 40008397.	PCR 1: Fwd: cgcaccggtGATTCGATCATTCACATCGGAGCAATTTTTGATG Rev: GTTCACAGGCTTCTTGAACTGCTTGGTCAGGGTTGTTGCCATCAACAAACGTCACTG PCR 2: Fwd: CAACAACCCTGACCAAGCAGTTCAAGAAGCC Rev: cgcggtaccTCCACGCATGTTATTCTCCAATTTCTTGTCAG	pHLsec	Joining PCR introducing mutation. Joined PCR product digested with AgeI and KpnI. Destination vector digested with AgeI and KpnI.
GluD2 Full-Length wt, aka GD33	GluD2: Asp24-Ile1007 with an N-terminal HA tag	Human GRID2, GenBank entry BC099653, Image clone 40008397.	Fwd: cgcaccggtTACCCCTACGACGTGCCCGACTACGCCGATTCGATCATTCACATCGGAGCAATTTTTGATG Rev: cgcggtaccTTATCATATGGAGGTGCCTCGGTCTGG	pHLsec	PCR product digested with AgeI and KpnI. Destination vector digested with AgeI and KpnI.
GluD2 Full-Length F76D, aka GD20	GluD2: Asp24-Ile1007, with Phe76Asp mutation with an N-terminal HA tag	Human GRID2, GenBank entry BC099653, Image clone 40008397.	PCR 1: Fwd: cgcaccggtTACCCCTACGACGTGCCCGACTACGCCGATTCGATCATTCACATCGGAGCAATTTTTGATG Rev: GTTCACAGGCTTCTTGAACTGCTTGGTCAGGGTTGTTGCCATCAACAAACGTCACTG PCR 2: Fwd: CAACAACCCTGACCAAGCAGTTCAAGAAGCC Rev: cgcggtaccTCCACGCATGTTATTCTCCAATTTCTTGTCAG	pHLsec	Joining PCR introducing mutation. Joined PCR product digested with AgeI and KpnI. Destination vector digested with AgeI and KpnI.
GluD2 TM ΔATD, aka GD26	GluD2: Gly440-Ile1007 with an N-terminal HA tag	Human GRID2, GenBank entry BC099653, Image clone 40008397.	Fwd: cgcaccggtTACCCCTACGACGTGCCCGACTACGCCGGAGTGGTTCTACGTGTAGTAACTGTTCTGG Rev: cgcggtaccTTATCATATGGAGGTGCCTCGGTCTGG	pHLsec	PCR product digested with AgeI and KpnI. Destination vector digested with AgeI and KpnI.

GluD2 ATD-Avitag	GluD2: Asp24-Gly440	Human GRID2, GenBank entry BC099653, Image clone 40008397.	Fwd: cgcaccggtGATTCGATCATTCACATCGGAGCAATTTTTGATG Rev: cgcggtaccTCCACGCATGTTATTCTCCAATTTCTTGTCAG	pHLsec-Avitag3	PCR product digested with AgeI and KpnI. Destination vector digested with AgeI and KpnI.
GluD2 ATD F76D - Avitag	GluD2: Asp24-Gly440, with Phe76Asp mutation	Human GRID2, GenBank entry BC099653, Image clone 40008397.	PCR 1: Fwd: cgcaccggtGATTCGATCATTCACATCGGAGCAATTTTTGATG Rev: GTTCACAGGCTTCTTGAACTGCTTGGTCAGGGTTGTTGCCATCAACAAACGTCACTG PCR 2: Fwd: CAACAACCCTGACCAAGCAGTTCAAGAAGCC Rev: cgcggtaccTCCACGCATGTTATTCTCCAATTTCTTGTCAG	pHLsec-Avitag3	Joining PCR introducing mutation. Joined PCR product digested with AgeI and KpnI. Destination vector digested with AgeI and KpnI.
CB1	Cbln1: Met1-Leu193	Human CBLN1, GenBank entry BC093692, Image clone 7939537	Fwd: cgaggaattcgccaccATGCTGGGCGTCGTGGAGCTG Rev: cgcggtaccGAGGGGAAACACGAGGAATCCAGAG	pHLsec	PCR product digested with EcoRI and KpnI. Destination vector digested with EcoRI and KpnI.
CB2	Cbln1: Gln22-Leu193	Human CBLN1, GenBank entry BC093692, Image clone 7939537	Fwd: cgcaccggtCAGAATGAGACAGAGCCCATCGTACTG Rev: cgcggtaccGAGGGGAAACACGAGGAATCCAGAG	pHLsec	PCR product digested with AgeI and KpnI. Destination vector digested with AgeI and KpnI.
CB3	Cbln1: Glu24-Leu193	Human CBLN1, GenBank entry BC093692, Image clone 7939537	Fwd: cgcaccggtGAGACAGAGCCCATCGTACTGGAG Rev: cgcggtaccGAGGGGAAACACGAGGAATCCAGAG	pHLsec	PCR product digested with AgeI and KpnI. Destination vector digested with AgeI and KpnI.
CB4 aka Cbln1 C1q	Cbln1: Ser59-Leu193	Human CBLN1, GenBank entry BC093692, Image clone 7939537	Fwd: cgcaccggtAGCGCCAAGGTGGCTTTCTCTGC Rev: cgcggtaccGAGGGGAAACACGAGGAATCCAGAG	pHLsec	PCR product digested with AgeI and KpnI. Destination vector digested with AgeI and KpnI.

Cbln1 CS	Cbln1: Gln22-Leu193 with C34S and C38S	Human CBLN1, GenBank entry BC093692, Image clone 7939537 encoding C34S and C38S, a gift from Prof. M. Yuzaki (Keio University Japan)	Fwd: cgcaccggtCAGAATGAGACAGAGCCCATCGTACTG Rev: cgcggtaccGAGGGGAAACACGAGGAATCCAGAG	pHLsec	PCR product digested with AgeI and KpnI. Destination vector digested with AgeI and KpnI.
CB9	Cbln1: Gln22-Leu193 with Arg56Gln	Human CBLN1, GenBank entry BC093692, Image clone 7939537	PCR 1: Fwd: cgcaccggtCAGAATGAGACAGAGCCCATCGTACTG Rev: CCACCTTGGCGCTGCCGGATTGCACAGAGATGCCCAGAG PCR 2: Fwd: CTCTGGGCATCTCTGTGCAATCCGGCAGCGCCAAGGTGG Rev: cgcggtaccGAGGGGAAACACGAGGAATCCAGAG	pHLsec	Joining PCR introducing mutation. Joined PCR product digested with AgeI and KpnI. Destination vector digested with AgeI and KpnI.
CB35	Cbln1: Gln22-Leu193 with deletion of Val55-Gly58	Human CBLN1, GenBank entry BC093692, Image clone 7939537 encoding deletion of Val55-Gly58, a gift from Prof. M. Yuzaki (Keio University Japan)	Fwd: cgcaccggtCAGAATGAGACAGAGCCCATCGTACTG Rev: cgcggtaccGAGGGGAAACACGAGGAATCCAGAG	pHLsec	PCR product digested with AgeI and KpnI. Destination vector digested with AgeI and KpnI.
βNeurexin1 +SS4	β-Neurexin1: His85-Val295, including splice site 4	A construct encoding human β-Neurexin1 (NP_620072) LNS(B) domain (H85-V295), including splice site 4 (SS4), was synthesised by Eurofins MWG Operon	N/A	pHLsec	Target sequence was digested from pCR2.1 supply vector with AgeI and KpnI. Destination vector digested with AgeI and KpnI.

Cbln1 Avitag aka CB2 Avitag	Cbln1: Gln22-Leu193	Human CBLN1, GenBank entry BC093692, Image clone 7939537	Fwd: cgcaccggtCAGAATGAGACAGAGCCCATCGTACTG Rev: cgcggtaccGAGGGGAAACACGAGGAATCCAGAG	pHLsec-Avitag3	PCR product digested with AgeI and KpnI. Destination vector digested with AgeI and KpnI.
Cbln1 C1q Avitag, aka CB4 avitag	Cbln1: Ser59-Leu193	Human CBLN1, GenBank entry BC093692, Image clone 7939537	Fwd: cgcaccggtAGCGCCAAGGTGGCTTTCTCTGC Rev: cgcggtaccGAGGGGAAACACGAGGAATCCAGAG	pHLsec-Avitag3	PCR product digested with AgeI and KpnI. Destination vector digested with AgeI and KpnI.
Cbln1 CS avitag	Cbln1: Gln22-Leu193 with Cys34Ser and Cys38Ser	Human CBLN1, GenBank entry BC093692, Image clone 7939537 encoding C34S and C38S, a gift from Prof. M. Yuzaki (Keio University Japan)	Fwd: cgcaccggtCAGAATGAGACAGAGCCCATCGTACTG Rev: cgcggtaccGAGGGGAAACACGAGGAATCCAGAG	pHLsec-Avitag3	PCR product digested with AgeI and KpnI. Destination vector digested with AgeI and KpnI.
CB50	Cbln1: Gln22-Leu193 with Val55-Gly58 deletion, and point mutations Gln41Met, Thr43Ala, Asp45Ala, Ser59Ala	A construct encoding human CBLN1, GenBank entry BC093692, with the additional details listed in the cell immedaitey left was synthesised by Eurofins MWG Operon	N/A	pHLsec-Avitag3	Target sequence was digested from pEX-A supply vector with AgeI and KpnI. Destination vector digested with AgeI and KpnI.
CB52	Cbln1: Gln22-Leu193 with Gly52-Gly58 deletion, and point mutations Gln41Met, Thr43Ala,	A construct encoding human CBLN1, GenBank entry BC093692, with the additional details listed in the cell immedaitey left was synthesised by	N/A	pHLsec-Avitag3	Target sequence was digested from pEX-A supply vector with AgeI and KpnI. Destination vector digested with AgeI and KpnI.

	Asp45Ala, Ser59Ala	Eurofins MWG Operon			
CB54	Cbln1: Gln22-Leu193 with Gly48-Gly58 deletion, and point mutations Gln41Met, Thr43Ala, Asp45Ala, Ser59Ala	A construct encoding human CBLN1, GenBank entry BC093692, with the additional details listed in the cell immedaitey left was synthesised by Eurofins MWG Operon	N/A	pHLsec-Avitag3	Target sequence was digested from pEX-A supply vector with AgeI and KpnI. Destination vector digested with AgeI and KpnI.
GluD2 K436A aka GD40	GluD2: Asp24-Gly440 with K346A mutation	Human GRID2, GenBank entry BC099653, Image clone 40008397.	PCR 1: Fwd: cgcaccggtGATTCGATCATTCACATCGGAGCAATTTTTGATG Rev: CAGACTTGCCATGCTGTGCCACgcTCGGTCCTCCAGCTTCTTATGAAAAG PCR 2: Fwd: CTTTTCATAAGAAGCTGGAGGACCGAgcGTGGCACAGCATGGCAAGTCTG Rev: cgcggtaccTCCACGCATGTTATTCTCCAATTTCTTGTCAG	pHLsec	Joining PCR introducing mutation. Joined PCR product digested with AgeI and KpnI. Destination vector digested with AgeI and KpnI.
Cbln1 C1q D147A - Avitag	Cbln1: Ser59-Leu193 with D147A mutation	Human CBLN1, GenBank entry BC093692, Image clone 7939537	PCR 1: Fwd: cgcaccggtAGCGCCAAGGTGGCTTTCTCTGC Rev: TGCTGGCGGCCTCGCGTGTCACGgcTTGGTCACCGGCGAAGGCTGAAATC PCR 2: Fwd: GATTTCAGCCTTCGCCGGTGACCAAgcCGTGACACGCGAGGCCGCCAGCA Rev: cgcggtaccGAGGGGAAACACGAGGAATCCAGAG	pHLsec-Avitag3	Joining PCR introducing mutation. Joined PCR product digested with AgeI and KpnI. Destination vector digested with AgeI and KpnI.
Cbln1 C1q Y122A R124A -	Cbln1: Ser59-Leu193 with Y122A, R124A	Human CBLN1, GenBank entry BC093692, Image	PCR 1: Fwd: cgcaccggtAGCGCCAAGGTGGCTTTCTCTGC Rev: ATGAGGCTCACCTGGATGGTCTGTgcGTTGgcGA	pHLsec-Avitag3	Joining PCR introducing mutation. Joined PCR product digested with AgeI

Avitag	mutation	clone 7939537	CTTTCACCACGTGGAAGTTAAAAC PCR 2: Fwd: GTTTTAACTTCCACGTGGTGAAAGTCgcCAACgcACAGACCATCCAGGTGAGCCTCAT Rev: cgcggtaccGAGGGGAAACACGAGGAATCCAGAG		and KpnI. Destination vector digested with AgeI and KpnI.
GluD1 ATD - Avitag	GluD1 Asp21-Gly436	Mouse GRID1, Genbank entry NM_008166.2	Fwd: cgcaccggtGACTCCATCATCCACATCGGTGCC Rev: cgcggtaccTCCTTGGAGGCGGCTGCCCATG	pHLsec-Avitag3	PCR product digested with AgeI and KpnI. Destination vector digested with AgeI and KpnI.
GluD2 Ecto-domain aka GD13	GluD2 Asp24-Arg551 and S664-Leu813 Joined y a GT linker	Human GRID2, GenBank entry BC099653, Image clone 40008397.	PCR 1: Fwd: cgcaccggtGATTCGATCATTCACATCGGAGCAATTTTTGATG Rev:CTGGATGGACGTTCCCCTTCGAAGTAGTACCCCCACCTGAG PCR 2: Fwd: CTTCGAAGGGGAACGTCCATCCAGTCTCTCCAGGACCTTTCC Rev: cgcggtaccCAGGTCACACTGGCCATTCTTAGGC	pHLsec	Joining PCR introducing mutation. Joined PCR product digested with AgeI and KpnI. Destination vector digested with AgeI and KpnI.
GD13 T538C	GluD2 Asp24-Arg551 and S664-Leu813 Joined y a GT linker with Thr538Cys mutation	GD13	PCR 1: Fwd: cgcaccggtGATTCGATCATTCACATCGGAGCAATTTTTGATG Rev: CATGTAACGACACGTAAAGTCCACCACATTTTCACG PCR 2: Fwd: GGTGGACTTTACGtgtCGTTACATGGACTAC Rev: cgcggtaccCAGGTCACACTGGCCATTCTTAGGC	pHLsec	Joining PCR introducing mutation. Joined PCR product digested with AgeI and KpnI. Destination vector digested with AgeI and KpnI.
GD13 P528C, E790C	GluD2 Asp24-Arg551 and S664-Leu813 Joined y a GT linker with Pro528Cys and	GD13 for PCR 1+2 and GD13 P528C for PCR 3+4	PCR 1: Fwd: cgcaccggtGATTCGATCATTCACATCGGAGCAATTTTTGATG Rev: CATTTTCACGATCgcaAGTGATGGTTAAAGCAG PCR 2: Fwd: CTTTAACCATCACTtgcGATCGTGAAAATGTGGT	pHLsec	Joining PCR 1+2 introducing P528C mutation. Joined PCR product digested with AgeI and KpnI. Destination vector digested with AgeI and KpnI. Second round of cloning

	GluE790Cys mutations		GG Rev: cgcggtaccCAGGTCACACTGGCCATTCTTAGGC PCR 3: Fwd: cgcaccggtGATTCGATCATTCACATCGGAGCAATTTTTGATG Rev: CATTCTGCTGAAGGCACAGGATCCTTTGTG PCR 4: Fwd: CAAAGGATCCTGtgcCTTCAGCAGAATGGTG Rev: cgcggtaccCAGGTCACACTGGCCATTCTTAGGC		where a second joining PCR 3+4 using GD13 P528C as a template to introduce second E790C mutation. Joined PCR product digested with AgeI and KpnI. Destination vector digested with AgeI and KpnI.
GD13 FC	GluD2 Asp24-Arg551 and S664-Leu813 Joined y a GT linker	Human GRID2, GenBank entry BC099653, Image clone 40008397.	PCR 1: Fwd: cgcaccggtGATTCGATCATTCACATCGGAGCAATTTTTGATG Rev:CTGGATGGACGTTCCCCTTCGAAGTAGTACCCCCACTGAG PCR 2: Fwd: CTTCGAAGGGGAACGTCCATCCAGTCTCTCCAGGACCTTTCC Rev: cgcggtaccCAGGTCACACTGGCCATTCTTAGGC	pHLsec FC	Joining PCR introducing mutation. Joined PCR product digested with AgeI and KpnI. Destination vector digested with AgeI and KpnI.
GD28	GluD2: Asp24-Ile1007 with an N-terminal HA tag and C-terminal mVenus tag	Human GRID2, GenBank entry BC099653, Image clone 40008397.	Fwd: cgcaccggtTACCCCTACGACGTGCCCGACTACGCCGATTCGATCATTCACATCGGAGCAATTTTTGATG Rev: cgcggtaccTTATCATATGGAGGTGCCTCGGTCTGG	pHLsec mVenus	PCR product digested with AgeI and KpnI. Destination vector digested with AgeI and KpnI.
GD30	GluD2: Asp24-Glu867 with a C-terminal mVenus tag	Human GRID2, GenBank entry BC099653, Image clone 40008397.	Fwd: cgcaccggtTACCCCTACGACGTGCCCGACTACGCCGATTCGATCATTCACATCGGAGCAATTTTTGATG Rev: CGCGGTACCCTCTTTTGATGGAACCCGGGAGCCTTTC	pHLsec mVenus	PCR product digested with AgeI and KpnI. Destination vector digested with AgeI and KpnI.
GD35	GluD2: Asp24-Glu867 with an N-terminal HA	Human GRID2, GenBank entry BC099653, Image	Fwd: cgcaccggtTACCCCTACGACGTGCCCGACTACGCCGATTCGATCATTCACATCGGAGCAATTTTTGATG Rev: CGCGGTACCCTCTTTTGATGGAACCCGGGAGCCTTTC	pHLsec mVenus	PCR product digested with AgeI and KpnI. Destination vector digested with AgeI and

	tag and C-terminal mVenus tag	clone 40008397.			KpnI.
GD31	GluD2: Asp24-Glu867 with a C-terminal 1D4	Human GRID2, GenBank entry BC099653, Image clone 40008397.	Fwd: cgcaccggtGATTCGATCATTCACATCGGAGCAATTTTTGATG Rev: CGCGGTACCCTCTTTTGATGGAACCCGGGAGCCTTTC	pHLsec-1D4	PCR product digested with AgeI and KpnI. Destination vector digested with AgeI and KpnI.

Appendix 8.2 Abbreviations

2 % Media	DMEM supplemented with NEAA, L-glutamine and 2 % FBS
10 % Media	DMEM supplemented with NEAA, L-glutamine and 10 % FBS
AGE	Agarose Gel Electrophoresis
AMPA	α-amino-3-hydroxy-5-methyl-4-isoxazole-propionic acid
APC	Allophycocyanin
ASDs	Autism Spectrum Disorders
ASU	Asymmetric Unit
ATD	Amino-Terminal Domain
Bmax	Maximum Amount Of Analyte Bound
CaMKII	Calcium/Calmodulin-Dependent Protein Kinase II
cDNA	Complementary DNA
CF	Climbing Fibre Neuron
CNS	Central Nervous System
CREB	cAMP Response Element-Binding
DDM	n-Dodecyl-ß-maltoside
DNMG	Decyl Maltose Neopentyl Glycol
DMEM	Dulbecco's Modified Eagle's Medium
DNA	Deoxyribonucleic Acid
DNAse	Deoxyribonuclease
dNTPs	Deoxyribonucleotide Triphosphate
EGF-like	Epidermal Growth-Factor-Like Domain
EM	Electron Microscopy

EndoH	Endoglycosidase H
EPSC	Excitatory Post-Synaptic Current
ER	Endoplasmic Reticulum
FACS	Fluorescence-Activated Cell Sorting
FBS	Fetal Bovine Serum
FSEC	Fluorescence Size Exclusion Chromatography
GNTI$^-$	N-acetylglucosaminyltransferase I deficient
GPCR	G Protein-Coupled Receptors
HEK293T	Human Embryonic Kidney 293 Cells Expressing SV40 Type T Antigen
HEK293S	Human Embryonic Kidney 293 Cells, GnT I Deficient
HEPES	*N*-[2-Hydroxyethyl]piperazine-*N'*-[2-ethanesulphonic acid]
IAC	Immuno-Affinity Chromatography
iGluRs	Ionotropic Glutamate Receptors
IMAC	Immobilised Metal Ion Affinity Chromatography
IP_3R	Ionositol Trisphosphate Receptor
ITC	Isothermal Calorimetry
K_d	Equilibrium Binding Constant
KO	Knock-Out
LAOBP	Bacterial Bilobal Lysine/Arginine/Ornithine-Binding Proteins
LBC	Ligand Binding Core
LIVBP	Bacterial Periplasmic Leucine/Isoleucine/Valine-Binding Proteins
LLG	Log-Likelihood Gain
LNS	LamininA/Neurexin/Sex Hormone-Binding Globulin Domain

LTD	Long-Term Synaptic Depression
LTP	Long-Term Synaptic Potentiation
MALS	Multi-Angle Light Scattering
mGluR1	Metabotropic Glutamate Receptor 1
MPBS	Marvel Milk powder containing PBS
MRI	Magnetic Resonance Imaging
NaBu	Sodium Butyrate
NEAA	Non-Essential Amino-Acids
NDSB	Non-Detergent SulfoBetaine
NMDA	*N*-methyl-d-aspartate
NTA	Nitrilotriacetic Acid
Oligo	Oligonucleotide
PBS	Phosphate Buffered Saline Solution
PBS-NaN_3	Phosphate Buffered Saline Solution Containing 0.05 % Sodium Azide
PC	Purkinje Cell
PCR	Polymerase Chain Reaction
PDB	Protein Data Bank
PEI	Polyethylenimine
PET	Positron Emission Tomography
PF	Parallel Fibre Neuron
PFA	Paraformaldehyde
PF-PC	Parallel Fibre-Purkinje Cell Synapse
PI_3 Kinase	Phosphatidylinositol-3-Kinase

PKA	cAMP-Dependent Protein Kinase
PKC	Protein Kinase C
PLC	Phospholipase C
PSD	Post-Synaptic Density
RMSD	Root Mean Square Deviation
RNAse	Ribonuclease
SDS	Sodium Dodecyl Sulphate
SDS-PAGE	Sodium Dodecyl Sulphate Polyacrylamide Gel Electrophoresis
SEC	Size Exclusion Chromatography
SEC-MALS	Size Exclusion Chromatography-Multi-Angle Light Scattering
SFM	DMEM Supplemented with NEAA and L-glutamine
SOC	Super Optimal Medium With Catabolite Repression
SPR	Surface Plasmon Resonance
SS4	Splice Site Four Of β-Neurexin1
STED	Stimulated Emission Depletion
STORM	Stochastic Optical Reconstruction Microscopy
STRUBI	Division of Structural Biology, University of Oxford
TACE	TNFα Converting Enzyme
TM	Transmembrane
TNF	Tumour Necrosis Factor
TPBS	0.1 % Tween 20 containing PBS
VGCC	Voltage-Gated Calcium Channels
VPA	Valproic Acid

v/v	Volume By Volume
w/v	Weight By Volume

Appendix 8.3 pHLsec Vector Series

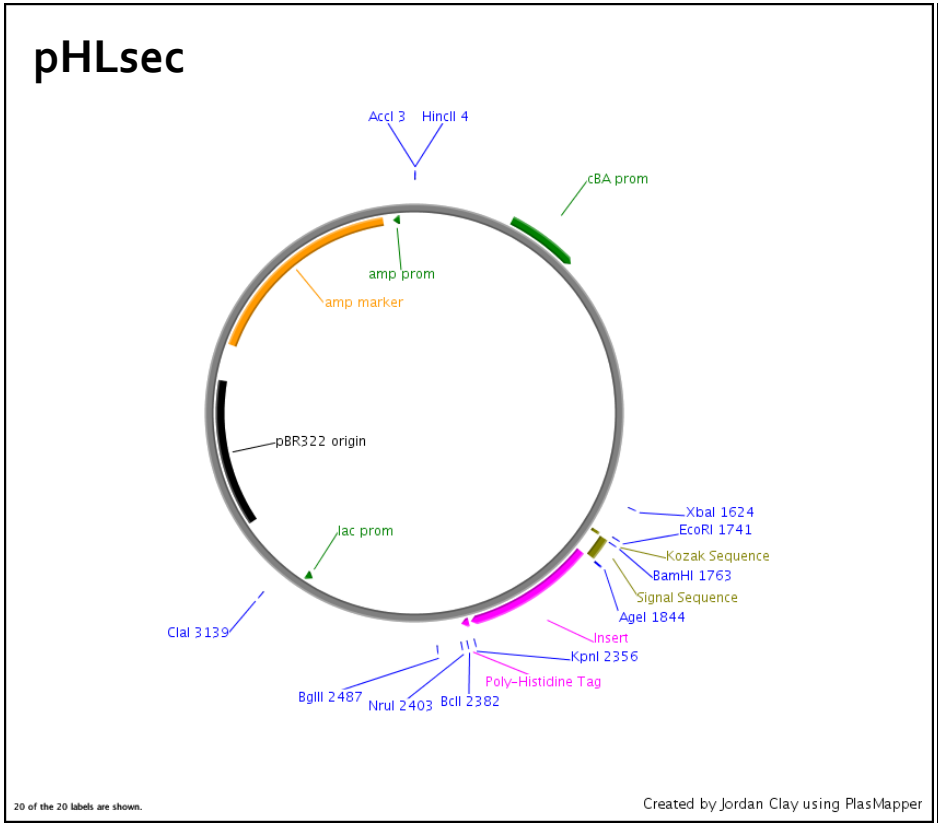

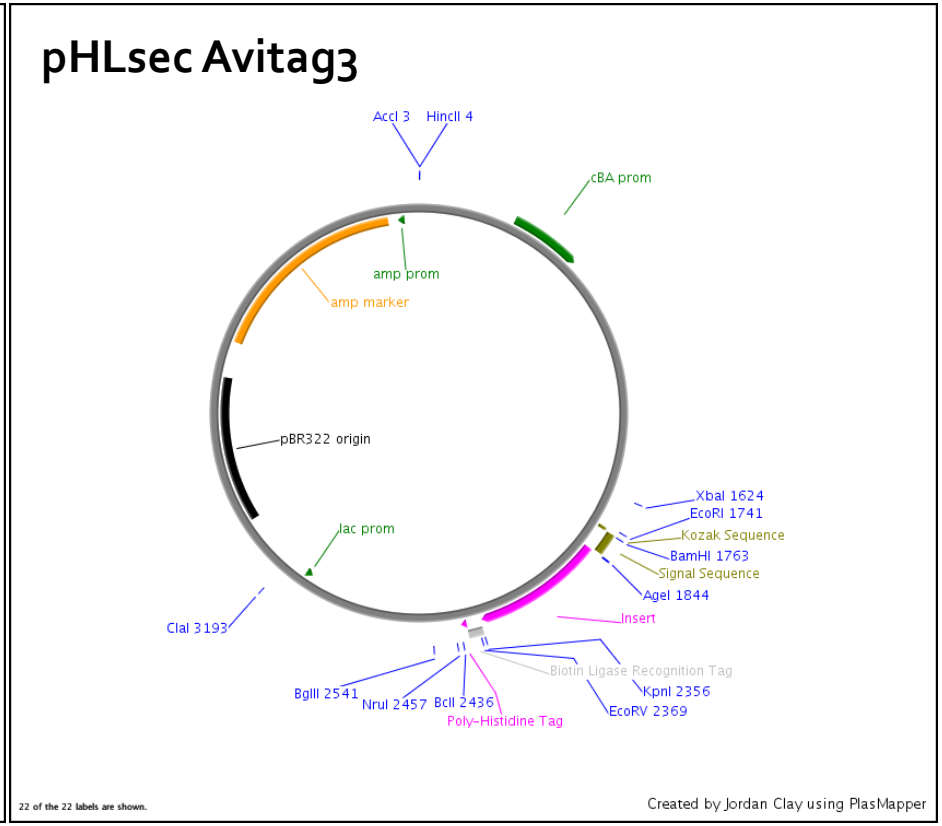

pHLsec mVenus

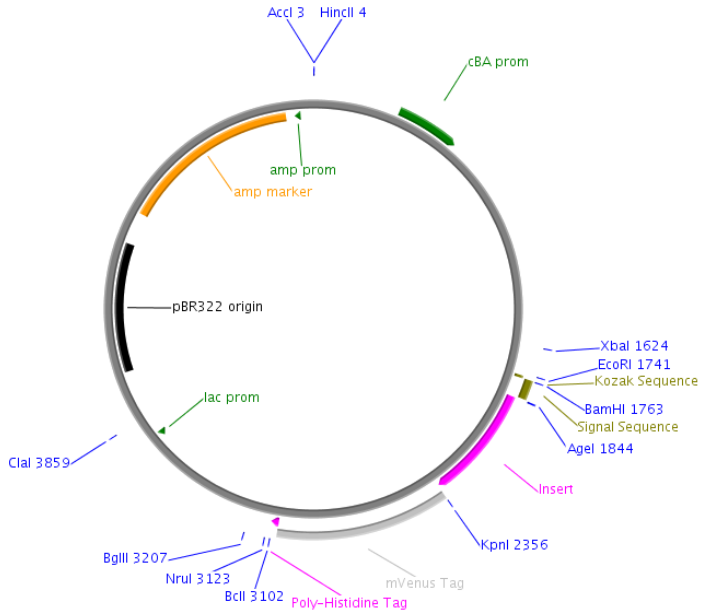

21 of the 21 labels are shown.

Created by Jordan Clay using PlasMapper

pHLsec FC

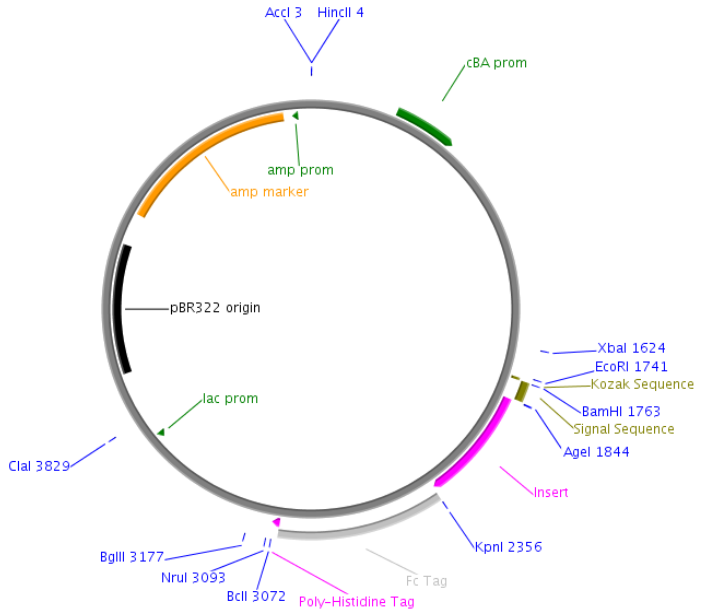

21 of the 21 labels are shown.

Created by Jordan Clay using PlasMapper

Appendix 8.4 Bibliography

Adams PD, Afonine PV, Bunkoczi G, Chen VB, Davis IW, Echols N, Headd JJ, Hung LW, Kapral GJ, Grosse-Kunstleve RW, McCoy AJ, Moriarty NW, Oeffner R, Read RJ, Richardson DC, Richardson JS, Terwilliger TC, Zwart PH (2010) PHENIX: a comprehensive Python-based system for macromolecular structure solution. *Acta crystallographica Section D, Biological crystallography* **66:** 213-221

Agnati LF, Genedani S, Leo G, Rivera A, Guidolin D, Fuxe K (2007) One century of progress in neuroscience founded on Golgi and Cajal's outstanding experimental and theoretical contributions. *Brain research reviews* **55:** 167-189

Ahmed AH, Wang Q, Sondermann H, Oswald RE (2009) Structure of the S1S2 glutamate binding domain of GLuR3. *Proteins* **75:** 628-637

Arac D, Boucard AA, Ozkan E, Strop P, Newell E, Sudhof TC, Brunger AT (2007) Structures of neuroligin-1 and the neuroligin-1/neurexin-1 beta complex reveal specific protein-protein and protein-Ca2+ interactions. *Neuron* **56:** 992-1003

Araki K, Meguro H, Kushiya E, Takayama C, Inoue Y, Mishina M (1993) Selective expression of the glutamate receptor channel delta 2 subunit in cerebellar Purkinje cells. *Biochemical and biophysical research communications* **197:** 1267-1276

Aricescu AR, Lu W, Jones EY (2006) A time- and cost-efficient system for high-level protein production in mammalian cells. *Acta crystallographica Section D, Biological crystallography* **62:** 1243-1250

Armstrong N, Gouaux E (2000) Mechanisms for activation and antagonism of an AMPA-sensitive glutamate receptor: crystal structures of the GluR2 ligand binding core. *Neuron* **28:** 165-181

Ashkenazy H, Erez E, Martz E, Pupko T, Ben-Tal N (2010) ConSurf 2010: calculating evolutionary conservation in sequence and structure of proteins and nucleic acids. *Nucleic acids research* **38:** W529-533

Ayalon G, Segev E, Elgavish S, Stern-Bach Y (2005) Two regions in the N-terminal domain of ionotropic glutamate receptor 3 form the subunit oligomerization interfaces that control subtype-specific receptor assembly. *The Journal of biological chemistry* **280:** 15053-15060

Azevedo FA, Carvalho LR, Grinberg LT, Farfel JM, Ferretti RE, Leite RE, Jacob Filho W, Lent R, Herculano-Houzel S (2009) Equal numbers of neuronal and nonneuronal cells make the human brain an isometrically scaled-up primate brain. *The Journal of comparative neurology* **513:** 532-541

Backliwal G, Hildinger M, Kuettel I, Delegrange F, Hacker DL, Wurm FM (2008) Valproic acid: a viable alternative to sodium butyrate for enhancing protein expression in mammalian cell cultures. *Biotechnology and bioengineering* **101:** 182-189

Baker NA, Sept D, Joseph S, Holst MJ, McCammon JA (2001) Electrostatics of nanosystems: application to microtubules and the ribosome. *Proceedings of the National Academy of Sciences of the United States of America* **98:** 10037-10041

Balciuniene J, Feng N, Iyadurai K, Hirsch B, Charnas L, Bill BR, Easterday MC, Staaf J, Oseth L, Czapansky-Beilman D, Avramopoulos D, Thomas GH, Borg A, Valle D, Schimmenti LA, Selleck SB (2007) Recurrent 10q22-q23 deletions: a genomic disorder on 10q associated with cognitive and behavioral abnormalities. *American journal of human genetics* **80:** 938-947

Bao D, Pang Z, Morgan JI (2005) The structure and proteolytic processing of Cbln1 complexes. *Journal of neurochemistry* **95:** 618-629

Bao D, Pang Z, Morgan MA, Parris J, Rong Y, Li L, Morgan JI (2006) Cbln1 is essential for interaction-dependent secretion of Cbln3. *Molecular and cellular biology* **26:** 9327-9337

Battye TG, Kontogiannis L, Johnson O, Powell HR, Leslie AG (2011) iMOSFLM: a new graphical interface for diffraction-image processing with MOSFLM. *Acta crystallographica Section D, Biological crystallography* **67:** 271-281

Bayes A, van de Lagemaat LN, Collins MO, Croning MD, Whittle IR, Choudhary JS, Grant SG (2011) Characterization of the proteome, diseases and evolution of the human postsynaptic density. *Nature neuroscience* **14:** 19-21

Benke TA, Luthi A, Isaac JT, Collingridge GL (1998) Modulation of AMPA receptor unitary conductance by synaptic activity. *Nature* **393:** 793-797

Berman HM, Westbrook J, Feng Z, Gilliland G, Bhat TN, Weissig H, Shindyalov IN, Bourne PE (2000) The Protein Data Bank. *Nucleic acids research* **28:** 235-242

Biederer T, Sara Y, Mozhayeva M, Atasoy D, Liu X, Kavalali ET, Sudhof TC (2002) SynCAM, a synaptic adhesion molecule that drives synapse assembly. *Science* **297:** 1525-1531

Birnboim HC, Doly J (1979) A rapid alkaline extraction procedure for screening recombinant plasmid DNA. *Nucleic acids research* **7:** 1513-1523

Blanc E, Roversi P, Vonrhein C, Flensburg C, Lea SM, Bricogne G (2004) Refinement of severely incomplete structures with maximum likelihood in BUSTER-TNT. *Acta crystallographica Section D, Biological crystallography* **60:** 2210-2221

Bliss TV, Collingridge GL (1993) A synaptic model of memory: long-term potentiation in the hippocampus. *Nature* **361:** 31-39

Bliss TV, Gardner-Medwin AR (1973) Long-lasting potentiation of synaptic transmission in the dentate area of the unanaestetized rabbit following stimulation of the perforant path. *The Journal of physiology* **232:** 357-374

Bliss TV, Lomo T (1973) Long-lasting potentiation of synaptic transmission in the dentate area of the anaesthetized rabbit following stimulation of the perforant path. *The Journal of physiology* **232:** 331-356

Block H, Maertens B, Spriestersbach A, Brinker N, Kubicek J, Fabis R, Labahn J, Schafer F (2009) Immobilized-metal affinity chromatography (IMAC): a review. *Methods in enzymology* **463:** 439-473

Bogin O, Kvansakul M, Rom E, Singer J, Yayon A, Hohenester E (2002) Insight into Schmid metaphyseal chondrodysplasia from the crystal structure of the collagen X NC1 domain trimer. *Structure* **10:** 165-173

Bottos A, Rissone A, Bussolino F, Arese M (2011) Neurexins and neuroligins: synapses look out of the nervous system. *Cellular and molecular life sciences : CMLS* **68:** 2655-2666

Boulter J, Hollmann M, O'Shea-Greenfield A, Hartley M, Deneris E, Maron C, Heinemann S (1990) Molecular cloning and functional expression of glutamate receptor subunit genes. *Science* **249:** 1033-1037

Chang VT, Crispin M, Aricescu AR, Harvey DJ, Nettleship JE, Fennelly JA, Yu C, Boles KS, Evans EJ, Stuart DI, Dwek RA, Jones EY, Owens RJ, Davis SJ (2007) Glycoprotein structural genomics: solving the glycosylation problem. *Structure* **15:** 267-273

Chen F, Venugopal V, Murray B, Rudenko G (2011) The structure of neurexin 1alpha reveals features promoting a role as synaptic organizer. *Structure* **19:** 779-789

Chen VB, Arendall WB, 3rd, Headd JJ, Keedy DA, Immormino RM, Kapral GJ, Murray LW, Richardson JS, Richardson DC (2010) MolProbity: all-atom structure validation for macromolecular crystallography. *Acta crystallographica Section D, Biological crystallography* **66:** 12-21

Chen X, Liu H, Shim AH, Focia PJ, He X (2008) Structural basis for synaptic adhesion mediated by neuroligin-neurexin interactions. *Nature structural & molecular biology* **15:** 50-56

Chung HJ, Steinberg JP, Huganir RL, Linden DJ (2003) Requirement of AMPA receptor GluR2 phosphorylation for cerebellar long-term depression. *Science* **300:** 1751-1755

Chung KY, Rasmussen SG, Liu T, Li S, DeVree BT, Chae PS, Calinski D, Kobilka BK, Woods VL, Jr., Sunahara RK (2011) Conformational changes in the G protein Gs induced by the beta2 adrenergic receptor. *Nature* **477:** 611-615

Clare R, King VG, Wirenfeldt M, Vinters HV (2010) Synapse loss in dementias. *Journal of neuroscience research* **88:** 2083-2090

Clayton A, Siebold C, Gilbert RJ, Sutton GC, Harlos K, McIlhinney RA, Jones EY, Aricescu AR (2009) Crystal structure of the GluR2 amino-terminal domain provides insights into the architecture and assembly of ionotropic glutamate receptors. *Journal of molecular biology* **392:** 1125-1132

Cline H (2005) Synaptogenesis: a balancing act between excitation and inhibition. *Current biology : CB* **15:** R203-205

Collingridge GL, Kehl SJ, McLennan H (1983) Excitatory amino acids in synaptic transmission in the Schaffer collateral-commissural pathway of the rat hippocampus. *The Journal of physiology* **334:** 33-46

Comoletti D, Flynn R, Jennings LL, Chubykin A, Matsumura T, Hasegawa H, Sudhof TC, Taylor P (2003) Characterization of the interaction of a recombinant soluble neuroligin-1 with neurexin-1beta. *The Journal of biological chemistry* **278:** 50497-50505

Conrad KL, Tseng KY, Uejima JL, Reimers JM, Heng LJ, Shaham Y, Marinelli M, Wolf ME (2008) Formation of accumbens GluR2-lacking AMPA receptors mediates incubation of cocaine craving. *Nature* **454:** 118-121

Corpet F (1988) Multiple sequence alignment with hierarchical clustering. *Nucleic acids research* **16:** 10881-10890

Dalva MB, McClelland AC, Kayser MS (2007) Cell adhesion molecules: signalling functions at the synapse. *Nature reviews Neuroscience* **8:** 206-220

Dalva MB, Takasu MA, Lin MZ, Shamah SM, Hu L, Gale NW, Greenberg ME (2000) EphB receptors interact with NMDA receptors and regulate excitatory synapse formation. *Cell* **103:** 945-956

Daniel E, Lin B, Diprose JM, Griffiths SL, Morris C, Berry IM, Owens RJ, Blake R, Wilson KS, Stuart DI, Esnouf RM (2011) xtalPiMS: a PiMS-based web application for the management and monitoring of crystallization trials. *Journal of structural biology* **175:** 230-235

Davis IW, Leaver-Fay A, Chen VB, Block JN, Kapral GJ, Wang X, Murray LW, Arendall WB, 3rd, Snoeyink J, Richardson JS, Richardson DC (2007) MolProbity: all-atom contacts and structure validation for proteins and nucleic acids. *Nucleic acids research* **35:** W375-383

Davletov BA, Krasnoperov V, Hata Y, Petrenko AG, Sudhof TC (1995) High affinity binding of alpha-latrotoxin to recombinant neurexin I alpha. *The Journal of biological chemistry* **270:** 23903-23905

de Vries SJ, van Dijk AD, Krzeminski M, van Dijk M, Thureau A, Hsu V, Wassenaar T, Bonvin AM (2007) HADDOCK versus HADDOCK: new features and performance of HADDOCK2.0 on the CAPRI targets. *Proteins* **69:** 726-733

Dean C, Dresbach T (2006) Neuroligins and neurexins: linking cell adhesion, synapse formation and cognitive function. *Trends in neurosciences* **29:** 21-29

Dingledine R, Borges K, Bowie D, Traynelis SF (1999) The glutamate receptor ion channels. *Pharmacological reviews* **51:** 7-61

Drachman DA (2005) Do we have brain to spare? *Neurology* **64:** 2004-2005

Eck MJ, Sprang SR (1989) The structure of tumor necrosis factor-alpha at 2.6 A resolution. Implications for receptor binding. *The Journal of biological chemistry* **264:** 17595-17605

Emsley P, Lohkamp B, Scott WG, Cowtan K (2010) Features and development of Coot. *Acta crystallographica Section D, Biological crystallography* **66:** 486-501

Fabrichny IP, Leone P, Sulzenbacher G, Comoletti D, Miller MT, Taylor P, Bourne Y, Marchot P (2007) Structural analysis of the synaptic protein neuroligin and its beta-neurexin complex: determinants for folding and cell adhesion. *Neuron* **56:** 979-991

Fallin MD, Lasseter VK, Avramopoulos D, Nicodemus KK, Wolyniec PS, McGrath JA, Steel G, Nestadt G, Liang KY, Huganir RL, Valle D, Pulver AE (2005) Bipolar I disorder and schizophrenia: a 440-single-nucleotide polymorphism screen of 64 candidate genes among Ashkenazi Jewish case-parent trios. *American journal of human genetics* **77:** 918-936

Farina AN, Blain KY, Maruo T, Kwiatkowski W, Choe S, Nakagawa T (2011) Separation of domain contacts is required for heterotetrameric assembly of functional NMDA receptors. *The Journal of neuroscience : the official journal of the Society for Neuroscience* **31:** 3565-3579

Fatemi SH, Aldinger KA, Ashwood P, Bauman ML, Blaha CD, Blatt GJ, Chauhan A, Chauhan V, Dager SR, Dickson PE, Estes AM, Goldowitz D, Heck DH, Kemper TL, King BH, Martin LA, Millen KJ, Mittleman G, Mosconi MW, Persico AM, Sweeney JA, Webb SJ, Welsh JP (2012) Consensus Paper: Pathological Role of the Cerebellum in Autism. *Cerebellum*

Feng J, Schroer R, Yan J, Song W, Yang C, Bockholt A, Cook EH, Jr., Skinner C, Schwartz CE, Sommer SS (2006) High frequency of neurexin 1beta signal peptide structural variants in patients with autism. *Neuroscience letters* **409:** 10-13

Fitzjohn SM, Collingridge GL (2002) Calcium stores and synaptic plasticity. *Cell calcium* **32:** 405-411

French S, Wilson K (1978) On the treatment of negative intensity observations. *Acta Crystallographica Section A* **34:** 517-525

Fukuoka T, Takeda H, Ohe Y, Deguchi I, Takahashi Y, Tanahashi N (2012) Anti-glutamate receptor delta2 antibody-positive migrating focal encephalitis. *Clinical neurology and neurosurgery*

Furukawa H (2012) Structure and function of glutamate receptor amino terminal domains. *The Journal of physiology* **590:** 63-72

Furukawa H, Gouaux E (2003) Mechanisms of activation, inhibition and specificity: crystal structures of the NMDA receptor NR1 ligand-binding core. *The EMBO journal* **22:** 2873-2885

Furukawa H, Singh SK, Mancusso R, Gouaux E (2005) Subunit arrangement and function in NMDA receptors. *Nature* **438:** 185-192

Gao J, Maison SF, Wu X, Hirose K, Jones SM, Bayazitov I, Tian Y, Mittleman G, Matthews DB, Zakharenko SS, Liberman MC, Zuo J (2007) Orphan glutamate receptor delta1 subunit required for high-frequency hearing. *Molecular and cellular biology* **27:** 4500-4512

Ghai R, Waters P, Roumenina LT, Gadjeva M, Kojouharova MS, Reid KB, Sim RB, Kishore U (2007) C1q and its growing family. *Immunobiology* **212:** 253-266

Gielen M, Siegler Retchless B, Mony L, Johnson JW, Paoletti P (2009) Mechanism of differential control of NMDA receptor activity by NR2 subunits. *Nature* **459:** 703-707

Gill A, Birdsey-Benson A, Jones BL, Henderson LP, Madden DR (2008) Correlating AMPA receptor activation and cleft closure across subunits: crystal structures of the GluR4 ligand-binding domain in complex with full and partial agonists. *Biochemistry* **47:** 13831-13841

Glessner JT, Wang K, Cai G, Korvatska O, Kim CE, Wood S, Zhang H, Estes A, Brune CW, Bradfield JP, Imielinski M, Frackelton EC, Reichert J, Crawford EL, Munson J, Sleiman PM, Chiavacci R, Annaiah K, Thomas K, Hou C, Glaberson W, Flory J, Otieno F, Garris M, Soorya L, Klei L, Piven J, Meyer KJ, Anagnostou E, Sakurai T, Game RM, Rudd DS, Zurawiecki D, McDougle CJ, Davis LK, Miller J, Posey DJ, Michaels S, Kolevzon A, Silverman JM, Bernier R, Levy SE, Schultz RT, Dawson G, Owley T, McMahon WM, Wassink TH, Sweeney JA, Nurnberger JI, Coon H, Sutcliffe JS, Minshew NJ, Grant SF, Bucan M, Cook EH, Buxbaum JD, Devlin B, Schellenberg GD, Hakonarson H (2009) Autism genome-wide copy number variation reveals ubiquitin and neuronal genes. *Nature* **459:** 569-573

Glickstein M, Strata P, Voogd J (2009) Cerebellum: history. *Neuroscience* **162:** 549-559

Golovanov AP, Hautbergue GM, Wilson SA, Lian LY (2004) A simple method for improving protein solubility and long-term stability. *Journal of the American Chemical Society* **126:** 8933-8939

Graf ER, Zhang X, Jin SX, Linhoff MW, Craig AM (2004) Neurexins induce differentiation of GABA and glutamate postsynaptic specializations via neuroligins. *Cell* **119:** 1013-1026

Grant SG (2012) Synaptopathies: diseases of the synaptome. *Current opinion in neurobiology*

Guo SZ, Huang K, Shi YY, Tang W, Zhou J, Feng GY, Zhu SM, Liu HJ, Chen Y, Sun XD, He L (2007) A case-control association study between the GRID1 gene and schizophrenia in the Chinese Northern Han population. *Schizophrenia research* **93:** 385-390

Hansen KB, Furukawa H, Traynelis SF (2010) Control of assembly and function of glutamate receptors by the amino-terminal domain. *Molecular pharmacology* **78:** 535-549

Henneberger C, Papouin T, Oliet SH, Rusakov DA (2010) Long-term potentiation depends on release of D-serine from astrocytes. *Nature* **463:** 232-236

Herculano-Houzel S (2012) The remarkable, yet not extraordinary, human brain as a scaled-up primate brain and its associated cost. *Proceedings of the National Academy of Sciences of the United States of America* **109 Suppl 1:** 10661-10668

Hirai H, Pang Z, Bao D, Miyazaki T, Li L, Miura E, Parris J, Rong Y, Watanabe M, Yuzaki M, Morgan JI (2005) Cbln1 is essential for synaptic integrity and plasticity in the cerebellum. *Nature neuroscience* **8:** 1534-1541

Hironaka K, Umemori H, Tezuka T, Mishina M, Yamamoto T (2000) The protein-tyrosine phosphatase PTPMEG interacts with glutamate receptor delta 2 and epsilon subunits. *The Journal of biological chemistry* **275:** 16167-16173

Hishimoto A, Liu QR, Drgon T, Pletnikova O, Walther D, Zhu XG, Troncoso JC, Uhl GR (2007) Neurexin 3 polymorphisms are associated with alcohol dependence and altered expression of specific isoforms. *Human molecular genetics* **16:** 2880-2891

Hollmann M, O'Shea-Greenfield A, Rogers SW, Heinemann S (1989) Cloning by functional expression of a member of the glutamate receptor family. *Nature* **342:** 643-648

Honore T, Lauridsen J, Krogsgaard-Larsen P (1982) The binding of [3H]AMPA, a structural analogue of glutamic acid, to rat brain membranes. *Journal of neurochemistry* **38:** 173-178

Huang B, Babcock H, Zhuang X (2010) Breaking the diffraction barrier: super-resolution imaging of cells. *Cell* **143:** 1047-1058

Ibiricu I, Huiskonen JT, Dohner K, Bradke F, Sodeik B, Grunewald K (2011) Cryo electron tomography of herpes simplex virus during axonal transport and secondary envelopment in primary neurons. *PLoS pathogens* **7:** e1002406

Ichikawa K, Kikuchi M, Takeshita S, Nezu A (2009) A case of chronic recurrent cerebellar ataxia responding to steroid therapy. *Brain & development* **31:** 83-85

Ito M (1989) Long-term depression. *Annual review of neuroscience* **12:** 85-102

Ito M (2002) The molecular organization of cerebellar long-term depression. *Nature reviews Neuroscience* **3:** 896-902

Janeway CA, Travers P, Walport M, Schlomchik MJ (2001) Immunobiology, 5th edition: The Immune System in Health and Disease. Garland Science, New York

Jin R, Singh SK, Gu S, Furukawa H, Sobolevsky AI, Zhou J, Jin Y, Gouaux E (2009) Crystal structure and association behaviour of the GluR2 amino-terminal domain. *The EMBO journal* **28:** 1812-1823

Jones EY, Stuart DI, Walker NP (1989) Structure of tumour necrosis factor. *Nature* **338:** 225-228

Joo JY, Lee SJ, Uemura T, Yoshida T, Yasumura M, Watanabe M, Mishina M (2011) Differential interactions of cerebellin precursor protein (Cbln) subtypes and neurexin variants for synapse formation of cortical neurons. *Biochemical and biophysical research communications* **406:** 627-632

Kabsch W, Sander C (1983) Dictionary of protein secondary structure: pattern recognition of hydrogen-bonded and geometrical features. *Biopolymers* **22:** 2577-2637

Kakegawa W, Kohda K, Yuzaki M (2007) The delta2 'ionotropic' glutamate receptor functions as a non-ionotropic receptor to control cerebellar synaptic plasticity. *The Journal of physiology* **584:** 89-96

Kakegawa W, Miyazaki T, Emi K, Matsuda K, Kohda K, Motohashi J, Mishina M, Kawahara S, Watanabe M, Yuzaki M (2008) Differential regulation of synaptic plasticity and cerebellar motor learning by the C-terminal PDZ-binding motif of GluRdelta2. *The Journal of neuroscience : the official journal of the Society for Neuroscience* **28:** 1460-1468

Kakegawa W, Miyazaki T, Kohda K, Matsuda K, Emi K, Motohashi J, Watanabe M, Yuzaki M (2009) The N-terminal domain of GluD2 (GluRdelta2) recruits presynaptic terminals and regulates synaptogenesis in the cerebellum in vivo. *The Journal of neuroscience : the official journal of the Society for Neuroscience* **29:** 5738-5748

Kakegawa W, Miyoshi Y, Hamase K, Matsuda S, Matsuda K, Kohda K, Emi K, Motohashi J, Konno R, Zaitsu K, Yuzaki M (2011) D-serine regulates cerebellar LTD and motor coordination through the delta2 glutamate receptor. *Nature neuroscience* **14:** 603-611

Kantardjieff KA, Rupp B (2003) Matthews coefficient probabilities: Improved estimates for unit cell contents of proteins, DNA, and protein-nucleic acid complex crystals. *Protein science : a publication of the Protein Society* **12:** 1865-1871

Karakas E, Simorowski N, Furukawa H (2009) Structure of the zinc-bound amino-terminal domain of the NMDA receptor NR2B subunit. *The EMBO journal* **28:** 3910-3920

Karakas E, Simorowski N, Furukawa H (2011) Subunit arrangement and phenylethanolamine binding in GluN1/GluN2B NMDA receptors. *Nature* **475:** 249-253

Karplus PA, Diederichs K (2012) Linking crystallographic model and data quality. *Science* **336:** 1030-1033

Kashiwabuchi N, Ikeda K, Araki K, Hirano T, Shibuki K, Takayama C, Inoue Y, Kutsuwada T, Yagi T, Kang Y, et al. (1995) Impairment of motor coordination, Purkinje cell synapse formation, and cerebellar long-term depression in GluR delta 2 mutant mice. *Cell* **81:** 245-252

Kawate T, Gouaux E (2006) Fluorescence-detection size-exclusion chromatography for precrystallization screening of integral membrane proteins. *Structure* **14:** 673-681

Kayser MS, McClelland AC, Hughes EG, Dalva MB (2006) Intracellular and trans-synaptic regulation of glutamatergic synaptogenesis by EphB receptors. *The Journal of neuroscience : the official journal of the Society for Neuroscience* **26:** 12152-12164

Kemp JA, McKernan RM (2002) NMDA receptor pathways as drug targets. *Nature neuroscience* **5 Suppl:** 1039-1042

Kim HG, Kishikawa S, Higgins AW, Seong IS, Donovan DJ, Shen Y, Lally E, Weiss LA, Najm J, Kutsche K, Descartes M, Holt L, Braddock S, Troxell R, Kaplan L, Volkmar F, Klin A, Tsatsanis K, Harris DJ, Noens I, Pauls DL, Daly MJ, MacDonald ME, Morton CC, Quade BJ, Gusella JF (2008) Disruption of neurexin 1 associated with autism spectrum disorder. *American journal of human genetics* **82:** 199-207

Kim KS, Yan D, Tomita S (2010) Assembly and stoichiometry of the AMPA receptor and transmembrane AMPA receptor regulatory protein complex. *The Journal of neuroscience : the official journal of the Society for Neuroscience* **30:** 1064-1072

Kirov G, Gumus D, Chen W, Norton N, Georgieva L, Sari M, O'Donovan MC, Erdogan F, Owen MJ, Ropers HH, Ullmann R (2008) Comparative genome hybridization suggests a role for NRXN1 and APBA2 in schizophrenia. *Human molecular genetics* **17:** 458-465

Kishore U, Reid KB (2000) C1q: structure, function, and receptors. *Immunopharmacology* **49:** 159-170

Kleywegt GJ, Henrick K, Dodson EJ, van Aalten DM (2003) Pound-wise but penny-foolish: How well do micromolecules fare in macromolecular refinement? *Structure* **11:** 1051-1059

Ko J, Kim S, Chung HS, Kim K, Han K, Kim H, Jun H, Kaang BK, Kim E (2006) SALM synaptic cell adhesion-like molecules regulate the differentiation of excitatory synapses. *Neuron* **50:** 233-245

Koehnke J, Jin X, Trbovic N, Katsamba PS, Brasch J, Ahlsen G, Scheiffele P, Honig B, Palmer AG, 3rd, Shapiro L (2008) Crystal structures of beta-neurexin 1 and beta-neurexin 2 ectodomains and dynamics of splice insertion sequence 4. *Structure* **16:** 410-421

Koehnke J, Katsamba PS, Ahlsen G, Bahna F, Vendome J, Honig B, Shapiro L, Jin X (2010) Splice form dependence of beta-neurexin/neuroligin binding interactions. *Neuron* **67:** 61-74

Kohda K, Kakegawa W, Matsuda S, Nakagami R, Kakiya N, Yuzaki M (2007) The extreme C-terminus of GluRdelta2 is essential for induction of long-term depression in cerebellar slices. *The European journal of neuroscience* **25:** 1357-1362

Krissinel E, Henrick K (2007) Inference of macromolecular assemblies from crystalline state. *Journal of molecular biology* **372:** 774-797

Kubota M, Takahashi Y (2008) Steroid-responsive chronic cerebellitis with positive glutamate receptor delta 2 antibody. *Journal of child neurology* **23:** 228-230

Kumar J, Mayer ML (2010) Crystal structures of the glutamate receptor ion channel GluK3 and GluK5 amino-terminal domains. *Journal of molecular biology* **404:** 680-696

Kumar J, Schuck P, Jin R, Mayer ML (2009) The N-terminal domain of GluR6-subtype glutamate receptor ion channels. *Nature structural & molecular biology* **16:** 631-638

Kumar J, Schuck P, Mayer ML (2011) Structure and assembly mechanism for heteromeric kainate receptors. *Neuron* **71:** 319-331

Kumar KN, Tilakaratne N, Johnson PS, Allen AE, Michaelis EK (1991) Cloning of cDNA for the glutamate-binding subunit of an NMDA receptor complex. *Nature* **354:** 70-73

Kunishima N, Shimada Y, Tsuji Y, Sato T, Yamamoto M, Kumasaka T, Nakanishi S, Jingami H, Morikawa K (2000) Structural basis of glutamate recognition by a dimeric metabotropic glutamate receptor. *Nature* **407:** 971-977

Kuroyanagi T, Hirano T (2010) Flap loop of GluD2 binds to Cbln1 and induces presynaptic differentiation. *Biochemical and biophysical research communications* **398:** 537-541

Lachman HM, Fann CS, Bartzis M, Evgrafov OV, Rosenthal RN, Nunes EV, Miner C, Santana M, Gaffney J, Riddick A, Hsu CL, Knowles JA (2007) Genomewide suggestive linkage of opioid dependence to chromosome 14q. *Human molecular genetics* **16:** 1327-1334

Lalouette A, Guenet JL, Vriz S (1998) Hotfoot mouse mutations affect the delta 2 glutamate receptor gene and are allelic to lurcher. *Genomics* **50:** 9-13

Lancaster E, Martinez-Hernandez E, Dalmau J (2011) Encephalitis and antibodies to synaptic and neuronal cell surface proteins. *Neurology* **77:** 179-189

Landsend AS, Amiry-Moghaddam M, Matsubara A, Bergersen L, Usami S, Wenthold RJ, Ottersen OP (1997) Differential localization of delta glutamate receptors in the rat cerebellum: coexpression with AMPA receptors in parallel fiber-spine synapses and absence from climbing fiber-spine synapses. *The Journal of neuroscience : the official journal of the Society for Neuroscience* **17:** 834-842

Langer G, Cohen SX, Lamzin VS, Perrakis A (2008) Automated macromolecular model building for X-ray crystallography using ARP/wARP version 7. *Nature protocols* **3:** 1171-1179

Lee HK, Takamiya K, Han JS, Man H, Kim CH, Rumbaugh G, Yu S, Ding L, He C, Petralia RS, Wenthold RJ, Gallagher M, Huganir RL (2003) Phosphorylation of the AMPA receptor GluR1 subunit is required for synaptic plasticity and retention of spatial memory. *Cell* **112:** 631-643

Lee SJ, Uemura T, Yoshida T, Mishina M (2012) GluRdelta2 assembles four neurexins into trans-synaptic triad to trigger synapse formation. *The Journal of neuroscience : the official journal of the Society for Neuroscience* **32:** 4688-4701

Leone P, Comoletti D, Ferracci G, Conrod S, Garcia SU, Taylor P, Bourne Y, Marchot P (2010) Structural insights into the exquisite selectivity of neurexin/neuroligin synaptic interactions. *The EMBO journal* **29:** 2461-2471

Leuschner WD, Hoch W (1999) Subtype-specific assembly of alpha-amino-3-hydroxy-5-methyl-4-isoxazole propionic acid receptor subunits is mediated by their n-terminal domains. *The Journal of biological chemistry* **274:** 16907-16916

Lomeli H, Sprengel R, Laurie DJ, Kohr G, Herb A, Seeburg PH, Wisden W (1993) The rat delta-1 and delta-2 subunits extend the excitatory amino acid receptor family. *FEBS letters* **315:** 318-322

Lucic V, Yang T, Schweikert G, Forster F, Baumeister W (2005) Morphological characterization of molecular complexes present in the synaptic cleft. *Structure* **13:** 423-434

Malenka RC, Bear MF (2004) LTP and LTD: an embarrassment of riches. *Neuron* **44:** 5-21

Malenka RC, Nicoll RA (1999) Long-term potentiation--a decade of progress? *Science* **285:** 1870-1874

Manto MU, Pandolfo M (2002) The cerebellum and its Disorders. Cambridge University Press

Marshall CR, Noor A, Vincent JB, Lionel AC, Feuk L, Skaug J, Shago M, Moessner R, Pinto D, Ren Y, Thiruvahindrapduram B, Fiebig A, Schreiber S, Friedman J, Ketelaars CE, Vos YJ, Ficicioglu C, Kirkpatrick S, Nicolson R, Sloman L, Summers A, Gibbons CA, Teebi A, Chitayat D, Weksberg R, Thompson A, Vardy C, Crosbie V, Luscombe S, Baatjes R, Zwaigenbaum L, Roberts W, Fernandez B, Szatmari P, Scherer SW (2008) Structural variation of chromosomes in autism spectrum disorder. *American journal of human genetics* **82:** 477-488

Matsuda K, Miura E, Miyazaki T, Kakegawa W, Emi K, Narumi S, Fukazawa Y, Ito-Ishida A, Kondo T, Shigemoto R, Watanabe M, Yuzaki M (2010) Cbln1 is a ligand for an orphan glutamate receptor delta2, a bidirectional synapse organizer. *Science* **328:** 363-368

Matsuda K, Yuzaki M (2011) Cbln family proteins promote synapse formation by regulating distinct neurexin signaling pathways in various brain regions. *The European journal of neuroscience* **33:** 1447-1461

Matsuda K, Yuzaki M (2012) Cbln1 and the delta2 glutamate receptor--an orphan ligand and an orphan receptor find their partners. *Cerebellum* **11:** 78-84

Matsuda S, Yuzaki M (2002) Mutation in hotfoot-4J mice results in retention of delta2 glutamate receptors in ER. *The European journal of neuroscience* **16:** 1507-1516

Matsuo M, Takahashi Y, Taniguchi K, Sasaki K, Hamasaki Y (2007) Chronic myoclonia of subcortical origin with antiglutamate receptor antibodies. *Journal of child neurology* **22:** 1393-1396

Mayer ML (2005) Crystal structures of the GluR5 and GluR6 ligand binding cores: molecular mechanisms underlying kainate receptor selectivity. *Neuron* **45:** 539-552

Mayer ML (2006) Glutamate receptors at atomic resolution. *Nature* **440:** 456-462

Mayer ML (2011a) Emerging models of glutamate receptor ion channel structure and function. *Structure* **19:** 1370-1380

Mayer ML (2011b) Structure and mechanism of glutamate receptor ion channel assembly, activation and modulation. *Current opinion in neurobiology* **21:** 283-290

Mayer ML, Westbrook GL, Guthrie PB (1984) Voltage-dependent block by Mg2+ of NMDA responses in spinal cord neurones. *Nature* **309:** 261-263

Mayo CJ, Diprose JM, Walter TS, Berry IM, Wilson J, Owens RJ, Jones EY, Harlos K, Stuart DI, Esnouf RM (2005) Benefits of automated crystallization plate tracking, imaging, and analysis. *Structure* **13:** 175-182

McAllister AK (2007) Dynamic aspects of CNS synapse formation. *Annual review of neuroscience* **30:** 425-450

McCoy AJ, Grosse-Kunstleve RW, Adams PD, Winn MD, Storoni LC, Read RJ (2007) Phaser crystallographic software. *Journal of applied crystallography* **40:** 658-674

Meddows E, Le Bourdelles B, Grimwood S, Wafford K, Sandhu S, Whiting P, McIlhinney RA (2001) Identification of molecular determinants that are important in the assembly of N-methyl-D-aspartate receptors. *The Journal of biological chemistry* **276:** 18795-18803

Miller MT, Mileni M, Comoletti D, Stevens RC, Harel M, Taylor P (2011) The crystal structure of the alpha-neurexin-1 extracellular region reveals a hinge point for mediating synaptic adhesion and function. *Structure* **19:** 767-778

Missler M, Sudhof TC (1998) Neurexins: three genes and 1001 products. *Trends in genetics : TIG* **14:** 20-26

Miura E, Iijima T, Yuzaki M, Watanabe M (2006) Distinct expression of Cbln family mRNAs in developing and adult mouse brains. *The European journal of neuroscience* **24:** 750-760

Miura E, Matsuda K, Morgan JI, Yuzaki M, Watanabe M (2009) Cbln1 accumulates and colocalizes with Cbln3 and GluRdelta2 at parallel fiber-Purkinje cell synapses in the mouse cerebellum. *The European journal of neuroscience* **29:** 693-706

Miyagi Y, Yamashita T, Fukaya M, Sonoda T, Okuno T, Yamada K, Watanabe M, Nagashima Y, Aoki I, Okuda K, Mishina M, Kawamoto S (2002) Delphilin: a novel PDZ and formin homology domain-containing protein that synaptically colocalizes and interacts with glutamate receptor delta 2 subunit. *The Journal of neuroscience : the official journal of the Society for Neuroscience* **22:** 803-814

Moremen KW, Tiemeyer M, Nairn AV (2012) Vertebrate protein glycosylation: diversity, synthesis and function. *Nature reviews Molecular cell biology* **13:** 448-462

Mullis KB, Faloona FA (1987) Specific synthesis of DNA in vitro via a polymerase-catalyzed chain reaction. *Methods in enzymology* **155:** 335-350

Murshudov GN, Vagin AA, Dodson EJ (1997a) Refinement of Macromolecular Structures by the Maximum-Likelihood Method. *Acta Crystallographica Section D* **53:** 240-255

Murshudov GN, Vagin AA, Dodson EJ (1997b) Refinement of macromolecular structures by the maximum-likelihood method. *Acta crystallographica Section D, Biological crystallography* **53:** 240-255

Nakagawa T (2010) The biochemistry, ultrastructure, and subunit assembly mechanism of AMPA receptors. *Molecular neurobiology* **42:** 161-184

Nakagawa T, Cheng Y, Ramm E, Sheng M, Walz T (2005) Structure and different conformational states of native AMPA receptor complexes. *Nature* **433:** 545-549

Naur P, Hansen KB, Kristensen AS, Dravid SM, Pickering DS, Olsen L, Vestergaard B, Egebjerg J, Gajhede M, Traynelis SF, Kastrup JS (2007) Ionotropic glutamate-like receptor delta2 binds D-serine and glycine. *Proceedings of the National Academy of Sciences of the United States of America* **104:** 14116-14121

Nomura T, Kakegawa W, Matsuda S, Kohda K, Nishiyama J, Takahashi T, Yuzaki M (2012) Cerebellar long-term depression requires dephosphorylation of TARP in Purkinje cells. *The European journal of neuroscience* **35:** 402-410

Nowak L, Bregestovski P, Ascher P, Herbet A, Prochiantz A (1984) Magnesium gates glutamate-activated channels in mouse central neurones. *Nature* **307:** 462-465

O'Brien RJ, Xu D, Petralia RS, Steward O, Huganir RL, Worley P (1999) Synaptic clustering of AMPA receptors by the extracellular immediate-early gene product Narp. *Neuron* **23:** 309-323

O'Halloran CJ, Kinsella GJ, Storey E (2012) The cerebellum and neuropsychological functioning: a critical review. *Journal of clinical and experimental neuropsychology* **34:** 35-56

Oliet SH, Mothet JP (2009) Regulation of N-methyl-D-aspartate receptors by astrocytic D-serine. *Neuroscience* **158:** 275-283

Orsetti M, Di Brisco F, Canonico PL, Genazzani AA, Ghi P (2008) Gene regulation in the frontal cortex of rats exposed to the chronic mild stress paradigm, an animal model of human depression. *The European journal of neuroscience* **27:** 2156-2164

Otwinowski Z, Minor W (1997) [20] Processing of X-ray diffraction data collected in oscillation mode. In *Methods Enzymol*, Charles W. Carter, Jr. (ed), Vol. Volume 276, pp 307-326. Academic Press

Padilla JE, Yeates TO (2003) A statistic for local intensity differences: robustness to anisotropy and pseudo-centering and utility for detecting twinning. *Acta crystallographica Section D, Biological crystallography* **59:** 1124-1130

Pang Z, Zuo J, Morgan JI (2000) Cbln3, a novel member of the precerebellin family that binds specifically to Cbln1. *The Journal of neuroscience : the official journal of the Society for Neuroscience* **20:** 6333-6339

Paoletti P, Perin-Dureau F, Fayyazuddin A, Le Goff A, Callebaut I, Neyton J (2000) Molecular organization of a zinc binding n-terminal modulatory domain in a NMDA receptor subunit. *Neuron* **28:** 911-925

Penzes P, Cahill ME, Jones KA, VanLeeuwen JE, Woolfrey KM (2011) Dendritic spine pathology in neuropsychiatric disorders. *Nature neuroscience* **14:** 285-293

Petersen TN, Brunak S, von Heijne G, Nielsen H (2011) SignalP 4.0: discriminating signal peptides from transmembrane regions. *Nature methods* **8:** 785-786

Reeves PJ, Callewaert N, Contreras R, Khorana HG (2002) Structure and function in rhodopsin: high-level expression of rhodopsin with restricted and homogeneous N-glycosylation by a tetracycline-inducible N-acetylglucosaminyltransferase I-negative HEK293S stable mammalian cell line. *Proceedings of the National Academy of Sciences of the United States of America* **99:** 13419-13424

Roche KW, Ly CD, Petralia RS, Wang YX, McGee AW, Bredt DS, Wenthold RJ (1999) Postsynaptic density-93 interacts with the delta2 glutamate receptor subunit at parallel fiber synapses. *The Journal of neuroscience : the official journal of the Society for Neuroscience* **19:** 3926-3934

Rogers SW, Andrews PI, Gahring LC, Whisenand T, Cauley K, Crain B, Hughes TE, Heinemann SF, McNamara JO (1994) Autoantibodies to glutamate receptor GluR3 in Rasmussen's encephalitis. *Science* **265:** 648-651

Rossmann M, Sukumaran M, Penn AC, Veprintsev DB, Babu MM, Greger IH (2011) Subunit-selective N-terminal domain associations organize the formation of AMPA receptor heteromers. *The EMBO journal* **30:** 959-971

Rudenko G, Nguyen T, Chelliah Y, Sudhof TC, Deisenhofer J (1999) The structure of the ligand-binding domain of neurexin Ibeta: regulation of LNS domain function by alternative splicing. *Cell* **99:** 93-101

Ryu K, Yokoyama M, Yamashita M, Hirano T (2012) Induction of excitatory and inhibitory presynaptic differentiation by GluD1. *Biochemical and biophysical research communications* **417:** 157-161

Sack JS, Saper MA, Quiocho FA (1989) Periplasmic binding protein structure and function. Refined X-ray structures of the leucine/isoleucine/valine-binding protein and its complex with leucine. *Journal of molecular biology* **206:** 171-191

Saglietti L, Dequidt C, Kamieniarz K, Rousset MC, Valnegri P, Thoumine O, Beretta F, Fagni L, Choquet D, Sala C, Sheng M, Passafaro M (2007) Extracellular interactions between GluR2 and N-cadherin in spine regulation. *Neuron* **54:** 461-477

Schmid SM, Hollmann M (2010) Bridging the synaptic cleft: lessons from orphan glutamate receptors. *Science signaling* **3:** pe28

Schmid SM, Kott S, Sager C, Huelsken T, Hollmann M (2009) The glutamate receptor subunit delta2 is capable of gating its intrinsic ion channel as revealed by ligand binding domain transplantation. *Proceedings of the National Academy of Sciences of the United States of America* **106:** 10320-10325

Schwarz F, Aebi M (2011) Mechanisms and principles of N-linked protein glycosylation. *Current opinion in structural biology* **21:** 576-582

Seiradake E, Harlos K, Sutton G, Aricescu AR, Jones EY (2010) An extracellular steric seeding mechanism for Eph-ephrin signaling platform assembly. *Nature structural & molecular biology* **17:** 398-402

Selkoe DJ (2002) Alzheimer's disease is a synaptic failure. *Science* **298:** 789-791

Sensi SL, Paoletti P, Bush AI, Sekler I (2009) Zinc in the physiology and pathology of the CNS. *Nature reviews Neuroscience* **10:** 780-791

Shanks NF, Maruo T, Farina AN, Ellisman MH, Nakagawa T (2010) Contribution of the global subunit structure and stargazin on the maturation of AMPA receptors. *The Journal of neuroscience : the official journal of the Society for Neuroscience* **30:** 2728-2740

Shapiro L, Scherer PE (1998) The crystal structure of a complement-1q family protein suggests an evolutionary link to tumor necrosis factor. *Current biology : CB* **8:** 335-338

Sheckler LR, Henry L, Sugita S, Sudhof TC, Rudenko G (2006) Crystal structure of the second LNS/LG domain from neurexin 1alpha: Ca2+ binding and the effects of alternative splicing. *The Journal of biological chemistry* **281:** 22896-22905

Shen K, Scheiffele P (2010) Genetics and cell biology of building specific synaptic connectivity. *Annual review of neuroscience* **33:** 473-507

Shen KC, Kuczynska DA, Wu IJ, Murray BH, Sheckler LR, Rudenko G (2008) Regulation of neurexin 1beta tertiary structure and ligand binding through alternative splicing. *Structure* **16:** 422-431

Shepherd JD, Huganir RL (2007) The cell biology of synaptic plasticity: AMPA receptor trafficking. *Annual review of cell and developmental biology* **23:** 613-643

Shiihara T, Kato M, Konno A, Takahashi Y, Hayasaka K (2007) Acute cerebellar ataxia and consecutive cerebellitis produced by glutamate receptor delta2 autoantibody. *Brain & development* **29:** 254-256

Shimokaze T, Kato M, Yoshimura Y, Takahashi Y, Hayasaka K (2007) A case of acute cerebellitis accompanied by autoantibodies against glutamate receptor delta2. *Brain & development* **29:** 224-226

Sia GM, Beique JC, Rumbaugh G, Cho R, Worley PF, Huganir RL (2007) Interaction of the N-terminal domain of the AMPA receptor GluR4 subunit with the neuronal pentraxin NP1 mediates GluR4 synaptic recruitment. *Neuron* **55:** 87-102

Simon JR, Contrera JF, Kuhar MJ (1976) Binding of [3H] kainic acid, and analogue of Lglutamate, to brain membranes. *Journal of neurochemistry* **26:** 141-147

Slemmon JR, Blacher R, Danho W, Hempstead JL, Morgan JI (1984) Isolation and sequencing of two cerebellum-specific peptides. *Proceedings of the National Academy of Sciences of the United States of America* **81:** 6866-6870

Smart OS, Womack TO, Flensburg C, Keller P, Paciorek W, Sharff A, Vonrhein C, Bricogne G (2012) Exploiting structure similarity in refinement: automated NCS and target-structure restraints in BUSTER. *Acta crystallographica Section D, Biological crystallography* **68:** 368-380

Smith M, Spence MA, Flodman P (2009) Nuclear and mitochondrial genome defects in autisms. *Annals of the New York Academy of Sciences* **1151:** 102-132

Sobolevsky AI, Rosconi MP, Gouaux E (2009) X-ray structure, symmetry and mechanism of an AMPA-subtype glutamate receptor. *Nature* **462:** 745-756

Soding J, Biegert A, Lupas AN (2005) The HHpred interactive server for protein homology detection and structure prediction. *Nucleic acids research* **33:** W244-248

Standfuss J, Edwards PC, D'Antona A, Fransen M, Xie G, Oprian DD, Schertler GF (2011) The structural basis of agonist-induced activation in constitutively active rhodopsin. *Nature* **471:** 656-660

Steinberg JP, Takamiya K, Shen Y, Xia J, Rubio ME, Yu S, Jin W, Thomas GM, Linden DJ, Huganir RL (2006) Targeted in vivo mutations of the AMPA receptor subunit GluR2 and its interacting protein PICK1 eliminate cerebellar long-term depression. *Neuron* **49:** 845-860

Stuart DI, Levine M, Muirhead H, Stammers DK (1979) Crystal structure of cat muscle pyruvate kinase at a resolution of 2.6 A. *Journal of molecular biology* **134:** 109-142

Sudhof TC (2008) Neuroligins and neurexins link synaptic function to cognitive disease. *Nature* **455:** 903-911

Sugiyama N, Hamano S, Mochizuki M, Tanaka M, Takahashi Y (2004) [A case of chronic cerebellitis with anti-glutamate receptor delta 2 antibody]. *No to hattatsu Brain and development* **36:** 60-63

Sukumaran M, Rossmann M, Shrivastava I, Dutta A, Bahar I, Greger IH (2011) Dynamics and allosteric potential of the AMPA receptor N-terminal domain. *The EMBO journal* **30:** 972-982

Sun Y, Olson R, Horning M, Armstrong N, Mayer M, Gouaux E (2002) Mechanism of glutamate receptor desensitization. *Nature* **417:** 245-253

Szatmari P, Paterson AD, Zwaigenbaum L, Roberts W, Brian J, Liu XQ, Vincent JB, Skaug JL, Thompson AP, Senman L, Feuk L, Qian C, Bryson SE, Jones MB, Marshall CR, Scherer SW, Vieland VJ, Bartlett C, Mangin LV, Goedken R, Segre A, Pericak-Vance MA, Cuccaro ML, Gilbert JR, Wright HH, Abramson RK, Betancur C, Bourgeron T, Gillberg C, Leboyer M, Buxbaum JD, Davis KL, Hollander E, Silverman JM, Hallmayer J, Lotspeich L, Sutcliffe JS, Haines JL, Folstein SE, Piven J, Wassink TH, Sheffield V, Geschwind DH, Bucan M, Brown WT, Cantor RM, Constantino JN, Gilliam TC, Herbert M, Lajonchere C, Ledbetter DH, Lese-Martin C, Miller J, Nelson S, Samango-Sprouse CA, Spence S, State M, Tanzi RE, Coon H, Dawson G, Devlin B, Estes A, Flodman P, Klei L, McMahon WM, Minshew N, Munson J, Korvatska E, Rodier PM, Schellenberg GD, Smith M, Spence MA, Stodgell C, Tepper PG, Wijsman EM, Yu CE, Roge B, Mantoulan C, Wittemeyer K, Poustka A, Felder B, Klauck SM, Schuster C, Poustka F, Bolte S, Feineis-Matthews S, Herbrecht E, Schmotzer G, Tsiantis J, Papanikolaou K, Maestrini E, Bacchelli E, Blasi F, Carone S, Toma C, Van Engeland H, de Jonge M, Kemner C, Koop F, Langemeijer M, Hijmans C, Staal WG, Baird G, Bolton PF, Rutter ML, Weisblatt E, Green J, Aldred C, Wilkinson JA, Pickles A, Le Couteur A, Berney T, McConachie H, Bailey AJ, Francis K, Honeyman G, Hutchinson A, Parr JR, Wallace S, Monaco AP, Barnby G, Kobayashi K, Lamb JA, Sousa I, Sykes N, Cook EH, Guter SJ, Leventhal BL, Salt J, Lord C, Corsello C, Hus V, Weeks DE, Volkmar F, Tauber M, Fombonne E, Shih A, Meyer KJ (2007) Mapping autism risk loci using genetic linkage and chromosomal rearrangements. *Nature genetics* **39:** 319-328

Takahashi H, Katayama K, Sohya K, Miyamoto H, Prasad T, Matsumoto Y, Ota M, Yasuda H, Tsumoto T, Aruga J, Craig AM (2012) Selective control of inhibitory synapse development by Slitrk3-PTPdelta trans-synaptic interaction. *Nature neuroscience* **15:** 389-398, S381-382

Takasu MA, Dalva MB, Zigmond RE, Greenberg ME (2002) Modulation of NMDA receptor-dependent calcium influx and gene expression through EphB receptors. *Science* **295:** 491-495

Takeuchi T, Miyazaki T, Watanabe M, Mori H, Sakimura K, Mishina M (2005) Control of synaptic connection by glutamate receptor delta2 in the adult cerebellum. *The Journal of neuroscience : the official journal of the Society for Neuroscience* **25:** 2146-2156

Tanaka H, Miyazaki N, Matoba K, Nogi T, Iwasaki K, Takagi J (2012) Higher-order architecture of cell adhesion mediated by polymorphic synaptic adhesion molecules neurexin and neuroligin. *Cell reports* **2:** 101-110

Tanaka H, Nogi T, Yasui N, Iwasaki K, Takagi J (2011) Structural basis for variant-specific neuroligin-binding by alpha-neurexin. *PloS one* **6:** e19411

Tichelaar W, Safferling M, Keinanen K, Stark H, Madden DR (2004) The Three-dimensional Structure of an Ionotropic Glutamate Receptor Reveals a Dimer-of-dimers Assembly. *Journal of molecular biology* **344:** 435-442

Togashi H, Abe K, Mizoguchi A, Takaoka K, Chisaka O, Takeichi M (2002) Cadherin regulates dendritic spine morphogenesis. *Neuron* **35:** 77-89

Tomioka S, Shimono M, Kato A, Takano K, Shiota N, Takahashi Y (2008) [A 16-year-old boy with meningoencephalitis with auto-antibody against glutamate receptor]. *No to hattatsu Brain and development* **40:** 42-46

Traynelis SF, Wollmuth LP, McBain CJ, Menniti FS, Vance KM, Ogden KK, Hansen KB, Yuan H, Myers SJ, Dingledine R (2010) Glutamate receptor ion channels: structure, regulation, and function. *Pharmacological reviews* **62:** 405-496

Treutlein J, Muhleisen TW, Frank J, Mattheisen M, Herms S, Ludwig KU, Treutlein T, Schmael C, Strohmaier J, Bosshenz KV, Breuer R, Paul T, Witt SH, Schulze TG, Schlosser RG, Nenadic I, Sauer H, Becker T, Maier W, Cichon S, Nothen MM, Rietschel M (2009) Dissection of phenotype reveals possible association between schizophrenia and Glutamate Receptor Delta 1 (GRID1) gene promoter. *Schizophrenia research* **111:** 123-130

Uemura T, Lee SJ, Yasumura M, Takeuchi T, Yoshida T, Ra M, Taguchi R, Sakimura K, Mishina M (2010) Trans-synaptic interaction of GluRdelta2 and Neurexin through Cbln1 mediates synapse formation in the cerebellum. *Cell* **141:** 1068-1079

Uemura T, Mishina M (2008) The amino-terminal domain of glutamate receptor delta2 triggers presynaptic differentiation. *Biochemical and biophysical research communications* **377:** 1315-1319

Urade Y, Oberdick J, Molinar-Rode R, Morgan JI (1991) Precerebellin is a cerebellum-specific protein with similarity to the globular domain of complement C1q B chain. *Proceedings of the National Academy of Sciences of the United States of America* **88:** 1069-1073

Ushkaryov YA, Petrenko AG, Geppert M, Sudhof TC (1992) Neurexins: synaptic cell surface proteins related to the alpha-latrotoxin receptor and laminin. *Science* **257:** 50-56

Usui D, Mitsuda N, Hosokawa T, Fujieda M, Takahashi Y, Wakiguchi H (2011) [A case of persistent cerebellar ataxia complicated by conversion disorder--confirmed by positive cerebrospinal fluid glutamate receptor delta2 and epsilon2 antibodies]. *No to hattatsu Brain and development* **43:** 41-45

van Bon BW, Balciuniene J, Fruhman G, Nagamani SC, Broome DL, Cameron E, Martinet D, Roulet E, Jacquemont S, Beckmann JS, Irons M, Potocki L, Lee B, Cheung SW, Patel A, Bellini M, Selicorni A, Ciccone R, Silengo M, Vetro A, Knoers NV, de Leeuw N, Pfundt R, Wolf B, Jira P, Aradhya S, Stankiewicz P, Brunner HG, Zuffardi O, Selleck SB, Lupski JR, de Vries BB (2011) The phenotype of recurrent 10q22q23 deletions and duplications. *European journal of human genetics : EJHG* **19:** 400-408

Van den Oever MC, Goriounova NA, Li KW, Van der Schors RC, Binnekade R, Schoffelmeer AN, Mansvelder HD, Smit AB, Spijker S, De Vries TJ (2008) Prefrontal cortex AMPA receptor plasticity is crucial for cue-induced relapse to heroin-seeking. *Nature neuroscience* **11:** 1053-1058

Venken T, Alaerts M, Souery D, Goossens D, Sluijs S, Navon R, Van Broeckhoven C, Mendlewicz J, Del-Favero J, Claes S (2008) Chromosome 10q harbors a susceptibility locus for bipolar disorder in Ashkenazi Jewish families. *Molecular psychiatry* **13:** 442-450

Venskutonyte R, Frydenvang K, Gajhede M, Bunch L, Pickering DS, Kastrup JS (2011) Binding site and interlobe interactions of the ionotropic glutamate receptor GluK3 ligand binding domain revealed by high resolution crystal structure in complex with (S)-glutamate. *Journal of structural biology* **176:** 307-314

Vincent A, Bien CG, Irani SR, Waters P (2011) Autoantibodies associated with diseases of the CNS: new developments and future challenges. *Lancet neurology* **10:** 759-772

Vogel M (2005) The cerebellum. *The American journal of psychiatry* **162:** 1253

Vogel MW, Caston J, Yuzaki M, Mariani J (2007) The Lurcher mouse: fresh insights from an old mutant. *Brain research* **1140:** 4-18

Waites CL, Craig AM, Garner CC (2005) Mechanisms of vertebrate synaptogenesis. *Annual review of neuroscience* **28:** 251-274

Walsh T, McClellan JM, McCarthy SE, Addington AM, Pierce SB, Cooper GM, Nord AS, Kusenda M, Malhotra D, Bhandari A, Stray SM, Rippey CF, Roccanova P, Makarov V, Lakshmi B, Findling RL, Sikich L, Stromberg T, Merriman B, Gogtay N, Butler P, Eckstrand K, Noory L, Gochman P, Long R, Chen Z, Davis S, Baker C, Eichler EE, Meltzer PS, Nelson SF, Singleton AB, Lee MK, Rapoport JL, King MC, Sebat J (2008) Rare structural variants disrupt multiple genes in neurodevelopmental pathways in schizophrenia. *Science* **320:** 539-543

Walter TS, Diprose JM, Mayo CJ, Siebold C, Pickford MG, Carter L, Sutton GC, Berrow NS, Brown J, Berry IM, Stewart-Jones GB, Grimes JM, Stammers DK, Esnouf RM, Jones EY, Owens RJ, Stuart DI, Harlos K (2005) A procedure for setting up high-throughput nanolitre crystallization experiments. Crystallization workflow for initial screening, automated storage, imaging and optimization. *Acta crystallographica Section D, Biological crystallography* **61:** 651-657

Walter TS, Mancini EJ, Kadlec J, Graham SC, Assenberg R, Ren J, Sainsbury S, Owens RJ, Stuart DI, Grimes JM, Harlos K (2008) Semi-automated microseeding of nanolitre crystallization experiments. *Acta crystallographica Section F, Structural biology and crystallization communications* **64:** 14-18

Walter TS, Meier C, Assenberg R, Au KF, Ren J, Verma A, Nettleship JE, Owens RJ, Stuart DI, Grimes JM (2006) Lysine methylation as a routine rescue strategy for protein crystallization. *Structure* **14:** 1617-1622

Wang LZ, Zhu XZ (2003) Spatiotemporal relationships among D-serine, serine racemase, and D-amino acid oxidase during mouse postnatal development. *Acta pharmacologica Sinica* **24:** 965-974

Wang Y, Matsuda S, Drews V, Torashima T, Meisler MH, Yuzaki M (2003) A hot spot for hotfoot mutations in the gene encoding the delta2 glutamate receptor. *The European journal of neuroscience* **17:** 1581-1590

Wang YT, Linden DJ (2000) Expression of cerebellar long-term depression requires postsynaptic clathrin-mediated endocytosis. *Neuron* **25:** 635-647

Wei P, Pattarini R, Rong Y, Guo H, Bansal PK, Kusnoor SV, Deutch AY, Parris J, Morgan JI (2012) The Cbln family of proteins interact with multiple signaling pathways. *Journal of neurochemistry* **121:** 717-729

Winn MD, Ballard CC, Cowtan KD, Dodson EJ, Emsley P, Evans PR, Keegan RM, Krissinel EB, Leslie AG, McCoy A, McNicholas SJ, Murshudov GN, Pannu NS, Potterton EA, Powell HR, Read RJ, Vagin A, Wilson KS (2011) Overview of the CCP4 suite and current developments. *Acta crystallographica Section D, Biological crystallography* **67:** 235-242

Winter G (2010) xia2: an expert system for macromolecular crystallography data reduction. *Journal of applied crystallography* **43:** 186-190

Wittig I, Braun HP, Schagger H (2006) Blue native PAGE. *Nature protocols* **1:** 418-428

Wollmuth LP, Sobolevsky AI (2004) Structure and gating of the glutamate receptor ion channel. *Trends in neurosciences* **27:** 321-328

Wong JP, Reboul E, Molday RS, Kast J (2009) A carboxy-terminal affinity tag for the purification and mass spectrometric characterization of integral membrane proteins. *Journal of proteome research* **8:** 2388-2396

Woo J, Kwon SK, Choi S, Kim S, Lee JR, Dunah AW, Sheng M, Kim E (2009) Trans-synaptic adhesion between NGL-3 and LAR regulates the formation of excitatory synapses. *Nature neuroscience* **12:** 428-437

Wulhfard S, Baldi L, Hacker DL, Wurm F (2010) Valproic acid enhances recombinant mRNA and protein levels in transiently transfected Chinese hamster ovary cells. *Journal of biotechnology* **148:** 128-132

Yadav R, Gupta SC, Hillman BG, Bhatt JM, Stairs DJ, Dravid SM (2012) Deletion of glutamate delta-1 receptor in mouse leads to aberrant emotional and social behaviors. *PloS one* **7:** e32969

Yadav R, Rimerman R, Scofield MA, Dravid SM (2011) Mutations in the transmembrane domain M3 generate spontaneously open orphan glutamate delta1 receptor. *Brain research* **1382:** 1-8

Yan J, Noltner K, Feng J, Li W, Schroer R, Skinner C, Zeng W, Schwartz CE, Sommer SS (2008) Neurexin 1alpha structural variants associated with autism. *Neuroscience letters* **438:** 368-370

Yang ZR, Thomson R, McNeil P, Esnouf RM (2005) RONN: the bio-basis function neural network technique applied to the detection of natively disordered regions in proteins. *Bioinformatics* **21:** 3369-3376

Yao G, Zong Y, Gu S, Zhou J, Xu H, Mathews, II, Jin R (2011) Crystal structure of the glutamate receptor GluA1 N-terminal domain. *The Biochemical journal* **438:** 255-263

Yao Y, Harrison CB, Freddolino PL, Schulten K, Mayer ML (2008) Molecular mechanism of ligand recognition by NR3 subtype glutamate receptors. *The EMBO journal* **27:** 2158-2170

Yap CC, Muto Y, Kishida H, Hashikawa T, Yano R (2003) PKC regulates the delta2 glutamate receptor interaction with S-SCAM/MAGI-2 protein. *Biochemical and biophysical research communications* **301:** 1122-1128

Yasumura M, Yoshida T, Lee SJ, Uemura T, Joo JY, Mishina M (2012) Glutamate receptor delta1 induces preferentially inhibitory presynaptic differentiation of cortical neurons by interacting with neurexins through cerebellin precursor protein subtypes. *Journal of neurochemistry* **121:** 705-716

Yuan H, Hansen KB, Vance KM, Ogden KK, Traynelis SF (2009) Control of NMDA receptor function by the NR2 subunit amino-terminal domain. *The Journal of neuroscience : the official journal of the Society for Neuroscience* **29:** 12045-12058

Yuzaki M (2003) The delta2 glutamate receptor: 10 years later. *Neuroscience research* **46:** 11-22

Yuzaki M (2008) Cbln and C1q family proteins: new transneuronal cytokines. *Cellular and molecular life sciences : CMLS* **65:** 1698-1705

Yuzaki M (2009) New (but old) molecules regulating synapse integrity and plasticity: Cbln1 and the delta2 glutamate receptor. *Neuroscience* **162:** 633-643

Yuzaki M (2012) The ins and outs of GluD2--why and how Purkinje cells use the special glutamate receptor. *Cerebellum* **11:** 438-439

Zahir FR, Baross A, Delaney AD, Eydoux P, Fernandes ND, Pugh T, Marra MA, Friedman JM (2008) A patient with vertebral, cognitive and behavioural abnormalities and a de novo deletion of NRXN1alpha. *Journal of medical genetics* **45:** 239-243

Zerem A, Vinkler C, Michelson M, Leshinsky-Silver E, Lerman-Sagie T, Lev D (2011) Mosaic marker chromosome 16 resulting in 16q11.2-q12.1 gain in a child with intellectual disability, microcephaly, and cerebellar cortical dysplasia. *American journal of medical genetics Part A* **155A:** 2991-2996

Zhao HM, Wenthold RJ, Petralia RS (1998) Glutamate receptor targeting to synaptic populations on Purkinje cells is developmentally regulated. *The Journal of neuroscience : the official journal of the Society for Neuroscience* **18:** 5517-5528

Zhao Y, Bishop B, Clay JE, Lu W, Jones M, Daenke S, Siebold C, Stuart DI, Jones EY, Aricescu AR (2011) Automation of large scale transient protein expression in mammalian cells. *Journal of structural biology* **175:** 209-215

Zhu Y, Kalbfleisch T, Brennan MD, Li Y (2009) A MicroRNA gene is hosted in an intron of a schizophrenia-susceptibility gene. *Schizophrenia research* **109:** 86-89

Zuber B, Nikonenko I, Klauser P, Muller D, Dubochet J (2005) The mammalian central nervous synaptic cleft contains a high density of periodically organized complexes. *Proceedings of the National Academy of Sciences of the United States of America* **102:** 19192-19197

Zuo J, De Jager PL, Takahashi KA, Jiang W, Linden DJ, Heintz N (1997) Neurodegeneration in Lurcher mice caused by mutation in delta2 glutamate receptor gene. *Nature* **388:** 769-773